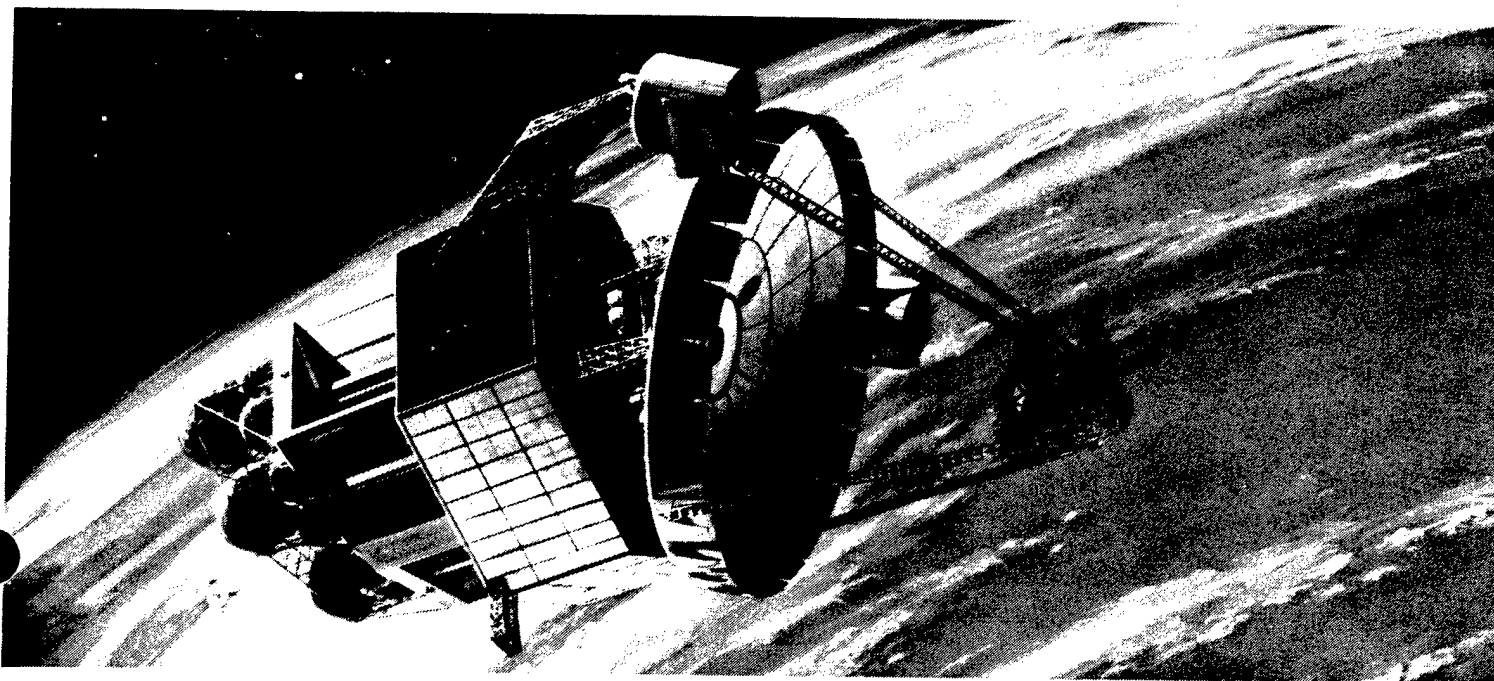


# ● **Advanced Phased Array Chemical High Energy (APACHE) Laser Program**

**DISTRIBUTION STATEMENT A**  
Approved for public release;  
Distribution Unlimited



## **Final Report – Volume II**

**19 January 1990**

G. Koop  
B. Bendow  
D. Dee  
J. Graham  
P. Jarecke  
S. Pfeiffer  
J. Reeve  
S. Taylor  
R. Wagner  
Space & Technology Group  
TRW Inc.  
One Space Park  
Redondo Beach, CA 90278

M. Kahan  
Optical Research, Associates  
Framingham, Massachusetts

19980513 002

U3246

**PLEASE RETURN TO:**  
BMD TECHNICAL INFORMATION CENTER  
BALLISTIC MISSILE DEFENSE ORGANIZATION  
7100 DEFENSE PENTAGON  
WASHINGTON D.C. 20301-7100

Prepared for  
**Strategic Defense Initiative Organization**  
Directed Energy Office  
Pentagon  
Washington, DC 20301-7100

**Naval Research Laboratory**  
4555 Overlook Avenue  
Washington, DC 20375

**DTIC QUALITY INSPECTED 3**

Accession Number: 3246

Publication Date: Jan 19, 1990

Title: Advanced Phased Array Chemical Energy (APACHE) Laser Program: Volume II

Personal Author: Koop, G.; Bendow, B.; Dee, D.; et al.

Corporate Author Or Publisher: TRW Inc., One Space Park, Redondo Beach, CA 90278 Report Number: AP-1985

Report Prepared for: Naval Research Laboratory, Washington, DC 20375-5000

Comments on Document: Inventory for TN Final Report-Volume II

Descriptors, Keywords: SBL Space Base Laser Phase Conjugation Oscillator Isolation Component Amplifier Model Analysis Chemical APACHE

Pages: 00384

Cataloged Date: Nov 11, 1991

Contract Number: N00014-86-C-2345

Document Type: HC

Number of Copies In Library: 000001

Record ID: 22859

Unclassified

SECURITY CLASSIFICATION OF THIS PAGE

VOLUME II

## REPORT DOCUMENTATION PAGE

1. REPORT SECURITY CLASSIFICATION Unclassified			1b. RESTRICTIVE MARKINGS		
2a. SECURITY CLASSIFICATION AUTHORITY OPNAVINST 5513.817			3. DISTRIBUTION/AVAILABILITY OF REPORT Unlimited		
2b. DECLASSIFICATION/DOWNGRADING SCHEDULE OADR					
4. PERFORMING ORGANIZATION REPORT NUMBER(S) AP-1985			5. MONITORING ORGANIZATION REPORT NUMBER(S)		
6a. NAME OF PERFORMING ORGANIZATION Applied Technology Division Space & Technology Group, TRW		6b. OFFICE SYMBOL (If applicable)	7a. NAME OF MONITORING ORGANIZATION Naval Research Laboratory		
6c. ADDRESS (City, State and ZIP Code) One Space Park Redondo Beach, California 90278			7b. ADDRESS (City, State and ZIP Code) Washington, D. C. 20375-5000		
8a. NAME OF FUNDING/SPONSORING ORGANIZATION Strategic Defense Initiative Organization		8b. OFFICE SYMBOL (If applicable) DEO	9. PROCUREMENT INSTRUMENT IDENTIFICATION NUMBER N00014-86-C-2345		
8c. ADDRESS (City, State and ZIP Code) Washington, D. C. 20301-7100			10. SOURCE OF FUNDING NOS.		
			PROGRAM ELEMENT NO.	PROJECT NO.	TASK NO.
			WORK UNIT NO.		
11. TITLE (Include Security Classification) Advanced Phased Array Chemical High Energy Laser System (APACHE) (U)					
12. PERSONAL AUTHOR(S) C. G. Koop, B. Bendow, D. Dee, J. Graham, P. Jarecke, S. Pfeifer, J. Reeve, S. Taylor and R. Wagner					
13a. TYPE OF REPORT Final		13b. TIME COVERED FROM 03/09/86 TO 11/20/89		14. DATE OF REPORT (Yr., Mo., Day) 1990 January 19	
				15. PAGE COUNT 384	
16. SUPPLEMENTARY NOTATION					
17. COSATI CODES			18. SUBJECT TERMS (Continue on reverse if necessary and identify by block number)		
FIELD	GROUP	SUB. GR.			
19. ABSTRACT (Continue on reverse if necessary and identify by block number) Volume II of the final report for the Advanced Phased Array Chemical High Energy (APACHE) laser program presents system engineering which specifies requirements, formulates conceptual designs and performs systems effectiveness analyses for phase conjugate space-based lasers (SBLs). The primary thrust of the systems engineering effort was the formulation of a conceptual design for an APACHE SBL based on the results of detailed modeling, simulation and analysis. The APACHE program also addressed the effectiveness of phase conjugated SBL systems, comparing "conventional" SBLs using active adaptive optics for wavefront correction with phase conjugate SBLs using passive means to both correct wavefronts as well as combine beams from multiple devices.					
20. DISTRIBUTION/AVAILABILITY OF ABSTRACT CLASSIFIED/UNLIMITED <input checked="" type="checkbox"/> SAME AS RPT. <input type="checkbox"/> DTIC USERS <input type="checkbox"/>			21. ABSTRACT SECURITY CLASSIFICATION Unclassified		
22a. NAME OF RESPONSIBLE INDIVIDUAL C.G. Koop C.G. Koop			22b. TELEPHONE NUMBER (Include Area Code) (213) 813.9527		22c. OFFICE SYMBOL

PLEASE RETURN TO:

BMD TECHNICAL INFORMATION CENTER  
BALLISTIC MISSILE DEFENSE ORGANIZATION  
7100 DEFENSE PENTAGON  
WASHINGTON D.C. 20301-7100

## CONTENTS

	Page
1. INTRODUCTION TO THE SYSTEMS ENGINEERING VOLUME	1-1
2. SBL REQUIREMENTS AND CONCEPTUAL DESIGN	2-1
2.1 Introduction and Background	2-1
2.2 System Functional Overview	2.2-1
2.3 System Requirements	2.3-1
2.4 Subsystem Definition and Description	2.4-1
2.4.1 Master Oscillator Subsystems — (MOSS)	2.4-1
2.4.2 Beam Director Subsystem (BDSS)	2.4-1
2.4.3 Amplifier Subsystem (AMSS)	2.4-8
2.4.4 Phase Conjugation Subsystem (PCSS)	2.4-8
2.5 Master Oscillator Subsystem	2.5-1
2.5.1 Requirements	2.5-1
2.5.2 Optical Design and Power Sizing	2.5-1
2.6 Beacon Design	2.6-1
2.6.1 Requirements	2.6-1
2.6.2 Optical Design and Spatial Filtering	2.6-1
2.6.3 Mechanical Design	2.6-3
2.6.4 Beacon Operational Concept and Engineering	2.6-3
2.7 Beam Director Subsystem	2.7-1
2.7.1 Requirements	2.7-1
2.7.2 Optical Design and Layout	2.7-1
2.7.3 Primary Mirror Phase Conjugation	2.7-4
2.7.4 Active Structural Control	2.7-7
2.7.5 Alignment Sensitivity and Requirements	2.7-11
2.7.6 Segment Size and Shape Considerations	2.7-11
2.7.7 Beam Director Mechanical Considerations	2.7-11
2.8 Alignment and Pointing Concept	2.8-1
2.8.1 Functional Requirements	2.8-1
2.8.2 Optical Alignment of Primary Mirror Segments and Beam Director Optical Elements	2.8-4
2.8.3 Target Acquisition, Illumination and Coarse Tracking	2.8-4
2.8.4 Target and Beacon Fine Tracking and Jitter Control	2.8-5



## CONTENTS (Continued)

	Page
2.8.5 Pupil Matching Error Correction	2.8-8
2.9 Amplifier Subsystem	2.9-1
2.10 Phase Conjugation Subsystem	2.10-1
2.10.1 Requirements	2.10-1
2.10.2 Optics Design	2.10-1
2.10.3 SBS Cell Layout and Mechanical Design	2.10-5
2.10.4 Aerowindow Concept for SBS Cell	2.10-11
2.10.5 Material SBS Cell Window Investigation	2.10-36
2.10.6 References	2.10-46
2.11 Master Oscillator Isolation Components	2.11-1
2.11.1 Functional Overview and Isolation Component Design	2.11-1
2.11.2 Coatings for Quarterwave Mirrors and Birefringent	2.11-11
2.11.3 Birefringent Wedge Design	2.11-28
3. OPTICAL MODELING AND ANALYSIS	3-1
3.1 Introduction	3-1
3.2 Beam Director Design	3.2-1
3.2.1 Introduction and Background	3.2-31
3.2.2 Optical Design Analysis and Results	3.2-4
3.3 Apache Beam Director Aberration and Misalignment Tolerancing Analyses	3.3-1
3.3.1 Overview	3.3-1
3.3.2 Segment Misalignment	3.3-3
3.3.3 Primary Mirror Misfigure	3.3-6
3.3.4 Misalignments of ABD Beam Train Optics	3.3-14
3.3.5 Beacon Misalignment	3.3-14
3.4 AMPLIFIER MODELING AND ANALYSIS	3.4-1
3.4.1 Introduction	3.4-1
3.4.2 Amplifier and Oscillator Models (Codes)	3.4-2
3.4.3 Amplifier Conceptual Design	3.4-3
3.4.4 Amplifier Gain Physics	3.4-5
3.4.5 Amplifier Performance--Calculated Results	3.4-11
3.5 Briwon Model of Stimulated Brillouin Scattering	3.5-1

## CONTENTS (Continued)

	Page
3.5.1 Applications	3.5-1
3.5.2 Physical SBS Model	3.5-2
3.5.3 Code Implementation	3.5-9
3.5.4 Numerical Results	3.5-13
3.5.5 Derivation of Equations	3.5-21
3.5.6 References	3.5-34
3.6 APACHE Optical Propagation Model (AOPM)	3.6-1
3.6.1 Introduction and Background	3.6-1
3.6.2 Overview of AOPM	3.6-2
3.6.3 AOPM Code Development	3.6-6
3.6.4 Phase Conjugate Amplifier Parameter Studies	3.6-9
4. ASAM MODEL	4-1
4.1 Background and Objectives	4-1
4.2 Brightness Model	4-2
4.2.1 Master Oscillator	4-3
4.2.2 Beacon Mirror and Spatial Filter	4-4
4.2.3 Beam Director	4-4
4.2.4 Bidirectional Amplifier Subsystem	4-5
4.2.5 SBS Subsystem	4-5
4.2.6 Isolation Subsystem	4-7
4.3 Cost and Weight Model	4-8
4.3.1 Weight Model	4-8
4.3.2 Cost Model	4-10
5. SBL SYSTEMS EFFECTIVENESS	5-1
5.1 Introduction	5-1
5.2 SBL Systems Resiliency Study	5.2-1
5.2.1 Background and Introduction	5.2-1
5.2.2 Resiliency Analyses and Results	5.2-13
5.2.3 Resiliency Study Summary and Conclusions	5.2-39
5.3 PRIMARY MIRROR COST AND WEIGHT	5.3-1
5.3.1 Introduction and Summary	5.3-1
5.3.2 Summary of Fabricability Study Methodology	5.3-7
5.3.3 Production Costs of Raw ULE Boules	5.3-8

## CONTENTS (Continued)

	Page
5.3.4 Facesheet Polishing Costs	5.3-11
5.3.5 Coating and HOE Costs	5.3-16
5.3.6 Figure and Phase Actuator Costs	5.3-18
5.3.7 Reaction and Support Structure Costs	5.3-21
5.3.8 Assembly, Test and Management Costs	5.3-31
5.3.9 Scale-Up Issues	5.3-34
5.4 Laser Device Cost and Weight Estimates	5.4-1

## ILLUSTRATIONS

		Page
2.2-1	The APACHE System Shown in Schematic Layout (The spacecraft subsystem is not shown.)	2.2-2
2.2-2	Top level APACHE Layout is Shown Scale (An end view showing the layout of the six amplifiers is shown in 2.4.5.)	2.2-3
2.3-1	Top Level APACHE System Requirements	2.3-2
2.3-2	Power Budget Flowdown to Each Subsystem	2.3-4
2.3-3	Beam Quality Allocation for Correlated Jitter Focus and Multispectral Effects	2.3-5
2.3-4	Beam Quality Allocation to Subsystems	2.3-6
2.3-5	Allocation to Components of the Beam Expander	2.3-7
2.4-1	Summary of Key Design Parameters for the High-Brightness SBL	2.4-2
2.4-2	The Master Oscillator Subsystem (Shown highlighted with two possible paths to the beacon)	2.4-5
2.4-3	The Beam Director Subsystem (Optics shown with the beacon unseen, 25-primary mirror diameters to the left.)	2.4-7
2.4-4	Amplifier Subsystem Highlighted	2.4-9
2.4-5	End View of the Six APACHE Amplifiers (laid out on the outline of the primary mirror)	2.4-10
2.4-6	Phase Conjugation Subsystem Highlighted	2.4-11
2.5-1	Master Oscillator Subsystem Requirements	2.5-2
2.6-1	Beacon Derived Requirements	2.6-2
2.6-2	Spatial filter throughput and wavefront quality For a wavefront quality of $1/60 \lambda$ , 0.375 is the filtered input to the beam director, and 0.68 is the return throughput The beam which hits the primary mirror is 2.4 cm at the beacon.	2.6-2
2.6-3	Beacon Orbital Tracking Geometry	2.6-7

## ILLUSTRATIONS (Continued)

	Page
2.6-4 Overall Beacon Arrangement	2.6-11
2.6-5 TRW Surface Accuracy Measurement System (SAMS) Concept	2.6-14
2.6-6 Orbital Tracking Control Simulation	2.6-16
2.6-7 OPD and Absorption Due to Beacon Thruster Plumes	2.6-20
2.6-8 Laser Interaction with Thruster Plumes (OPD Method)	2.6-21
2.6-9 Laser Interaction with Thruster Plumes (Absorption Method)	2.6-22
2.6-10 Beacon Deployment Trajectory to Mitigate Plume Contamination of APT Optics	2.6-24
2.7-1 The Beam Director Subsystem Requirements with Opto-Mechanical Interface Requirements	2.7-2
2.7-2 The Beam Director Subsystem (Optics shown with the beacon unseen 25-primary mirror diameters to the left.)	2.7-3
2.7-3 Beam Director Throughput Budgeted to Components for Path from Amplifier to Target	2.7-5
2.7-4 Beam Director Throughput from Master Oscillator to Amplifiers	2.7-6
2.7-5 Beam Director for NASTRAN Model	2.7-8
2.7-6 Segment Piston and Tilt Control Loops	2.7-9
2.7-7 Segment Displacement Correction Factors	2.7-10
2.7-8 Beam Director Alignment Requirements for Un-phase Configuration Nonsegmented Elements	2.7-12
2.7-9 Segment shape and size is driven by creating equal annular input to six amplifiers Fifty-four trapezoidal segments are allowed to one of six annuli Maximum segment size is 17% of primary diameter.	2.7-13
2.7-10 Structure Mass to Stiffness Relation	2.7-17

## ILLUSTRATIONS (Continued)

		Page
2.8-1	Alignment Flowchart (Details both the beacon and target at the alignment focal plane with a shared aperture greatly eases initial pointing tolerances)	2.8-2
2.8-2	Beacon and target pointing components (including the alignment reference structure, derotation mirrors, high-quality segment and alignment focal plane)	2.8-3
2.8-3	Target and Beacon Fine Pointing Concept (The beam energy to the SBS cell is coaligned with the outgoing high-energy beam. Thus, incoming beacon image at LOS FPA can be aligned to 1.06 target image from target path.)	2.8-6
2.8-4	Pupil Rotation (deleted by creating a tracer beam from the beacon off a localized piece of the primary which returns round trip to be detected at the FPA shown above)	2.8-9
2.9-1	Amplifier Subsystem Requirements	2.9-2
2.9-2	Throughputs Requirements to the Component Level for the Amplifier Subsystem	2.9-3
2.9-3	Beam distribution optics split the beam equally to six amplifiers by concentric annuli of proper width. They are supported on the outer edge, and the inner edge produces no signeting.	2.9-4
2.9-4	The path length to and from each amplifier is mode equal (to within cm) for coherent recombining after phase conjugation by amplifier spacing.	2.9-5
2.9-5	Annular Optics in the Amplifier Is Similar to ALPHA	2.9-6
2.10-1	PCSS Requirements	2.10-2
2.10-2	PCSS Layout	2.10-3
2.10-3	The Relation of Focussing Element Fresnel Number Interaction Length in the SBS Medium Is Determined	2.10-6
2.10-4	PCSS Throughput Values Derived for Each Optical Element	2.10-7
2.10-5	Transverse Flow SBS Cell	2.10-9

## ILLUSTRATIONS (Continued)

	Page
2.10-6      Flowing Xe Cell Velocity Requirements	2.10-10
2.10-7      Axial Aerowindow Conceptual Design	2.10-12
2.10-8      Transverse Aerowindow Conceptual Design	2.10-13
2.10-9      Material Window Conceptual Design	2.10-14
2.10-10     Effect of Pressure Ratio on Transverse Aerowindow Mass Flowrate	2.10-19
2.10-11     Effect of Gas Total Temperature on Transverse Aerowindow Mass Flowrate	2.10-20
2.10-12     Effect of Flow Turning Angle on Transverse Aerowindow Mass Flowrate	2.10-21
2.10-13     Aerowindow Gas Requirements	2.10-32
2.10-14     SBS Cell/Aerowindow Dry Mass	2.10-33
2.10-15     Three Types of Window Surface Temperature Limits	2.10-44
2.10-16     Comparison of Window Coolant Flow Geometries	2.10-45
2.11-1      Isolation Subsystem Highlighted	2.11-2
2.11-2      Brightness Sensitivity as a Function of Oscillator Power	2.11-5
2.11-3      Isolation Analysis of ALPHA HEXDARR Resonator	2.11-6
2.11-4      SBL Master Oscillator. Isolation as a Function of Errors in Quarter Wave Retardation and Grating Extension Factor	2.11-8
2.11-5      SBL Master Oscillator as a Function of Amplifier Birefringence and Grating Extinction Ratio (GER)	2.11-9
2.11-6      Bulk Material and Thin Film Absorption Coefficients at 9.2 $\mu\text{m}$ Wavelength	2.11-15
2.11-7      Phase Retardance Versus Wavelength: Recommended Design for 90-Degree Phase Retarder with Random Layer Variations	2.11-19

## ILLUSTRATIONS (Continued)

		Page
2.11-8	Phase Retardance Versus Wavelength: Recommended Design for Positive Slope Reflector for Annular Optics with Random Layer Thickness Variations	2.11-23
2.11-9	Phase Retardance Versus Wavelength: Recommended Design for Negative Slope Reflector for Annular Optics with Random Layer Thickness Variations	2.11-24
2.11-10	Net Round Trip Phase Retardance for Each of Six Position of Rays on the Amplifier Annular Optics — Recommended Design	2.11-25
2.11-11	Flow Chart of Target and Unwanted Polarization Through the Apache System with Birefringent Wedge in Place	2.11-30
2.11-12	Birefringent Wedge Isolates the Master Oscillator from Amplifier Depolarization Leakage	2.11-31
2.11-13	Birefringent Wedge Design	2.11-34
2.11-14	Birefringent Wedge Design with AR Coating	2.11-36
3.2-1	APACHE Beam Director (ABD) Optical Subsystem Schematic	3.2-2
3.2-2	Starting Point Concept for Current ABD Design	3.2-7
3.3-1	Segmented APACHE Beam Director	3.3-2
3.3-2	Tile and Piston Error Correction	3.3-7
3.3-3	Piston Error Correction	3.3-8
3.3-4	Tilt Error Correction	3.3-9
3.3-5	Residual RMS OPD for the Misfigured Primary	3.3-12
3.3-6	Correction Factor for the Misfigured Primary	3.3-12
3.3-7	Ray Spot Diagram for the Primary Misfigure	3.3-13
3.3-8	Misfigured Surface Correction	3.3-15
3.3-9	Correction of Primary Misfigure Spectrum	3.3-16
3.3-10	Double-Pass OPD for Off-Axis Beacon Displacement	3.3-18



## ILLUSTRATIONS (Continued)

	Page
3.3-11	Sensitivity of OPD to Beacon Off-Axis Displacement 3.3-18
3.4-1	Schematic of Beam Path Through Amplifier Annular Leg 3.4-4
3.4-2	ALPHA Sized Oscillator 3.4-7
3.4-3	Two-Way Amplifier with Input from Oscillator with 200-cm Gain Length 3.4-9
3.4-4	Two-Way Amplifier with Input from Oscillator with 200-cm Gain Length 3.4-10
3.4-5	Input Intensity Amplification Versus Frequency Shift of Return 3.4-12
3.4-6(a)	Normalized Roundtrip Amplifier Output Power, Normalized Power to Phase Conjugator, and Roundtrip Amplification Versus Input Power to Amplifier 3.4-13
3.4-6(b)	SBS Reflectivity and Ratio of Input Pass to Return Pass Amplification Versus Input Power to Amplifier to Amplifier 3.4-14
3.5-1	Power Throughout the Cell 3.5-14
3.5-2	Fields at the Entrance/Exit 3.5-15
3.5-3	Fields at the Front of the Cell 3.5-16
3.5-4	Pump Field in the Cell 3.5-17
3.5-5	Stokes Field in the Cell 3.5-18
3.5-6	Far-Field Intensity 3.5-19
3.5-7	Far-Field Power 3.5-20
3.6-1	APACHE Optical Propagation Model 3.6-3
3.6-2	Beam Intensity and Phase Distributions Computed by ASAP as Input to LFCM Code 3.6-5
3.6-3	Amplifier Code Logic Chart 3.6-7
3.6-4	Examples of APOPM Code Calculations; Bare Cavity, No Input Aberration 3.6-11

## ILLUSTRATIONS (Continued)

		Page
3.6-5	Examples of APOPM Code Calculations; with Gain, 2-1/2 Cycles of Aberration Superposed on Input Beam	3.6-12
5.2-1	SBL Degradation Sources	5.2-4
5.2-2	Resiliency Definition	5.2-8
5.2-3	Resiliency Examples	5.2-9
5.2-4	System Error Budget Begins with System Level Requirements	5.2-14
5.2-5	Residual OPD Due to Segment Piston and Tilt	5.2-18
5.2-6	Brightness Sensitivity to Segment Piston Errors	5.2-18
5.2-7	Brightness Sensitivity to Segment Tilt Errors	5.2-18
5.2-8	Thermo-Optics Drive Facesheet Thickness/Actuator Spacing	5.2-20
5.2-9	APACHE Aberration Correctability as Function of Spatial Scale	5.2-23
5.2-10	Brightness Sensitivity to Coating Degradation	5.2-23
5.2-11	Brightness Sensitivity to HACS Residual	5.2-26
5.2-12	Brightness Sensitivity to SBS Conjugation Fidelity	5.2-28
5.2-13	Brightness Versus Increase in SBS Threshold	5.2-28
5.2-14	Edge Sensor Intensity vs Optical Path Difference	5.2-31
5.2-15	Brightness Sensitivity to Amplifier and Inter-Telescope Cophasing Errors	5.2-32
5.2-16	Residual OPD Due to Beacon Tracking Misalignment	5.2-35
5.2-17	Brightness Sensitivity to Beacon Tracking Angle	5.2-35
5.2-18	Resiliency to APACHE Unconjugated Optics	5.2-37
5.2-19	Brightness Sensitivity to Unconjugated Optics Aberrations	5.2-38
5.2-20	Brightness Versus Percent Increase in Isolation Factor	5.2-39

## ILLUSTRATIONS (Continued)

	Page
5.2-21      Resiliency Summary	5.2-40
5.3-1        HI-BRITE SBL Primary Mirror Assembly	5.3-2
5.3-2        Summary of Cost and Weight Results	5.3-3
5.3-3        Cost and Weight Comparison - Generic 10-m Primary Mirror (solid 3-m petals)	5.3-5
5.3-4        Cost and Areal Density by Percent for 10m Primary Mirror of APACHE and AO SBLs	5.3-6
5.3-5        Allowable Life and Facesheet Thickness	5.3-9
5.3-6        Manufacturing of Ultralite Facesheets	5.3-10
5.3-7        Cost Reductions Achieved Through Recent Advances in Computer-Controlled	5.3-13
5.3-8        Single-Shift Polishing Schedule	5.3-14
5.3-9        Coatings Cost Versus Tile Diameter	5.3-17
5.3-10       Actuator Concepts	5.3-19
5.3-11       Lamp-Like Segment Phase Actuators	5.3-20
5.3-12       Flowdown of Error Budgets to Set Requirements for Reaction and Support Structures	5.3-22
5.3-13       Reaction and Support Structures for APACHE and AO SBL	5.3-23
5.3-14       Deformation of APACHE and AO SBL Reaction Structures	5.3-25
5.3-15       Deformation of APACHE and SO SBL Support Structures	5.3-26
5.3-16       Allowable WFE for APACHE and AO SBL PM Segments	5.3-28
5.3-17       State-of-the-Art Reaction and Support Structure Material Parameters and Costs	5.3-29
5.3-18       Stiffness, Weight, and Cost	5.3-30
5.3-19       Summary of Vendor Survey Used to Establish Cost Base for Lightweight Structures	5.3-32
5.3-20       SBL PM Assembly, Test, and Management Costs	5.3-33

## ILLUSTRATIONS (Continued)

		Page
5.4-1	Weight Is Primarily Dependent Upon Power and Runtime	5.4-5
5.4-2	The Runtime Dependent Components Are the Dominating Weight Drivers	5.4-6
5.4-3	Cost Estimating Relationship (CER) Development Methodology	5.4-7
5.4-4	Cost Is Mainly Driven by Power Requirements	5.4-8
5.4-5	The Nonruntime Dependent Costs Are Dominating	5.4-11

# TABLE

		Page
2.6-1	Mission Requirements Significant to Beacon Design	2.6-4
2.6-2	Baseline Beacon Maneuver Scenario	2.6-4
2.6-3	Beacon Feasibility Studies	2.6-5
2.6-4	Equivalent Delta-V and Propellant Requirements	2.6-6
2.6-5	Beacon Dry Mass and Power Summary, Close Range Case	2.6-9
2.6-6	Beacon Position Sensing Requirements and Capabilities	2.6-13
2.6-7	Qualitative Tether Evaluation	2.6-18
2.7-1	Comparison of Beam Director Structure Frequency Required To Meet WFE Budget	2.7-15
2.10-1	Particular Requirements on Material Window	2.10-37
2.10.5.1	Window Survivability Analysis	2.10-37
2.10-2	Candidate Solid Window Materials	2.10-38
2.10-3	Effect of Radial Preload on Window Survivability at 1.5 MW Cell Input Power	2.10-41
2.11-1	Design Values for Isolation Components	2.11-10
2.11-2	Coating Requirements	2.11-12
2.11-3	Ion Assisted Deposition Test Results	2.11-16
2.11-4	Coating Design Comparison: Quarterwave Mirrors	2.11-20
2.11-5	Birefringent Wedge Analysis Summary	2.11-33
3.2-1	ADB Design Specification Goals	2.11-5
3.2-2	P-V and RMS OPD Wavefront Errors, Target and Beacon Channel ( $\lambda = 2.9 \mu\text{m}$ )	3.2-11
3.3-1	APACHE Beam Director Correction of Random Piston and Tilt	3.3-5
3.3-2	APACHE Beam Director Correction of Primary Mirror Misfigure (Design D)	3.3-11

# TABLE (Continued)

		Page
3.3-3	Impact of Misalignments on Beam Director Wavefront Quality	3.3-17
5.2-1	Degradation Sources and Associated Parameters	5.2-6
5.2-2	System Resiliency Summary (Classified design values appear in Addendum) Low resiliency degradation sources identified by boxes around figure of merit.	5.2-11
5.2-3	SBL Systems Resiliency--Conclusions	5.2-12
5.2-4	Thermo-Optical Errors Primarily Due To ULE Variations in CTE	5.2-21
5.4-1	HEL power Requirements Are Derived Directly from System Requirements	5.4-2
5.4-2	Weight and Cost Algorithms Developed for the Laser Device on the ALPHA and SBL CF&TDP Programs	5.4-3
5.4-3	Laser and Reactant Cost and Weight Summary	5.4-10

## 1. INTRODUCTION TO THE SYSTEMS ENGINEERING VOLUME

The APACHE Program consisted of two major thrusts:

1. Phase conjugate laser technology, which is covered in Volume I of this report, verifies and demonstrates the key technologies associated with phase conjugated continuous wave chemical lasers.
2. SBL systems engineering, covered in this volume of the APACHE Final Report, specifies requirements, formulates conceptual designs and performs systems effectiveness analyses for phase conjugate space-based lasers (SBLs).

As indicated in Volume I of this report, the APACHE Program has successfully performed a wide variety of experiments and technology demonstrations addressing key issues associated with phase conjugate chemical lasers. The primary thrust of the systems engineering portion of the program was the formulation of a conceptual design for an APACHE SBL, based on the results of detailed modeling, simulation and analyses. Along with conceptual design, APACHE also addressed the effectiveness of phase conjugate SBL systems. Where feasible, comparisons were conducted between "conventional" SBLs using active adaptive optics for wavefront correction, with phase conjugate SBLs using passive means to both correct wavefronts as well as combine beams from multiple devices.

SBLs operating at high-brightness levels were used both in the SBL conceptual design, as well as for effectiveness analyses. The high brightness regime was chosen because it encompassed the broadest range of technical issues and most comprehensive set of design requirements associated with implementation of phase conjugated SBL systems. Systems engineering for this regime provides the deepest insight into the opportunities offered by phase conjugate SBLs, as well as the potential limitations. For the most part, it is expected that the technical issues and challenges related to lower brightness systems will be easier to deal with than those for higher brightness.

The material in this volume has been organized into four sections, covering SBL conceptual design, optical modeling and analysis, APACHE

systems analysis modeling, and SBL systems effectiveness analyses. Both the optical modeling and the systems analysis modeling have been used extensively to support the conceptual design as well as the systems effectiveness analyses.

Section 2 presents the requirements and describes in detail the conceptual design developed under APACHE for a high-brightness, phase conjugate SBL. Full optimization of the design was beyond the scope of the present program. However, the present results have clearly demonstrated that the major conceptual design issues associated with phase conjugate SBLs have been addressed in-depth and successfully resolved. Further information is presented in the Classified Addendum which will be supplied under separate cover. The discussion emphasizes those technical issues which are unique to phase conjugate laser systems, as opposed to generic SBLs.

The section begins with a functional overview describing the overall system concept and its key constituents, followed by a summary of the systems requirements flow-down and the budgeting of beam quality and power through the major functional elements of the system. The remainder of the section consists of detailed discussions of design and performance attributes of key subsystems and functional elements of the SBL, including the master oscillator, beacon, beam director, alignment and pointing system, amplifiers, SBS cell and isolation components. Major issues related to both optical as well as mechanical design of the system are addressed in the section.

Section 3 describes the principal optical modeling and analyses efforts performed in support of the design of the APACHE SBL. Several new models were formulated to address unique aspects of the APACHE SBL, while existing models, generally with some modifications, were used where appropriate. The optical modeling was concentrated in five main areas: first, an optical design of a phase conjugate beam director was formulated using Code V, which displays excellent performance over the required fields of view; second, the ASAP optical propagation code was used to model the performance of the beam director for an aberrated segmented primary mirror, and for departures of the beacon from its nominal position. The wavefront



correction was found to be excellent over a wide range of applicable parameters; third, the amplifier modeling section describes analyses of the bidirectional amplifiers in APACHE. The key characteristic displayed is a "self-healing" of the amplifier, resulting in high output powers which, above a certain level, depend only weakly on the input power; fourth, the SBS cell was modelled using the BRIWON code, which facilitated the prediction of SBS cell output characteristics as a function of the conjugation medium and input beam properties. The fifth modeling effort involved the end-to-end APACHE optical propagation model (APOPM), comprised of interconnected propagation modules for the various subsystems. Calculations were successfully performed using both individual modules in APOPM, as well as certain combinations of modules.

Section 4 describes the APACHE Systems Analysis Model (ASAM), developed as a comprehensive, yet convenient (runs on a PC), modeling tool to support both the SBL design effort, as well as systems effectiveness studies. The ASAM relates systems level measures of performance such as brightness, weight and cost, to subsystem and component performance parameters throughout the APACHE SBL system. ASAM serves as a focal point for incorporating the results of fundamental analyses as well as technology experiments, into a single, stratified model with multiple levels of detail accessible to the analyst. The model has been used extensively to perform design trades and to compute the resiliency of the APACHE system.

And, finally, Section 5 describes the systems effectiveness work performed under the APACHE Program. The objective of this effort was to determine the potential opportunities for enhancing SBL performance using phase conjugation rather than active adaptive optics. The scope of the work was intentionally limited to the analysis of selected aspects of two representative high-brightness systems satisfying equivalent mission requirements: the APACHE SBL, and an adaptive optics SBL consisting of a hybrid between Lockheed's System 3 design and Perkin-Elmer's ABCS beam control system. The two aspects selected for study were:

1. Resiliency--the SBL system's ability to continue performing despite degradations in subsystem or component performance.

2. Cost and weight of key portions of an SBL, namely, the primary mirror and laser devices.

The results indicate that phase conjugate SBLs are considerably more resilient to subsystem degradation than adaptive optic SBLs. Moreover, the degradations to which the adaptive optics are sensitive are much more likely to degrade over time than are those for the APACHE system. The cost and weight portions of the effectiveness study demonstrate that the APACHE primary mirror is lighter and less expensive than for adaptive optics, as are the laser devices. The present work has yet to fully exploit, through the design of novel structures and alternative materials, the potential cost and weight advantages stemming from the relaxed tolerances achievable with phase conjugation.

In conclusion, under the APACHE Program, significant advances were made in phase conjugated SBL conceptual design; in modeling and analysis of phase conjugated laser performance; and in evaluating the resiliency and the cost and weight of phase conjugated SBLs relative to their adaptive optics counterparts. The results indicate the feasibility and attractiveness of phase conjugated SBLs, and reveal significant opportunities for enhancing SBL systems performance using phase conjugation.

## 2. SBL REQUIREMENTS AND CONCEPTUAL DESIGN

### 2.1 INTRODUCTION AND BACKGROUND

The APACHE space-based laser (SBL) concept was motivated by the desire to correct the many sources of wavefront aberration in high-energy, space-based lasers by passive means, thereby eliminating requirements for active adaptive optics, and associated figure actuators, wavefront sensors and hierarchical control systems. The application of phase conjugation to passive wavefront correction in SBLs was initially explored under the PALS Program, which identified the primary constituents and basic configuration for a phase conjugated SBL system. The key elements included:

1. Master oscillator to generate a probe beam which samples the primary mirror and seeds the amplifiers
2. "Beacon" mirror to spatially filter and direct the MO beam to the primary mirror
3. Two-channel beam director with a common primary, capable of steering the output beam to a target
4. Set of bidirectional amplifiers and associated beam division and combination optics
5. SBS cell to phase conjugate the beam, thereby effecting wavefront correction on the return pass through the system, as well as coherently combining the outputs from multiple amplifiers
6. Isolation scheme which directs the return-pass beam to the target channel and prevents detrimental feedback along the beacon channel to the MO.

The six elements indicated above were investigated initially under PALS, and subsequently became the basis for an APACHE SBL design. A primary objective of the APACHE Program was formulation of a comprehensive conceptual design for a high-brightness SBL, using phase conjugation to correct wavefront aberrations and to coherently combine the outputs of multiple amplifiers. Design issues, whether optical, mechanical, or otherwise were to be addressed at both the systems level as well as the subsystem and component levels, as appropriate.

Another objective of the SBL design effort was to determine a configuration in which system hardware was efficiently packaged and to

produce the mechanical drawings which displayed this configuration to scale.

The design process relied heavily on a variety of modeling and analysis tools, described in Sections 3 and 4 of this volume. While certain top-level systems requirements were dictated by the mission scenario, trade studies were required to select the majority of systems and subsystem parameters. Also, fabricability and technical risk were often used as criteria to restrict the physical dimensions or performance parameters of various functional elements. For example, the size of the primary mirror was constrained to what was believed to be a practical limit in terms of manufacturing and handling. Similarly, there was deemed to be a practical limit on the size of annular laser amplifiers that could be fabricated. One example of a performance limit impacting component design is the limit on power densities which the optical elements are capable of handling, determined in turn by practical limits on achievable coating reflectivities and cooling capabilities for high-power optics.

A key analysis tool used in the design process was the APACHE Systems Analysis Model (ASAM), described in some detail in Section 4. ASAM contains a brightness model as well as weight and cost models. ASAM was invaluable to the design process because virtually all the primary relationships between system, subsystem and component properties and their performance characteristics, whether determined by analysis or experiment, were collected and consolidated within a single model. The more fundamental models such as the APACHE Optical Propagation Model (APOPM) and its constituent modules (e.g., ASAP for the beam director (BD), LFCM for the amplifiers, and BRIWON for the SBS cell), served as a source of many of the relationships contained in ASAM, but were also used in their own right to support design analyses and trades, where appropriate.

Detailed, quantitative optimizations of the systems design were postponed to later work because of uncertainties in the weight and cost relationships for certain key portions of the SBL system. Rather than attempting to fully optimize the design, it was judged more appropriate at this time to formulate balanced designs in which technical risks were distributed as evenly as possible among the various subsystems while

maintaining overall systems performance. Designs obtained in this way are expected to be close to those resulting, eventually, from a more detailed optimization process.

The discussion presented in the following sections demonstrates that the key design issues for an APACHE high-brightness system have been addressed and successfully resolved. Design approaches have been formulated and design parameters specified for all of the key functional elements, including the MO, beacon, primary mirror and beam director, bidirectional amplifiers, stimulated Brillouin scattering (SBS) cell and polarization isolation components.

The following subsections provide a detailed description of the baseline design for an APACHE high-brightness SBL formulated under this program. Section 2.2 provides a generic description of the principal functional elements and the overall configuration of the APACHE SBL. Section 2.3 summarizes the systems level requirements used in the design, as well as the detailed power and beam quality budgets tiered down to the subsystem level, which drive subsystem and component design. The designs which have been formulated for each of the individual subsystems and their key attributes are described in some detail in Sections 2.4 through 2.10.

## 2.2 SYSTEM FUNCTIONAL OVERVIEW

The basic purpose of the APACHE concept is to fully exploit the intrinsic advantages of SBS phase conjugation for beam combination and ultra-high bandwidth wavefront error correction in the design of a space-based laser system. SBS phase conjugation has been experimentally demonstrated to provide correction of severe aberrations, many waves in magnitude to near the diffraction limit at megahertz bandwidths. Incorporation of such a powerful aberration corrector acting passively without the need for complex adaptive optics control and wavefront sensing significantly simplifies design complexity. Furthermore, the high fidelity and wide dynamic range associated with the SBS process allows substantial relaxation in design tolerances in several key areas including surface figure requirements for the large primary mirror segments, intersegment co-phasing, and alignment tolerances, and multi-amplifier path length control requirements. In all of these areas, the utilization of SBS phase conjugation in the APACHE concept has resulted in relaxation of system design tolerances by factors of 10 to several hundred, thus providing the potential for a substantially simplified, lower cost, and lower weight SBL design concept.

Before proceeding to a detailed discussion of the APACHE concept, it is instructive to examine the design at a very top level, so that the basic elements of the design are understood. The four APACHE subsystems shown schematically in Figure 2.2-1 are the master oscillator (MO), beam director (BD), amplifiers, and phase conjugator. The complete top level layout shown in Figure 2.2-2 contains all the major optical components except the beacon, which is to the left at a distance of 25-primary mirror diameters.

The process begins (referring to Figure 2.2-1) with the introduction of a beam with p-plane linear polarization output from the MO, an ALPHA class device; this beam is directed to a beacon mirror. Some spatial filtering is done by this mirror, and some additional filtering occurs when the primary mirror is overfilled by the beam which is reflected from the beacon. The net result of spatially filtering the MO output is the production of a high-quality beam, which serves as the beam quality

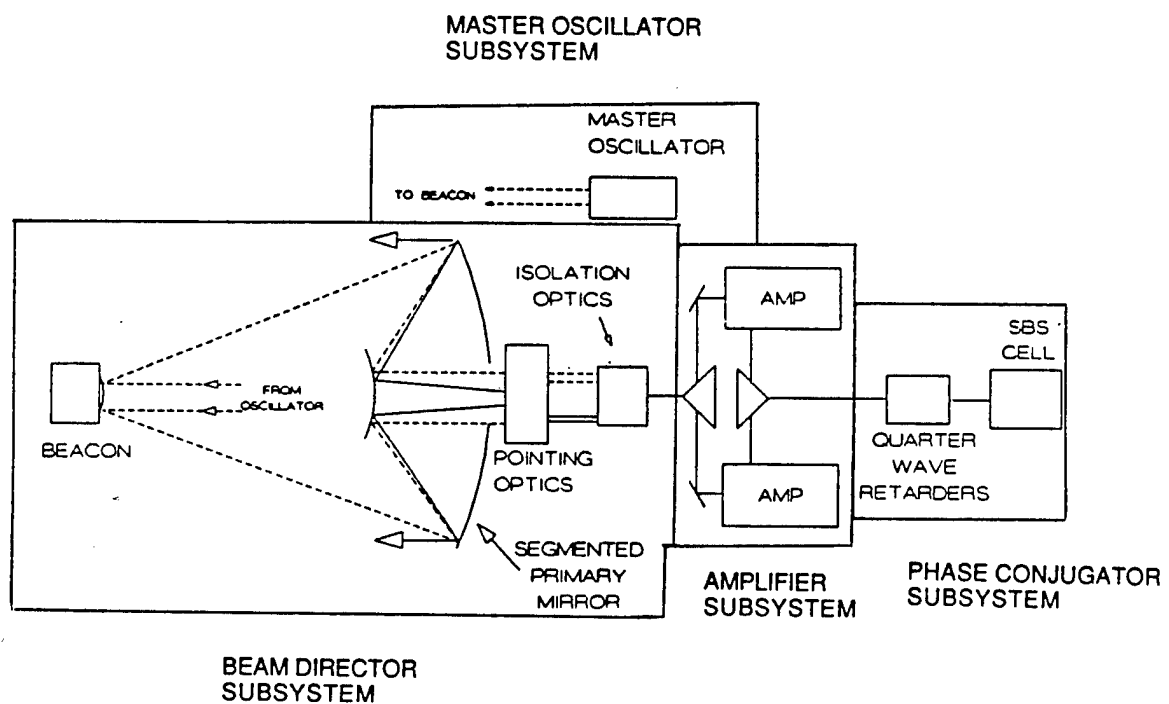


Figure 2.2-1. The APACHE System Shown in Schematic Layout  
(The spacecraft subsystem is not shown.)

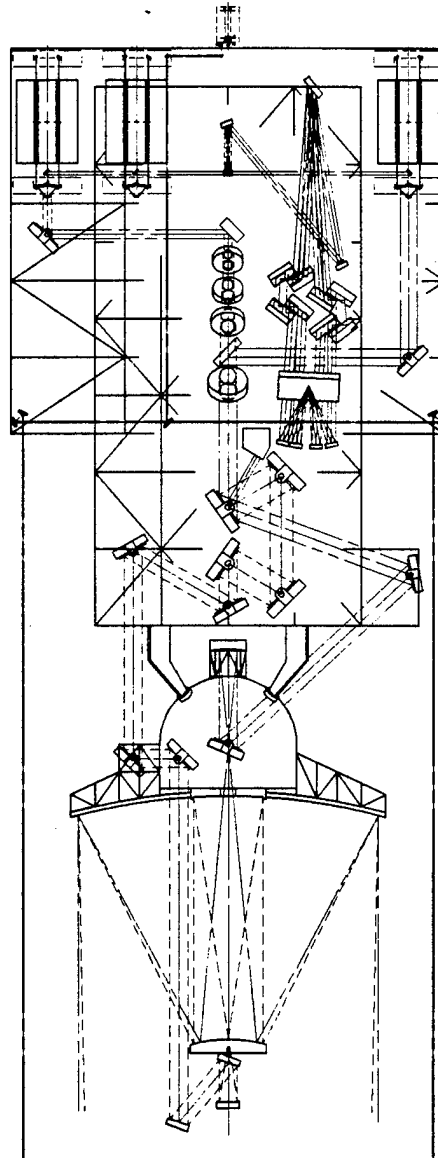


Figure 2.2-2. Top level APACHE Layout is Shown Scale  
(An end view showing the layout of the six  
amplifiers is shown in Figure 2.4.5.)



reference for the remainder of the system. The beam director sends this low power, spatially filtered through the amplifiers, on its way to the phase conjugator. The beam now contains all the wavefront errors introduced up to this point. The beam then passes through the quarter wave phase retarder making the beam circularly polarized, and is focussed into the phase conjugation SBS Cell.

On the return, a second pass through the quarter wave retarder transforms the beam to s-plane linear polarization. Because the beam is phase conjugated, most of the wavefront errors introduced by the primary mirror and amplification process encountered on the first pass are cancelled out on the return path. To prevent the high-power beam from returning to the MO, a grating designed to reflect p-plane polarization into first order and s-plane into zero order causes the beam to take a different path to the primary mirror, and ultimately to the target. Note that the wavefront errors introduced by the mirrors not common in the two paths are not cancelled, and these optical elements must have inherently good wavefront performance.

An important issue in the APACHE design is the degree to which the MO can be isolated from the return target beam. Any p-plane linear polarized energy will, on the return path, return directly to the oscillator and cause feedback interference to the laser. The performance requirements for isolation are covered in detail in Section 2.11.

## 2.3 SYSTEM REQUIREMENTS

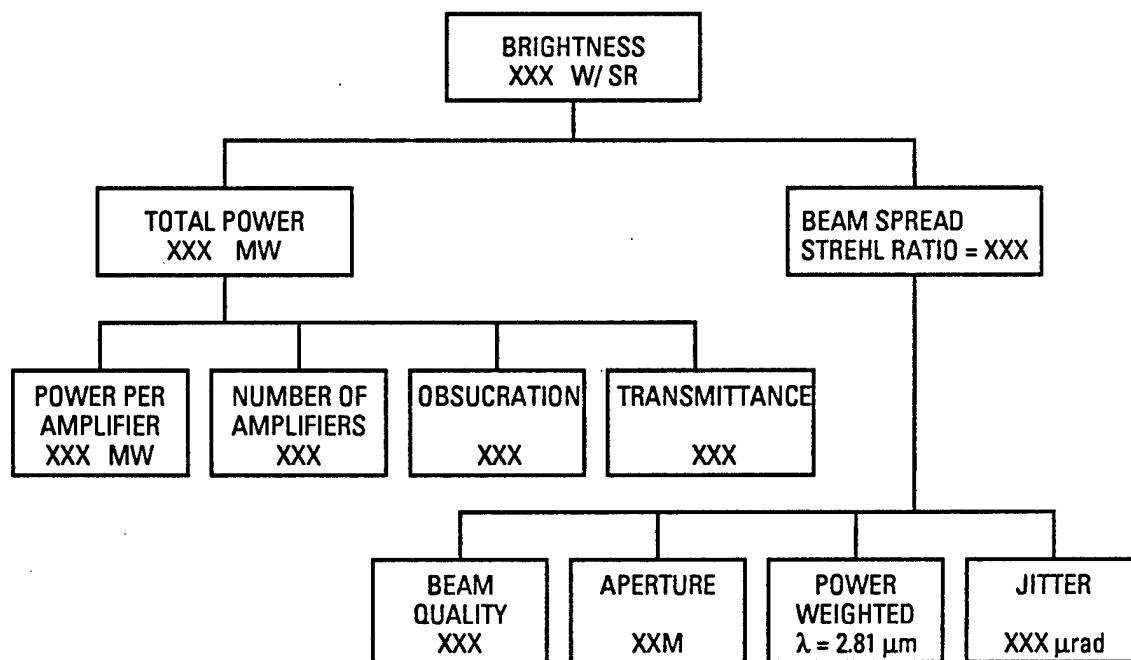
The APACHE system concept has been designed to meet a consistent set of system requirements that are listed in Figure 2.3-1. A classified addendum, which will be provided under separate cover, includes the classified figures that pertain to this report. These requirements were provided by an Air Force mission analysis study and documented in the Technical Guidelines Document, SBL Phase II, USAF Space Division (Secret), February 1985. The results of the mission analysis formed the basis for all subsequent SBL design conducted on the APACHE program. This set of requirements, which corresponds to what is loosely termed the "high-brightness" system, defines the largest and most robust SBL concept considered in detail for strategic defense applications. Subsequent mission analyses performed by SDIO and the Air Force have considered alternative requirements for various applications and mission scenarios. For the purpose of the APACHE design effort, however, a fundamental decision made early in the program was that all design would work to the high-brightness design requirements. This decision was made for basically two reasons:

1. The high-brightness regime constituted the most difficult to be addressed. Phase conjugation appeared to be one of the few growth paths available to such a large system. Having successfully formulated a consistent and workable design for this large system, smaller and less robust systems would be easier to design.
2. It was deemed desirable to work to one fixed set of requirements rather than continuously altering the design as new mission requirements were developed.

For these reasons, the present APACHE design relates to a high-brightness system. Having completed the high-brightness concept, however, additional design activity consistent with smaller and more modest brightness requirements is presently being conducted as part of the APEX program, a follow-on program to APACHE.

As part of the system engineering analysis, the system requirements defined in Figure 2.3-1 were tiered down one level to specify key design features for all of the subsystems. These included parameters such as the aperture of the beam projecting optics, the power of each amplifier, the number of amplifiers, the size of the MO, the degree of spatial filtering

Brightness	W/cm <sup>2</sup> steradian
Total firing time	s
Deployment time	s
Time before refueling	yr
Number of restarts	
Slew angle	deg
Slew acceleration	mrad/s <sup>2</sup>
Field of regard	mrad
Retargeting time	s
Pointing accuracy	Diffraction spot



01M.160.90.03-5005

Figure 2.3-1. Top Level APACHE System Requirements

by the beacon mirror, the reflectivity of the SBS cell, and the isolation requirements for the gratings and quarter wave retarders, to mention a few.

An essential ingredient in this system engineering analysis was the APACHE ASAM (see Section 4) which was used to derive the flowdown to subsystem performance requirements using parametric expressions for all the functions necessary to create the required system brightness. The derived system weight is tracked as a figure of merit. Some requirements above are assigned directly to specific subsystems.

The brightness requirement is budgeted to each of the subsystem levels from its relation to power, beam quality, and system jitter as

$$\text{Brightness} = \frac{\text{Power} \times \text{Aperture} \times (1 - \text{Obsc}^2) \times \text{Trans}}{(\text{Lambda} \times \text{Beam Quality}^2 \times (1 + \text{Jitter}^2))}$$

Obsc is the secondary mirror to primary mirror linear obscuration ratio. Trans is the beam director optics transmission, and jitter is normalized to the beam spread due to diffraction.

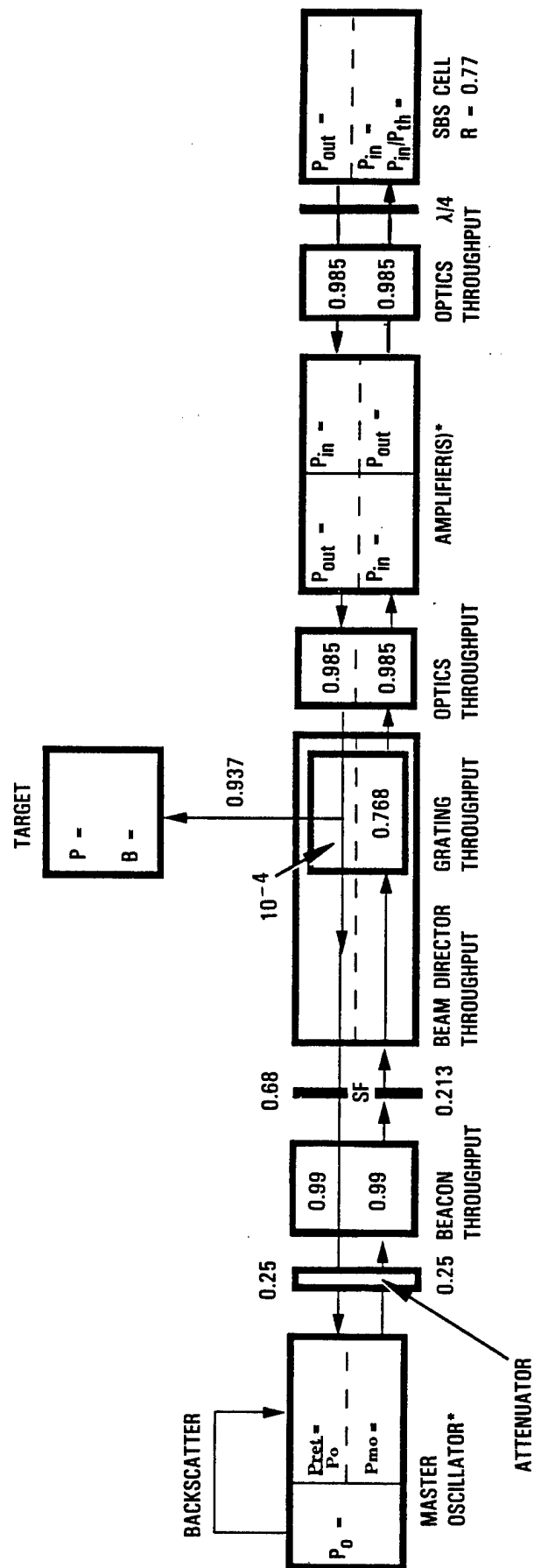
Power requirements flow into the subsystems as shown in Figure 2.3-2. The end-to-end beam quality (BQ) budget is shown in Figures 2.3-3, 2.3-4, and 2.3-5. Figure 2.3-3 splits out the correlated jitter from the total system BQ. Correlated jitter arises from rigid body angular motions of the primary mirror. At the next level down, two terms (focus error and multispectral effects) are split off from the remaining system BQ budget.

Figure 2.3-4 flows the system BQ budget, after focus, jitter, and multispectral effects are removed, down to the major subsystems. Four of the seven beam quality terms shown at the first tier down relate to:

1. The residual input wavefront error (with perfect isolation) after the spatial filtering is done by the beacon and primary mirror
2. Degradation due to imperfect isolation of the MO
3. Phase conjugation fidelity
4. Amplifier residual errors after phase conjugation.

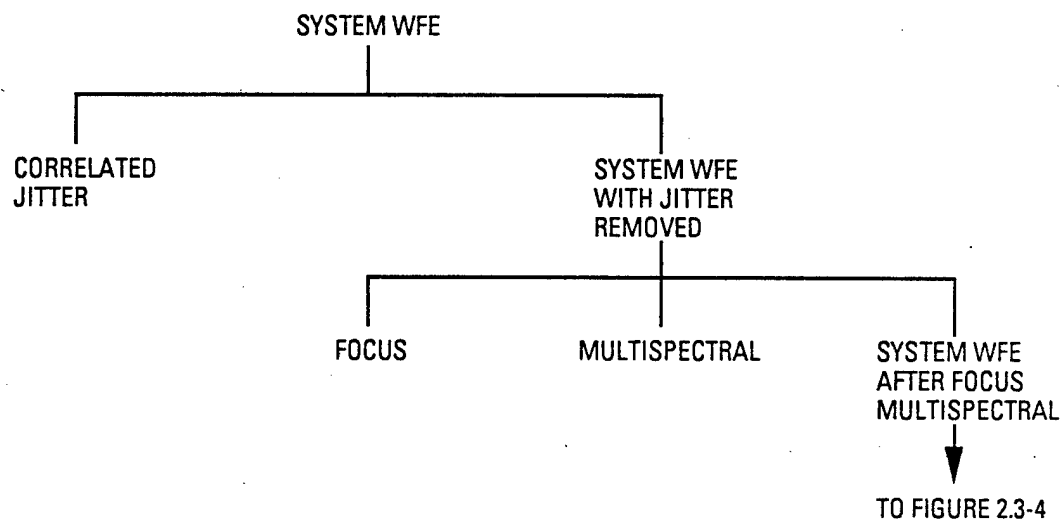
The last three terms are allocated to the BD subsystem. They are:

5. Beacon misalignments and misfigure



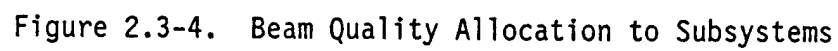
\*DIMENSIONS BASED UPON HYLTE TECHNOLOGY

Figure 2.3-2. Power Budget Flowdown to Each Subsystem



01M.160.90.02-5005

Figure 2.3-3. Beam Quality Allocation for Correlated Jitter Focus and Multispectral Effects



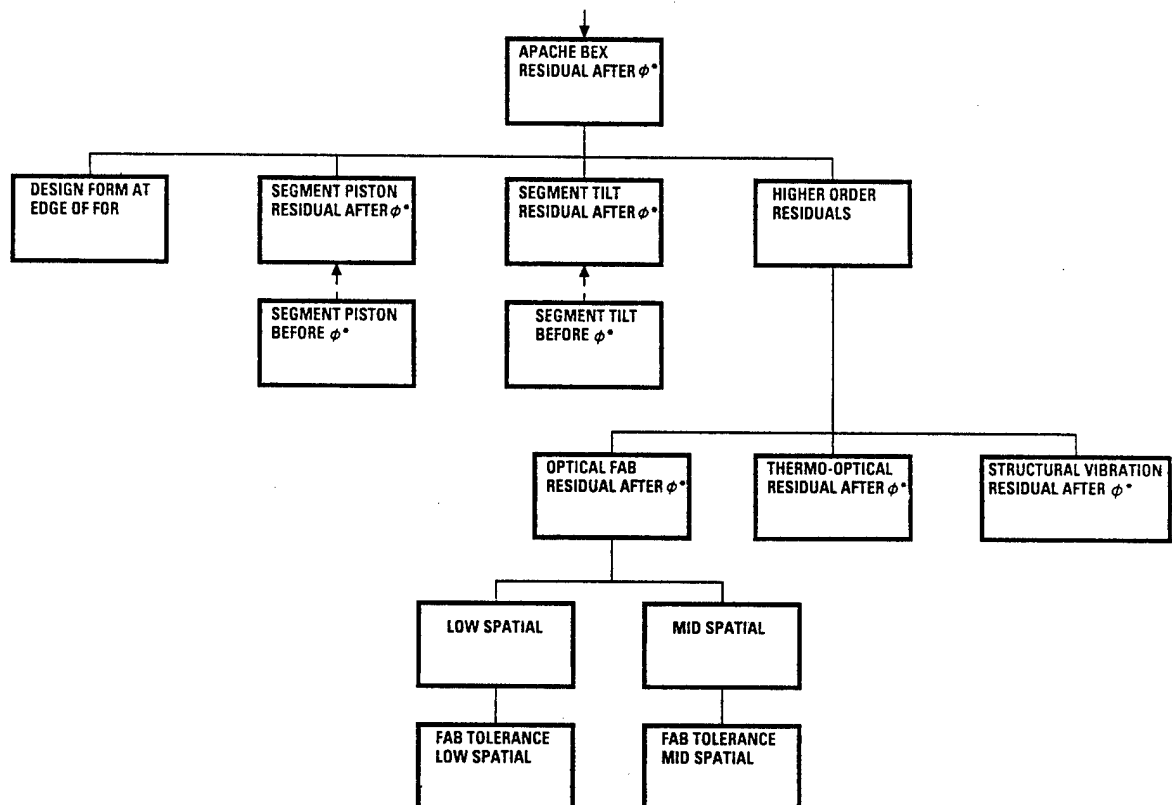


Figure 2.3-5. Allocation to Components of the Beam Expander



6. Distortions from unconjugated optics, including misfigure and misalignment
7. All remaining effects from the BD subsystem.

The seventh term is flowed down further in Figure 2.3-5 to the residual (i.e., after phase correction by conjugation) alignment and optical fabrication errors.

## 2.4 SUBSYSTEM DEFINITION AND DESCRIPTION

The APACHE system is comprised of the following four subsystems:

1. Master Oscillator Subsystem (MOSS)
2. Beam Director Subsystem (BDSS)
3. Amplifier Subsystem (AMSS)
4. Phase Conjugator Subsystem (PCSS)

A summary of the key design parameters for each subsystem (SS) is given in Figure 2.4-1. Classified parameters are identified as "xxx," and are specified in the classified addendum. A top-level description of each SS is provided in the remainder of this section. Subsequent sections will provide detailed design descriptions of each SS based upon the tierdown of requirements discussed in Section 2.2.

### 2.4.1 Master Oscillator Subsystem (MOSS)

The first SS encountered in the power generation train is the MOSS which is highlighted in Figure 2.4-2 with the major optical components identified. The purpose of the MO is to provide a low-power, high-quality reference beam which sets the BQ and jitter reference for the rest of the system. The oscillator itself is located in the rear behind the amplifiers, before the tank farm. This limits torques due to its exhaust and the path length to the source of fuel. The beam leaves the MO and is directed up or down to one of two sets of pointing optics which also control power throughput (for isolation purposes as discussed in Section 2.2). Two sets of pointing optics are required due to slewing motions of the beam director. When the beam director slews downward the upper pointing optics set are not able to view the beacon and vice versa.

### 2.4.2 Beam Director Subsystem (BDSS)

The second SS is the BDSS. The purpose of the BDSS is twofold. First, this SS accepts the low-power, high-quality reference beam from the MOSS, upon which the primary mirror phase aberrations are impressed. This distorted beam is then directed to the AMSS. Secondly, the high-power phase conjugated beam returning from and AMSS is directed by a separate train of optics in the BDSS toward the target. Rapid retargeting over the

Subsystem or Functional Element	Design Parameter	Value
Master oscillator	Power	xxx MW
	Attenuator	0.25
	Beam quality	
	Before spatial filtering	1.xxx
	After spatial filtering	1.005
	Polarization	
Isolation optics	p	0.98
	s	0.02
	Gratings	
	Number	4
	Zeroth order transmission	
	p	2.6%
	s	90.0%
	Extinction ratio	35:1
	First order transmission	
	p	93.7%
	s	8.4%
	Extinction ratio	11:1
	Quarter wave retardation	
	Retardance per optic	22.5 deg
	Total number of optics	4
	Maximum retardation error	0.5 deg
Beacon	Mirror diameter	10 cm
	Location (PM diameters)	25
	Radius of curvature	120 cm
	Peak irradiance	xxx w/cm <sup>2</sup>
	Spatial filter throughput	0.213
	Stationkeeping requirements	
	Lateral	+0.5 mrad
	Longitudinal (% PM dia)	1.25%
	Tilt	+0.5 deg
	Roll	No requirement
	Beacon satellite	
	Dimensions	0.6 x 0.6 x 0.7 m <sup>3</sup>
	Mass	
	Dry	358 kg
	With fuel	520 kg
	Thrusters	
	Coarse control	500 lb (12 required)
	Fine control	5 lb (12 required)
	Fuel	N <sub>2</sub> O <sub>4</sub> /N <sub>2</sub> H <sub>4</sub>
	Tracking concept	SAMS sensors

Figure 2.4-1. Summary of Key Design Parameters for the High-Brightness SBL

Subsystem or Functional Element	Design Parameter	Value
Beam director	Primary mirror	
	Diameter	xxx m
	F/#	1
	Shape	Parabolic
	WFE after conjugation	$\lambda_{HF}/xx$
	Magnification	16.7
	Instantaneous field of view	0.001 deg
	Field of regard	$\pm xx$ mrad
	Large angle slew	
	Mirror segments	
	Total number	54
	Shape	Trapezoidal
	Size	xx m by xx m
	Figure	
	Low spatial (rms)	$\lambda_{HF}/2.85$
	Mid spatial (rms)	$\lambda_{HF}/10$
	Alignment tolerances	
	Piston (rms)	$4 \lambda_{HF}$
	Tilt (rms)	$0.8 \lambda_{HF}$
Amplifier	Beacon tracking requirements	
	Lateral	80 $\mu$ rad
	Longitudinal	20 cm
	Output power per module	xx MW
	Number of modules	6
	Nozzle type	HYLTE
	Dimensions	
	Length	6.7 m
	Diameter	2.0 m

Figure 2.4-1. Summary of Key Design Parameters for the High-Brightness SBL (Continued)

Subsystem or Functional Element	Design Parameter	Value
SBS	Conjugation medium	
	Gas	Xe
	Pressure	40 atm
	Absorption requirement	$5 \times 10^{-5}/\text{cm}$
	Xenon flow velocity	10 m/sec
	Min input power (x threshold)	3
	Reflectivity	0.77
	Focusing F/#	F/10
	Multiline concept	Separate foci
	Dimensions	
	Flow direction	1 cm
	Beam direction	7 cm
	Transverse direction	16 cm
	Cell (and turbo machinery) weight	1150 kg
	Aerowindow	
	Gas	He
	Mass flow rate	
	Recirculated	34 kg/sec
	Rate of mass loss	3.7 kg/sec

Figure 2.4-1. Summary of Key Design Parameters for the High-Brightness SBL (Continued)

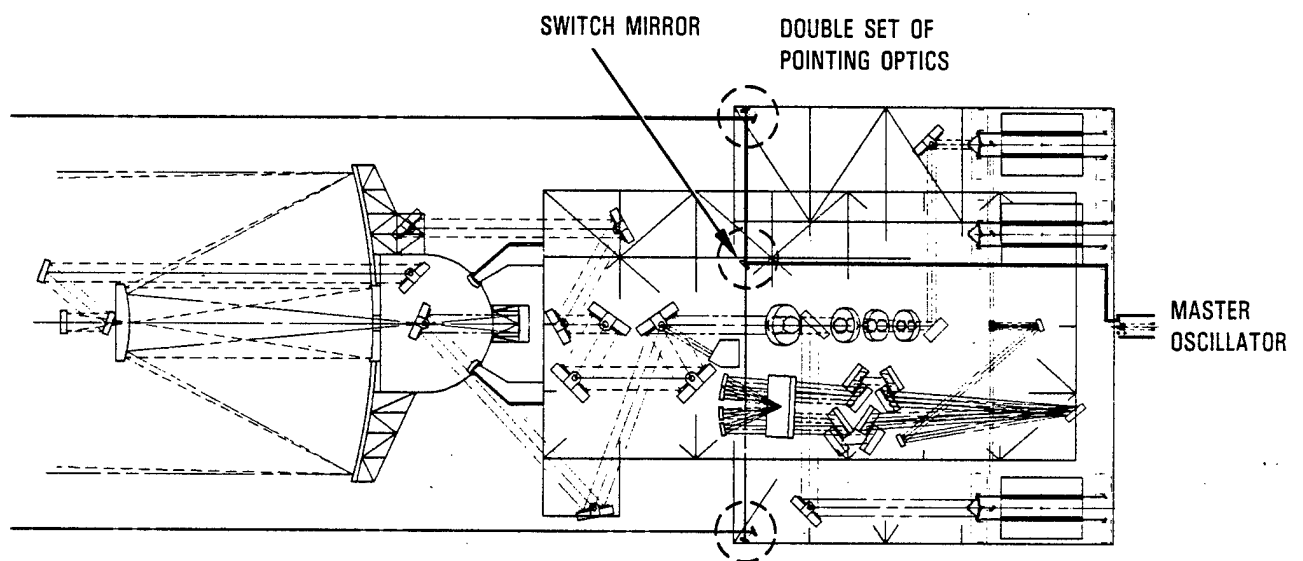


Figure 2.4-2. The Master Oscillator Subsystem (Shown highlighted with two possible paths to the beacon)

required field of regard is accomplished by a small agile steering mirror. Slower, large angle slewing is performed using a gimbal mechanism which articulates the entire BD.

The beacon, a separate assembly in the BDSS, moves as a free flying satellite to stay within the field of regard of the BD's beacon tracking optics. The field of regard is a 1 mrad radius which provides for relaxed beacon stationkeeping requirements as is described in Section 2.6. This field of regard is fixed during the time that the BD is doing agile, rapid retargeting. Hence, no specific beacon motion is required as part of the rapid retargeting process. The beacon optic is a simple convex 10-cm mirror designed to diverge the beam from the MO pointing optics back to BD so as to significantly overfill the primary mirror. This serves to spatially filter the beam so that the wavefront of the beam striking the primary mirror is within a small part of a wave of being spherical.

The BD shown in Figure 2.4-3 contracts the beam by a factor of 16.7 as it propagates down the beacon path optics (consisting of eight optical components following the primary and secondary mirrors as described in Section 2.6). On the return (target) path (consisting of three optical elements plus the secondary and primary), the BD expands the beam by  $16.7 \times$  and focuses the beam on the target.

The two paths are isolated from one another by the set of four gratings set up in two rhombs which reflect the p-plane of polarization into the first order and the s-plane into the zeroth order (i.e., the specular direction). The incoming beam from MO is made mostly p-plane polarized. After four diffractions into first order, the incoming MO beam is highly p-plane polarized. A single rhomb will cause the four spectral lines to be co-aligned but sheared after two diffractions,. The second rhomb realigns the four beams on top of one another. This incoming p-plane power is converted to s-plane in the phase conjugator SS so that the outgoing beam goes down the target path. Further discussion appears in Section 2.6.

The alignment unit utilizes a portion of the beam directed to it from the last grating in the set of four. The location of the fine tracking sensors is shown in Figure 2.4-3, and the concept is discussed in Section 2.8.

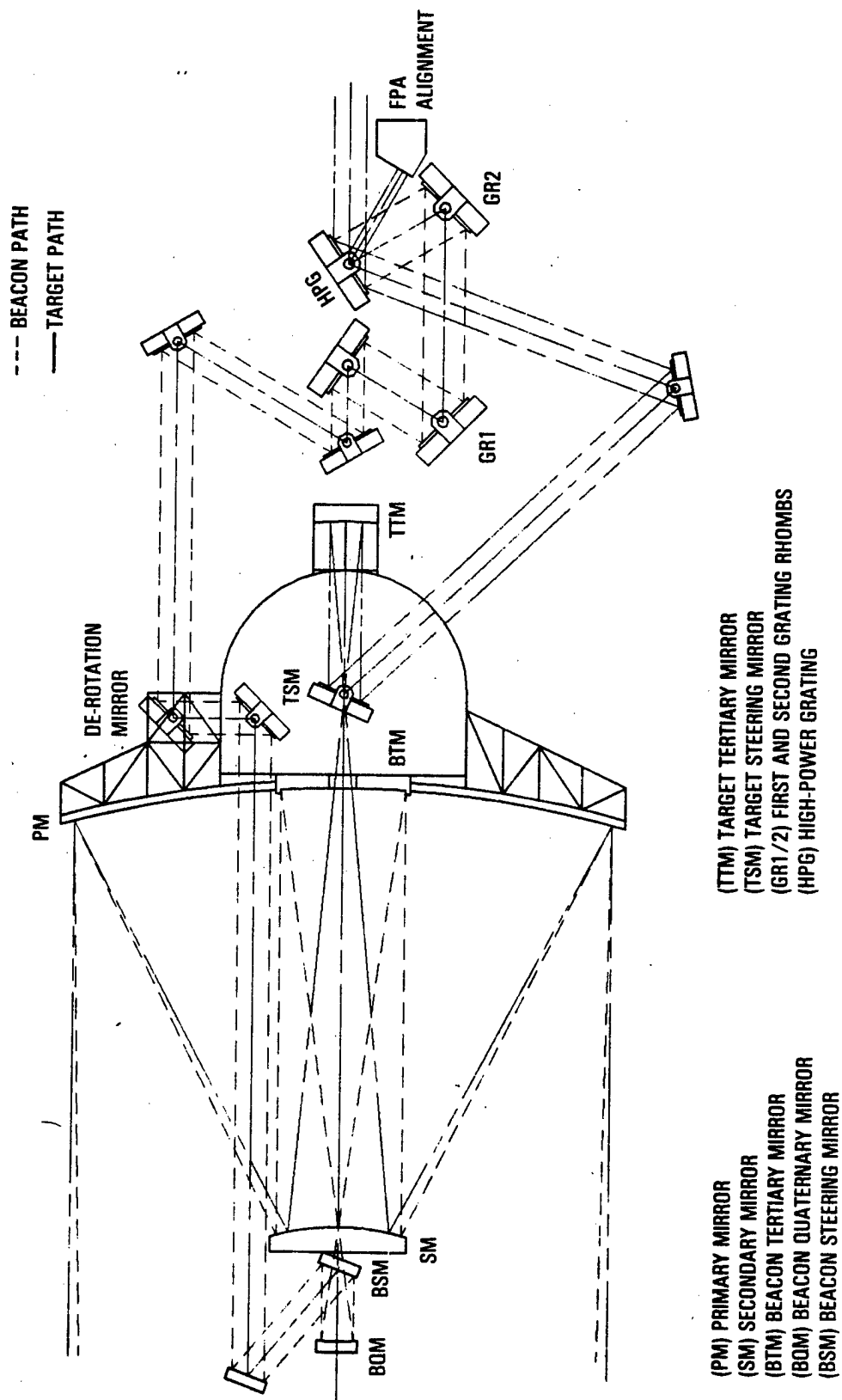


Figure 2.4-3. The Beam Director Subsystem (Optics shown with the beacon unseen, 25-primary mirror diameters to the left.)



### 2.4.3 Amplifier Subsystem (AMSS)

The six amplifiers shown in the AMSS in Figures 2.4-4 and 2.4-5 are designed as a scaled up version of the ALPHA gain generator. Each works in a bidirectional mode, first amplifying the beam on the way in from the BD to the SBS phase conjugator, and then a second time on the way back from the phase conjugator to the BD.

The AMSS begins with six nested annuli sized to direct the same power from the aperture into each of six amplifiers. The annular optics in each amplifier resize the diameter of the input ring of power directed to it to the same diameter of the gain region in each amplifier. The output of each amplifier is a circle with a diameter equal to 1/3 of the diameter of the output beam from the BD. These output circles from each amplifier are recombined at the same location of six flats into an array of 2 x 3 circles which are directed into a phase conjugation subsystem.

### 2.4.4 Phase Conjugation Subsystem (PCSS)

The PCSS shown in Figure 2.4-6 contains both the quarter-wave retarder mirrors and the SBS cell. In addition, a grating is used to separate the four laser wavelengths spatially in order that each beam will phase conjugate separately in the SBS cell. An alternate approach involving common volume multiline phase conjugation is also being considered based on recent experimental results at NRL (Reference 1). Phase conjugation takes place in the far field (i.e., the four beams must be brought to four separate foci). One SBS cell is used which dictates that each beam should have its own focussing element to redirect the four diverging beams into a single cell.

The quarter wave mirrors are packaged between the grating and the cell. The retardation of the polarization state requires four mirrors; thus each is required to produce only 22-1/2 degrees of retardation. In addition, two sets are used so that each set is required only to work on two spectral lines.

The following Sections 2.5 through 2.11 expand upon this top level description to provide a detailed account of each SS design based on requirements specified in Section 2.3.

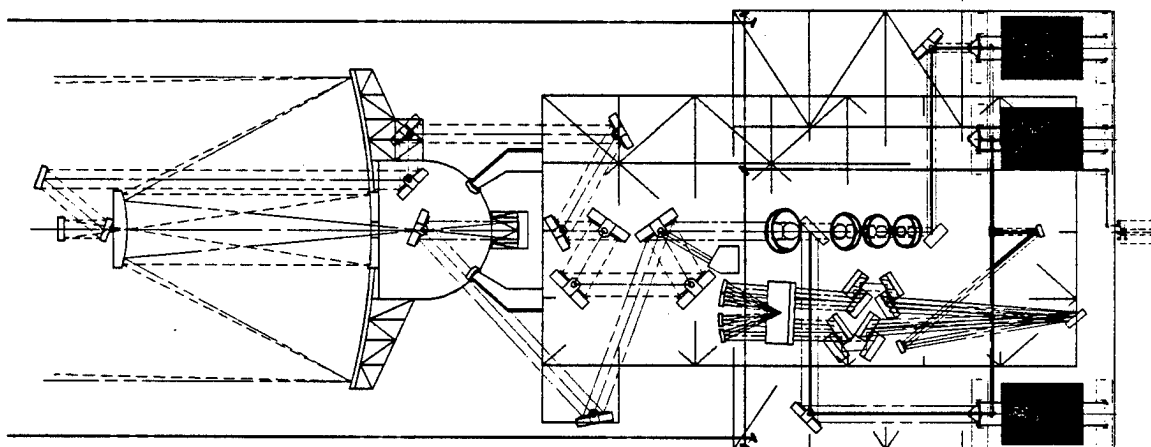


Figure 2.4-4. Amplifier Subsystem Highlighted

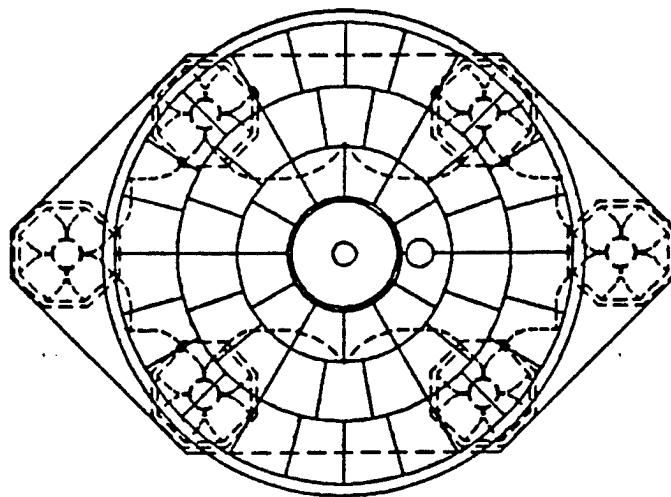


Figure 2.4-5. End View of the Six APACHE Amplifiers (laid out on the outline of the primary mirror)

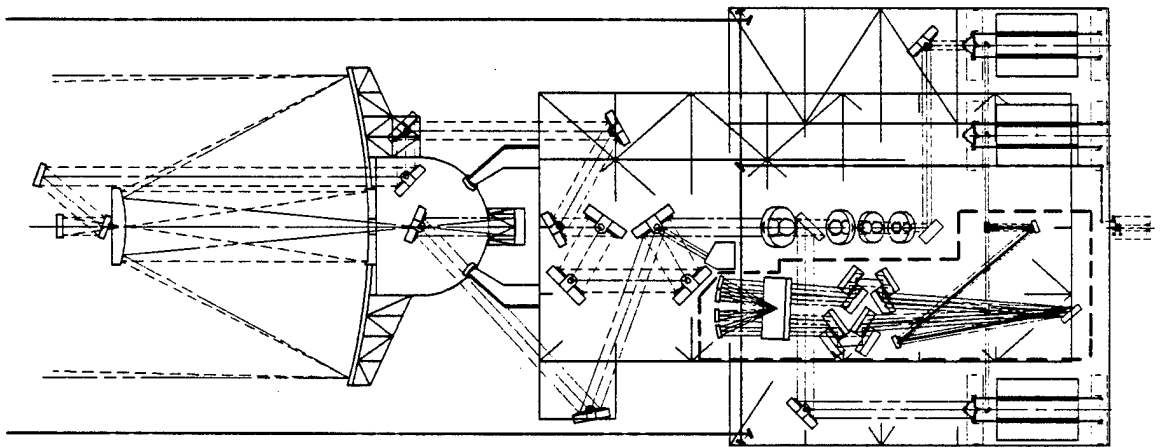


Figure 2.4-6. Phase Conjugation Subsystem Highlighted

## REFERENCES

1. Whitney, W., Feldman, B., and Duignan, M.; "Stimulated Brillouin Scattering of Multiline Hydrogen Fluoride Laser Radiation," SPIE Proceedings, Volume 874, 1988.

## 2.5 MASTER OSCILLATOR SUBSYSTEM

### 2.5.1 Requirements

The subsystem requirements for the MOSS are given in Figure 2.5-1. Two issues dominate the requirements for this subsystem. The first is oscillator size and power output. The second is beacon tracking and pointing accuracy.

### 2.5.2 Optical Design and Power Sizing

The basic concept for the oscillator subsystem is a scaled up version of the ALPHA laser. The output beam is converted from elliptical to linear polarization using a quarter wave plate of the type described in Section 2.11. A low-efficiency grating is used as the attenuator to improve isolation performance, as discussed in Section 2.11. The oscillator power requirement is driven primarily by the need to exceed the minimum power requirement for phase conjugation by a sufficient amount to assure high-fidelity conjugation and to operate the oscillator in the presence of return power leaking back through the beacon path. Two design parameters are the allowed amount of leakage back to the MO due to imperfect polarization of the s-plane return beam and the performance degradation in the MO due to this leakage. Amplifier extraction efficiency is also an important part of the trade space. The APACHE ASAM (see Section 4) calculates the oscillator power iteratively from the performance curves (derived analytically and validated experimentally, see Section 6, Volume 1) for the oscillator with feedback, the amplifier power equations, and the fraction of power feeding back into the oscillator. The ASAM-derived MO power requirement is given in Figure 2.5-1.

A free variable in this process is the external throughput in the oscillator optical path. By lowering the throughput (e.g., mirror reflectance) and raising the oscillator power by the same fraction, the input to the beam director is the same, but the effective ratio of power leaking back to the oscillator is reduced. Note that in this process the return power is reduced by the throughput term on the return path. This reduction in power throughput (power dump) will be done by a grating working at the required efficiency in the first order for p-plane

SOURCE	ENGINEERING	REQUIREMENT	
Mission	Mechanical	Total Firing Time	xxx sec
		Time Before Refueling	xxx yr
Power	Optical	Laser Power	xxx MW
		Beam Quality	xxx
		Optical Train Attenuation	0.25
		Aperture	5 cm
		Pointing	25 $\mu$ rad
	Mechanical	Gain Generator Diameter	1.1 m
		Gain Generator Length	xxx m
Isolation	Optical	Depolarized Power	2%

Figure 2.5-1. Master Oscillator Subsystem Requirements

polarization, which is the required input polarization. The baseline external throughput value for the MOSS is shown as an estimate in the requirements table in Figure 2.5-1.

The beacon has a requirement to be aligned with the nominal BD optical axis (Section 2.6). In addition, the MOSS is required to track the beacon and illuminate it with a beam centered on the center of curvature of the beacon to 0.16 of a diffraction spot or 25  $\mu$ rad). This results in a uniformly illuminated primary mirror centered on the central lobe of the far-field energy distribution. Section 2.6.4 describes the control system concept for the MO tracking.



## 2.6 BEACON DESIGN

### 2.6.1 Requirements

The beacon is included in the BDSS (see Section 2.7), and is an important part of the optical design of the BD. However, design issues arise due to the free-flying nature of the beacon and its interface with the MOSS which merit coverage in this separate section. Specific beacon requirements listed in Figure 2.6-1 are derived from the optical design considerations for the beam expander.

### 2.6.2 Optical Design and Spatial Filtering

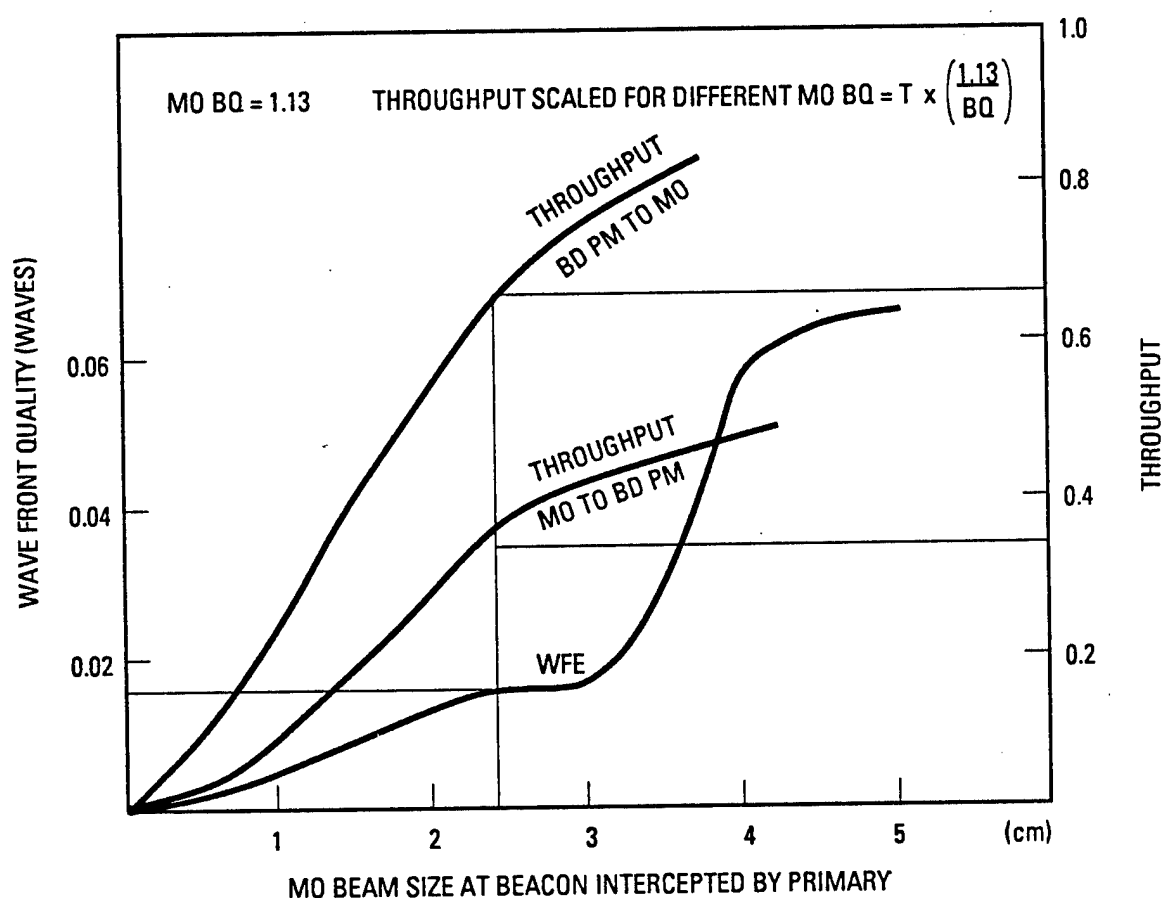
In the baseline design, the beacon provides an input wavefront with  $1/60$  of a wave wavefront error to illuminate the primary mirror. The wavefront error is minimized by spatial filtering at the beacon optic and the primary mirror. The beacon optic is a spherical mirror. By changing the radius of curvature, the part of the beam intercepted by the primary mirror can be changed. The less the primary receives, the more highly spatially filtered is the MO beam, and the better the wavefront quality is which enters the BD. Two design parameters associated with spatial filtering are the resulting power throughput achieved and the profile of the illumination on the primary mirror.

To evaluate the throughput as a function of residual wavefront error after spatial filtering, a model (CROQ plus deformable mirror) of the ALPHA output wavefront error was used to create a simulation of MOSS output. This wavefront was propagated to the beacon optic and back to the primary mirror using the TPROP analysis code. The fraction of power entering the BD and the residual wavefront error at the primary mirror are plotted in Figure 2.6-2 as a function of the degree of spatial filtering that was applied.

In addition, the phase conjugated power leakage returning to the beacon (instead of the target) is spatially filtered again because its far field distribution back at the output aperture of the MOSS has been rediffracted. This throughput and the design point chosen for the baseline are also shown in Figure 2.6-2.

Item	Specification
Stationkeeping	+1/2 mrad (translation) 1/80 x PM dia. (axial) 9 mrad (tilt)
Beacon Optic	10-cm diameter 120-cm radius of curvature 99.5% reflectivity

Figure 2.6-1. Beacon Derived Requirements



01M160.89.05-5005

Figure 2.6-2. Spatial filter throughput and wavefront quality. For a wavefront quality of  $1/60 \lambda$ , 0.375 is the filtered input to the beam director, and 0.68 is the return throughput. The beam which hits the primary mirror is 2.4 cm at the beacon.

At this design point the resulting illumination profile of the input beam on the primary mirror is modelled as flat in the ASAM.

### 2.6.3 Mechanical Design

### 2.6.4 Beacon Operational Concept and Engineering

The fundamental concept of the APACHE beacon assembly is that of a small free-flying vehicle which supports a figured mirror at a distance of 25 primary mirror diameters from the host SBL vehicle. This beacon vehicle must integrate all equipment necessary to satisfy the APACHE mission requirements in 46818-6003-SX-00. Table 2.6-1 summarizes these requirements in unclassified form. Table 2.6-2 summarizes the baseline maneuvers implied by the mission requirements with classified values suppressed. An alternate method of satisfying the mission requirements, without deployment or rendezvous, would be to leave the beacon deployed at its orbital station for the entire operational lifetime of the SBL. The former scenario was selected early in the APACHE program as baseline, because the propulsion requirements to hold the beacon on station for years instead of days, and provide power, communications, and survivability over the same period would turn the beacon into a significant satellite in its own right without conferring any particular advantage. It was decided instead to hold the beacon's size and mass to the minimum required to perform one worst-case mission and enhance the resiliency of this assembly by providing one or two redundant beacons.

Table 2.6-3 summarizes the feasibility studies performed on the beacon.

#### 2.6.4.1 Propulsion Analysis

A beacon mass summary was prepared early in the APACHE program and later reviewed and updated by a department within TRW, having the charter of satellite preliminary design. Table 2.6-4 summarizes the most recent velocity change requirements for each type of beacon maneuver. The "close" and "long" range cases correspond to near-term and high-brightness SBLs, respectively. Throughout one operational cycle the beacon must deploy from the host vehicle to its nominal range along the primary mirror centerline, maintain

Table 2.6-1. Mission Requirements Significant to Beacon Design

Deploy time = [S] seconds

Orbital Altitude = [S] km (assumed circular)

Maximum slew angle = [S] degrees

Maximum slew rate = [S] rad/s<sup>2</sup>

Control translation and rotation from nominal aligned position during [S] beam on time to tolerances:

Translation transverse to optic axis = +0.5 mrad relative to host

Translation along optic axis =  $\pm 1/80 \times \overline{PM}$  dia.

Yaw and pitch rotation = 9 mrad

Roll rotation = not constrained by beam director, but alignment sensors may require rough control.

Capable of periodic testing; hence capable of rendezvous, docking and refueling at host vehicle

Table 2.6-2. Baseline Beacon Maneuver Scenario

Deploy from host vehicle to 25D. Stop relative to host.  
Acquire host and lock on.

Maintain tracking relative to host while pointing at target for one orbital pass.

Control translation and rotation from nominal aligned position while beam on.

Perform 3 maximum angle slews.

Rendezvous and dock with host vehicle.

Refuel beacon from host tankage.

Redundancy is enhanced by providing three beacons. Two are deployed with third held in reserve on host vehicle. This permits "leapfrog" mode during large angle slews, but sufficient propellant is provided for either beacon to perform above maneuvers.

Table 2.6-3. Beacon Feasibility Studies

Issue	Approach	Conclusion
Mass	Weight using state of art and advanced technology	System of three beacons requires less than 0.2% of SBL mass
Sensing beacon/host relative position for stationkeeping	Apply TRW SAMS sensors used on other programs	Available resolution about 100 times finer than required
Control of beacon/host position to APACHE tolerances	Stationkeeping analysis	Thruster alignment tolerance only disturbance. Set of small thrusters required for tilt
Laser beam interaction with thruster plumes	Integrate OPD and absorption through plumes	Interaction negligible
Thruster contamination of optics	Upper bound plume impingement calculations	No problem if beam director cover opened after beacon launch
Utility of tethering beacon to host vehicle	Review tether literature, apply to beacon	Advantage in retrieval balanced by penalties in use

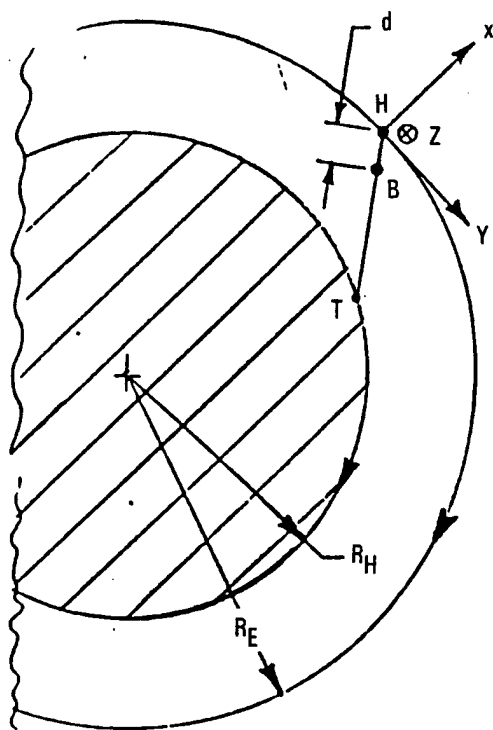
itself in an orbit that places it along a vector from host to target as shown in Figure 2.6-3, stationkeep its position and attitude to within APACHE optical tolerances during laser burn, perform several large angle-slew maneuvers, and rendezvous and dock with the host vehicle. A 10,000-second holding period on orbital station in addition to the laser burn duration is assumed. The table allows propellant for one orbital readiness test and one operational mission. If it is desired to test operation of the SBL more often, provision should be made to refuel the beacon from the host while docked, to prevent mass growth of the beacon.

Originally  $N_2O_4/MMH$  storable propellants having a specific impulse of 310 lbf-s/lbm were baselined for the APACHE beacon. As more detailed studies were performed, it was found that an  $N_2O_4/N_2H_4$  propellant combination offers two advantages in the beacon application. Attitude/

Table 2.6-4. Equivalent Delta-V and Propellant Requirements

Mode	Close Range $\Delta V$ (m/s)	Long Range $\Delta V$ (m/s)
Deployments (2)	100	400
Deployment trims	10	40
Maximum slews (4)	130	472
Docking with host (1)	10	20
Attitude/position control		
Orbit maintenance	15	60
Stationkeeping during burn	2	8
Engine disturbances	30	71
Limit cycle	28	17
<u>Total Equivalent Delta-V:</u>	<u>325 m/s</u>	<u>1,135 m/s</u>
Beacon dry mass, $m_0$ =	247 kg	358 kg
$m_p/m_0 = \exp(DV/V_e) - 1$ =	0.1128	0.4526
Propellant mass =	27.9 kg	162 kg
Deployed mass =	274.9 kg	520 kg
Propellant fraction of deployed mass	10.1%	31.1%
Reference Thruster Exhaust Velocity, $V_e$ = 3040 m/s (Isp = 310 sec)		

position control studies indicated a need for a low thrust set of attitude control thrusters in addition to the larger bipropellant thrusters needed to reach peak deployment and slew accelerations. Plume contamination studies found that the most significant species are carbon compounds from MMH combustion that are not present in  $N_2O_4/N_2H_4$  exhaust plumes. The use of  $N_2O_4/N_2H_4$  propellants also permits a dual-mode system where small monopropellant  $N_2H_4$  thrusters can be fed from the same tanks as the larger bipropellant thrusters with the same or greater specific impulse.



USE HILL EQUATIONS FOR RELATIVE MOTION DURING RENDEZVOUS =

$$\ddot{X} - 2N\dot{Y} - 3N^2X = F_X$$

$$\ddot{Y} + 2N\dot{X} = F_Y$$

$$\ddot{Z} + N^2Z = F_Z$$

WHERE

$$N = \text{MEAN ANGULAR VELOCITY} = \frac{G(M_E + M)^{1/2}}{R_H^3}$$

R<sub>H</sub> = ORBITAL RADIUS

Figure 2.6-3. Beacon Orbital Tracking Geometry

#### 2.6.4.2 Mass and Power Summary

Table 2.6-5 shows the results of a detailed estimate of beacon mass and electric power requirements. Advanced, but under development, technology is assumed which is consistent with other studies of conventional SBLs. Beacon mirror cooling is provided by heat pipe mirror technology. Beam heating absorbed by the mirror is dissipated by vaporization of  $\text{NH}_3$  coolant. This mirror was weighed as a solid silicon carbide disk. The mass of graphite-epoxy overwrapped propellant tanks was scaled down by volume from that of existing tanks.

It is understood that the beacon will remain attached to the host vehicle throughout the majority of the mission, with only brief sorties to conduct maneuvers. The battery can thus be kept at trickle charge from the host most of the time, and will undergo only two charge/discharge cycles apart from ground test. The charge controller should be part of the host, where a single unit can service multiple beacons.

Battery experts advise that NiCd cells lack life credibility for the beacon mission, and that carrying redundant batteries would not improve the situation. Also, they are bulky and heavy.  $\text{NiH}_2$  batteries have credible life credentials, are somewhat lighter but are bulkier than NiCd.

Advanced lithium secondary cells are still in the laboratory demonstration stage, but can be assumed to be developed and available in the time frame of the beacon mission. Their chemistry promises long life if the number of charge/discharge cycles is limited to the order of 100. This makes them unsuitable for most satellite applications -- hence the slow pace of development -- but especially appropriate for missions of the beacon type.

Individual power consumptions were estimated with sufficient accuracy to size a battery with some life derating and an assumed 50% depth of discharge.

Table 2.6-5 lists average load power as 170 W, including 25% contingency. The longest sortie from the host in the mission scenario is less than 3 hours. This implies that a nameplate storage capacity of about 1,000 W-hr is adequate to support the load at 50% depth discharge.



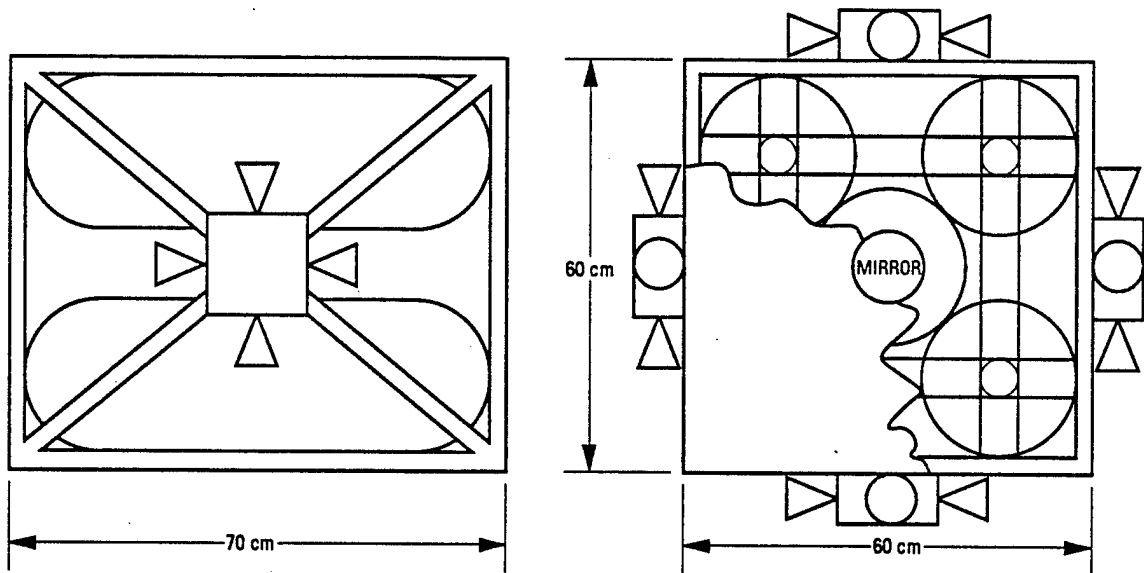
Table 2.6-5. Beacon Dry Mass and Power Summary, Close Range Case

Item	Mass (kg)	Power (W)
<b>PAYLOAD</b>		
Mirror (6.5-cm moly substrate)	2	-
Mirror mount	1	-
Mirror cooling assembly (with evaporated NH <sub>3</sub> coolant)	20	-
<b>THERMAL CONTROL</b>		
Heaters	2	40
Heater drive electronics	2	4
Insulation/mirrors	2	-
Transducers, etc.	0.5	-
<b>AVIONICS</b>		
<u>TT&amp;C (SGLS)</u>		
SGLS transponders (2)	6.5	14
CMD/TLM electronics (Redundant, with embedded encryptor)	4.5	10
Transfer switch	0.2	-
Diplexer	0.5	-
Omniantenna(s)	1	-
<u>ATTITUDE/POSITION CONTROL</u>		
Control electronics (Redundant)	1	3
Data processing (computer) (2)	11	10
IMU (2) (Gyros and accelerometers)	9	30
SAMS (Optical range/attitude sensor)	1.5	3
Valve drive electronics	1	1
<b>ELECTRIC POWER</b>		
Power switching and fuses	2	1
Battery (1) (Lithium 40 AH)	25	10
Harness (Power, data and coax)	8	8

Table 2.6-5. Beacon Dry Mass and Power Summary, Close Range Case  
(Continued)

Item	Mass (kg)	Power (W)
PROPULSION		
Valves, regulator, filters transducers and lines	35.5	-
250 lbf engines (2) (NTO/MMH with heat shields)	16.5	-
5 lbf dual thrusters (12)	13.5	2
Helium pressurant tank (1) (6.5 in. dia. sphere at 4500 psi)	1.2	-
Oxidizer tank (1) (8 in. dia. X 15.5 in.)	1.3	-
Propellant tank (1) (8 in. dia. X 15.5 in.)	1.3	-
SUBTOTALS:	170 kg	136 W
STRUCTURE		
Primary + mounting hardware (18% of deployed mass including 30 kg assumed propellant)	36	-
CONTINGENCY		
20% of mass without propellant, 25% of estimated power	41	34
TOTAL DRY MASS AND LOAD POWER:	247 kg	170 W

The overall size and arrangement of this equipment is shown in Figure 2.6-4. Note that the side of the beacon facing the host will be covered with a reflective shroud to protect its other components from parts of the oscillator beam falling outside the beacon mirror. This shroud can be cooled by ammonia evaporation as used in the beacon mirror, but the shroud need meet only a gross thermal distortion requirement to keep spatially filtered oscillator power off the beacon return path.



01M.160.90.01-5005

Figure 2.6-4. Overall Beacon Arrangement

#### 2.6.4.3 Beacon Control

An investigation of beacon control feasibility was performed to uncover any problems with the concept. This investigation was further subdivided into two parts, addressing the feasibility of sensing beacon position to the required tolerances, and the feasibility (and mass implications) of controlling to these tolerances. The two investigations are documented in References 1 and 2.

Table 2.6-6 summarizes the optical requirements imposed on beacon to host relative position and angular attitude as well as the achievable resolution of our baseline sensing system in the same degrees of freedom. Figure 2.6-5 illustrates the appearance, method of operation, and some bench test data on the TRW Surface Accuracy Measurement System (SAMS). This relative position sensing system uses several collimated and uncollimated flashing lights a known distance apart on one vehicle, and an optical system on the second vehicle that images these lights on linear arrays. Combination of the centroided image positions in orthogonal arrays with their known absolute distance apart permits calculation of the relative position of the two vehicles in 6 degrees of freedom. The known blink frequency of the lamps permits distinguishing between several images and allows the filtering out of background light sources. The baseline design places the light sources on the host vehicle (separated by the primary mirror diameter) and the SAMS sensors on each beacon. This placement maximizes both light source separation and beacon autonomy. If the SAMS sensors were placed on the host vehicle, position and attitude data would have to be continuously relayed to the active beacon through a communications link. While such a link normally would be maintained between host and beacon computers to enable the beacon to anticipate host requirements, an interruption in this link would cause no disruption of beacon control. The beacon, as a cooperative subsatellite, would carry navigational lights or retroreflectors to assist the beacon tracking optics assembly on the host SBL in keeping the oscillator beam centered on the beacon's return mirror.

Table 2.6-6. Beacon Position Sensing Requirements and Capabilities

Beacon to Host Range (m)	Lateral Displacement (cm)		Lateral Tilt (Radian)		Range Displacement (cm)		Roll About Range Vector (Radian)	
	Actual	Required	Actual	Required	Actual	Required	Actual	Required
250	0.11	10	4.4E-6	9E-3	2.7	25	0.2 E-3	100E-3
500	0.22	20	4.4E-6	9E-3	5.5	50	0.2 E-3	100E-3
750	0.33	30	4.4E-6	9E-3	8.2	75	0.2 E-3	100E-3
1000	0.44	40	4.4E-6	9E-3	10.9	100	0.2 E-3	100E-3

The achievable resolutions of the beacon sensing system shown in Table 2.6-6 are based on an angular resolution of 1/20000 of the SAMS lens system's field of view (FOV). This resolution was demonstrated during TRW's JOSE program. The resolution values shown are based on a 5-degree FOV. As resolution requirements are exceeded by a factor of at least 9, this FOV could be increased into the 10- to 20-degree range to ensure against loss of control loop lock. Alternatively, a larger FOV SAMS system could be provided that hands off to the fine resolution sensors, although with present alignment tolerances, this coarse system is not required. In any event, the beacon will carry an inertial measurement unit (IMU) to provide an absolute attitude reference used during deployment and acquisition of the SAMS lights.

Measurement of the beacon position relative to the host in 6 degrees of freedom will require three SAMS sensor heads (each providing signals from two orthogonal linear arrays), three uncollimated light sources, and one collimated light source. The light sources can be employed in the control of several redundant and/or multiple beacons.

Having determined that the beacon could locate itself much more accurately than required, the study focused on how well position tolerances could be held. While the thrust levels of the main engines are set by the mass of the beacon and the acceleration required during the deployment and slew maneuvers, the precision of control during stationkeeping is set by

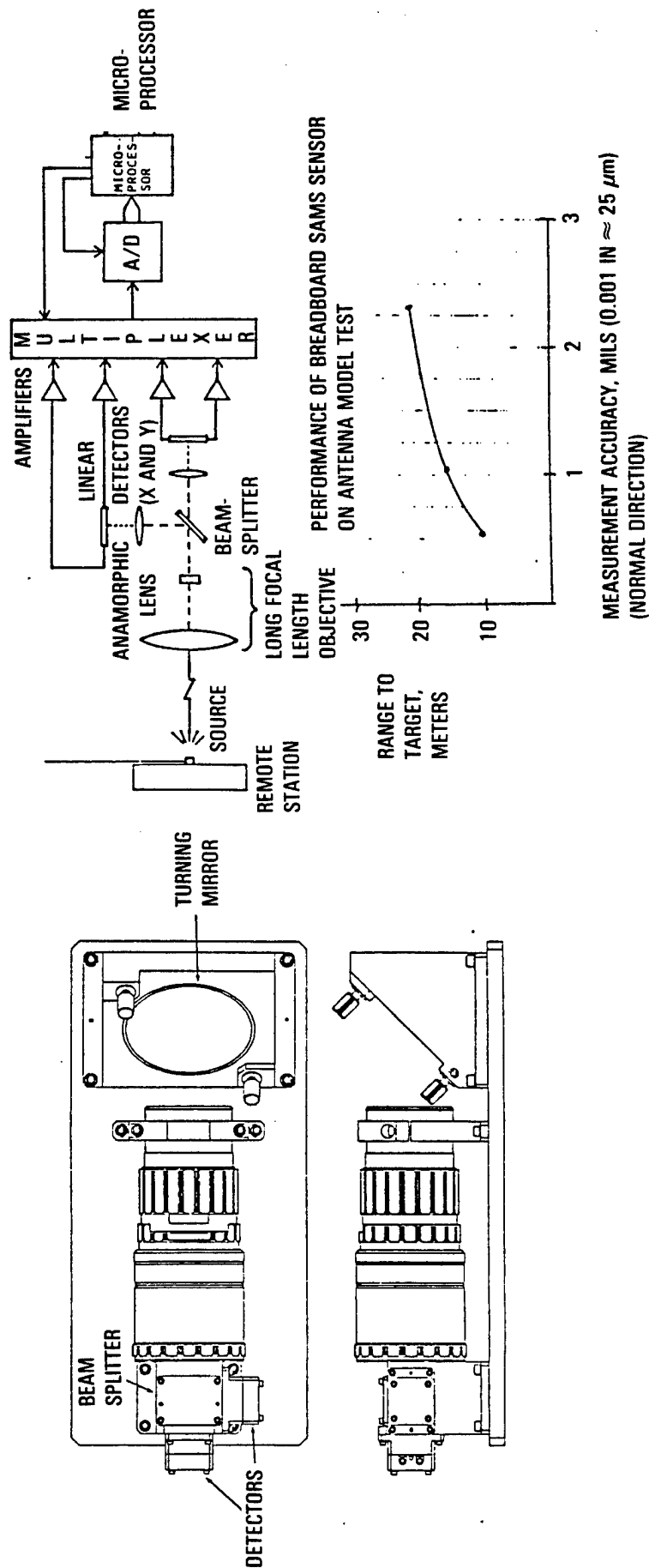


Figure 2.6-5. TRW Surface Accuracy Measurement System (SAMS) Concept

the minimum impulse bit commandable by the thruster. This value was assumed to be 10 ms times the steady thrust of the engine based on the performance of a family of bipropellant Marquardt thrusters covering approximately the same range of thrust. Positional accuracy, and particularly the propellant required to maintain it, are functions of the disturbance forces tending to move the beacon from its nominal position.

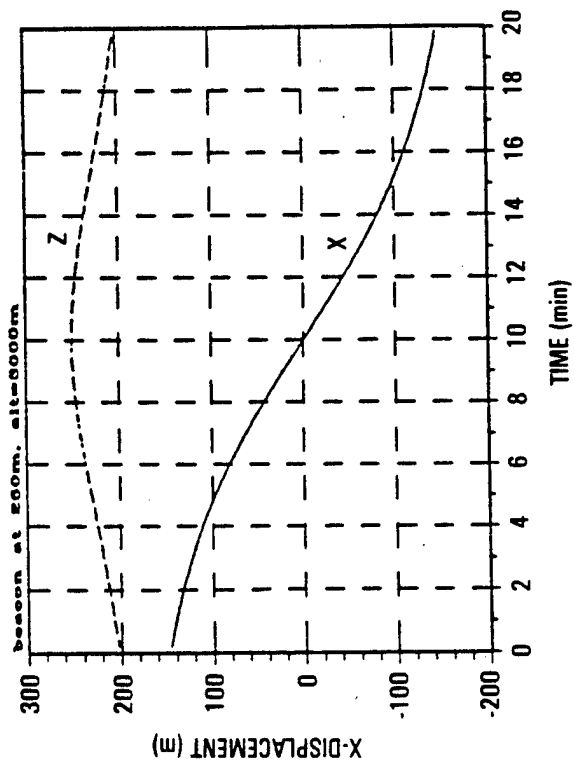
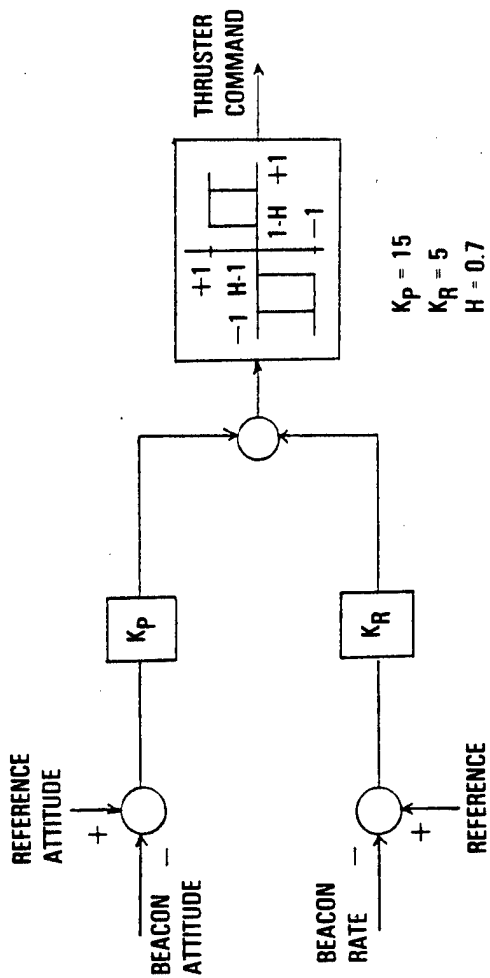
The magnitude of several disturbance forces were examined including:

- Solar light pressure
- Aerodynamic drag (assumed altitude = 3000 km)
- Linear and angular main thruster misalignment
- Beacon center of mass migration.

The first two disturbance sources were found to be totally negligible compared to the last two sources. It was estimated that the latter two disturbances would increase stationkeeping propellant requirements by only 10% above an ideal "bang-bang" control requirement.

It was further concluded that while the main thrusters would hold the translational beacon position with reasonable propellant, control of the angular attitude tolerance of 0.5 degree required significant amounts of propellant and a 6.5-Hz pulse rate because of the large impulse bit of these thrusters. It was therefore decided to add a set of smaller (22 NT) thrusters for attitude control.

As a check on classical calculations of control requirements during orbital tracking, a simple bang-bang positional control was simulated with positional commands generated by the Hills relative orbital position equations (Clohessy-Wiltshire equations). Figure 2.6-6 shows the control block diagram, the beacon path commanded, and the control systems response in the x and z directions.



**A: BLOCK DIAGRAM OF THE THRUSTER NAVIGATION CONTROL LAW**

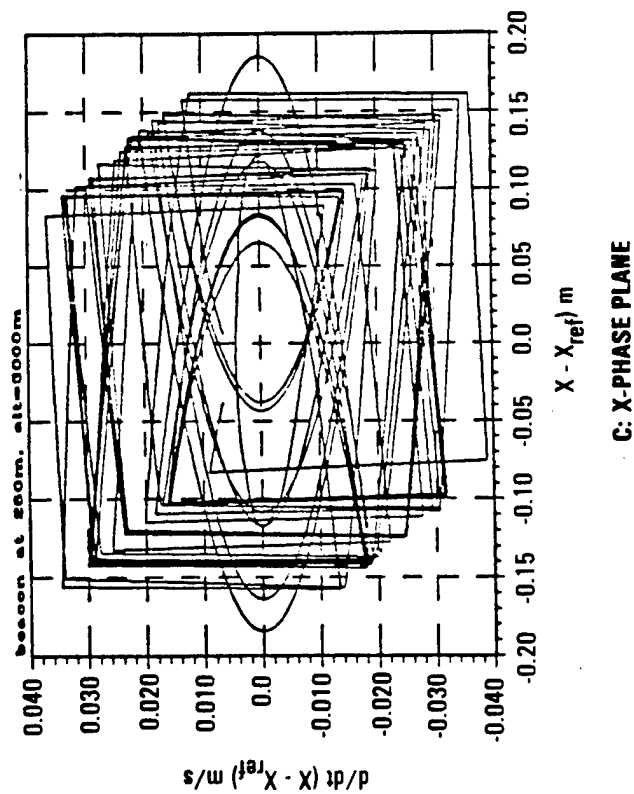
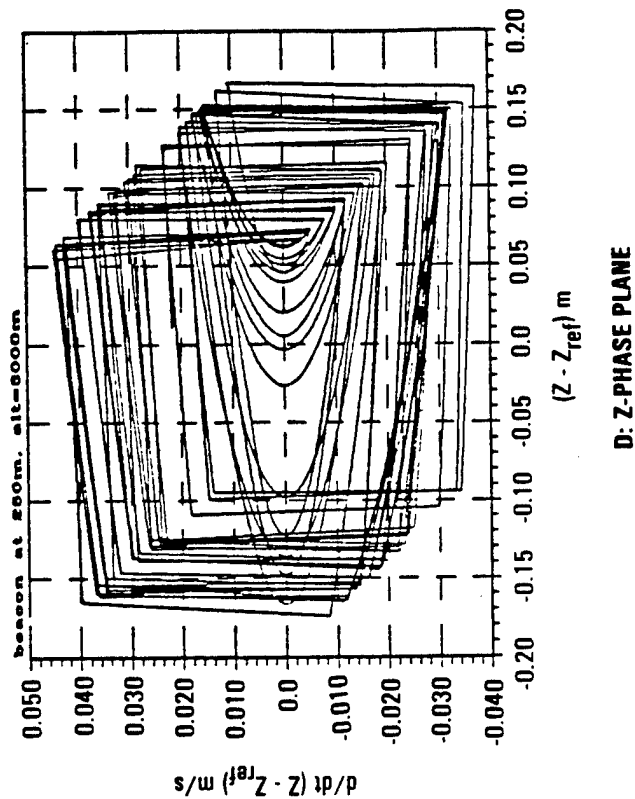


**Figure 2.6-6. Orbital Tracking Control Simulation**



#### 2.6.4.4 Tethered Beacon Investigation

Several times during review of the evolving APACHE beacon concept, the suggestion that perhaps keeping the beacon permanently tethered to its host SBL would offer some advantages. This version of the basic concept would seem to offer an intermediate degree of beacon to host vehicle connection between rigid connection with stiff structure and the baseline free-flying beacon.

The open literature on tether applications was reviewed and a qualitative assessment of tethered beacon was prepared, which is summarized in Table 2.6-7. Previously proposed uses of tethers have involved slow maneuvers over large fractions of an orbit, often relying on gravity gradients to maintain tension in the tether. Where more rapid maneuvers are contemplated, rocket thrust may be used to hold the tether taut, although this strategy may become an expensive use of propulsion. Table 2.6-7 distinguishes four modes in which a tether might be used on a beacon and enumerates the advantages and disadvantages of each. One stated advantage of a tether incorporating hoses would be to keep the beacon's propellant tanks full at all times without discrete refueling operations. While this advantage is real, propellant is not a large fraction of the beacon mass in any event unless monthly or weekly beacon demonstration testing is required. It was concluded, however, that readiness testing at infrequent time intervals coupled with provision of redundant beacons is a more reliable operational mode.

If a tether were used with the beacon, the mode designated "C" in Table 2.6-7 appears to offer the most benefit with the least risk. In this mode, beacon retrieval and refueling is simplified and the risk of the tether fouling or inputting significant dynamic forces to the beacon position control system during slew maneuver is eliminated, as the tether is cut loose in actual battle. The accompanying disadvantage of this mode is that a beacon readiness test with tether attached does not really demonstrate the actual control situations that would be used in battle.

Table 2.6-7. Qualitative Tether Evaluation

Mode of Use	Advantages	Disadvantages
A. Supply all beacon propellant through tether. Leave beacon deployed over service life	<ul style="list-style-type: none"> <li>• Up to 19% beacon mass saving</li> <li>• Eliminates need for recovery/redeploy capability</li> <li>• Low contamination if tether will resist compression</li> </ul>	<ul style="list-style-type: none"> <li>• Complicated control dynamics</li> <li>• Risk if multiple beacons used in slew</li> <li>• Survivability of 2 to 4 objects instead of 1 must be assured</li> <li>• Stationkeeping propellant probably increased</li> </ul>
B. Tether supplies propellant to top off beacon tanks only. Deploy and retrieve with tether attached. In battle, beacon slews on tether	<ul style="list-style-type: none"> <li>• Beacon protected during storage</li> <li>• Beacon retrieval simplified to soft docking</li> </ul>	<ul style="list-style-type: none"> <li>• Complicated control dynamics</li> <li>• Risk if multiple beacons used in slew</li> <li>• Stationkeeping propellant probably increased</li> </ul>
C. Tether supplies propellant to top off beacon tanks only. Deploy and retrieve with tether attached. In battle, beacon separates from tether and flies autonomously	<ul style="list-style-type: none"> <li>• Beacon protected during storage</li> <li>• Beacon retrieval simplified to soft docking</li> </ul>	<ul style="list-style-type: none"> <li>• Control dynamics simplified but orbital test control not same as battle</li> </ul>
D. Tether used for host/beacon communication in A or B above	<ul style="list-style-type: none"> <li>• Difficult to jam</li> <li>• High bandwidth</li> </ul>	<ul style="list-style-type: none"> <li>• Modulated light beam has same advantages</li> </ul>

#### 2.6.4.5 Thruster Plume Studies

The issue of exhaust plumes from the beacon's thrusters and their impact on various SBL systems emerged from early reviews and several investigations were initiated. Analyses were performed in three distinct areas, i.e., optical path difference (OPD) induced in the SBL output beam

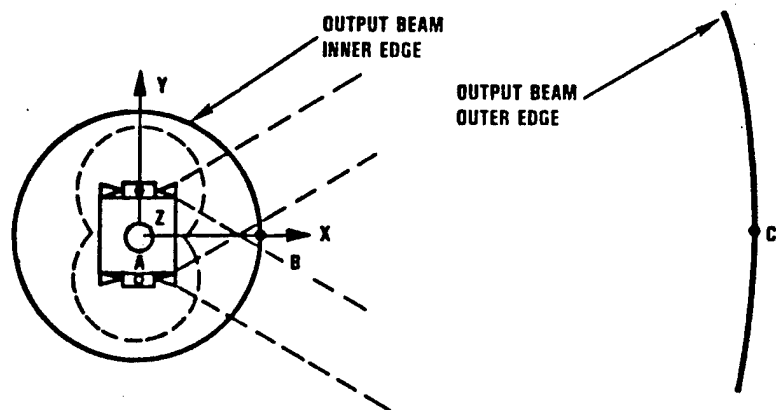
by beacon plumes, absorption of beam power by the same plumes, and severity of optical surface contamination by the beacon thrusters.

Figure 2.6-7 shows the SBL output beam surrounding the beacon when deployed and the thruster plumes which might interact with this beam. The sketch and results are applicable to a near-term system which represents the worst case for these optical effects. As the scale of the system increases, all plume densities vary inversely as the square of some characteristic dimension, such as the beam director diameter. The values shown are based on worst-case, upper-bound assumptions and are local values. The effective RMS averages over the projected area of the output beam are perhaps another factor of 4 lower. In view of the small values of these disturbances, the RMS averaging was not performed.

Figures 2.6-8 and -9 outline the methods used to compute the OPD and absorption due to beacon plumes. The absorption calculation is particularly conservative in that all of the potential absorptive species were considered to have the absorption characteristics of the worst species, i.e., water vapor at the  $P_1(8)$  wavelength.

Further studies were made of potential optical contamination both during beacon deployment and while it is on station. Preliminary calculations indicated little concern once the beacon is on station and little concern for ambient temperature mirrors even during the deployment maneuver, as contaminant films would evaporate almost as fast as they are deposited. Contamination of the primary mirror can be reduced to insignificant levels by recessing the mirror in its open cover, by beginning to open the cover after the first half of the beacon deployment maneuver, and by substituting  $N_2O_4/N_2H_4$  propellants for the  $N_2O_4/MMH$  propellants assumed in the analysis (the latter substitution eliminates carbon based contaminants).

Our remaining concern is contamination of cryogenically cooled mirrors and/or detectors in the Acquisition Pointer and Tracker (APT) assembly. At typical detector temperatures contaminants, once deposited, do not evaporate at significant rates. It probably is undesirable to cover the APT before or during beacon deployment, as it should be tracking



Beam	Thruster Firing Direction	Point	OPD TIME AVERAGED (IR Waves)	Fraction Absorbed
Beacon	+Z (to host)	A	5.5 E-5	<0.8 E-6
Output	-Z (to target)	B	5.5 E-6	<0.8 E-6
	$\pm X, \pm Y$	B	1.1 E-5	<1.2 E-9
	$\pm X, \pm Y$	C	2.3 E-6	<4.2 E-12

\* HIGHER FOR ~ 20 MILLISECONDS AT 30 SECOND INTERVALS WITH THRUSTERS FIRING.

Figure 2.6-7. OPD and Absorption Due to Beacon Thruster Plumes

$$O \quad O.P.D. = \int_0^L (n - 1) \, dL$$

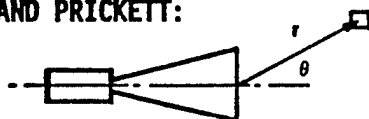
(RELATIVE TO PATH IN VACUUM)

- o EXHAUST FROM BASELINE  $N_2O_4/MMH$  THRUSTERS IS COMPOSED OF SEVERAL SPECIES ( $CO$ ,  $CO_2$ ,  $H$ ,  $H_2$ ,  $H_2O$ ,  $NO$ ,  $N_2$ ,  $O$ ,  $OH$ ,  $O_2$ ) SO DERIVE:

$$(n - 1)_{MIX} = \frac{1}{\rho_{STP} W_{MIX}} \left[ \sum_{i=1}^N (n - 1)_i X_i \right] \rho_{MIX}$$

WHICH IS LIMITED TO LOW DENSITY, PERFECT GASES

- o EVALUATE LOCAL PLUME DENSITY FROM SIMPLIFIED EXPRESSION OF MAYER AND PRICKETT:



$$\rho_{MIX}(r, \theta) = \frac{K [\cos(\theta/2)]^\beta}{V_E r^2}$$

Figure 2.6-8. Laser Interaction with Thruster Plumes (OPD Method)

- o MAJOR ABSORPTIVE SPECIES IS H<sub>2</sub>O VAPOR BOTH IN UNIT ABSORPTION AND CONCENTRATION. DATA ON A FEW OF THE OTHER SPECIES AT HF WAVELENGTH IS EXCEEDED BY H<sub>2</sub>O. THEREFORE AS A CONSERVATIVE SIMPLIFICATION ASSUME:
  - MOLE FRACTION OF WATER IS INCREASED BY FRACTIONS OF ALL LESSER ABSORBERS
  - USE ABSORPTION OF WORST MAJOR HF LINE [P<sub>1</sub>(8)] FOR ABSORPTION OF ALL LINES
- o THEN ABSORPTION MAY BE FOUND FROM

$$\alpha(r) = K_2 (X_{H_2O} + 4.0 X_{H_2O}^2) \frac{P^2}{T}$$

- o LOCAL PRESSURE AND TEMPERATURE ARE EVALUATED AS A FUNCTION OF  $\rho(r, 0)$  BY ASSUMING AN ISENTROPIC EXPANSION.

Figure 2.6-9. Laser Interaction with Thruster Plumes (Absorption Method)

continuously. Figure 2.6-10 shows a modified beacon deployment trajectory that would mitigate this contamination at the cost of somewhat more propellant and larger main thrusters. We plan to revisit this problem during the APEX program as more information on APT requirements and placement becomes available.

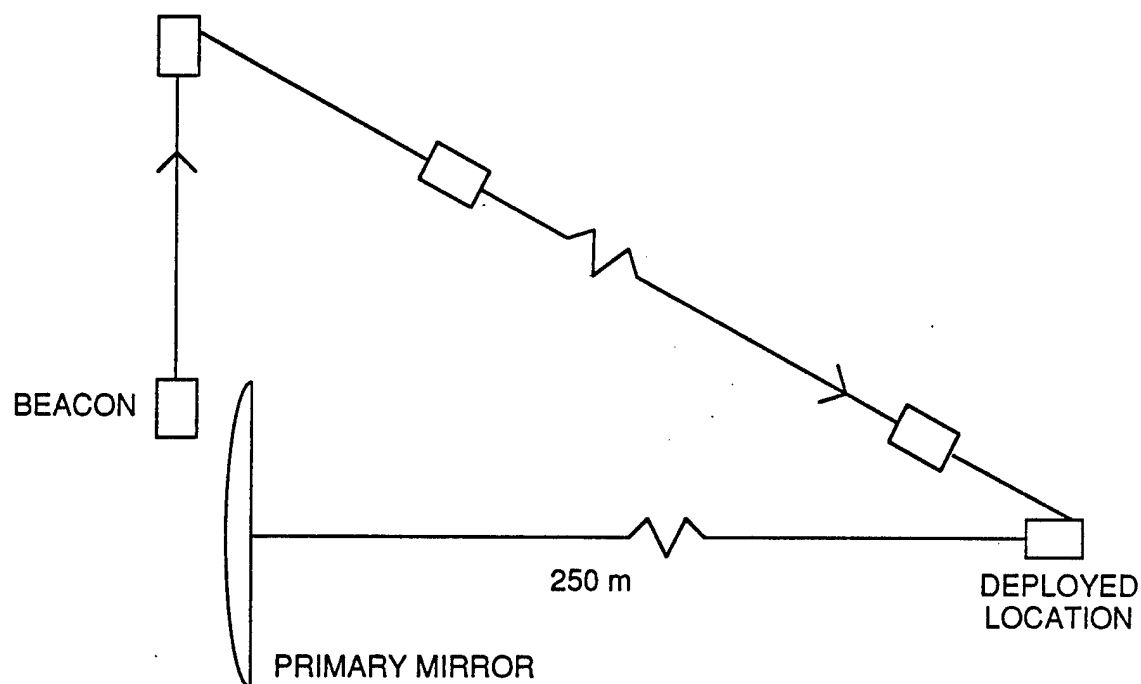


Figure 2.6-10. Beacon Deployment Trajectory to Mitigate Plume Contamination of APT Optics



## 2.7 BEAM DIRECTOR SUBSYSTEM

### 2.7.1 Requirements

The requirements and a summary of the design parameters for the BDSS are listed in Figure 2.7-1, and a layout of the optical elements is shown in Figure 2.7-2.

### 2.7.2 Optical Design and Layout

The optical design is constrained by the requirement to operate at two very different conjugates (the beacon and the target) simultaneously, with a shared primary and secondary. The optical prescription and design characteristics are discussed in Section 3.2. All optical elements (except the primary and secondary mirrors) in each path are not common. The optical design for each of the two paths must operate essentially independently, and the wavefront produced by the round trip path is limited by the usual geometric aberrations, optical misalignments, and manufacturing and thermal misfiguring.

The two paths, beacon and target, which are different, are recombined at the high-power grating in the two grating rhombs. The beacon path separates from the target path at the beacon tertiary which has a hole in its center to let the target path pass through to the target image plane. This hole is the limiting obscuration in the system. The hole in the target pointing flat is sized relative to the target beam incident on it to match the limiting obscuration. A similar construct occurs at the beacon image plane behind the secondary, except the beacon FOV is much smaller than the target FOV.

The phase conjugation process cancels wavefront errors only at the primary mirror in the BDSS (as well as in the common path in the AMSS and PCSS). While the secondary mirror is common to each path, the mapping of the beacon and target path footprints on the mirror is too mismatched to experience substantial common wavefront error correction.

The cancellation of primary mirror wavefront error is good enough to provide a reduction factor on the order of 200 to 500, depending on the particular aberration. The limit to perfect cancellation is due to the

Source		Requirement
Mission	Aperture	m
	Slew angle	deg
	Slew rate	mrad/s <sup>2</sup>
	Field of view	mrad
	Retargeting time	
	Pointing accuracy	spots
Power	Oscillator beam throughput	$0.37 \times 0_{sc.} P/BQ^2$
	Target beam throughput	0.94
Beam Quality	Uncorrected BQ	
	degradation BQ to amplifier Subsystem	(TBD)
Isolation	Extinction	$10^{-4}$
	Return beam throughput	0.64

Figure 2.7-1. The Beam Director Subsystem Requirements with Opto-Mechanical Interface Requirements

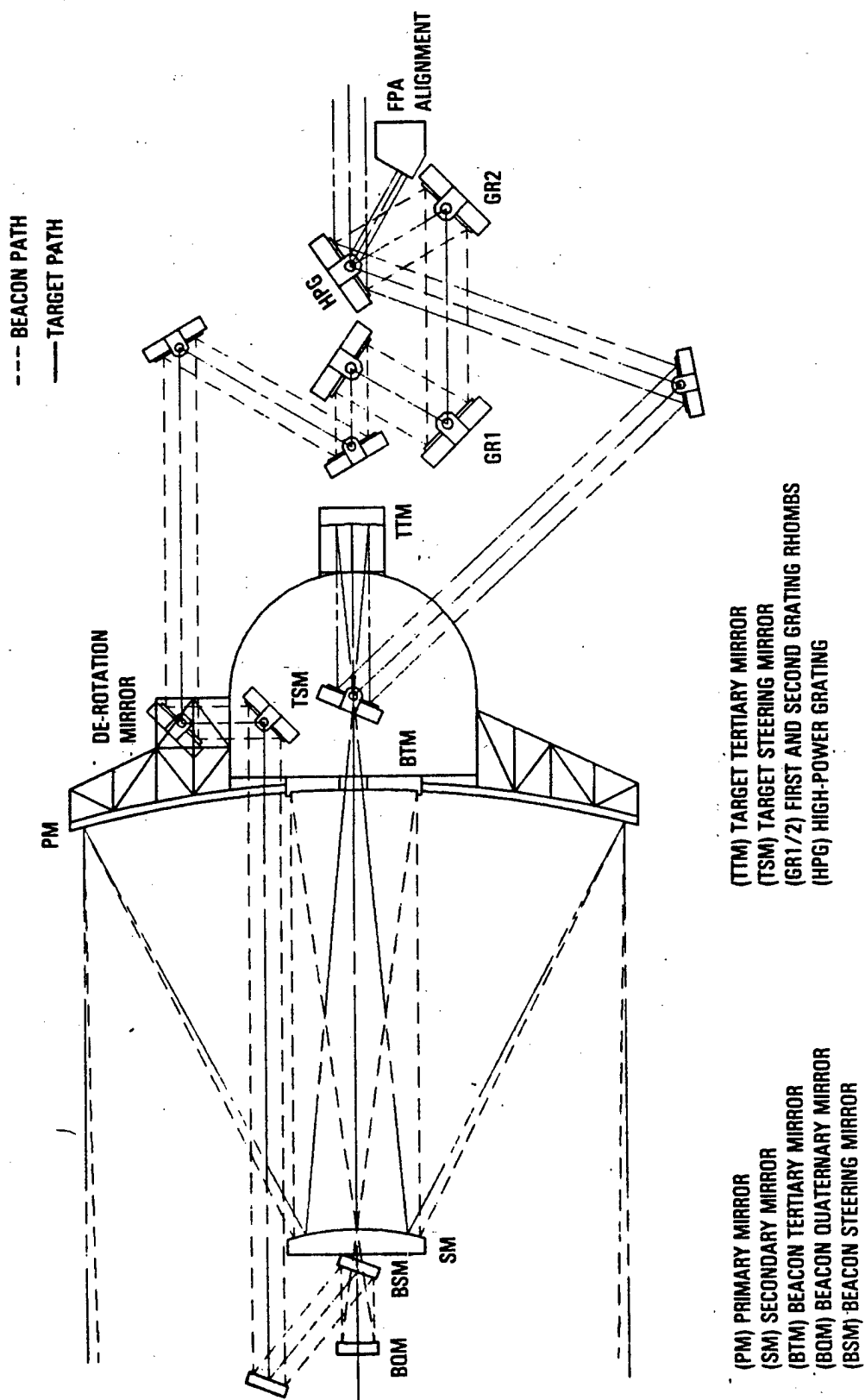


Figure 2.7-2. The Beam Director Subsystem (Optics shown with the beacon unseen 25-primary mirror diameters to the left.)

difference between beacon and target distances. The rays from the beacon and to the target strike the primary mirror at two different angles. Thus, the wavefront error due to mirror segment location error is slightly different for each ray. This is discussed in more detail below.

Pupil rotation is necessary because the pupil orientation will be different in the target and beacon paths in general due to the gimbal scan over the large field of regard; this cannot be tolerated due to the need to have pupil matching at the primary for phase error cancellation between the beacon and target paths. The three flats denoted as derotation mirrors (Figure 2.7-2) in the beacon path are utilized as an approximation to a K-mirror to rotate the beacon path pupil orientation relative to the target path. The middle mirror is translated out of plane and all three are pointed to cause the beacon beam to return in-plane to enter the grating rhombs. This process can be executed open loop to first order as a known function of beam director scan angles. Pupil matching error is measured as described in Section 2.8.

Two grating rhombs are necessary: the first rhomb recollimates the four beams produced by the dispersion of the four laser lines with some shear; the second grating rhomb pair produces the opposite dispersion and recollimation of the four lines into a single beam. Each of the four gratings is designed to efficiently diffract the p-plane polarized light into the first order (90% throughput per grating) and reflect the s-plane polarized energy into the zeroth order (95% throughput). The grating extinction performance is calculated in Section 2.11.1.

The collective component reflectances, obscurations and spatial filtering losses in throughput for the BDSS are listed in Figures 2.7-3 and -4. The throughputs are different, depending on direction of propagation, as shown.

### 2.7.3 Primary Mirror Phase Conjugation

Cancellation of phase errors produced by relatively large primary mirror segment misfigure, tilt, and piston is the primary goal of the phase conjugation approach in APACHE. The expected performance was analyzed

High-Power Grating (s-plane)	0.970
Target Turning Flat Reflectance	0.995
Target Pointing Flat Reflectance	0.995
Target Tertiary Mirror Reflectance	0.995
Secondary Mirror Reflectance	0.995
Primary Mirror Reflectance	0.995
Mapping Losses at Segment Edges	0.990
	0.9365
Secondary Obstruction	0.102
Beacon Path Hold Obscuration	0.0036
	0.106

Figure 2.7-3. Beam Director Throughput Budgeted to Components for Path from Amplifier to Target

Beacon Mirror Reflectance	0.990
Primary Mirror Reflectance	0.995
Intersegment Gaps	0.990
Secondary Mirror Reflectance	0.995
Beacon Tertiary Mirror Reflectance	0.995
Beacon Quaternary Mirror Reflectance	0.995
Beacon Pointing Flat	0.995
Beacon Turning Flat	0.995
Three Gimbal Flats	0.985
Jitter Flat	0.995
Form P-plane First-Order Grating Rift	0.768
	0.716

Figure 2.7-4. Beam Director Throughput from Master Oscillator to Amplifiers

using the ASAP optical design code by simulating segment piston and tilt errors and various degrees of misfigure (see Section 3). The results are discussed in Section 3.3.2 in detail.

#### 2.7.4 Active Structural Control

A corollary to the APACHE concepts' phase conjugation of the primary mirror has been to eliminate or simplify as many active control channels as possible. In the baseline APACHE design it was decided to completely eliminate primary segment figure actuators. Currently  $9/\text{m}^2$  figure actuators and control channels (707 for 10-m primary mirror) are planned for the alternative adaptive optics system. It was decided to retain a degree of active control of segment piston and tilt, however, at least to assure static segment alignment and control of the lower natural modes. To get some idea of the correctability factors achievable in various frequency ranges, the experience gained on the JOSE program was applied to a NASTRAN model of a 10-m dia., segmented BD pictured in Figure 2.7-5. Figure 2.7-6 shows our selected control architecture based on JOSE program experience. The alignment loops sense absolute position of the segments relative to an unperturbed aligned position. The multivariable loops sense the output of a single accelerometer per loop which sense motion relative to an inertial coordinate system at medium frequency. The derivation of positional information from accelerometer output becomes subject to drift error as the bandwidth of the alignment system is approached. The high-frequency response inner loops are closed around the relative position of the two ends of each actuator to reduce the input of this environment to the outer loops.

Figure 2.7-7 shows the disturbance rejection ratio or correction factor indicated by our analysis for typical loop parameters. This analysis and JOSE experience indicates that correction factors of 40 to 100 can be reached in the range of the first BD resonances, i.e., 10 to 50 Hz. A conservative factor of 40 was assumed for BD structural deflection and mass analyses performed under the systems advantage study.

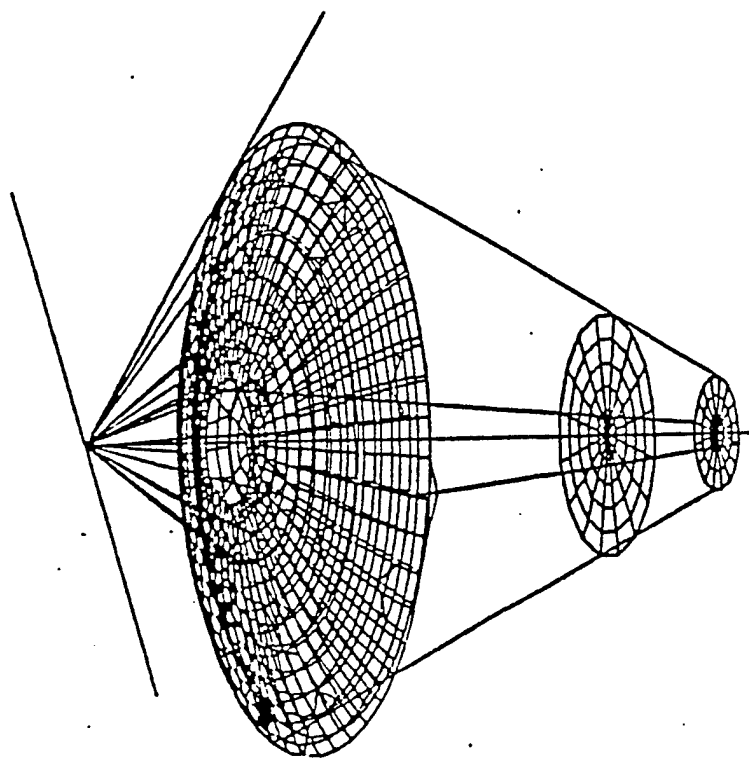


Figure 2.7-5. Beam Director for NASTRAN Model



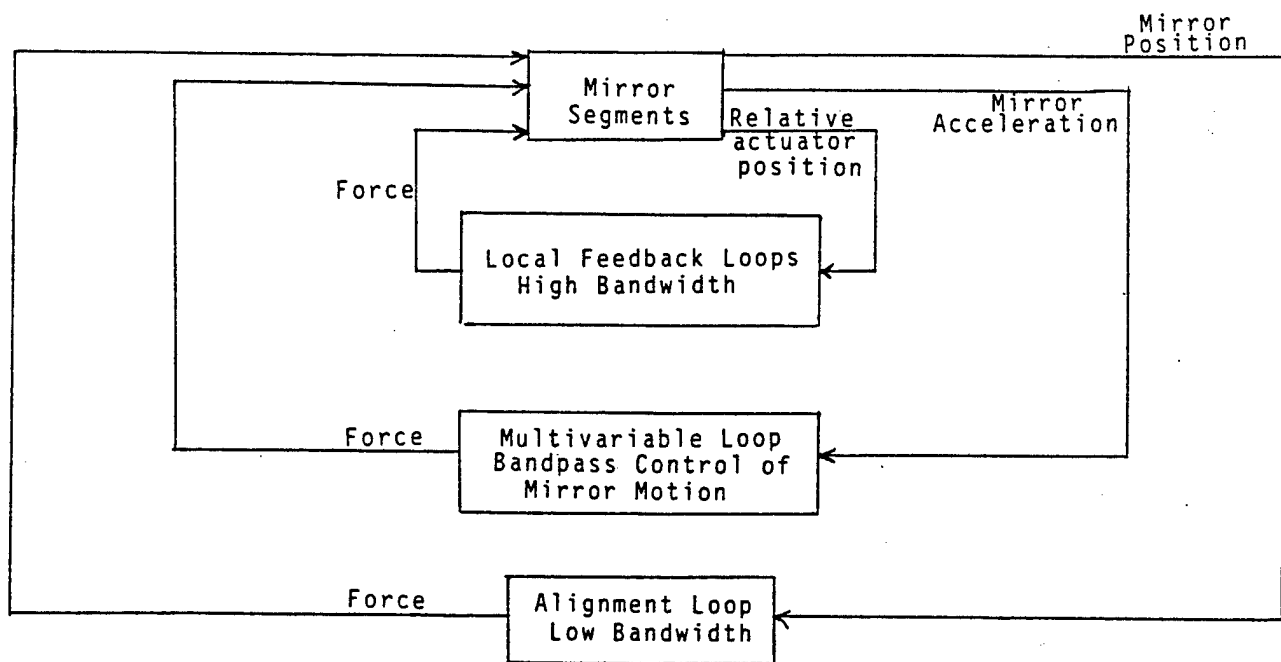


Figure 2.7-6. Segment Piston and Tilt Control Loops

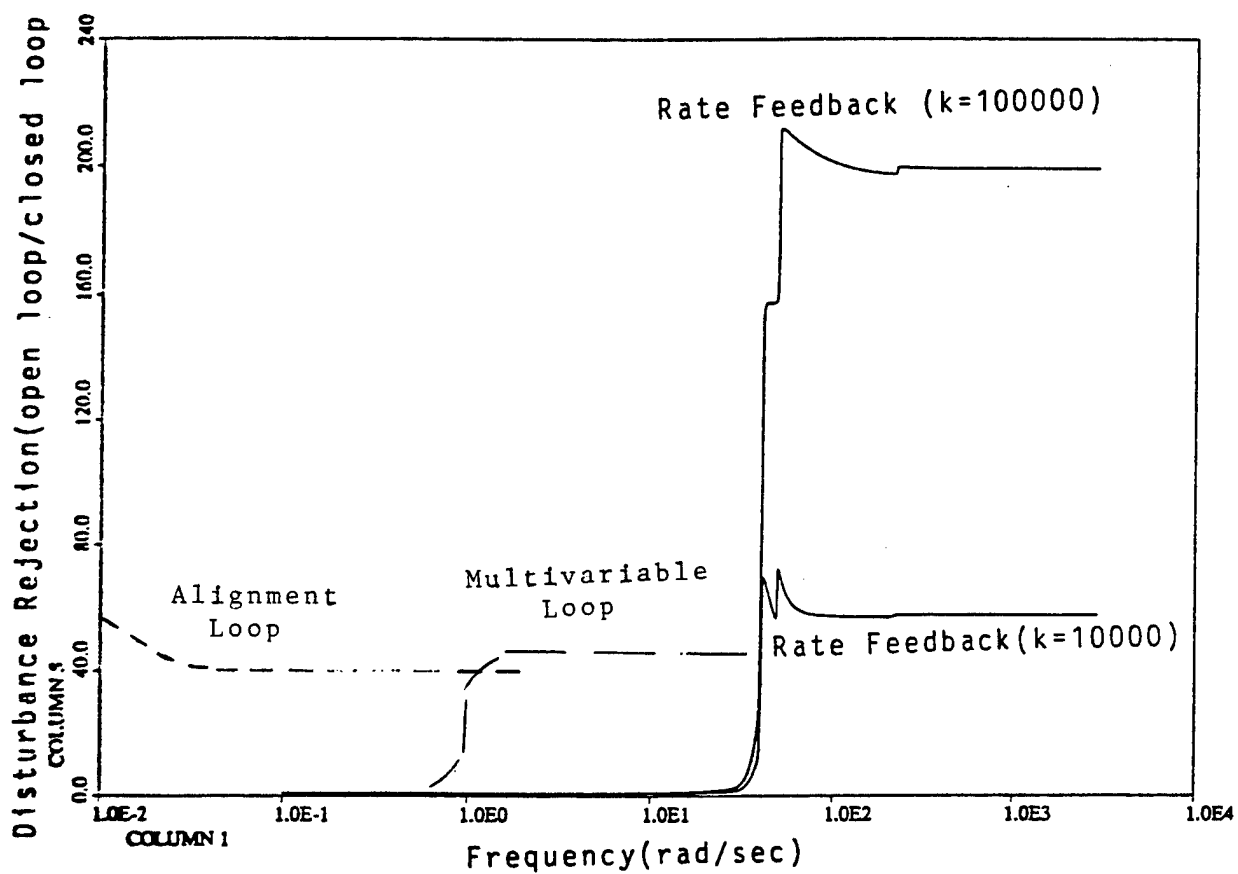


Figure 2.7-7. Segment Displacement Correction Factors

### 2.7.5 Alignment Sensitivity and Requirements

The optical design analysis derived the beam quality degradation rate due to misalignments of the optical elements (tilt, decenter, and despace). From this analysis, alignment requirements were selected to keep the resulting beam quality within budget. These requirements are listed in Figure 2.7-8.

### 2.7.6 Segment Size and Shape Considerations

The concept for splitting the beam into six parts for feeding each amplifier is described in Section 2.9. Each amplifier is configured so that it needs a circularly symmetric energy distribution as input. This leads to a desire to segment the primary into trapezoids as shown in Figure 2.7-9. Each of the six rings of segments shown has about the same area so that the energy sent to each amplifier is governed by the energy distribution.

### 2.7.7 Beam Director Mechanical Considerations

First-order estimates of primary mirror structural mass differences were needed for use in the systems advantage studies (see Section 2.6.2). As a part of these studies, it was desired to quantitatively compare an APACHE phase conjugated primary mirror beam director to a system using a conventional adaptive optics beam director on a weight basis. It was expected that the orders of magnitude relaxation in piston, tilt, and higher order aberration tolerances allowable with a phase conjugate primary mirror would permit significant reduction in structural stiffness and, hence, structural mass. As many of the structural cost algorithms arriving from various vendors involved the mass of a structure in estimating its cost, it was anticipated that mass reductions arising from phase conjugation would produce corresponding cost reductions.

A review of available SBL design documents uncovered several mass estimates for primary mirror structures of various diameters, but insufficient detail on materials of construction, load levels considered, allowed deflections under those load levels, scaling laws and structural design were presented to enable a comparison of the systems based on these viewgraphs and reports. We attempted to use these point designs as guides to the state of the art where appropriate.

Mirror	Tilt	Decenter	Despace
Secondary	10 $\mu$ r (0.017 $\lambda$ )	100 $\mu$ m (0.015)	20 $\mu$ m (0.17 $\lambda$ )
Beacon tertiary	10 $\mu$ r (0.016 $\lambda$ )	50 $\mu$ m (0.015)	10 $\mu$ m (0.014 $\lambda$ )
Beacon quaternary	440 $\mu$ r (0.008)	200 $\mu$ m (0.018)	10 $\mu$ m (0.014 $\lambda$ )
Target tertiary	440 $\mu$ r (0.10)	1000 $\mu$ m (0.012)	50 $\mu$ m (0.18 $\lambda$ )

\*Wavefront error in parenthesis (in waves) resulting from alignment tolerance analysis

Figure 2.7-8. Beam Director Alignment Requirements for Un-phase Configuration Nonsegmented Elements

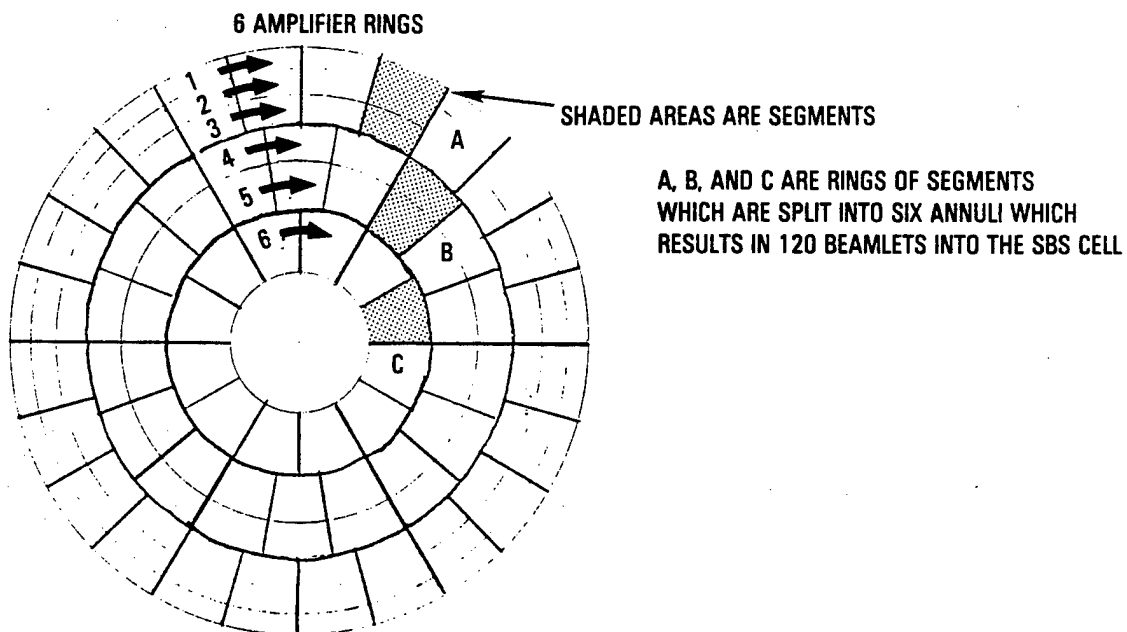


Figure 2.7-9. Segment shape and size is driven by creating equal annular input to six amplifiers. Fifty-four trapezoidal segments are allowed to one of six annuli. Maximum segment size is 17% of primary diameter.

Accordingly, it was decided on APACHE to develop a mass and stiffness estimation method for the primary mirror and its backing structure. NASTRAN finite element modeling of a previous beam director point design had shown that, while necessary for serious preliminary design, this method was too cumbersome for conceptual parametric analysis. Instead, we chose to set up a set of parametric relationships solvable in closed form by making several idealized assumptions as follows:

- A five-tier structure consisting of mirror faceplate segments, faceplate actuator/flexures, segment reaction structure, segment actuators and a support structure of primary mirror diameter to tie all segments together would be analyzed for both APACHE and Adaptive Optic primary mirrors.
- All faceplate, reaction and support structures, in reality shallow spherical shells, would be analyzed as flat plates.
- The only classes of loads considered to produce optical distortion of the primary mirror would be thermal distortion from beam heating, random vibration excitation from the SBL, and deterministic vibration after settling following a maximum rate slew maneuver.
- Dynamic responses of each structure were calculated as that of a single degree of freedom mechanical oscillator at the first fundamental frequency of the idealized plate (segment or support structure).

Clearly, the last assumption is the least accurate, as the quadripod mounting of the secondary mirror will change the primary mirror modes from those of an idealized plate. Conceivably at some design points, a second vibration mode may be close enough to the fundamental to make a significant contribution to the RMS maximum distortion. Thus, while the absolute accuracy of the present simplified method can only be assessed by performing a number of point designs using detailed finite element modeling, it should give the proper relative assessment of APACHE and conventional SBL primaries if the same loads and optical tolerances consistent with the aberration budgets of each system are applied.

When in use the distortion model is programmed into a Lotus spreadsheet. Table 2.7-1 shows sample output for a 10-m primary mirror diameter. The fundamental natural frequency of both individual segments and the overall support structure is then varied until both APACHE and

Table 2.7-1. Comparison of Beam Director Structure Frequency Required To Meet WFE Budget

PARAMETER	APACHE PRIMARY		ADAPTIVE PRIMARY	
	SEGMENT	SUPPORT	SEGMENT	SUPPORT
oDIAMETER (M)	3	10	3	10
oFACEPLATE MATERIAL	ULE		ULE	
oREACTION STRUCT. MATERIAL	GR/EP		GR/EP	
oCONSTRUCTION	EGG CRT		EGG CRT	
oFACE ELASTIC MODULUS (NT/CM2)	6600000		6600000	
oREACT. MODULUS (NT/CM2)	34500000		34500000	
oCORE SOLIDITY	0.05		0.05	
oCORE MODULUS (NT/CM2)	1725000		1725000	
oFACEPLATE DENSITY (GM/CM3)	2.2		2.2	
oREACT. DENSITY (GM/CM3)	1.661		1.661	
oFACE POISSON RATIO	0.17		0.17	
oREACT. POISSON RATIO	0.3		0.3	
oFACE THERMAL EXPANSION (/K)	3.00E-08		3.00E-08	
oFACE HEAT CAPACITY (J/GM-K)	0.77		0.77	
oTHERMAL CONDUCTIVITY (W/CM-K)	0.013		0.013	
oFACEPLATE THICKNESS (CM)	0.75		1	
oREACTION STRUCTURE FACE/BACK SHEET THICKNESS (CM)				
oCORE THICKNESS (CM)	49		49	
oOVERALL STRUCTURE THICKNESS (CM)	50		50	
oFACE OR SEGMENT MASS DENSITY	22	27	22	27
oREACTION OR SUPPORT STRUCT. MASS DENSITY (KG/M2)	5	5	5	5
oBENDING STIFFNESS (NT-CM2/CM)				
oFUND. FREQUENCY, ABOVE GEOMETRY				
oBENDING STIFFNESS REQUIRED (NT-CM2/CM)	86685.572	3170940	346742.28	12683760
oFUNDAMENTAL FREQ. (RAD/SEC)	125.66370	62.831853	251.32741	125.66370
oSTRUCTURAL PERIOD (SEC)	0.05	0.1	0.025	0.05
oDAMPING RATIO	0.02	0.02	0.02	0.02
oRANDOM INPUT (NT2/HZ)	0.006	0.006	0.006	0.006
oRANDOM RESPONSE, 1 SIGMA PEAK (MICRON)	11.122781	2.3889919	3.9324970	0.8446362
oRANDOM RESPONSE, 1 SIGMA RMS (MICRON)	2.7806953	0.5972479	0.9831242	0.2111590
oCONTROL REJECTION RATIO	1	40	40	40
oRANDOM CONTROL RESIDUAL RMS (MICRON)	2.7806953	0.0149311	0.0245781	0.0052789
oSLEW PERIOD (SEC)	1	1	1	1
oSETTLING PERIOD (SEC)	10	10	10	10
oSLEW FREQUENCY (RAD/SEC)	6.2831853	6.2831853	6.2831853	6.2831853
oPEAK SLEW ACCEL. (RAD/SEC2)	0.0007853	0.0007853	0.0007853	0.0007853
oPOST SLEW AMPLITUDE (MICRON)	0.1057669	2.8418182	0.0131860	0.3525563
oDAMPING FACTOR	0.7777676	0.8819113	0.6049225	0.7777676
oSETTLE AMPLITUDE, PEAK	0.0822620	2.5062318	0.0079825	0.2742069
oSETTLE AMPLITUDE, RMS	0.0205655	0.6265579	0.0019956	0.0685517
oSLEW CONTROL RESIDUAL (MICRON)	0.0822620	0.0626557	0.0001995	0.0068551
oABSORBED FLUX (W/CM2)	0.060271		0.060271	
oFACEPLATE EQUIV. LINEAR GRADIENT (K)	1.4430268		1.9240357	
oTHERMAL BENDING, PEAK (MICRON)	0.1571892		0.1254359	
oTHERMAL BENDING, RMS (MICRON)	0.0392973		0.0313589	
oTHERMAL CONTROL RESIDUAL (MICRON)	0.0392973	0	0.0007839	0
oRMS STRUCTURAL DEFLECT. (MICRON)	2.7821893	0.0644103	0.0245914	0.0086522
oBUDGETED STRUCTURAL WFE (HF WAVES)	1.974		0.0167	
oBUDGETED STRUCT. DEFLECT. (MICRON)	2.7636		0.02338	
oFRACTION OF BUDGET USED	1.0067265		1.0518142	
oRANDOM FRACTION OF TOTAL	0.9989262	0.0537375	0.9989178	0.3722577
oSLEW FRACTION OF TOTAL	0.0008742	0.9462623	0.0000658	0.6277422
oTHERMAL FRACTION OF TOTAL	0.0001995		0	0.0010163

conventional systems just satisfy their respective structural distortion budgets. An important area in this analysis is the correctability factors assumed for phase conjugation in the APACHE design; figure actuators and deformable mirrors in the adaptive optics design and segment piston and tilt correction in both designs. In most cases, the correctability factor used was derived from detailed optical design calculations performed for both the adaptive optics and nonlinear optics system concepts.

A final piece of information needed for the primary mirror distortion model was the structural weight for a given required stiffness. A review of available references revealed a host of detailed designs for sandwich plates, together with several candidate materials. After consultation with a subcontractor, Optical Research Associates, it was decided that monolithic ULE glass would be used for the segment faceplate and that magnesium-graphite composite represented the best near-future material for reaction and support structure panels. Minimum gauge for this composite material in a symmetric, isotropic layup is six plies of 0.0025 inch each, for a total sheet thickness of 0.015 inch. Our analysis for the sandwich panel construction that maximizes bending stiffness for a given area density (e.g.,  $\text{kg/m}^2$  of face sheets plus connecting core) indicates minimum gauge face sheets separated across the depth of the sandwich panel by a minimum gauge core structure. In a sense the fraction of the total area density devoted to core sets the allowable depth of the panel which in turn determines the panel's bending stiffness. It was decided to use an isogrid (equilateral triangle) cell, rather than a square cell, core to ensure isotropic deflection behavior. The core cell size was set by requiring that the minimum gauge cell walls have a fundamental vibration frequency  $\geq 2$  times that to which the overall sandwich structure was being designed. Thus a 40-Hz support structure would have a core cell size such that the lowest resonant frequency of any sheet in the panel would equal or exceed 80 Hz. A family of curves of bending stiffness as a function area density was constructed and curve fit so that area density required to satisfy a required bending stiffness could be determined within the spreadsheet (see Figure 2.7-10).



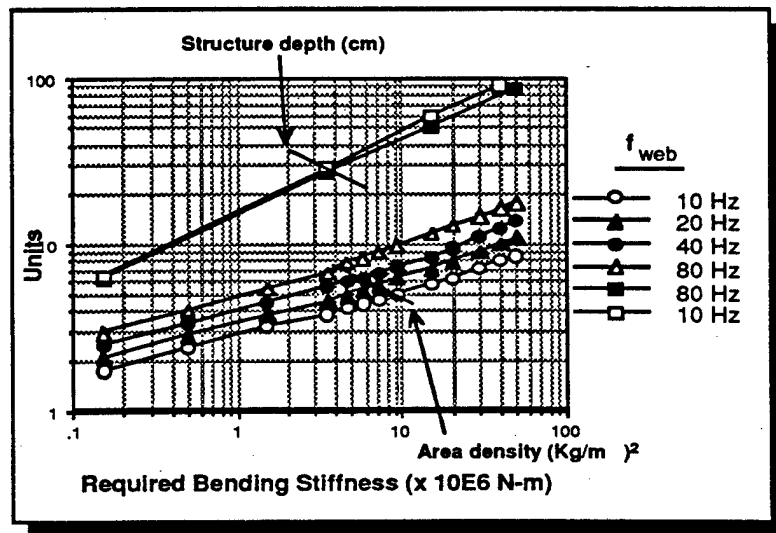


Figure 2.7-10. Structure Mass to Stiffness Relation

## 2.8 ALIGNMENT AND POINTING CONCEPT

### 2.8.1 Functional Requirements

The quantitative precision and accuracy requirements are listed in the BDSS requirements list in Figure 2.7-1. The top level flow chart is shown in Figure 2.8-1. Alignment components are identified in Figure 2.8-2. The functional requirements for alignment and pointing are listed below.

1. Provide a mechanical truss metering structure to serve as an optical bench alignment reference for the BD optical elements
2. Provide sources on the optical reference structure which defines the optical axis
3. Autonomously position and maintain the beacon relative to the optical axis to the required precision after the BD slews
4. Align the primary segments, the secondary, and the beacon tertiary mirrors relative to the optical axis
5. Track the beacon position and continuously point the beacon quaternary mirror to position the beacon within the specified FOV
6. Acquire and track two targets simultaneously with two acquisition and tracking sensors and provide coarse line-of-sight data for the first target to the optical bench
7. Illuminate the first target with a 1.06- $\mu\text{m}$  laser
8. Provide a single primary mirror segment with an optical surface figure accurate enough to provide good imagery in the target path
9. Track the target with the target path pointing optics to within the coarse precision provided by the acquisition sensor. Derive an error signal by comparing the line of sight generated by the 1.06- $\mu\text{m}$  image coming down the target path to the line of sight defined by the beam from the beacon coming off the high-power isolation grating
10. Using the relative lines of sight above, detect jitter and correct using the jitter correction mirror
11. Correct pupil matching errors in translation and rotation.

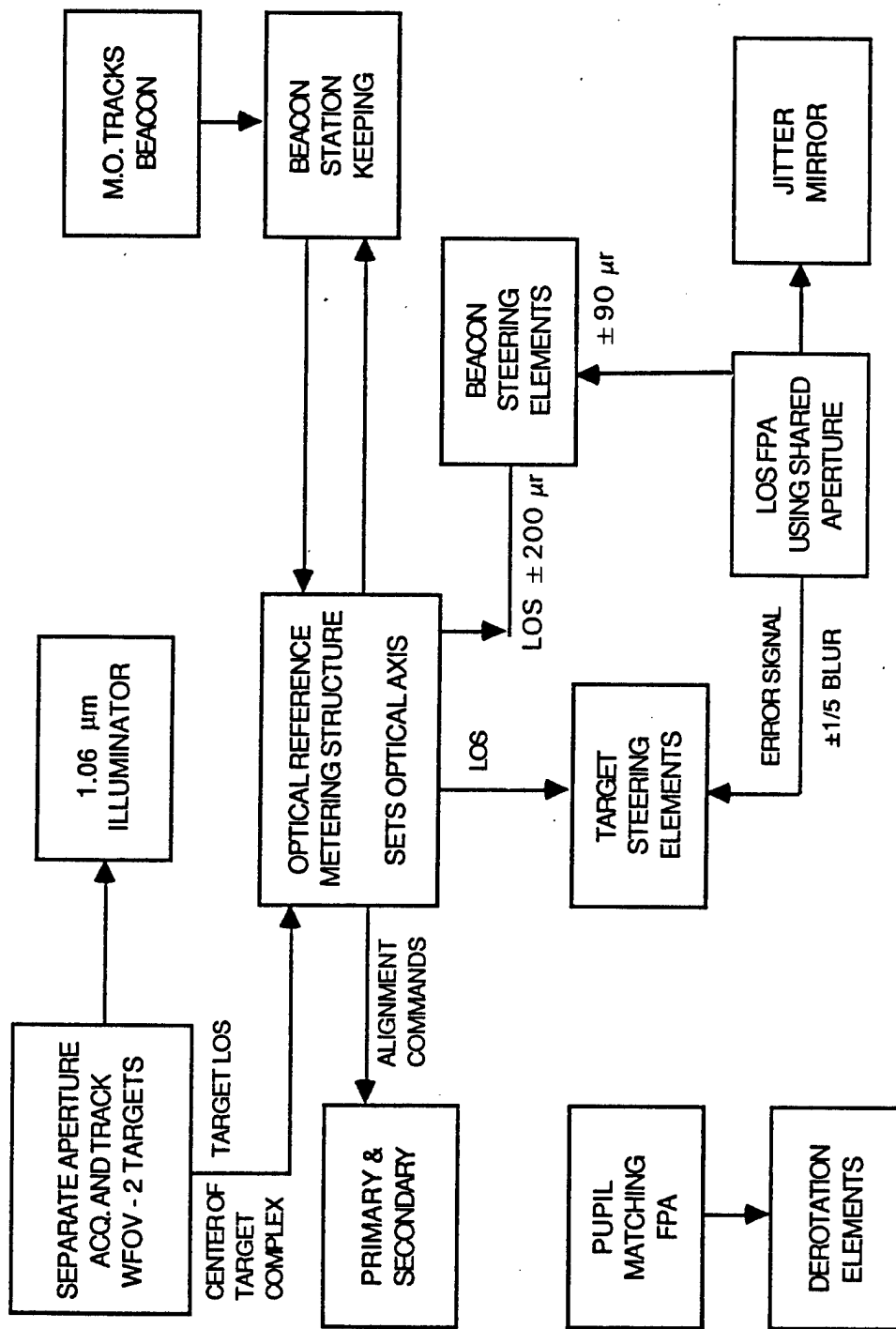


Figure 2.8-1. Alignment Flowchart (Details both the beacon and target at the alignment focal plane with a shared aperture greatly eases initial pointing tolerances)

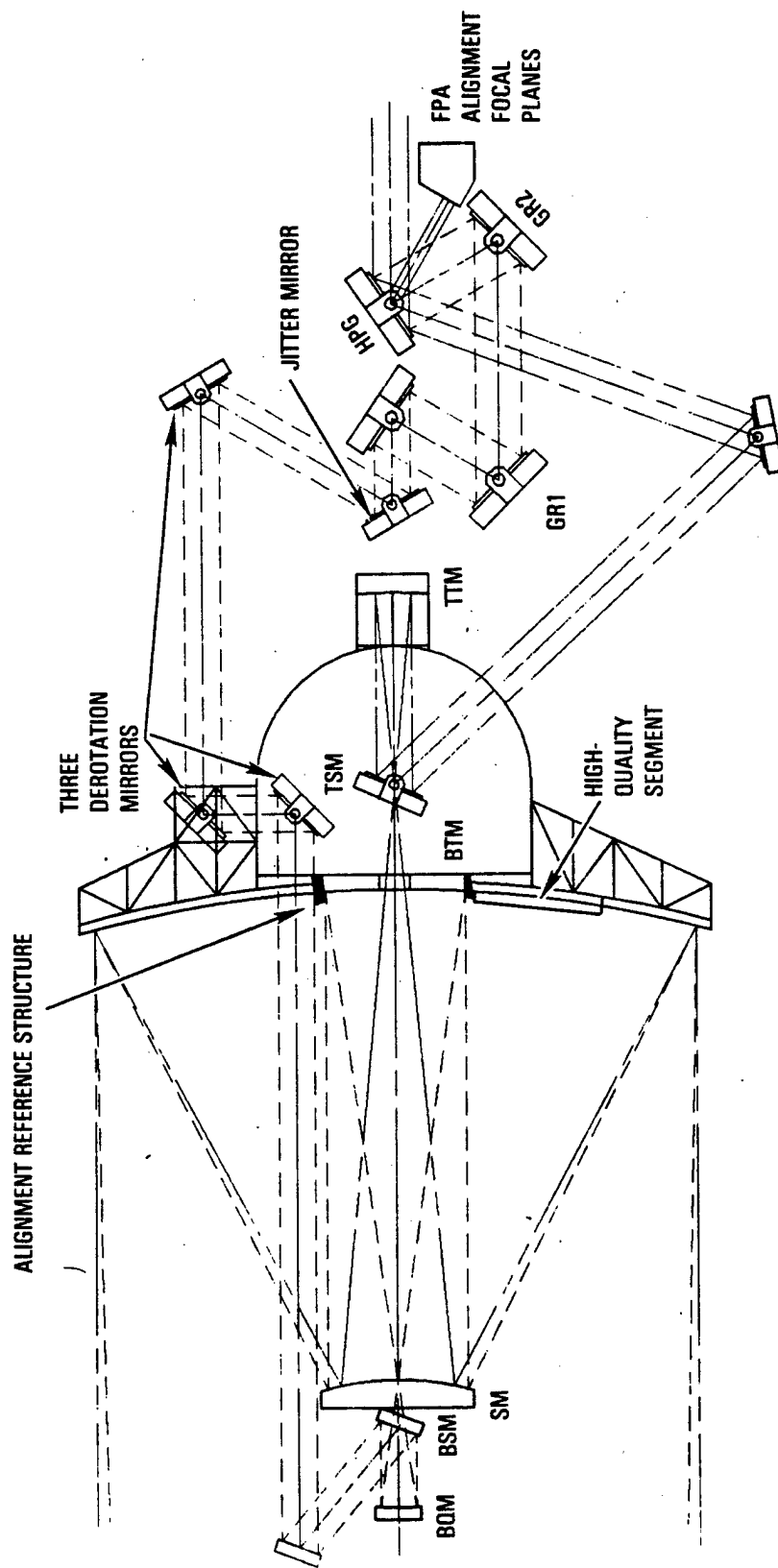


Figure 2.8-2. Beacon and target pointing components (including the alignment reference structure, derotation mirrors, high-quality segment and alignment focal plane)

The various steps in the top level alignment block diagram in Figure 2.8-1 are discussed in the next four subsections.

#### 2.8.2 Optical Alignment of Primary Mirror Segments and Beam Director Optical Elements

#### 2.8.3 Target Acquisition, Illumination and Coarse Tracking

Target acquisition is done by each of the two acquisition sensors upon receiving handover inertial position data on a target cluster. The acquisition sensors and the BD calibrate their own line of sight (LOS) inertially with star sensors. The entire BD is slewed to the direction of the target cluster, and the LOS knowledge supplied by the star sensor is transferred optically to the optical bench on the metering structure, which defines the optical axis of the BD. The fixed optical elements, the primary mirror segments and the beacon are then brought into alignment with the optical axis, and the beacon pointing optics of the BD are aligned with the beacon direction.

Each acquisition sensor has a three-mirror telescope with a 2-deg FOV and an aperture of less than 50 cm. This provides performance adequate to acquire and track a specific target in the cluster and illuminate it with a 1.06- $\mu\text{m}$  laser. Two sensors are needed so that the illumination step can be carried out in advance on the next target without adding to the timeline.

The BD image quality meets the beam quality specification simultaneously over the entire FOV required for rapid retargeting. However, the target pointing flat can pass only that portion of the image plane which fits through the hole in its center. This hole size is maximized by matching the 22% linear obscuration created by the hole in the beacon tertiary. The beacon tertiary hole is set by the optical design requirement to pass the target path ray bundle coming through it to a focus behind the primary. This tertiary hole turns out to be the limiting obscuration of the two paths; the obscuration of the primary mirror caused by the secondary mirror is slightly less. The result of all this is that about 1/3 of the target FOV fits through the hole in the pointing flat.

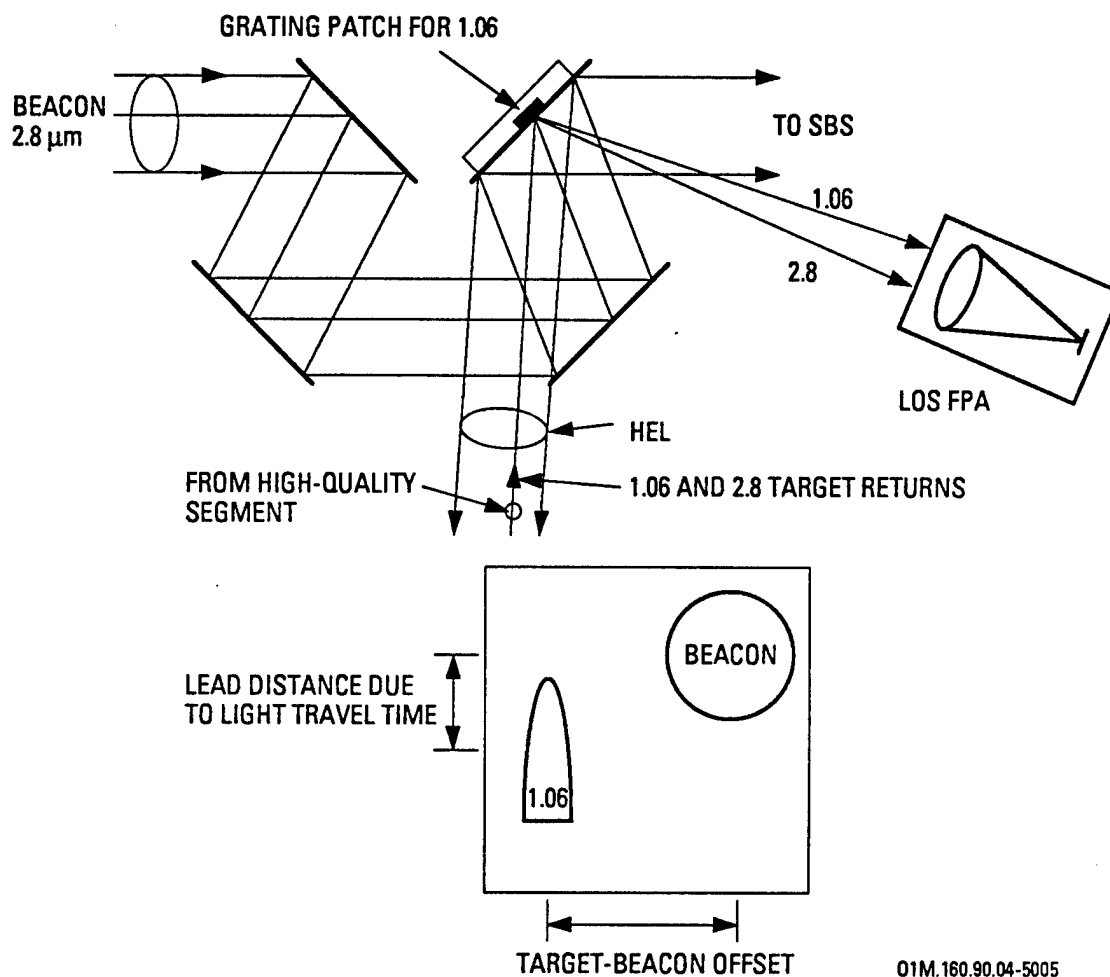
The LOS knowledge to the illuminated target generated by the star sensor and transferred to the beam expander is more than accurate enough to assure that the target is within 1/3 of FOV defined by the target pointing mirror hole after slewing to the target is complete. At this point the fine-pointing process begins.

#### 2.8.4 Target and Beacon Fine Tracking and Jitter Control

For a high-brightness system, providing a target LOS from the acquisition sensor to the optical bench that is accurate at angles less than the diffraction blur of the beam director is extremely difficult. Instead, the approach adopted here is to use the acquisition sensor only for coarse targeting. Fine LOS control is provided by viewing the target directly in the target path which is illuminated by a laser at  $1.06\ \mu\text{m}$ .

This approach requires that one segment have good optical figure and tilt alignment to generate an image with acceptable quality for fine pointing. The concept is illustrated in Figure 2.8-3. On the high-power isolation grating, an additional grating patch shares the aperture at the point in the aperture that reflects the segment position on the primary mirror. This grating patch is designed to reflect the  $1.06\text{-}\mu\text{m}$  laser energy into the first order. The first order diffraction angle of the  $1.06\text{-}\mu\text{m}$  beam is set to nearly match the zero order reflection of the  $2.8\text{-}\mu\text{m}$  beacon beam, which is mostly diffracting into the first order on its way to the amplifiers.

The two beams are compared in the alignment unit which has a focal plane for each wavelength and a means of attenuating the much brighter  $2.8\text{-}\mu\text{m}$  image. The resolution of the  $1.06\text{-}\mu\text{m}$  image of the target return is adequate to coarsely resolve the target image and calculate the aim point, including the look-ahead angle needed to compensate for target velocity and windage. This resolution is roughly three times better (due to wavelength difference) than the beacon image. The beacon beam image is roughly five times the  $2.8\text{-}\mu\text{m}$  far-field spot size of the target beam (due to aperture size difference). The required pointing accuracy within a 1/5 spot diameter is achieved with centroiding of the two alignment images as shown in Figure 2.8-3.



01M.160.90.04-5005

Figure 2.8-3. Target and Beacon Fine Pointing Concept  
 (The beam energy to the SBS cell is  
 coaligned with the outgoing high-energy beam.  
 Thus, incoming beacon image at LOS FPA can be  
 aligned to 1.06 target image from target path.)

The coarse position of the beacon image is the 2.8- $\mu\text{m}$  focal plane is set by referencing the alignment focal planes to the alignment reference structure. The beacon pointing optics are set correctly when the beacon image is nominally in the right position. If the beacon pointing error is less than about 90  $\mu\text{rad}$  (the worst case in the beacon FOV), the beacon image will appear in focus with minimal wavefront error. Larger errors will produce a poor image with an offset from the nominal image plane position. The image spot size and position produce an error signal which will guide the beacon pointing optics into proper alignment. This procedure will relax the requirements on the sensors which must measure beacon position and initially preset the beacon pointing optics in an open-loop manner. The requirement on the open-loop pointing is that the beacon image must be detectable and recognizable in the alignment focal plane. This requirement might be as large as several hundred microradians.

Initially, the target image at 1.06- $\mu\text{m}$  can also be driven to its nominal position in the alignment focal plane. Its image quality, however, is acceptable anywhere in the focal plane as stated above. Once the beacon image quality is made acceptable by the beacon pointing optics, the fine pointing is completed by driving the centroided target image to the same angular direction as the centroided beacon image.

Once the LOS error for the high-quality segment has been reduced to zero by proper alignment of the target pointing optics, it will also be cancelled for all other segments because each segment shares the same beacon input wavefront and the same beacon and target path optical paths. Phase conjugation assures all relative segment tilts also cancel.

High-frequency and small amplitude LOS errors (jitter) due to the un-phase conjugated optical elements are detected as relative jitter between the 1.06- and 2.8- $\mu\text{m}$  images. The jitter is removed by the jitter mirror which is driven by the relative jitter error signal.

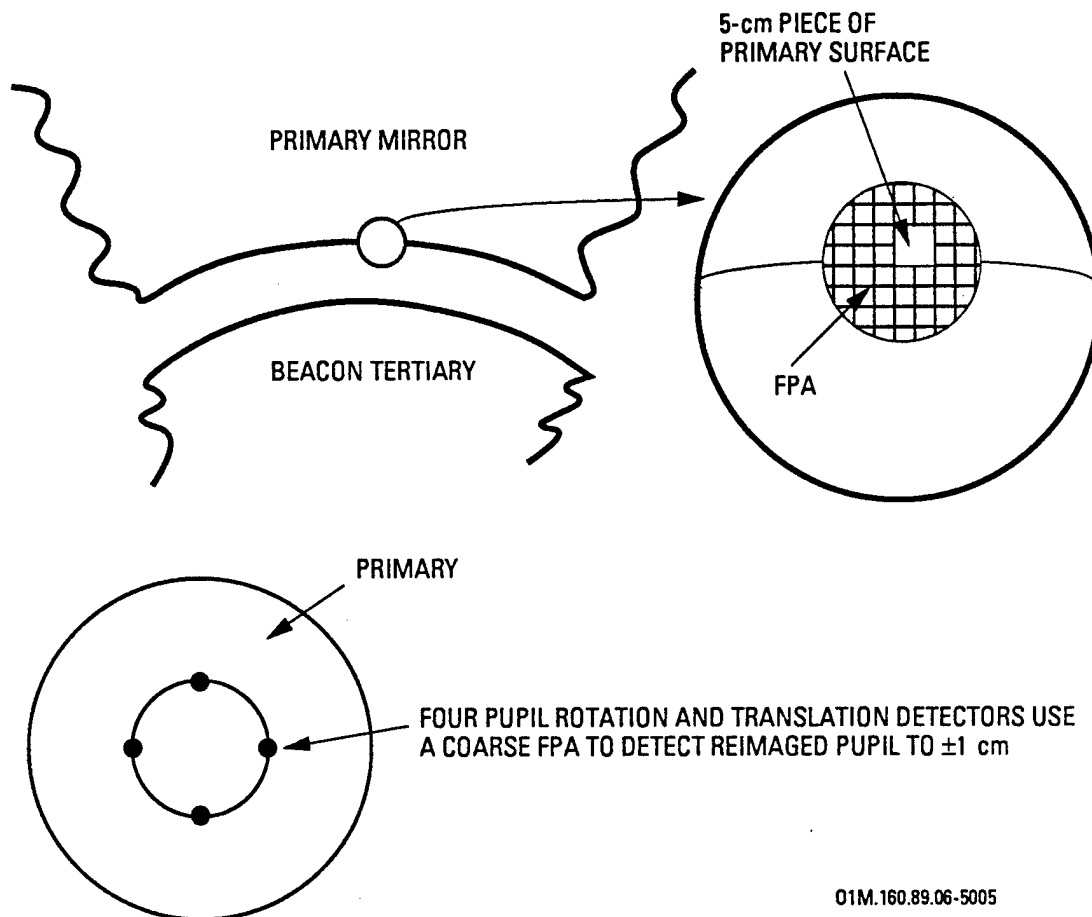


### 2.8.5 Pupil Matching Error Correction

The input beam from the beacon strikes a primary mirror segment at some point, and it must return to that point on the target output path within a few tenths of a percent of the primary mirror diameter for the wavefront error on the segment to be adequately cancelled. Pupil matching errors are due to relative image rotation between the target and beacon paths during slew to a new target angle and beam translation due to despace position errors of turning flats.

Correction of pupil rotation is done with three derotation mirrors set up to act like a K-mirror set. These mirrors are shown in Figure 2.8-2. By translating the middle mirror perpendicular to the plane of incidence and tilting the other two mirrors to follow it, the image will rotate. The presence of rotation can be predicted to first order as a function of slew angle. Second-order errors in relative pupil rotation are detected as shown in Figure 2.8-4, and an error signal is sent to the "K-mirror" set.

Translation errors in pupil alignment due to translations in flat mirror alignment will be removed by moving the jitter correction mirror perpendicular to the mirror's surface. Error signals will be generated as shown in Figure 2.8-4.



01M.160.89.06-5005

Figure 2.8-4. Pupil Rotation (deleted by creating a tracer beam from the beacon off a localized piece of the primary which returns round trip to be detected at the FPA shown above)

## 2.9 AMPLIFIER SUBSYSTEM

The AMSS requirements are listed in Figure 2.9-1. The throughput budget at the component level is given in Figure 2.9-2.

The optics in this subsystem perform three functions. The first is to separate the beam coming from the grating rhombs into six beams each directed to one of the six amplifiers. The second is to provide the annular path through the amplifier similar to the ALPHA laser annular optics. The third function is to recombine each of the output beams into the format required as input to the PCSS and provide coarse amplifier jitter stabilization for SBS cell conjugation fidelity.

The beam separation elements are shown in Figure 2.9-3. The input into the amplifier must be a ring to conveniently fit the amplifier annular gain region. Each ring from the beam director must have a different diameter and, thus, the design for the input optics for each amplifier is different so that the beam can be expanded to match the amplifier diameter. In addition, each amplifier input path (the optics leading from the grating rhombs up to the amplifier optics) must have reflections that are only in-plane or perpendicular to the plane defined by the grating rhombs so that the beam can be kept p-plane linearly polarized. Finally, the path length for each amplifier must be matched to the others to a few centimeters to assure the beams in each path stay coherent to permit phase conjugation. A geometry which provides path matching is shown in Figure 2.9-4.

For beam recombination, the output beam from each amplifier is reformatted by the annular optics into a circle with a diameter of one-sixth that of the beam exiting the grating rhombs. Each follows a path to one of six mirrors located together in the middle of the amplifier array similar to the paths followed on the input side (Figure 2.9-4). The six circular beams are formatted into a 2 x 3 rectangular array. The size and shape is chosen to keep the packaging in the PCSS manageable while not driving the power density too high on those elements. This is described in Section 2.10. In addition, the six reformating flats provide coarse jitter control sufficient to allow the SBS cell to work in the presence of severe amplifier vibration.

SOURCE	ENGINEERING	REQUIREMENT	
Mission	Mechanical	Total Run Time	s
		Time Before Refueling	s
Power	Optical	Forward Train Throughput	0.985
		Rear Train Throughput	0.985
	Mechanical	Gain Generator Diameter	2 m
		Gain Generator Length	6.75 m
		Reynolds Scaling Factor	2
Beam Quality	Optical	Beam Power at Interfaces	MW
		Beam Director Subsystem	MW
		Phase Conjugation Subsystem	MW
	Interface	Amplifier Mode Width	cm
		Absorbed Flux	300 W/cm <sup>2</sup>
Isolation	Optical	Birefringence	0.38 deg

Figure 2.9-1. Amplifier Subsystem Requirements

Beam Director Side	One annular element	0.995
	Two flats	$(0.995)^2$
	Amplifier optics	Reflected in amplifier Power requirement
Phase Conjugation Side	Two flats	$(0.995)^2$
	Collimator and jitter elements	$\frac{0.995}{0.970}$

Figure 2.9-2. Throughputs Requirements to the Component Level  
for the Amplifier Subsystem

The annular optics internal to the amplifier are shown in Figure 2.9-5. They are the same concept as the ALPHA laser optics. It is noted, however, that an alternate amplifier optical design consisting of a single collimated pass through the amplifier is being considered as part of the APEX program. This alternate concept has the effect of raising the F# of the amplifier which facilitates the propagation of an aberated beam through the long, thin annular path of the amplifier.

Because reflections occur at all planes of incidence angles on the annular optics, birefringence will occur if special measures are not taken. Special mirror coating designs have been developed so that after the six bounces in the one-way path, almost all depolarization is cancelled out. The performance impact on oscillator isolation is discussed in detail in Section 2.11.2.

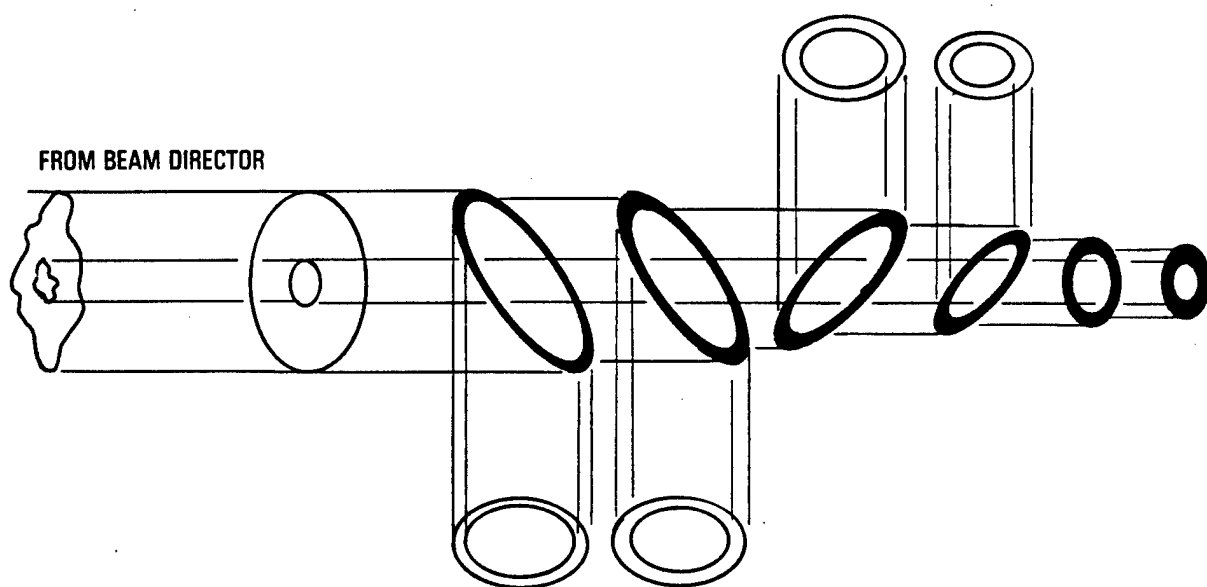


Figure 2.9-3. Beam distribution optics split the beam equally to six amplifiers by concentric annuli of proper width. They are supported on the outer edge, and the inner edge produces no signeting.

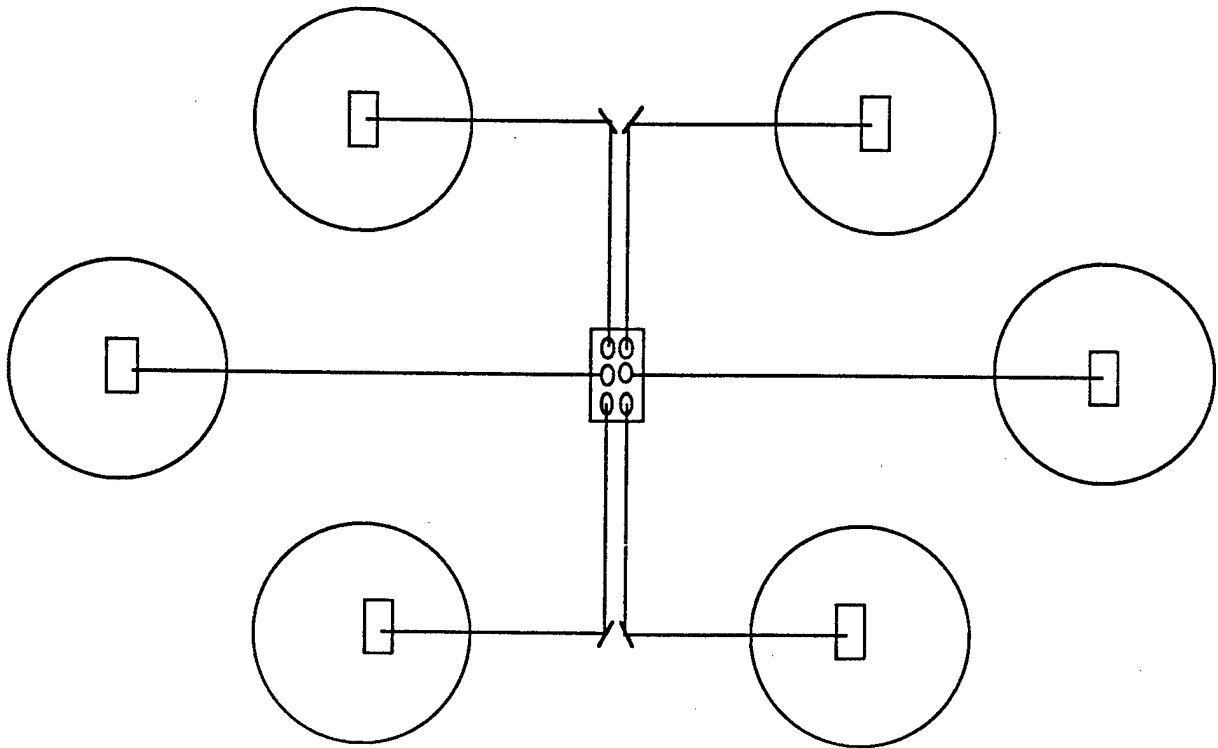


Figure 2.9-4. The path length to and from each amplifier is made equal (to within cm) for coherent recombining after phase conjugation by amplifier spacing.

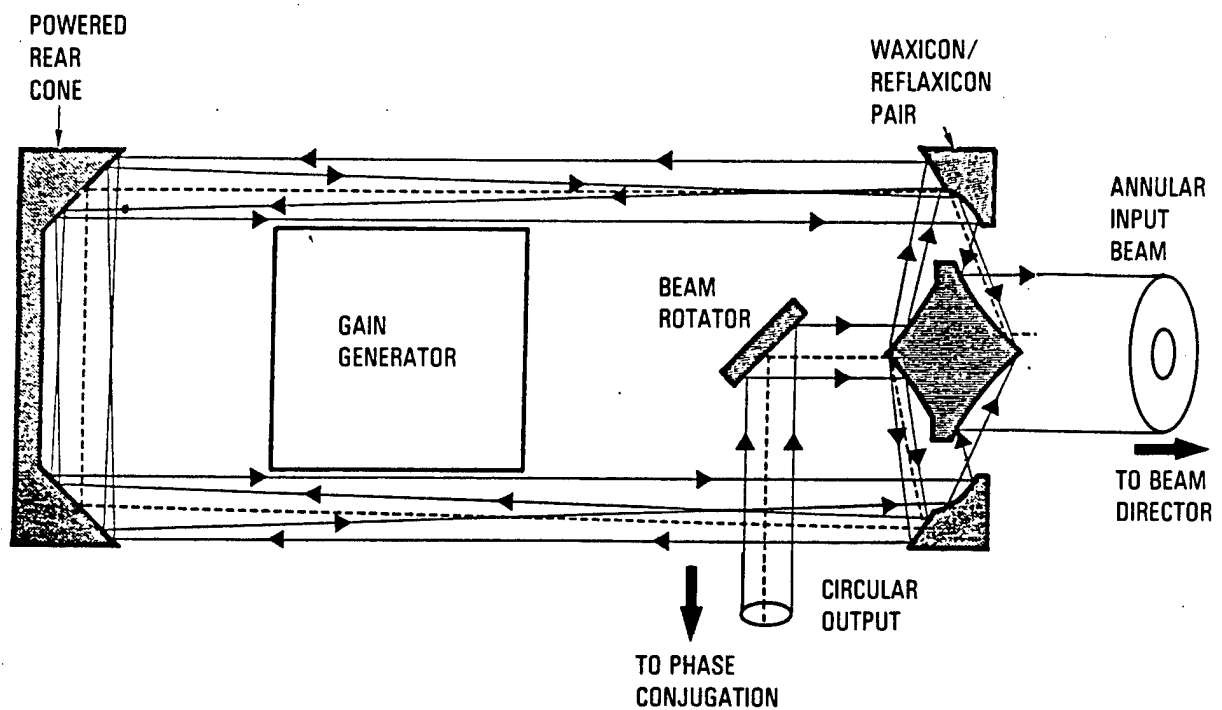


Figure 2.9-5. Annular Optics in the Amplifier Is Similar to ALPHA



## 2.10 PHASE CONJUGATION SUBSYSTEM

### 2.10.1 Requirements

The requirements for the Phase Conjugation Subsystem (PCSS) are given in Figure 2.10-1. A layout of the subsystem is presented in Figure 2.10-2. The functional requirements are listed below:

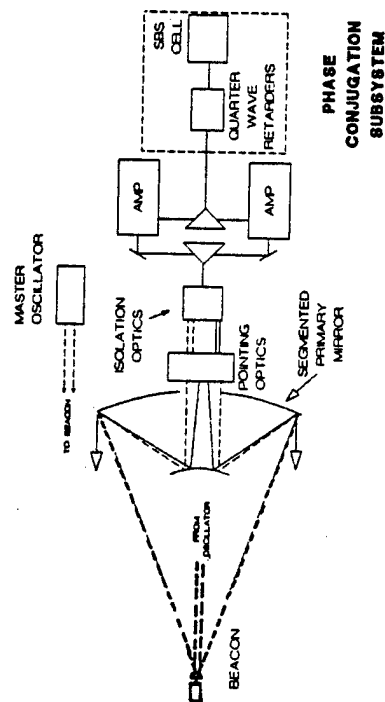
1. The fidelity of the SBS process to conjugate the phase front of the input beam shall be consistent with the wavefront error budget established in Section 2.3.
2. The beam is spectrally dispersed by a grating so that each of four wavelengths can be phase conjugated separately in the cell.
3. As the beam disperses into four distinct beams, the 2.74- and 2.78- $\mu\text{m}$  separates from the 2.87- and 2.91- $\mu\text{m}$  pair. At this point (see Figure 2.10-2), the p-plane linear polarization of the beams is made circular by a pair of quarter wave phase retarders. Each retarder is a set of four mirrors with specially developed phase retarding thin film coatings, see Section 2.11. One of the pair is optimized to work on the 2.74/2.78- $\mu\text{m}$  line pair, and the other works on the 2.87/2.91- $\mu\text{m}$  line pair. More detail is given below.
4. After the beams propagate far enough, each of the four lines will have separated completely. At this point, each beam is focused into the SBS cell and phase conjugated. On the return path, all wavefront distortion occurring on the way into the cell is cancelled up to the high-power isolation grating.
5. Also on the return path, the polarization of each beam is changed from circularly polarized to s-plane linearly polarized.

### 2.10.2 Optics Design

The grating has a profile of 2 x 3 to intercept the six spots coming from the amplifier subsystem which are arranged in a 2 x 3 array. The long dimension is aligned along the direction of the grating lines. The grating is designed to have a Littrow diffraction angle (equal to the angle of incidence) at 55 deg. By using it at an angle of incidence of 60 deg, the first-order diffraction angles are as shown in Figure 2.10-2 for each line. No other order except specular is possible; this maximizes the diffracted energy.

The difference in diffraction angles is very important because this determines how fast the lines separate from each other and how much area is required to package all the functional units. The first requirement is

- SBS model needed to respond to subsystem requirements



SOURCE	REQUIREMENT		
Mission	Total Run Time	s	
Power	Power to Amplifier Subsystem	MW for	MW from Amp Subsystem
Beam Quality	Conjugation Fidelity	1.03	
Isolation	Power Depolarized	[TBD] est. of $1.1 \times 10^{-4}$ , quarter wave mirror residual retardance of 0.5 deg. rms	

Figure 2.10-1. PCSS Requirements

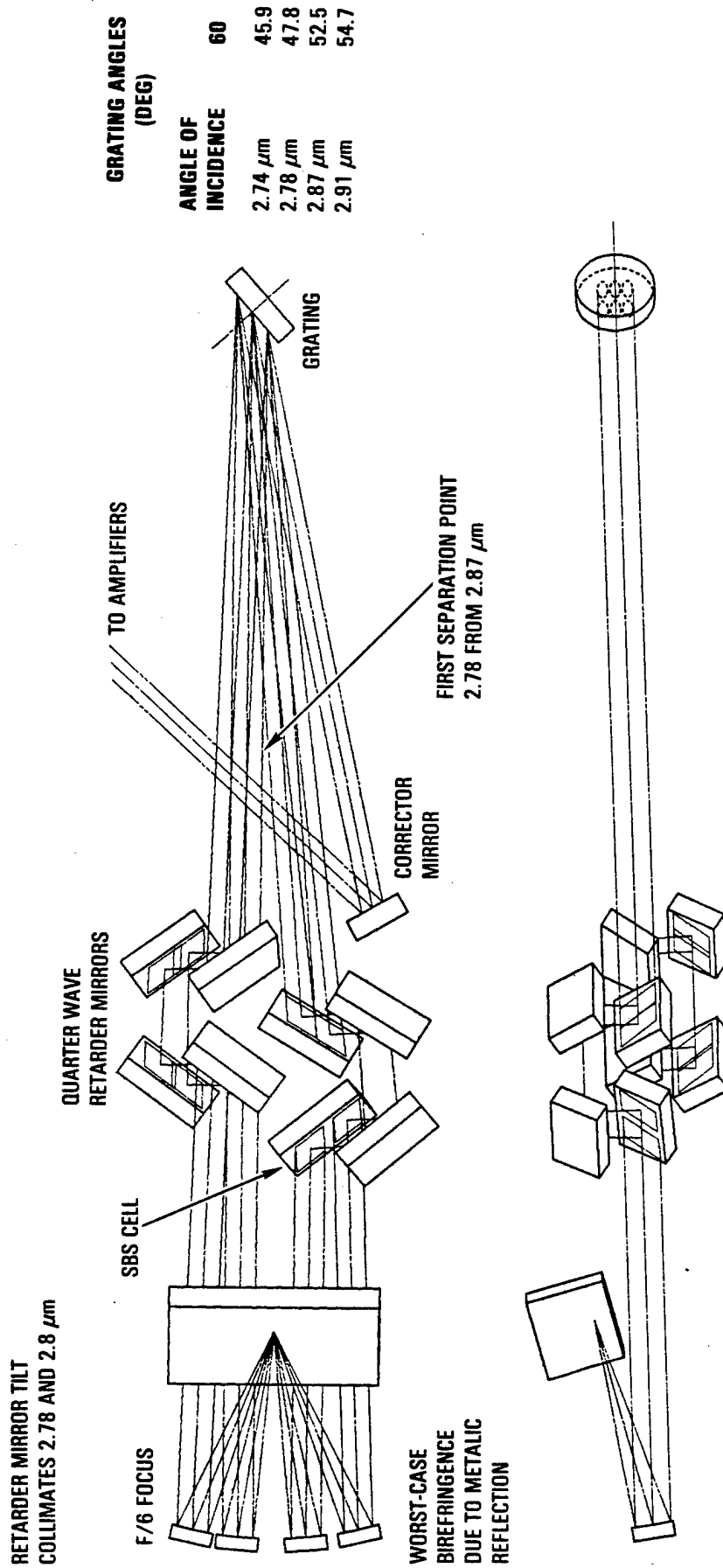


Figure 2.10-2. PCSS Layout

that the diffraction angles shown must be great enough to cause the two beams (each with a line pair) to separate in a distance that permits the packaging of the eight quarter wave retarder mirrors before too great a volume is used up.

Next, each of the two lines in each beam must separate into two separate beams to produce four distinct beams, each containing energy from only one line. At the point where this happens, each beam is focused into the SBS cell separately.

At the angles given for the grating design, the two longer lines will separate too much from the shorter wavelength lines to permit focusing all four lines into a single SBS cell. To remedy this, the two sets of four quarter wave retarder mirrors are used at angles of incidence which realign the longer and shorter wavelength pairs of beams. This prevents the line pairs from separating further after the retarder mirror components.

The mirrors are coated with a dielectric stack of thin films designed to phase delay one plane of polarization relative to the other by 90 deg. Four mirrors are used to do this to relieve the requirements on any one mirror coating to 22-1/2 degrees of phase delay.

In packaging the four mirrors, each is used at a nominal 45-deg angle of incidence so that after four bounces, the input beam is aligned to its initial direction with small correction, as described above, to stop further beam divergence. The input beam is p-plane polarized relative to a plane of incidence lying in the plane of the paper in Figure 2.10-2. The beam is made circularly polarized by phase delaying one plane of polarization relative to the other. The plane of incidence of all the quarter wave mirrors is rotated 45 deg out of the plane of the paper. This transforms one half of the p-plane polarized laser beams into s-plane relative to the plane of incidence for the retarder mirrors.

The performance of the coatings is very demanding because any residual p-plane energy cannot be prevented from returning directly to the MO. Coating design development work at OCLI was carried out on APACHE to improve the accuracy with which the manufactured coatings could be made. The results of the design analysis are presented in Section 2.11.

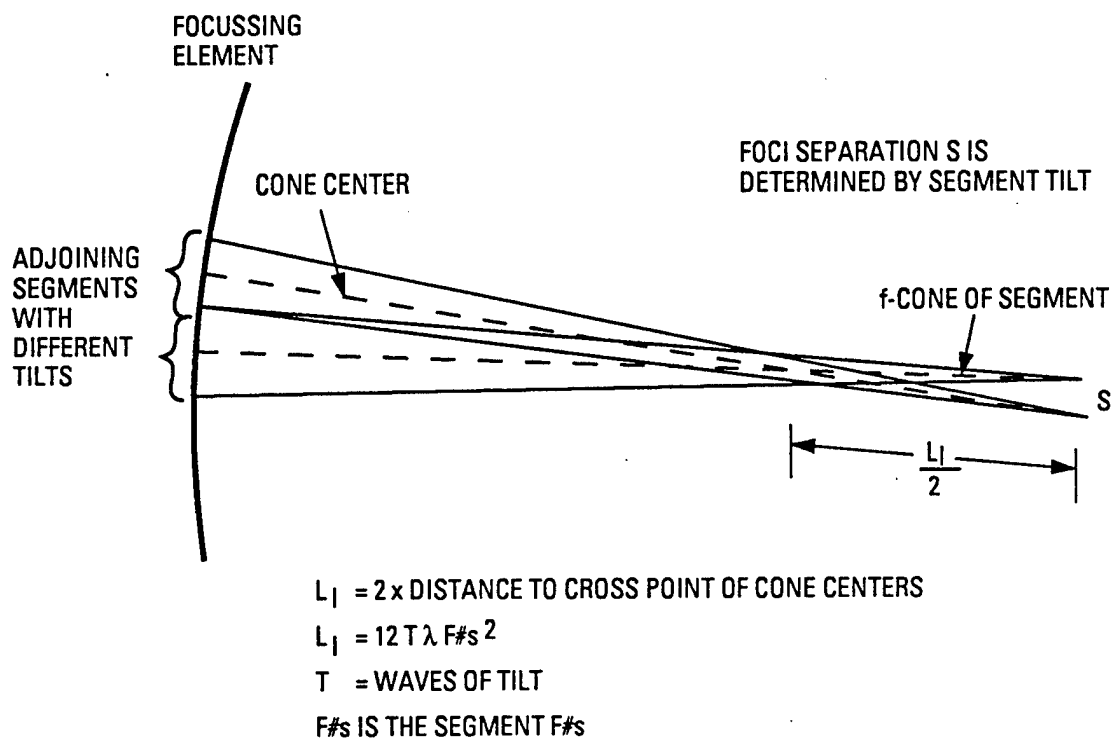
Optical interface with the SBS cell. To minimize the size of the SBS cell, the four mirrors which focus each spectral line beam into the cell are placed as close together as possible. To get the two shorter spectral lines next to the two longer ones, the two sets of retarder mirrors are tilted to cancel the dispersion angle between the line pairs which is causing them to become separated at this point. The distance to the four focusing elements is just long enough to permit the two beams in each line pair to separate.

The F-number ( $F\#$ ) of the focusing elements is a critical parameter. Each of the four line beams is made up of 120 beamlets due to segment and amplifier splitting and reformatting. Because of segment tilt, the focused spots in the cell will intersect over some depth in the cell. The interaction region is defined as the SBS gain region in the cell. In this region, SBS occurs and the cell must be wide enough to capture the region within the Xe gas. The  $F\#$  determines the region depth as shown in Figure 2.10-3, and the cell design needs a small  $F\#$  for compact packaging. However, smaller  $F\#$  drive the worst-case angle of incidence on the focusing mirrors larger, as seen in Figure 2.10-3. This is detrimental because birefringence of the circularly polarized light will occur by reflection off the metal surface. The baseline design point was set at  $F/10$ .

The throughput values for each element are shown in Figure 2.10-4.

### 2.10.3 SBS Cell Layout and Mechanical Design

The evolution of APACHE system SBS cell concepts throughout the APACHE program may be understood as a continual effort to reduce the total mass of the cell, its support system, and any expended gas flows while meeting CW phase conjugation requirements. Xe gas at 40 atmosphere pressure and about 300 K ambient temperature was chosen for the conjugating medium early in the program based on known experimental high performance. The very earliest cell concepts sought to suppress the Stokes frequency shift of the reflected beam by flowing the medium at sonic velocity in the direction of this beam's propagation. Extraction efficiency analysis indicated that the



01M160.89.07-5005

Figure 2.10-3. The Relation of Focussing Element Fresnel Number Interaction Length in the SBS Medium Is Determined

Corrector mirror	0.995	
4 x (quarter wave retarder)	$(0.995)^4$	
Focussing element	0.995	
p-state grating	0.96	} One value to SBS cell, and other value from SBS cell
s-state grating	0.96	
	<u>0.932</u>	

Figure 2.10-4. PCSS Throughput Values Derived for Each Optical Element

loss in extraction due to Stokes frequency shift was only a few percent and, therefore, not worth the large OPD and flow losses associated with flowing Xe at sonic velocity. As some flow of the medium through a high-power focus was necessary in CW operation to suppress thermal blooming, attention shifted to a cell concept featuring a low velocity transverse flow of Xe at focus. The transverse stream is isolated from the surrounding vacuum by He aerowindows or other designs which permit passage of the pump, Stokes, and transmitted beam (Figure 2.10-5). This concept allows a large fraction of the flowing Xe to be recirculated, saving expended mass and bypassing concerns that liquid or solid Xe particles would condense from a jet expanding into vacuum and produce unacceptable pump scattering.

SBS analysis using the BRIWON code, corroborated by data from the CWCS experiment (Section 2 of Volume I), established the media velocity requirements shown in Figure 2.10-6. Other requirements and issues in flowing SBS cell design include:

- Feasibility of multiline conjugation in the same focal volume
- Provisions for threshold reduction
- Requirements on pump beam F# to accommodate primary mirror segment tilt tolerances
- Permissible absorption and particulate count of Xe media
- RMS optical path differences introduced in SBS cell leading to a decrease of intensity at focus
- Birefringence effects in cell.

The baseline concept for multiline conjugation is to separate the four major ALPHA lines such that each line conjugates in a separate volume. However, common volume multiline conjugation has been demonstrated in tests at NRL. As its use reduces the number of separate foci by a factor of four, such an approach will be considered in future SBL studies, pending detailed measurements of conjugation fidelity with and without multiline operation.



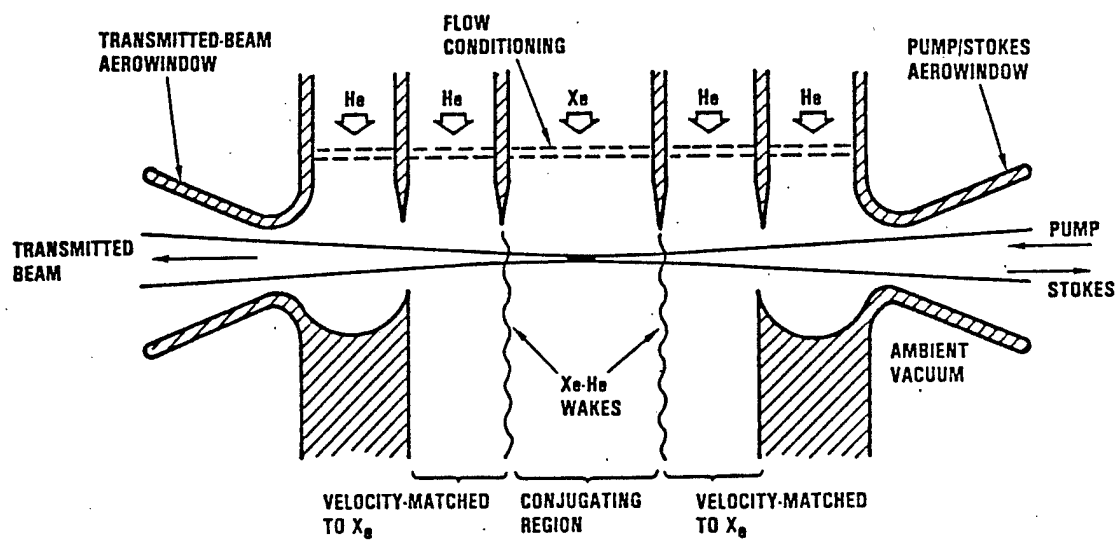


Figure 2.10-5. Transverse Flow SBS Cell

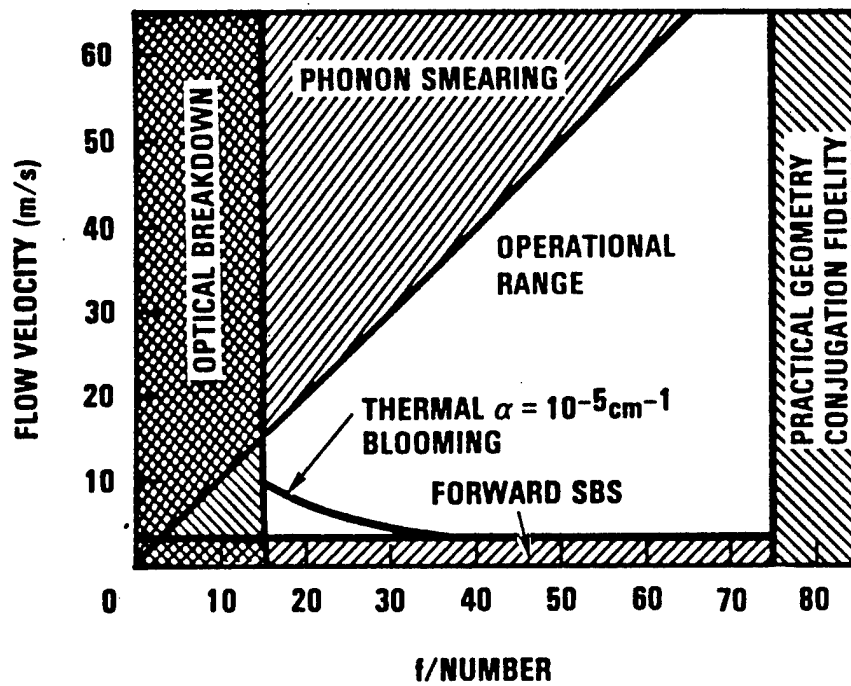


Figure 2.10-6. Flowing Xe Cell Velocity Requirements

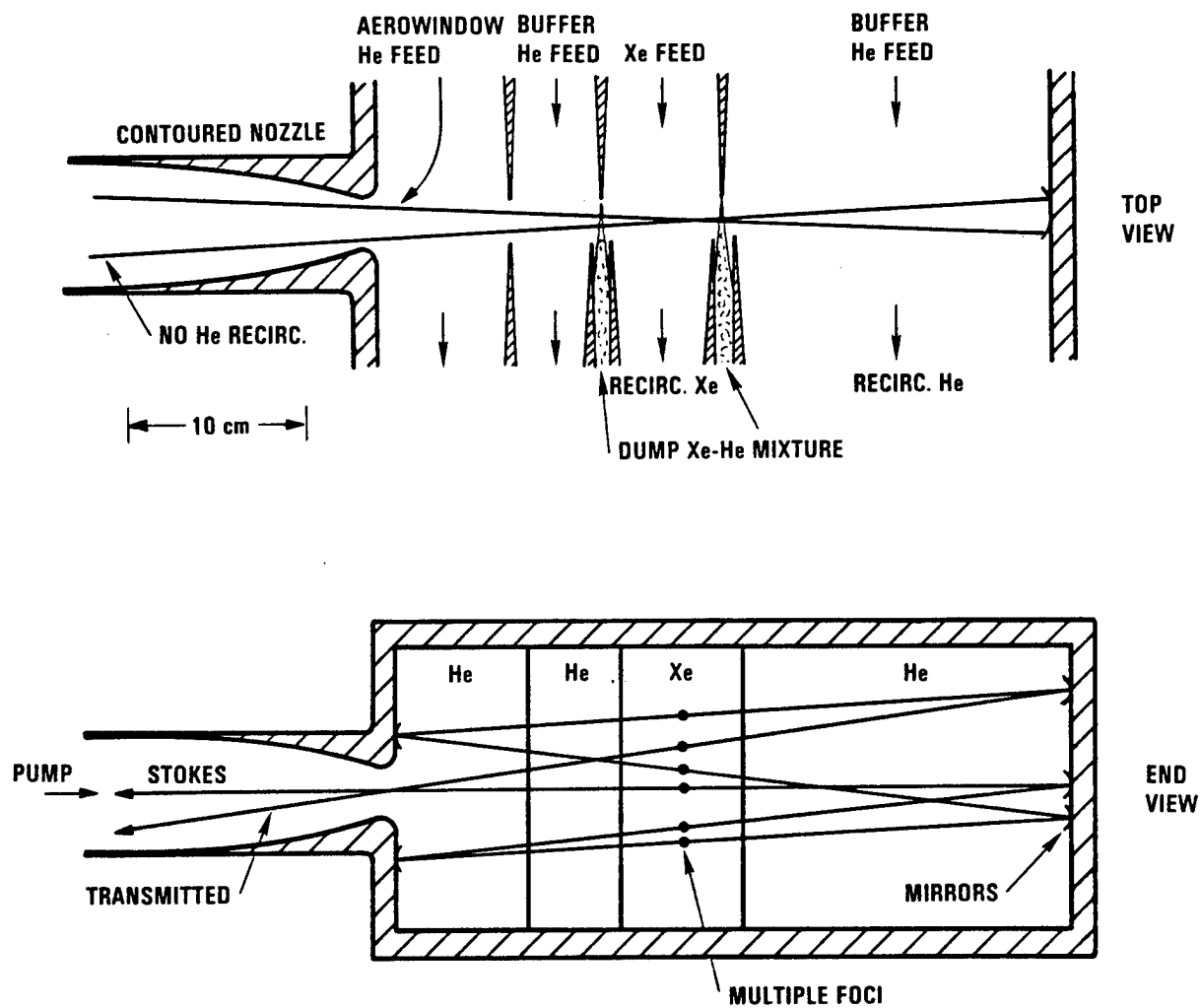
The APACHE requirement to conjugate a segmented primary mirror imposes a requirement on the SBS cell to not only accommodate the F# of a beamlet arising from a given segment on the primary mirror but also to accommodate the larger composite F# of all such beamlets arising from the relative segment tilt tolerances. The depth of the Xe flow stream must also be sufficient to assure crossing of all segment beamlets and consequent beam combination.

Maintenance of very low impurity concentrations of gases and particulates is important in both SBL and experiment SBL cells. Briefly, a high absorption in Xe aggravates beam quality degradation due to thermal blooming at focus and causes spatial sonic velocity variations in the focal region as intensity variations are mapped into media temperature variations. The latter effect will decrease conjugation fidelity. The heating of an impurity particle passing through a high-intensity focus may also ionize the gas at focus leading to breakdown which inhibits phase conjugation. A subscale absorption experiment was conducted to quantify typical absorption levels (c.f. Section 7, Volume 1) and experiments to quantify particulate breakdown are planned for APEX.

The layout and dimensions of transverse flow SBS cells, as well as the sizing and mass of the cell support system to supply, recirculate, purify and temperature condition the cell's flowing gases, are a strong function of the window design used to separate the 40 atmosphere pressure inside the cell from vacuum. Figures 2.10-7, 2.10-8, and 2.10-9 show similar scale layouts of SBS cells employing axial aerodynamic, transverse aerodynamic, and solid material windows, respectively. Note that even though these three cells have been designed to a common set of requirements, the number, type, width and degree of recirculation of at least some of the gas streams vary between each design. The conceptual design of each type of cell and its impact on SBS cell and support system mass will be discussed in more detail in the next sections.

#### 2.10.4 Aerowindow Concept for SBS Cell

A flowing-gas SBS cell has been proposed to provide phase conjugation for a chemical laser system. For the phase conjugation process to work, the SBS cell must be operated at an elevated pressure. The nominal



NOTE: DESIGN IS APPLICABLE TO HIGH- AND LOW-BRIGHTNESS SYSTEMS

Figure 2.10-7. Axial Aerowindow Conceptual Design

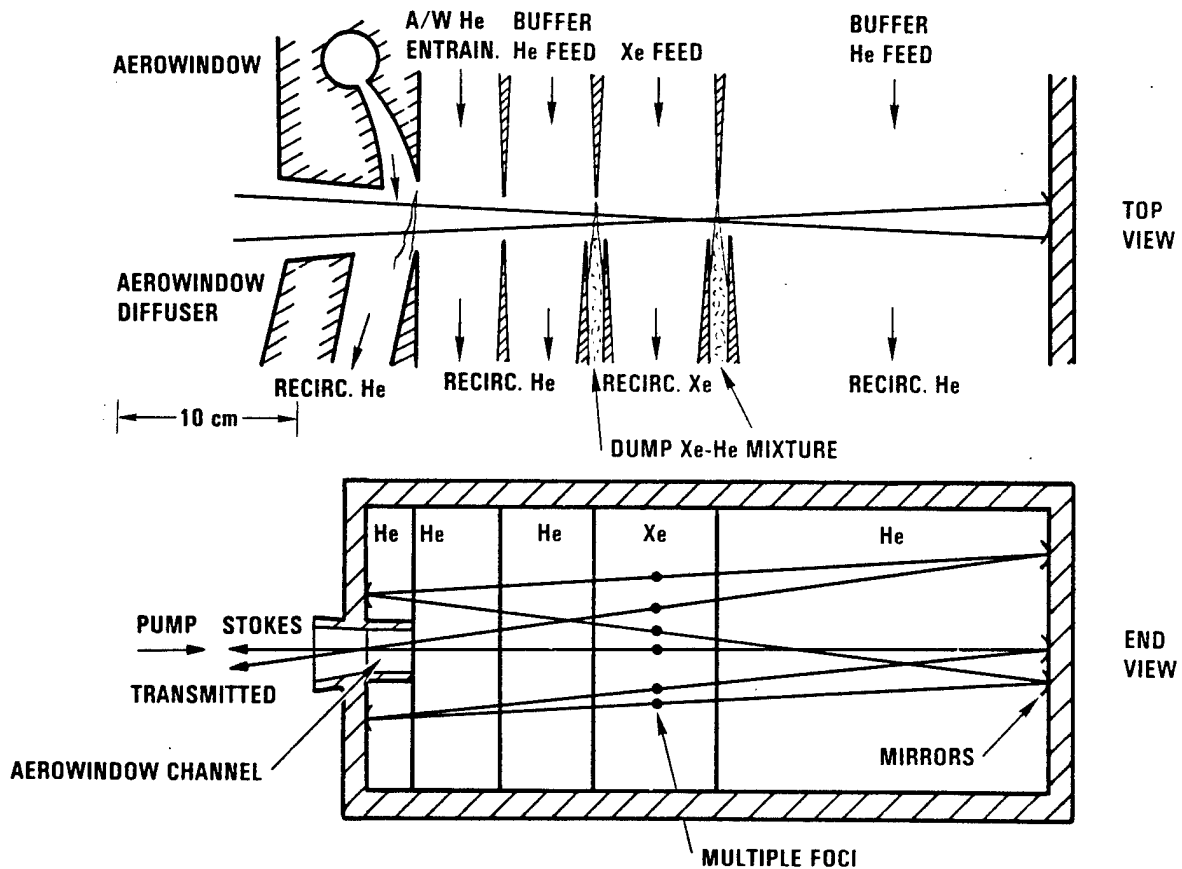


Figure 2.10-8. Transverse Aerowindow Conceptual Design

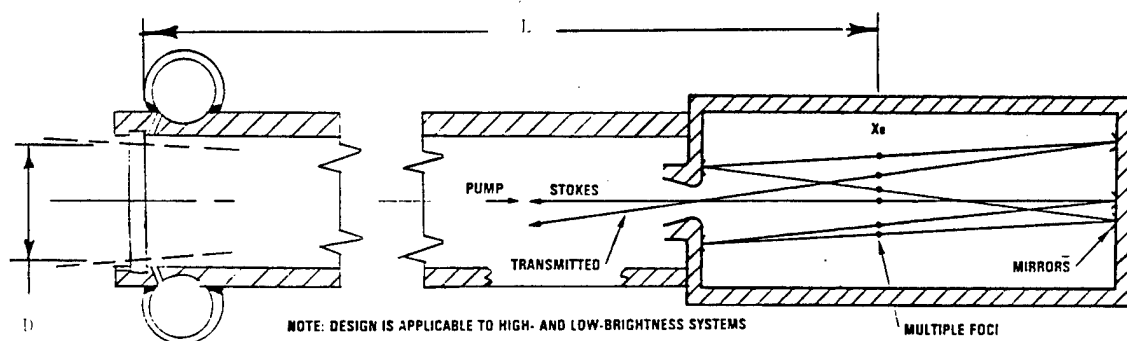


Figure 2.10-9. Material Window Conceptual Design

operating pressure for the proposed SBS cell is 40 atmospheres. The laser beam that is injected into the cell originates at near-vacuum conditions. Some means must be provided to interface the high-pressure SBS cell and the laser at low pressure. This interface may be either an aerodynamic window (aerowindow) or a material window. In this section a discussion of the work performed to define viable aerowindow concepts for the SBS cell is presented. A subsequent section addresses material window concepts.

An aerowindow is a device that uses the acceleration of a gas flow to provide a pressure gradient for interfacing a high-pressure region with a low-pressure region. There are two types of aerowindows. In a transverse aerowindow the laser beam is propagated in a direction normal to the window's mean flow direction. In an axial aerowindow the beam is propagated in a direction that is parallel to the mean flow direction. Both types of aerowindows were studied.

Conceptual designs of an axial and a transverse aerowindow flowing-gas SBS cell are presented in Figures 2.10-7 and 2.10-8, respectively. Although not part of the baseline design, the cells are compatible with the use of multiple foci for threshold reduction (Volume I, Section 4). Common features of the concepts include a central Xe channel, two He buffer channels whose velocities are matched to the Xe velocity, and two downstream channels to capture and dump the narrow Xe-He wakes. The axial aerowindow (Figure 2.10-7) is fed by an additional helium channel next to one of the helium buffer channels. This aerowindow uses a contoured axisymmetric nozzle. The nozzle gas flow is not recirculated, but is instead dumped to vacuum. The transverse aerowindow (Figure 2.10-8) uses a contoured two-dimensional nozzle. The aerowindow is separated from the SBS cell by a He channel used to supply the gas that is entrained by the aerowindow flow. Most of the gas used to drive this aerowindow is recovered in a diffuser and is recirculated by a pump back into the aerowindow nozzle plenum. Both types of aerowindow use He as the driver gas.

A summary of the analytical approach and conclusions is presented in Section 2.10.4.1, followed by a discussion of the analysis and presentation of conclusions in Sections 2.10.4.2 through 2.10.4.5.

#### 2.10.4.1 Summary

The analytical approach used in the aerowindow study was as follows. First, parametric analyses were performed for both types of aerowindow to determine nominal geometries and flow conditions for each. Aerowindow and SBS cell flows were then input to the SBS system dry mass model. Issues such as optical quality and acoustic noise interference were assessed qualitatively. The results of the various analyses were then assessed to identify the preferred aerowindow concept.

The axial aerowindow concept was found to be superior to the transverse aerowindow concept in each of the following five areas used to assess the two concepts:

1. Lower dry mass
2. Smaller mass flow losses to vacuum
3. Less complexity for the overall SBS system
4. Less acoustic noise radiated into the SBS cell
5. Less optical degradation based on previous TRW experience with aerowindows for chemical lasers.

#### 2.10.4.2 Analysis

The approach taken to assess the viability of either an axial or a transverse aerowindow mated with the SBS cell was to first define gas flow rates, both for gas recirculated and gas lost to vacuum, and then to use these flow rates as inputs to the SBS system dry mass model. The resultant dry masses and mass flows lost to vacuum were used to assess overall subsystem weight, an important factor in the selection process. Other factors considered were optical quality, acoustic noise and its effect on the phase conjugation process, and system complexity. The analysis methodology and results are presented below.

##### 2.10.4.2.1 Transverse Aerowindow

Key elements of the transverse aerowindow analysis that fed into the system model are:

- Selection of an operating point for the aerowindow and its associated mass flow rate



- Achievable pressure recovery in the aerowindow diffuser for the portion of the aerowindow driver gas that is recirculated
- Mass flow loss to vacuum.

These are discussed below.

A parametric analysis was performed to study the effects of different operating points on the required aerowindow mass flow rate. Guile and Hilding derived an expression for mass flow rate per unit aperture area (Reference 1):

$$\frac{\dot{M}}{D^2} = \frac{-\gamma}{2(\gamma + 1)} \frac{M_1^* P_0}{a^* \sin\left(\frac{\Delta\theta}{2}\right)} \int_{(M_1^*)^2}^{(M_2^*)^2} \frac{\left[1 - \left(\frac{\gamma - 1}{\gamma + 1}\right) (M^*)^2\right]^{\frac{1}{\gamma - 1}}}{(M^*)^2} d(M^*)^2$$

where:

$\gamma$  = ratio of specific heats

$a^*$  = critical sound speed

$$= \sqrt{\left(\frac{2\gamma}{\gamma + 1}\right) \frac{R_u}{MW} T_0}$$

$R_u$  = universal gas constant

$T_0$  = gas total temperature

$P_0$  = gas total pressure (=  $P_{TAW}$ )

$MW$  = gas molecular weight

$M^*$  =  $u/a^*$

$u$  = gas velocity

$\Delta\theta$  = flow turning angle, i.e., the angle of the arc that the gas travels as it moves across the aperture

$( )_1$  = value on low pressure side of aerowindow

$( )_2$  = value on high pressure side of aerowindow

D is the characteristic dimension of the aerowindow aperture. The aperture is assumed to be square for the transverse aerowindow, so the aperture cross-sectional area is

$$A_{ap} = D^2$$

The pressure on the high-pressure side of the aerowindow is set equal to the SBS cell pressure, or:

$$P_2 = 40 \text{ atm}$$

The aerowindow driver gas is He, for which

$$\gamma = 5/3$$

$$MW = 4.003 \text{ gm/mole}$$

Parameters that were varied were  $P_0$ ,  $T_0$ ,  $\Delta\theta$ , and the pressure ratio  $P_2/P_1$  across the aerowindow. Results are presented in Figures 2.10-10 through 2.10-12. Based on these results, the operating point was selected as:

$$P_0 = 180 \text{ atm}$$

$$T_0 = 300\text{K}$$

$$\Delta\theta = 30^\circ$$

$$P_1/P_2 = 0.01$$

For this operating point, the mass flow rate per unit area is:

$$\dot{M}/A_{ap} = 716.3 \text{ gm/s-cm}^2$$

A small portion of the aerowindow flow is lost to vacuum. The remainder of the flow is captured in a diffuser downstream of the aperture, decelerated, and then pumped back to pressure  $P_0$  and reinjected into the aerowindow nozzle plenum. The pumping requirement for recirculating the aerowindow gas depends on the recirculating flow rate in two ways. First, the pump power is proportional to the mass flow rate being pumped (Reference 2). Second, the diffuser pressure recovery is proportional to

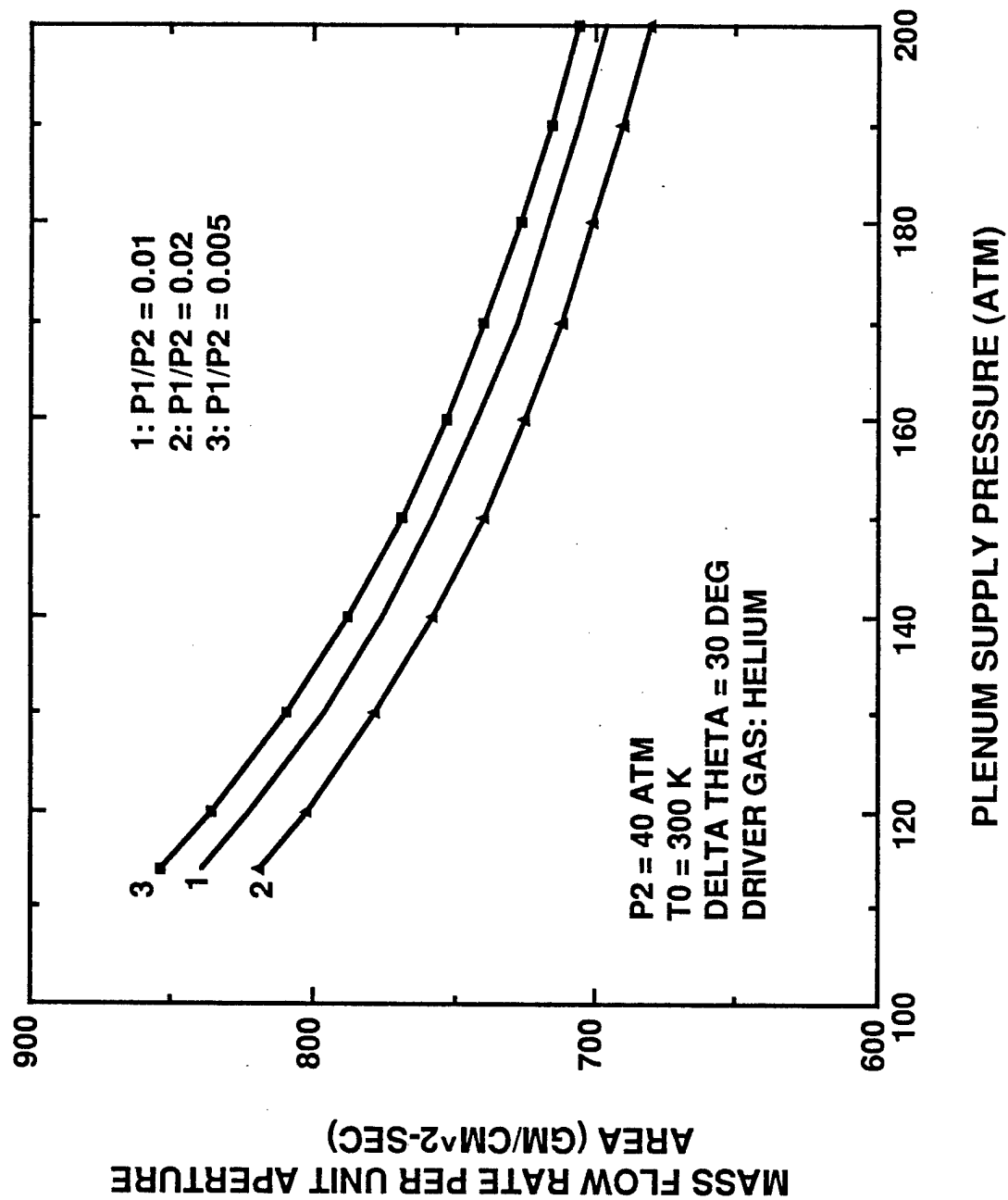


Figure 2.10-10. Effect of Pressure Ratio on Transverse Aerowindow Mass Flowrate

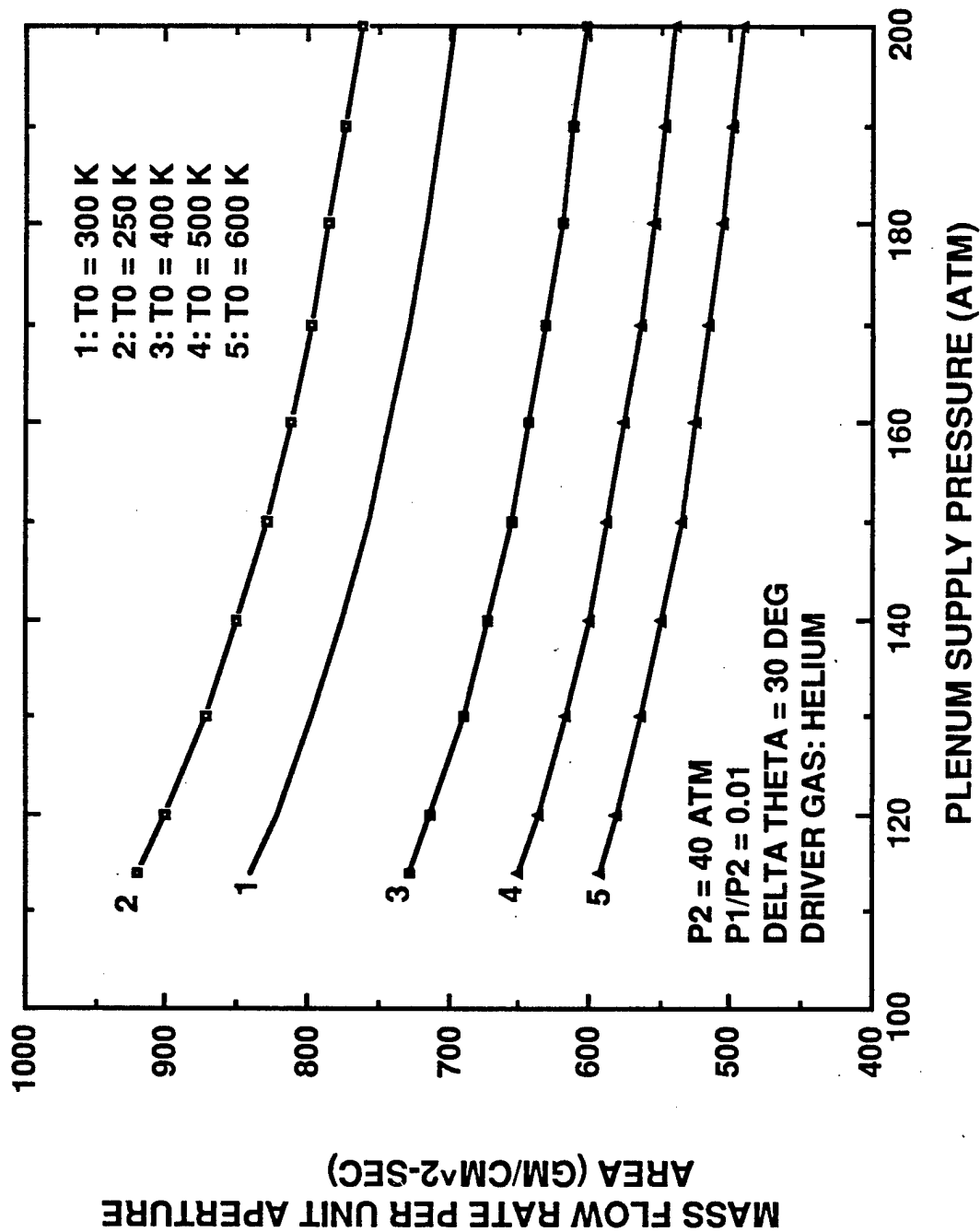


Figure 2.10-11. Effect of Gas Total Temperature on Transverse Aerowindow Mass Flowrate

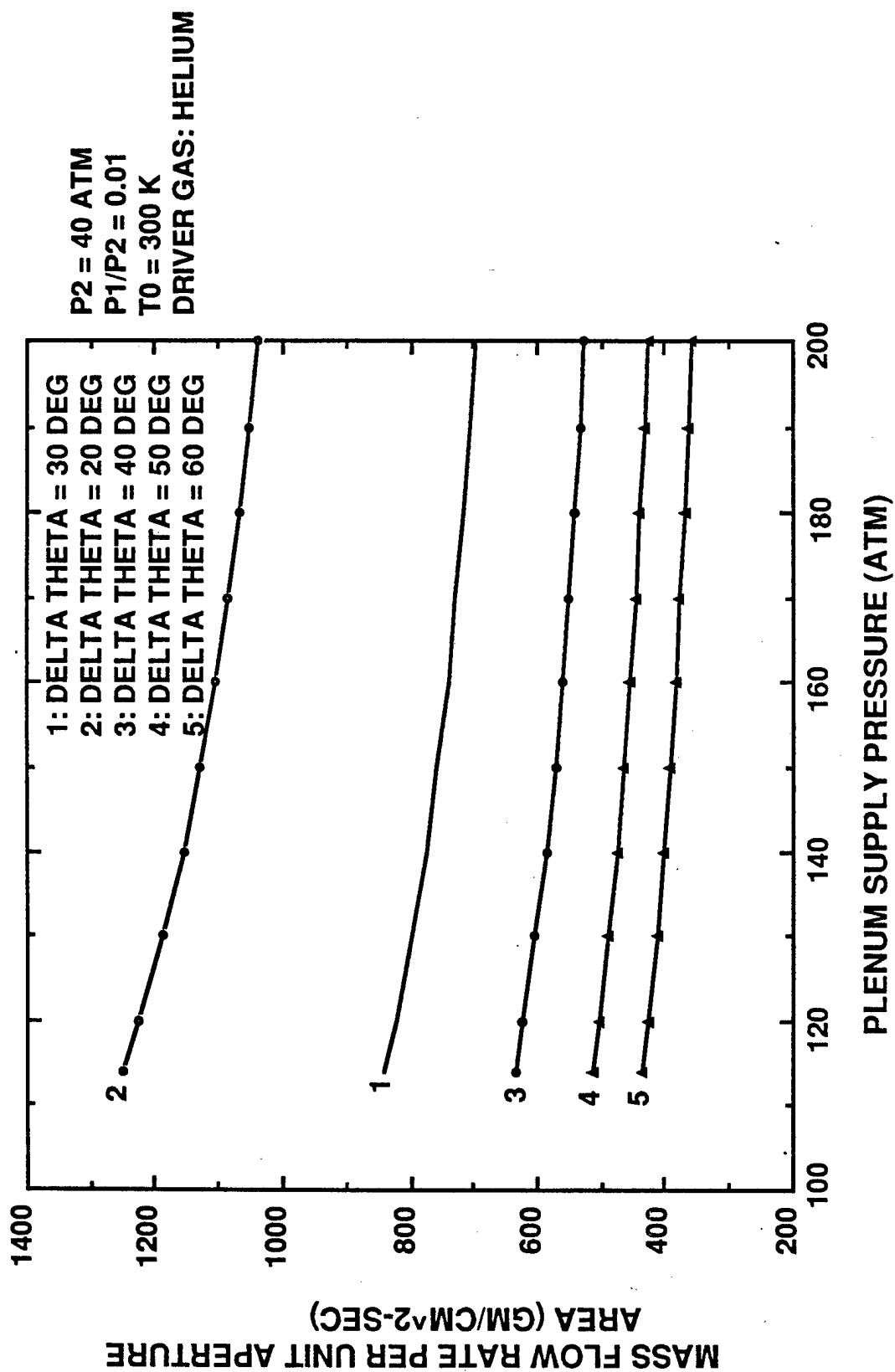


Figure 2.10-12. Effect of Flow Turning Angle on Transverse Aerowindow Mass Flowrate

the mass flow rate to be pumped. A larger pressure recovery means that a smaller pressure differential must be provided by the pump. Because of the importance of knowing the recirculating gas flow rate, the issue of mass loss to vacuum will be discussed first, followed by the issue of diffuser pressure recovery.

It was assumed that only the mass flow in the boundary layer on the low-pressure side of the aerowindow nozzle is lost to vacuum. The boundary layer thickness  $\delta$  was estimated assuming a turbulent flat plate boundary layer. The  $\delta$  was calculated assuming a number of different nozzle sizes and using both throat properties and nozzle exit plane properties. For all cases, the Reynolds number  $Re$  was large enough that the assumption of a turbulent boundary layer was valid. Giles (Reference 3) gives expressions for  $\delta$  for an incompressible turbulent boundary layer as a function of  $Re$ . These were combined with results of Van Driest (Reference 4) relating  $\delta$  for incompressible and compressible flow as a function of Mach number to estimate  $\delta$ . The mass flow rate per unit width of boundary layer can be shown to be:

$$(\dot{M})_{uw} = \rho_e U_e (\delta - \delta^*)$$

where:

$\rho$  = gas density

$\delta^*$  = boundary layer displacement thickness

$( )_e$  = freestream conditions at edge of boundary layer

From Schlichting (Reference 5)  $\delta^*$  is small compared to  $\delta$  for a flat plate turbulent boundary layer in supersonic flow:

$$\delta^* < 0.1 \delta$$

Therefore only a small error is introduced by neglecting  $\delta^*$ , or:

$$(\dot{M})_{uw} \approx \rho_e U_e \delta$$

Using this model, it was found that for all cases hypothesized the mass flow rate in the boundary layer was less than 1% of the total mass flow rate. To be conservative, it was then assumed that the mass flow lost to vacuum is 2% of the total mass flow rate.

The pressure recovery achieved by the aerowindow diffuser was calculated using the Behrens/Sugimura correlation (Reference 6):

$$P_{\text{rec}} = 5.14 \left( \frac{\dot{M}}{A_{\text{diff}}} \right) \sqrt{\frac{T_0}{MW}} F(\gamma)$$

where:

$P_{\text{rec}}$  = recovery pressure, in torr

$\dot{M}$  = mass flow rate into diffuser, in gm/s

$A_{\text{diff}}$  = diffuser inlet cross-sectional area, in  $\text{cm}^2$

$T_0$  = gas total temperature, in K

$MW$  = gas molecular weight, in gm/mole

$F(\gamma)$  = function of  $\gamma$

$$= \sqrt{\frac{2}{\gamma - 1}} \left( \frac{\gamma + 1}{2\sqrt{\gamma}} \right)^{\frac{\gamma + 1}{\gamma - 1}}$$

The mass flux into the diffuser is related to the mass flow per unit aperture area by:

$$\left( \frac{\dot{M}}{A_{\text{diff}}} \right) = \left( \frac{\dot{M}}{A_{\text{ap}}} \right) \left( \frac{A_{\text{ap}}}{A_{\text{diff}}} \right) \left( 1 - \frac{\dot{M}_{\text{lost}}}{\dot{M}_{\text{total}}} \right)$$

It was assumed that the diffuser width is equal to the aperture width D. The diffuser inlet height was assumed to be twice the aerowindow nozzle exit plane height. Using relations from Guile and Hilding, it can be shown that

$$\left( \frac{A_{ap}}{A_{diff}} \right) = \frac{\sin \left( \frac{\Delta \theta}{2} \right)}{\left[ \left( \frac{M_1^*}{M_2^*} \right) - 1 \right]}$$

Substituting in appropriate values for the designated operating point, the recovery pressure is

$$P_{rec} = 49.8 \text{ atm}$$

The aerowindow nozzle operates at a total pressure of 180 atm, so the recirculated driver gas must be pumped through a pressure differential of 130.2 atmosphere.

#### 2.10.4.2.2 Axial Aerowindow

The concept for mating an axial aerowindow to the SBS cell is shown in Figure 2.10-7. Gas is fed to the aerowindow nozzle at the SBS cell pressure of 40 atm. Neglecting the real gas compressibility factor Z, the mass flow per unit aperture area is (Reference 7):

$$\frac{\dot{M}}{A_{ap}} = \sqrt{\gamma \left( \frac{2}{\gamma + 1} \right)^{\frac{\gamma + 1}{\gamma - 1}}} \frac{P_0}{\sqrt{\frac{R_u}{MW} T_0}}$$

where the aperture is located at the aerowindow nozzle throat. For He at the nozzle throat conditions, the real gas compressibility effect (Reference 8) is on the order of 2%. Therefore, no appreciable error is introduced by neglecting this effect. For a given gas, the mass flux will depend only on  $P_0$  and  $T_0$ . Since  $P_0$  is fixed at 40 atm, the mass flux at the aperture will vary only with  $T_0$ . For the system analysis, described below,  $T_0$  was assumed to be 300 K. For this value of  $T_0$ , the mass flux is



$$\frac{\dot{M}}{A_{ap}} = 373 \text{ gm/s-cm}^2$$

The aerowindow is axisymmetric, with the beam propagated into the SBS cell along the nozzle axis. The nozzle contour was specified using the AMES nozzle code. The AMES code specifies a contour such that uniform flow is achieved at the nozzle exit plane. Contours were designed for several different nozzle exit plane Mach numbers. The AMES code results were checked using the approximate method of Foelsch (Reference 9) and were found to be reasonable. The contour corresponding to a Mach number of 4.0 was selected for the nominal design of the axial aerowindow.

The mass flow lost to vacuum was calculated. An attempt was first made to recirculate the annular region of the flow surrounding the beam. The mass flow to be recirculated was calculated for an F# of 6, exit plane Mach number of 4.0, and a focus-to-aperture displacement of approximately 14 cm. Only 20% of the total aerowindow flow was captured. This figure is optimistic since the nozzle wall boundary layer was not taken into account. The actual mass flow recovered by the diffuser would be less. Because only a small fraction of the total flow can be captured and recirculated, it was decided to not recirculate any of the aerowindow nozzle flow. This also minimizes complexity.

There is, however, some gas that must be recirculated for the axial aerowindow. Part of the gas flows past the aerowindow as shown in Figure 2.10-7. This ensures that there is no stagnant gas or recirculation zones in the beam path and that the feed channel/helium buffer channel interface is clean. The flow rate split was selected so that the aerowindow flow rate is 90% of the total feed channel flow rate.

#### 2.10.4.2.3 SBS Cell Flows

The SBS cell Xe and He flow rates were calculated and used as inputs to the SBS system dry mass model. Total flow rates, mass flow lost to vacuum, and the pressure differentials through which the recirculated gas flows need to be pumped were calculated. The calculations are discussed below.

There are several factors in determining mass flow rates that are common to the Xe and He channel flows. The SBS cell channel height, where the height is defined as the dimension normal to both the mean beam propagation direction and the mean channel flow direction, has been set at 16 cm. This dimension is based on optical considerations for a multiple foci SBS cell. This can be seen by consideration of Figures 2.10-7 and 2.10-8 which show the SBS cell integrated with an axial and a transverse aerowindow, respectively. Each focus must be separated from its nearest neighbor by at least 10 aberrated spot diameters to prevent undesirable cross-talk. Furthermore, the beams are restricted from crossing within the conjugating medium. Also, the transmitted beam must exit out the aerowindow aperture. These requirements, in combination with channel depth and window flux requirements, determine the placement of the mirrors inside the cell and, hence, the channel height.

Other common factors were gas pressures, temperatures, and flow velocities. The pressure was 40 atmosphere in each channel and the total gas temperature in each channel was assumed to be 300 K. The mean flow velocity in each channel was 10 m/s so the flow was low subsonic and the static temperature was very nearly equal to the total temperature. Knowing pressure and temperature, Xe and He densities were calculated. Real gas compressibility was accounted for in density calculations (References 8 and 11).

Given the gas density and mean flow velocity, the mass flux in a channel may be computed. Once the channel cross-sectional area is specified, the total mass flow rate in the channel is fixed. Since the channel heights are fixed, calculating the total mass flow rate in a channel is reduced to determining the channel depth, where the depth is the dimension in the mean beam propagation direction.

The Xe channel depth was calculated from the requirement that the full-width Xe depth is 125 Rayleigh ranges, based on the conglomerate F#, to ensure beamlet crossing within the Xe. This requirement is based on the analysis by Clendening (Reference 19) which suggests that Xe widths of order 25-100 Rayleigh ranges may be necessary to accommodate one wave of physical segment tilt (two waves of phase).

The depth of the helium buffer channel on the side of the Xe channel opposite that of the aerowindow was specified based on keeping the incident flux on the mirrors below  $100 \text{ kW/cm}^2$ . This yields a channel depth of 19 cm.

The depth of the other He buffer channel was specified by requiring that the Xe/He wake be isolated from the He-He shear layer at the aerowindow/He buffer channel interface. This requirement could be interpreted either as the amount of gas entrained into the He-He shear layer is small compared to the total buffer channel flow rate, or as the shear layer thickness is small compared to the buffer channel depth. The shear layer thickness was estimated using results presented by Ikawa (Reference 10), and the buffer channel depth was specified by requiring it to be at least an order of magnitude larger than the shear layer thickness. Based on this rationale, the channel depth was set at 5 cm.

Portions of the Xe and He buffer flows mix in the wakes at the two Xe He interfaces. The Xe-He mixtures are dumped to vacuum rather than trying to separate the two gases for recirculation, which would increase system complexity and risk. The mass flow lost to vacuum was calculated as follows. All of the gas in the two wakes was assumed to be lost. Incompressible turbulent mixing layer results (Reference 10) were used to estimate the wake growth rate. The wake was assumed to grow at an equal rate into both the He and Xe channels. The wake grew over a length  $\Delta x$  equal to the separation of the upstream and downstream splitter plate edges and related to the  $F\#$  by

$$\Delta x = 125 \lambda F\# + 0.6 \text{ cm}$$

where the 0.6 cm is twice the clearance between beam and splitter plate edge. The Xe mass flow loss was then calculated:

$$\begin{aligned}\dot{M}_{\text{Xe, loss}} &= 0.57 \text{ kg/s at } F/6 \\ &= 0.67 \text{ kg/s at } F/10\end{aligned}$$

The He mass flow rate was calculated to be:

$$\begin{aligned}\dot{M}_{\text{He, loss}} &= .012 \text{ kg/s at F/6} \\ &= .015 \text{ kg/s at F/10}\end{aligned}$$

The pressure differential through which the recirculated cell gas, either Xe or He, must be pumped was estimated using the dynamic pressure in the cell. The Xe dynamic pressure (dynamic head) was 2.1 psia. Assuming the recirculated xenon was subjected to four 90 deg turns with the pressure loss equal to one dynamic head per turn gave a pressure drop of 8.4 psia (0.57 atm). To be conservative, the pressure differential for the Xe was assumed to be 1.0 atmosphere. The same analysis was performed for the recirculated He flows. The He dynamic pressure in the SBS cell was 0.046 psia. This is much smaller than that for the Xe. Combining this with the fact that the recirculated He buffer flows are small compared to the recirculated Xe flow, the pumping requirement for the cell He recirculation is negligibly small for the purpose of concept selection.

#### 2.10.4.3 SBS System Dry Mass Model and Results

A model for the approximation of the SBS system dry mass as a function of gas flow rates has been formulated (Reference 12). The model is based on the results of a detailed systems analysis of the APACHE system, and can be expressed as:

$$M_{\text{SBS ASSY}} = M_{\text{CELL}} + M_{\text{SUPPORT SYSTEM}} + \dot{M}_{\text{EXPENDED FLOW}} \tau$$

where:

$M_{\text{CELL}}$	= mass of the SBS cell
$M_{\text{SUPPORT SYSTEM}}$	= mass of support system, including filters, purifiers, initial loop fill, heat exchangers, and turbopumps/gas generators
$\dot{M}_{\text{EXPENDED FLOW}}$	= mass flow lost to vacuum, including Xe, He, and hydrazine used to drive turbopumps
$\tau$	= device run time

The mass of the SBS cell is assumed to be fixed and is approximated as:

$$M_{\text{CELL}} = 300 \text{ kg}$$

The support system mass can be broken down into a fixed component and components that are functions of various gas flow rates:

$$M_{\text{SUPPORT SYSTEM}} = M_{\text{FIXED}} + M_{\text{FLOW DEPENDENT}} + M_{\text{POWER DEPENDENT DRY MASS}}$$

where:

$M_{\text{FIXED}}$  = mass of filter, purifier, and initial loop fill

$M_{\text{FLOW DEPENDENT}}$  = mass of xenon and helium heat exchangers

$M_{\text{POWER DEPENDENT DRY MASS}}$  = mass of turbopumps and gas generators for recirculating Xe and He

The mass of the combined filter, purifier, and initial loop fill is assumed to be a fixed quantity and is approximated as:

$$M_{\text{FIXED}} = 62 \text{ kg}$$

The heat exchanger mass can be broken into two parts, one for the Xe and one for the He. It is modelled as:

$$M_{\text{FLOW DEPENDENT}} = 0.02238 \dot{M}_{\text{Xe,TOT}} + 0.00444 \dot{M}_{\text{He,RECIRC}}$$

where:  $M_{\text{FLOW DEPENDENT}}$  = mass, in kg

$\dot{M}_{\text{Xe,TOT}}$  = total xenon mass flow rate, in gm/s

$\dot{M}_{\text{He,RECIRC}}$  = recirculated helium mass flow rate, in gm/s

The turbopump gas generator mass can also be broken into two parts, one for the Xe and one for the He. It is modelled as:

$$\begin{aligned} \dot{M}_{\text{POWER DEPENDENT}} \\ \text{DRY MASS} &= 0.00160 \dot{M}_{\text{Xe,RECIRC}} \Delta P_{\text{Xe}} \\ &+ 0.00160 \dot{M}_{\text{He,RECIRC,AW}} \Delta P_{\text{He}} \end{aligned}$$

where:

$\dot{M}_{\text{POWER DEPENDENT}}$  = mass, in kg  
DRY MASS

$\dot{M}_{\text{Xe,RECIRC}}$  = recirculated Xe mass flow rate, in gm/s

$\Delta P_{\text{Xe}}$  = pressure differential through which Xe is pumped, in atm

$\dot{M}_{\text{He,RECIRC,AW}}$  = recirculated aerowindow He mass flow rate, in gm/s

$\Delta P_{\text{He}}$  = pressure differential through which the aerowindow helium is pumped, in atm

The mass flow lost to vacuum includes the Xe and He dumped overboard from the SBS cell due to gas mixing at Xe/He interfaces, He lost from the aerowindow, and the hydrazine ( $\text{N}_2\text{H}_4$ ) required to drive the turbopumps. This is modelled as:

$$\dot{M}_{\text{expended}} = \dot{M}_{\text{Xe,Ex}} + \dot{M}_{\text{He,Ex}} + \dot{M}_{\text{N}_2\text{H}_4}$$

and

$$\begin{aligned} \dot{M}_{\text{N}_2\text{H}_4} &= .0221 \dot{M}_{\text{Xe,RECIRC}} \Delta P_{\text{Xe}} \\ &+ .02211 \dot{M}_{\text{He, RECIRC,AW}} \Delta P_{\text{He}} \end{aligned}$$

where the mass flow rates are in kg/s and the pressure differentials are in atm.

It should be noted that only that part of the recirculated He associated with the aerowindow is included in the sizing of the turbopump/gas generator and the calculation of hydrazine mass flow. This is because the pressure drop associated with the SBS cell recirculated helium is small compared to those for the recirculated Xe and recirculated aerowindow He.

The aerowindow flow rates discussed above were calculated on a per unit aperture area basis. To use the SBS system dry mass model, the aperture size must be defined. The characteristic aperture size D was defined as:

$$D = \frac{L}{F\#} + 2\Delta$$

where

L = focus to aperture displacement

F# = beam F#

$\Delta$  = beam aperture clearance required for misalignment and jitter.

The aperture for the transverse aerowindow is square in cross section, so the aperture area is  $D^2$ . For the axial aerowindow, the aperture cross section is circular, and the aperture area is  $(\pi/4)D^2$ . The beam-aperture clearance was assumed to be 0.3 cm.

Analysis results are presented in Figures 2.10-13 and 2.10-14 as functions of the aerowindow aperture displacement from the focus for two different F#. Total mass flowrate losses to vacuum and total recirculating mass flowrate are shown in Figure 2.10-13 for both axial and transverse aerowindows. Variations in flow rates with the focus-to-aperture displacement are due to variations in aerowindow aperture size. The SBS cell Xe and He flow rates are fixed.

For the axial aerowindow case, the main contributor to flow rate losses is the aerowindow itself. The recirculating flow rate is dominated by the Xe channel flow rate.

## AEROWINDOW GAS REQUIREMENTS (PRELIMINARY)

FOR ALL CASES: XENON VELOCITY = 10 M/SEC  
CHANNEL HEIGHTS = 16CM  
5.0 R. R. FULL WIDTH

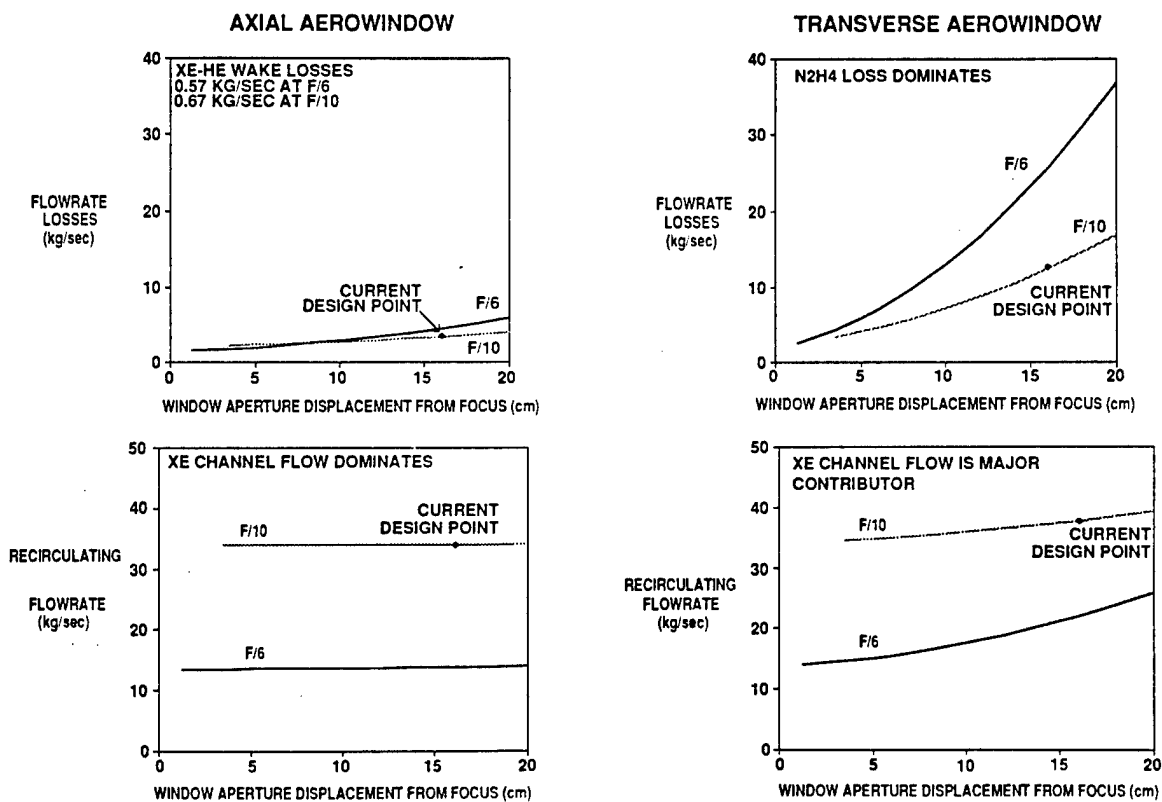


Figure 2.10-13. Aerowindow Gas Requirements



FOR ALL CASES : XENON VELOCITY = 10 M/SEC  
 CHANNEL HEIGHTS = 16 CM  
 5.0 R. R. FULL WIDTH

DRY MASS INCLUDES : SBS CELL  
 SUPPORT SYSTEM - FILTER, PURIFIERS, INITIAL LOOP FILL  
 - HEAT EXCHANGES  
 - TURBO PUMPS

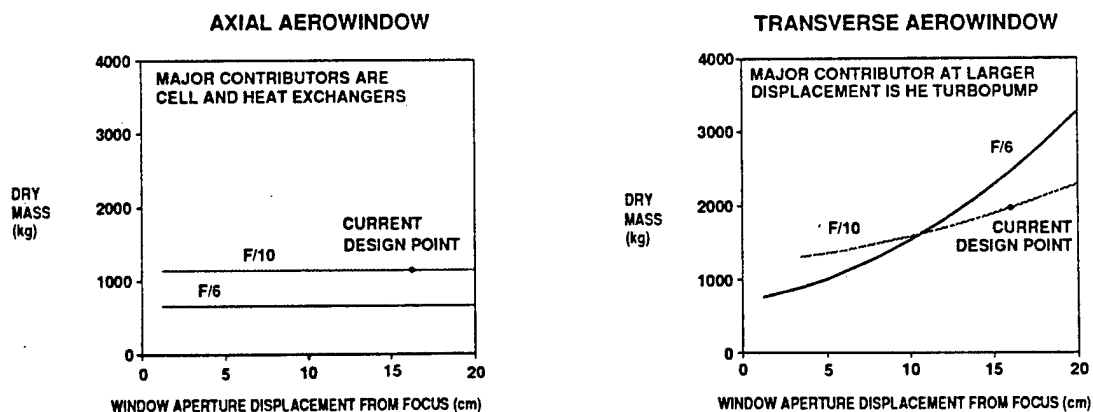


Figure 2.10-14. SBS Cell/Aerowindow Dry Mass

The dominant contributor to flow rate losses for the transverse aerowindow case is the hydrazine required to drive the He turbopump. This is due to the large pressure differential ( $\sim 130$  atm) through which the recirculating aerowindow flow must be pumped. The Xe channel flow is the main contributor to the recirculating flow. However, the aerowindow provides a significant contribution, especially at an F# of 6.

The system dry mass, i.e.,  $M_{CELL}$  and  $M_{SUPPORT}$ , is plotted in Figure 2.10-14. For the axial aerowindow, the major contributors are the SBS cell and the Xe heat exchangers. The difference in dry mass for the two numbers is due to the Xe heat exchanger at F/10 being approximately 460 kg larger than that for F/6. The major contributor to the dry mass for the transverse aerowindow is the He turbopump/gas generator. As with the hydrazine flow rate discussed in the previous paragraph, this is the result of the large pressure differential through which the recirculating aerowindow flow must be pumped.

In terms of both flow rates and dry mass, the axial aerowindow SBS system is superior to the transverse aerowindow SBS system.

#### 2.10.4.4 Other Aerowindow Issues

Several other issues besides dry masses and mass flow losses must be considered in the aerowindow selection process. These are:

- Optical quality
- Acoustic noise and its effect on the phase conjugation process
- SBS system complexity.

For purposes of the present aerowindow comparison, these issues were addressed qualitatively.

Optical quality refers to aberrations introduced into the focusing beam by aerowindow density gradients normal to the propagation path and affects beam spot size at the focal plane. TRW has experience with both axial and transverse aerowindows used with chemical lasers. Those aerowindows were used to interface the chemical lasers (BDL, NACL, and MIRACL), whose cavities operate at pressures ranging from 5 to 40 torr, with atmosphere. Beam quality measurements were performed on the BDL laser

beam both in vacuum and after propagation through an axial aerowindow (Reference 13). Within the experimental accuracy there was no discernible difference in beam quality for the two measurements, indicating excellent optical quality for the axial aerowindow. Beam quality measurements have also been made for the MIRACL laser after propagation through a transverse aerowindow. It was found that to achieve good optical quality refractive index matching at the shear layer interface on the high-pressure side of the aerowindow is required. Therefore, it can be concluded that it is inherently easier to achieve good optical quality for an axial aerowindow.

It is noted that the beam quality measurements discussed above were performed at lower pressures, and densities, than those at which the SBS cell aerowindow would operate. This implies that it will be more difficult to get good optical quality with the SBS cell aerowindow than with the aforementioned chemical laser aerowindows. However, the conclusion that an axial aerowindow is preferable from an optical quality viewpoint will not alter.

Acoustic noise generated by the aerowindow and radiated into the SBS cell might affect the phase conjugation process by inducing unacceptable pressure fluctuations in the Xe channel flow at the focal plane. The sound radiation pattern for an axisymmetric jet (Reference 14) was used to get a qualitative feel for the sound radiation pattern of an axial aerowindow. The intensity level of acoustic waves propagated into the SBS cell will be small compared to the maximum sound intensity level. Sound pressure level measurements were made for the MIRACL transverse aerowindow. Overall sound pressure level (OASPL) measurements on the optical axis on the high-pressure side of the aerowindow (equivalent to the direction of the SBS cell from a transverse aerowindow) were about 120 dB (Reference 15). Scaling from the MIRACL aerowindow to the SBS cell transverse aerowindow indicates that a similar OASPL can be expected for the SBS transverse aerowindow. Using the same scaling arguments to compare maximum sound generated for axial and transverse aerowindows, the maximum OASPL may be similar for both types. However, very little of the acoustic energy of the axial aerowindow flow will be radiated into the SBS cell compared to that for the transverse aerowindow. Therefore, the axial aerowindow is more desirable from an acoustic interference viewpoint.

Complexity is an issue to be considered in selecting an aerowindow. An aerowindow, either axial or transverse, is a simple device. However, the transverse aerowindow has additional hardware, such as a turbopump, gas generator, and extra piping, because its driver gas is recirculated. Therefore, the axial aerowindow is more desirable based on the complexity criterion.

#### 2.10.4.5 Conclusions

Axial and transverse aerowindow concepts were examined for the SBS system. For all of the criteria used to assess the concepts, the axial aerowindow was preferred. Compared to an SBS system with transverse aerowindow, the SBS system with an axial aerowindow exhibited:

- Lower dry mass
- Smaller mass flow losses
- Less complexity
- Lower acoustical noise transmitted into the SBS cell
- Less optical degradation based on previous TRW experience with chemical laser aerowindows.

For these reasons, the axial aerowindow has been selected over the transverse aerowindow concept.

#### 2.10.5 Material SBS Cell Window Investigation

A number of studies have been performed to determine the feasibility of a material SBS cell window as an alternative to either type of aerodynamic window. It is anticipated that a material window would offer significant reductions in gas flows lost to vacuum and the support equipment needed to provide such flows, while simplifying operation and test sequences.

Table 2.10-1 summarizes the particular requirements placed on the SBS material window. The input power to the cell in the APACHE application is expected to be in the 1.0- to 1.5-MW range (earlier studies had been performed for 3 MW).

Table 2.10-1. Particular Requirements on Material Window

Parameter	Value	Comments
Power transmitted	$\leq 1.5$ MW	Heat flux varies inversely with square of window to focus distance
Safety factor on any pressure or thermal stress failure mode	$> 4$	Allowance for statistical nature of brittle material strength
Safety factor on substrate and coating service temperature limits	$> 1$	Margin required material dependent
Power loss from surface reflection (goal)	$< 4\%$ per Surface	Implies AR coatings, consequent higher surface absorption and lower temperature limits
RMS OPD introduced by thermal boundary layers in Xe, He, and/or H <sub>2</sub> Coolants	$\lambda/6.2$ ( $\Delta BQ=2$ )	Upper bound
Intrinsic and stress induced birefringence introduced into SBS return beam	TBD	Will depend on polarization budget, power loss trades and isolation performance

A material window cell design is shown in Figure 2.10-9. It features an extended length cell which will move the material window sufficiently far from focus to permit thermomechanical survival of the window and supply manifolds which will provide both faces with cooling. The study focused on thermal and structural survival of the window, rather than optical performance issues.

#### 2.10.5.1 Window Survivability Analysis

The survival of IR transmissive windows under high incident fluxes and pressure difference depend on several properties. These properties were assembled from various sources for the leading candidate materials. Often values from two or more sources conflicted or the absorption was not available at HF wavelengths. Table 2.10-2 summarizes the material properties we chose to use for analysis. Particularly for AR coatings, fluoride glasses, and synthetic diamond, the absorption obtainable in the

Table 2.10-2. Candidate Solid Window Materials

MATERIAL	ABSORPTION		SERVICE TEMP LIMIT (K)	RUPTURE MODULUS (LB/IN <sup>2</sup> )	THERMAL CONDUCTIVITY (W/CM-OK)	ELASTIC MODULUS (E6 LB/IN <sup>2</sup> )	THERMAL EXPANSION (E-6/K)	MERIT FUNCTION $E \propto \beta_V$ ** E6 (1-V)K F <sub>R</sub>
	PRESENT	FUTURE						
AR COATING	IE-3/SURF.	IE-4/SURF.	400	—	—	—	—	—
ZBLAN FLUORIDE GLASS	IE-4/CM*	IE-5/CM*	423	9000 ?	0.04	8.0	17.0	49
ZBT GLASS	2.5E-3CM*	IE-5/CM*	573	9000	0.04 ?	2.4	14.0	329
ZnSe	7E-4/CM	—	1793 (M.P.)	6000	0.19	10.0	7.2	61
ZnS	IE-3/CM	—	1293	8700	0.17	10.8	7.3	74
CaF <sub>2</sub>	8E-4/CM	—	873	3000	0.08	17.5	21.3	1726
AL <sub>2</sub> O <sub>3</sub>	2E-4/CM	—	2313 (M.P.)	65,000	0.27	59.5	5.6	5
C(DIAMOND)	1.5EO/CM	1E-4/CM	3773	386,000	20	142.2	0.4	0.001

\* VALUES SHOWN NOT AT 2.8 MICRON

\*\* LOW VALUE INDICATES LOW THERMAL STRESS IN WINDOW

future may be much lower than at present. Both the present and expected future values are shown. A merit function expressing the suitability of the candidate for enduring thermal stress under high beam intensities was tabulated as shown. A lower value indicates ability to survive higher intensities. We conclude that diamond (if available in needed sizes),  $\text{Al}_2\text{O}_3$ , ZnSe, ZnS and some fluoride glass like ZBLAN are the best candidate materials. The hexagonal crystal structure of  $\text{Al}_2\text{O}_3$  will exhibit some intrinsic birefringence in the noncollimated beams passing through an SBS cell window; otherwise, it is a clear second choice after diamond. The fluoride glass material system permits a certain amount of variation in composition to tailor the product to a specific application. ZBLAN has shown a low merit function value but has a very limited service temperature. Comparable merit function values are obtained with zinc selenide and sulfide.

In the evaluation of alternative window materials and geometries for high power applications, one needs a simplified closed form method of calculating approximate temperature and stress levels and comparing these levels to allowable values. It is generally agreed that finite element stress and thermal models, Weibull fracture analysis and actual beam intensity predictions should be applied to the detailed design of window hardware, but these methods are usually very unwieldy for feasibility studies and preliminary sizing.

The one-dimensional method of Reference 16 was reviewed and compared to our calculations on a point design. Use of the one-dimensional temperature solution for a uniform intensity, "top hat" beam proved fully valid for the very low thermal conductivities of most of the window materials.

In the area of thermal stress prediction, however, the one-dimensional solution of Reference 16 requires some modification. The solution used, Equation (3) of Reference 16 is

$$\sigma_T(z) = \frac{\alpha E}{1-\nu} \left[ -T(z) + \frac{1}{L} \int_{-L/2}^{L/2} T(z) dz + \frac{12z}{L^3} \int_{-L/2}^{L/2} T(z) z dz \right]$$

where:

$E$  = elastic modulus (lbf/in<sup>2</sup> or NT/cm<sup>2</sup>)

$L$  = window pane thickness (cm)

$T$  = temperature (K)

$z$  = coordinate from midplane parallel to surface normal (cm)

$\alpha$  = thermal expansion coefficient (1/K)

$\sigma_T$  = thermal stress, positive when tensile (lbf/in<sup>2</sup> or NT/cm<sup>2</sup>)

$\nu$  = Poisson's ratio

This equation states that the thermal stress depends on three terms inside the square brackets. The first term from the left represents the compression a window element would experience if totally restrained by its surroundings. The second term represents the relaxation to zero average stress if the plate is allowed to expand freely. The third term represents the relaxation to zero net bending moment if the plate is allowed to bend freely and is zero for the symmetrical temperature profile under consideration.

Our modification to the above model is that the solution assumes that the irradiated portion of the window is able to expand without restraint, generating high tensile stresses at the surfaces. This implies that the beam fills the window all the way out to the edge; for example, there is no annular unheated edge region restraining the growth of the central irradiated region. In the APACHE application, this condition would be very difficult to achieve because a beam alignment tolerance is needed to avoid irradiating the window frame. The beam is composed of beamlets having a range of random segment tilts; a structural support and sealing annulus is needed to react the 40 atmosphere pressure load. If a thin, coolant temperature annulus surrounding the circular irradiated region of the window is analyzed, it is found that a high tension exists in this ring at the edge of the beam. This tensile stress exceeds the peak tensile stress calculated at the center of the heated area by the method of Reference 16 for all cases examined. As the tensile safety factors for most materials were below 4.0 in that analysis, they are expected to be still lower.



A solution to the foregoing problem is to shrink fit a metal ring around the edge of the window, prestressing it into compression. Table 2.10-3 shows the results of a series of calculations at a 1.5-MW cell input power level applying various amounts of radial preload to windows of the best performing materials from the study of Reference 16. To enable direct comparisons the same material properties and optimum thicknesses were used as used in the Reference 16 study; however, we have differing values for some properties and somewhat different thicknesses may be optimum if preload effects are included.

The first case in Table 2.10-3 assumes a 12.5-cm diameter limit on an  $\text{Al}_2\text{O}_3$  window. As shown the window has an edge safety factor less than 1.0 without radial preload. Relatively large preload stresses are required to raise the tensile safety factor first to the goal of 4.0, then to infinity (zero tension). While the stresses are acceptable, the surface temperature rise would require an AR coating that withstands 611 K, if ambient temperature coolants are used.

Table 2.10-3. Effect of Radial Preload on Window Survivability at 1.5 MW Cell Input Power

Material	Diameter (cm)	Thickness (cm)	Applied Radial Compression (psi)	Tensile Safety Factor at Center	Tensile Safety Factor at Edge	Peak Compressive Stress at Center (psi)	Surface Temperature Rise* (°C)
$\text{Al}_2\text{O}_3$	12.5	1.50	0	2.56	0.46	-12660	311
			-123958	$\infty$	4.00	-136618	
			-140208	$\infty$	$\infty$	-152868	
$\text{Al}_2\text{O}_3$	20.0	2.40	0	2.56	0.85	-12660	160
			-60553	$\infty$	4.00	-73213	
			-76803	$\infty$	$\infty$	-89463	
ZnS	20.0	3.57	0	1.29	0.93	-5818	169
			-12453	$\infty$	4.00	-18271	
			-16203	$\infty$	$\infty$	-22021	
ZnSe	20.0	4.092	0	0.90	0.62	-4407	139
			-10800	$\infty$	4.0	-15207	
			-12800	$\infty$	$\infty$	-17207	

\*At a heat transfer coefficient of  $0.15 \text{ W/cm}^2 - \text{K}$  (Mach 0.2 xenon)

Reference 17 offers sapphire windows up to 20 cm in diameter. The second main case in the table explores the performance of such windows. As shown, lower compressive preloads are required, and the lower incident flux heats the AR coating to only 460 K. These preloads are well within the capability of a 15-5 PH stainless-steel preload ring, which will begin to yield above 147,000 psi.

The sapphire window designs might be considered risky due to the intrinsic birefringence of sapphire. To alleviate this problem, we are considering providing a collimated beam as an input to the SBS cell, with beam focusing being provided by figuring the window as a plano convex lens and orienting the "c" crystallographic direction to that of the input beam to mitigate this issue. By placing the plano portion of the window on the outside of the cell, the beam passing through the window will be collimated and the effects of birefringent in the window minimized.

If birefringent  $\text{Al}_2\text{O}_3$  is still an issue, other materials are still usable. The third case in the table shows characteristics of a ZnS window. This material is available up to 90 cm in diameter. A comparison with  $\text{Al}_2\text{O}_3$  at 20-cm diameter shows that somewhat higher surface temperatures are produced, and lower preloads are required.

The compressive strengths of candidate window materials are presently unknown to us, although it is anticipated that they will exceed tensile failure stresses involving crack propagation by large factors. There is indirect evidence that some yielding of  $\text{Al}_2\text{O}_3$  begins to occur at stresses over 200,000 psi at 900°C. This area will receive further study during the APEX program.

#### 2.10.5.2 Thermal Constraints

Our initial analysis concentrated on defining the limits on window surface and interior temperatures and the corresponding limits on incident heat flux that occur with realistic cooling methods. Several issues may limit the allowed temperature of a material window; for example,

- Service temperature limit of the window material due to phase changes, etc.
- Failure of AR coating
- Thermal stresses, although these are functions of temperature differences only

- Unacceptable aberration levels from thickness and index changes in the window material
- Unacceptable aberration levels from coolant thermal boundary layers (both high and low spatial frequency issues).

Only the first three items involve actual survival of the window, but all must be considered in selecting a design point. Figure 2.10-15 shows the absorbed heat flux limits corresponding to several types of window surface temperature limits. The effect of cooling one face of the window rather than both faces is also indicated. Clearly one would prefer to cool only the window face on the inside of the cell because some helium (or perhaps hydrogen) will be lost to vacuum in cooling the opposite face. The search for window designs with adequate structural margins has been sufficiently difficult even with both faces cooled that little attention was given to the single cooled face case.

The horizontal line marked "turbulent" OPD limit in Figure 2.10-15 is the result of an analysis of OPD aberrations introduced by window coolant thermal boundary layers. It was found that  $\lambda/6.2$  is budgeted for aberrations from this source, this limit is reached at a temperature difference of 54°C between window surface and freestream Xe coolant. It is also found, however, that the spatial distribution of this OPD is well approximated by a tilt in the direction of boundary layer development. It is expected that this tilt will be phase conjugated. The OPD remaining after tilt subtraction would permit operating with the window face  $> 1000^\circ\text{C}$  above freestream Xe temperature, at least at low spatial frequencies. There remains an issue as to whether the beam quality degradation due to high spatial frequency turbulent density fluctuations might be a problem. This issue will be addressed on the APEX program.

The feasible magnitude of window coolant heat transfer coefficients was also investigated. The high-power window cooling investigation of Reference 18 demonstrated laser window cooling by stagnating a cooling gas on the window. Heat transfer coefficients obtainable for a laminar stagnation on a flat plate were compared to those from a turbulent boundary layer flowing along the window face, as shown in Figure 2.10-16. For conditions typical of an SBS window design, for example, window diameters

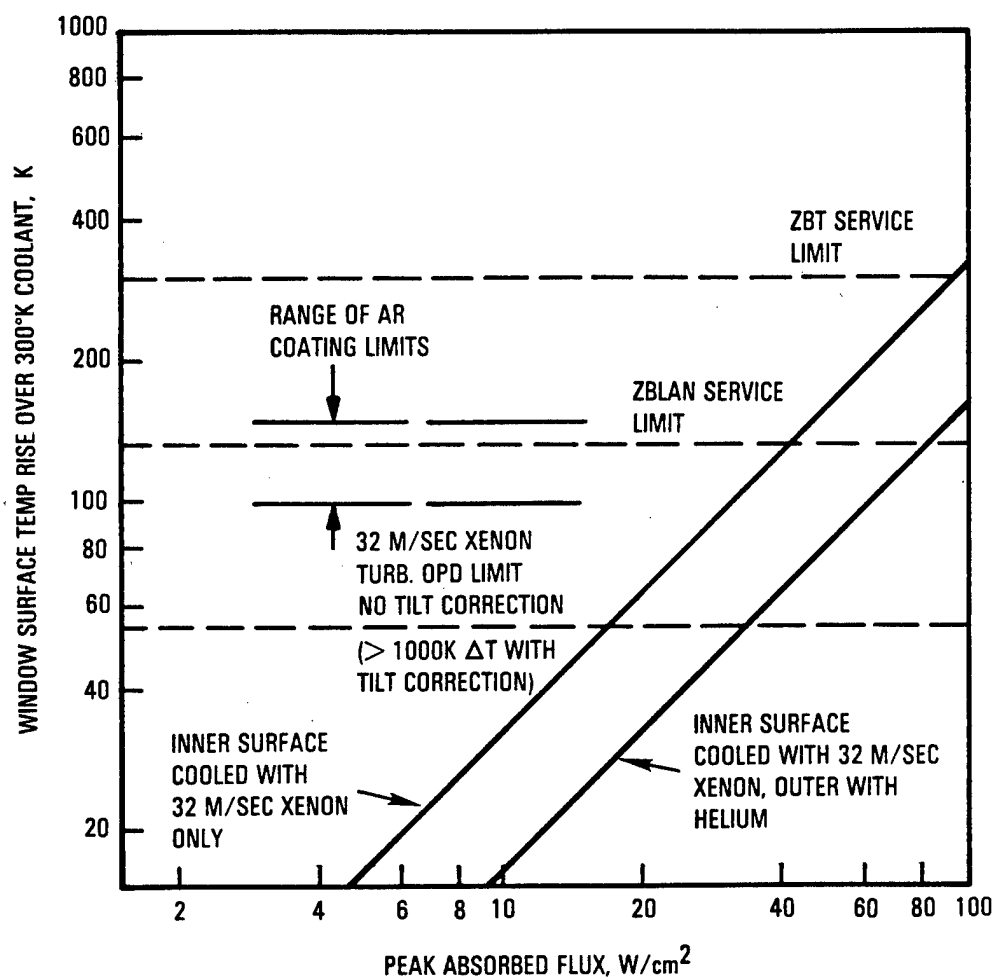


Figure 2.10-15. Three Types of Window Surface Temperature Limits

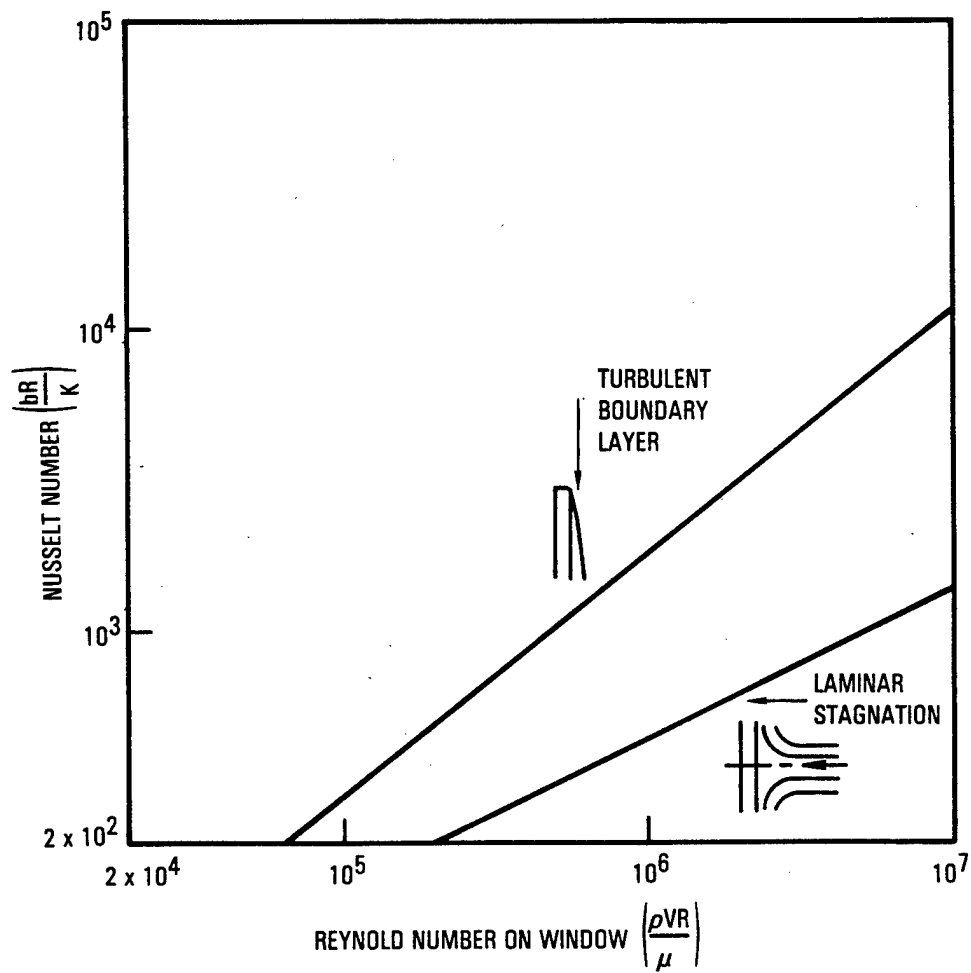


Figure 2.10-16. Comparison of Window Coolant Flow Geometries

in the 10's of centimeters and Xe Mach numbers  $\leq 0.2$  (velocities  $\leq 32$  m/s), the turbulent boundary layer approach gives superior window cooling. A low Mach number within the Xe cell is desirable to minimize density, hence index, inhomogeneities. At a xenon velocity of 32 m/s a heat transfer coefficient in the neighborhood of  $0.15 \text{ W/cm}^2\text{-K}$  is predicted.

#### 2.10.6 References

##### References

1. Guile, R. N., and Hilding, W. E., "Investigation of a Free-Vortex Aerodynamic Window," AIAA Paper 75-122, presented at the AIAA Thirteenth Aerospace Sciences Meeting, January 20-22, 1975.
2. Liepmann, H. W., and Roshko, A., Elements of Gasdynamics, John Wiley and Sons, Inc., New York, 1957.
3. Giles, R. B., Fluid Mechanics and Hydraulics, Second Ed., Schaum's Outline Series in Engineering, McGraw-Hill Book Co., New York 1962.
4. Van Drist, E. R., "Turbulent Boundary Layer in Compressible Fluids," J.6 of Aero Sci., Vol. 18, No. 3, March 1951.
5. Schlichting, H., Boundary Layer Theory, Sixth Ed., McGraw-Hill Book Co., New York, 1968.
6. Behrens, H. W. and Sugimura, T., "Pressure Recovery Analysis", presented at Tri-Service Chemical Laser Symposium, Kirtland Air Force Base, New Mexico, February 19-21, 1975.
7. Shapiro, A. H., The Dynamics and Thermodynamics of Compressible Fluid Flow, Vol. I. The Ronald Press Co., New York, 1953.
8. Kunkle, J. S., Wilson, S. D., and Cota, R. A., eds, Compressed Gas Handbook, NASA SP-3045, 1969.
9. Foelsch, K., "The Analytical Design of an Axial by Symmetric Laval Nozzle for a Parallel and Uniform Jet," J. of Aero Sci, Vol. 16, No. 3 March 1949.
10. Ikawa, H., Turbulent Mixing Layer Experiment in Supersonic Flow, Ph.D. Thesis, California Institute of Technology, Pasadena, CA, 1973.
11. Reid, R. C., Prausnitz, J. M., and Poling, B. E., The Properties of Gases and Liquids, Fourth Ed., McGraw-Hill Book Co., New York, 1987.
12. Reeve, J., Private Communication, June 1989.

13. Behrens, H. W., and Witte, R. S., Aerodynamic and Beam Quality Performance of Aerodynamic Window, TRW Technical Letter Report 25384-6001-TU-00. February 1974.
14. Ribner, H.S., "The Generation of Sound by Turbulent Jets," Advances in Applied Mechanics, Volume 8, Academic Press, New York, 1964.
15. Eckerle, W. A., Taylor, K. D., Guile, R. N., and Palma, G. E., Qualification Testing of an Aerodynamic Window for the 2454 Laser Program (unapproved draft), United Technology Research Center, January 1980.
16. Lieto, C. J., "Analytical Evaluation of Material Window Feasibility for APACHE SBS Cell, APX-2124, W. J. Schafer Associates, October 23, 1989.
17. Crystal Systems brochure on HEM Sapphire, p. 1.
18. G. Holderbaum and R. Phillips, "Spherical Vacuum Interface Window with Axial Flow Impingement Cooling," MIT Lincoln Laboratory (under submission to SPIE).
19. Clendening, C., "Segmented Mirror Effects on Beam Size," TRW IOC AP-1624, August 1988.

## 2.11 MASTER OSCILLATOR ISOLATION COMPONENTS

### 2.11.1 Functional Overview and Isolation Component Design

A fundamental aspect of phase conjugation is that it returns light to its point of origin. Unless precautions are taken to prevent this return, however, there will be substantial feedback into the master oscillator (MO). Although shifted in frequency by the SBS cell, this feedback could still interfere with the lasing action to the point of output power degradation, as stated in Section 2. In order to reduce this feedback, two grating rhombs have been installed in the optical train between the beam director (BD) and the amplifier(s). In conjunction with these rhombs, quarter wave mirrors have been placed in the optical train between the amplifier(s) and the SBS cell. Figure 2.11-1 shows the position of these elements in the system. The quarter wave mirrors turn the linearly polarized light into circularly polarized light prior to its entrance into the SBS cell. Since SBS phase conjugation does not conjugate the polarization of the incoming beam, the backward pass through the quarter wave plates rotates the beam polarization. What was P-state polarization upon hitting the quarter wave plate on the forward pass is converted to S-state polarization on the backward pass. The grating rhombs are designed such that on the backward pass most of the zeroth order S-state polarized light is directed to the target. The remaining depolarized light is first order P- and S-state (the latter from leakage through the rhombs) and will return along the beacon path to the MO. To further reduce the feedback, an attenuator with a throughput of 0.25 has been incorporated into the external cavity of the MO.

The requirements for the isolation components were based on the polarization budget, which is presented here, beginning with the MO.

The output power of the MO (98% P-state polarization in first order) is somewhat oversized to ameliorate the effects of detrimental feedback. Oscillator power is lost at the attenuator, as well as at the beacon where only 0.75 of the central Airy disk gets through. The power to the amplifier train is further diminished by overfilling the primary mirror so that it functions as a spatial filter. The primary is assumed to contribute a 5-degree phase retardation to the system due to the complex angles of



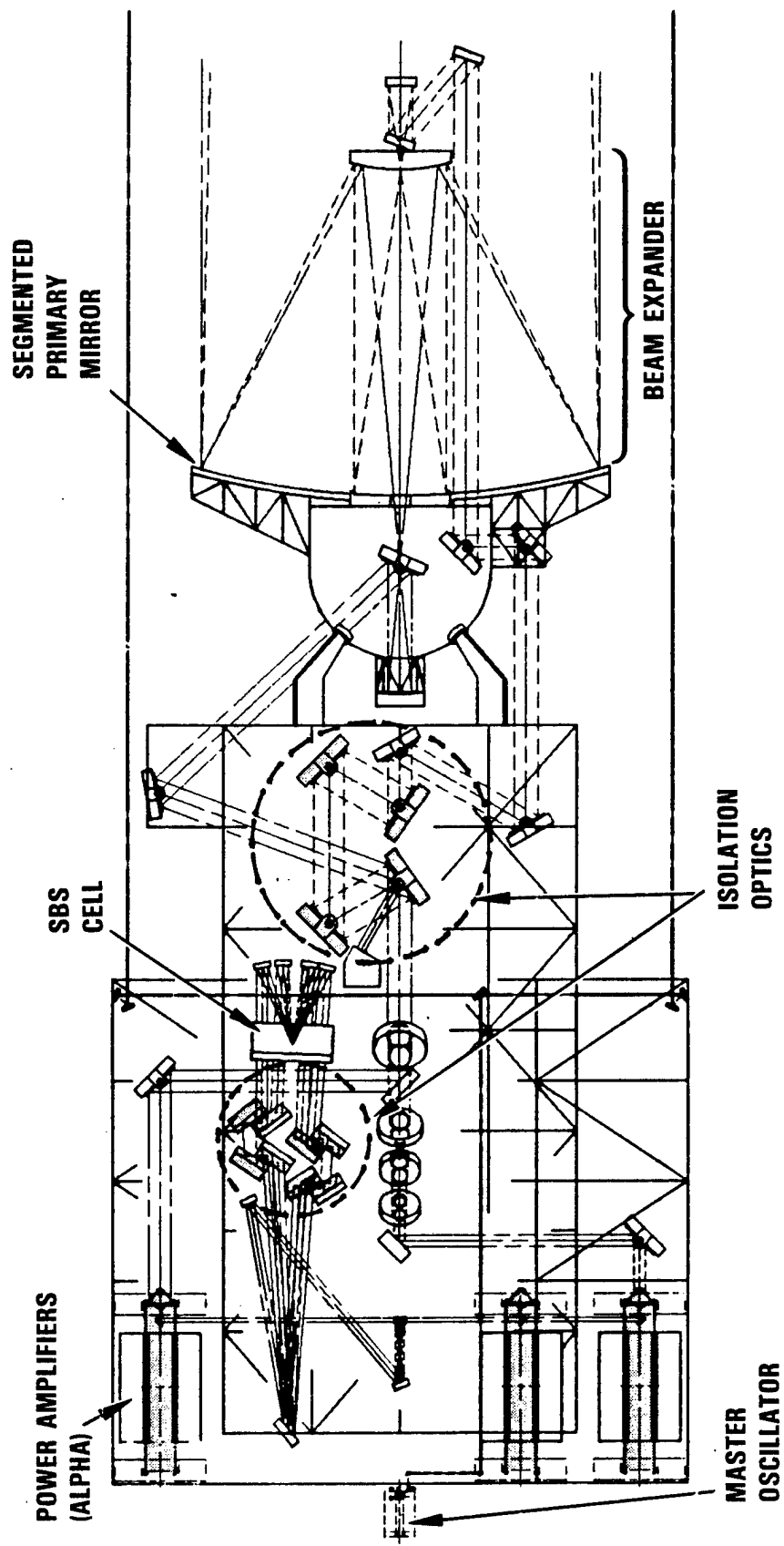


Figure 2.11-1. Schematic of the System Design. Isolation components are highlighted. The birefringent wedge is not shown

irradiation. Most of this depolarized power fails to pass the grating rhombs, which are designed to pass P-state (first order), and shunt the undesirable S-state (zeroth order). The gratings, however, will also induce some phase retardation in the beam. The amount of depolarization from the grating rhombs must therefore be kept small relative to that induced by the quarter wave mirrors and amplifier. If the depolarization should exceed this limit, a backup concept employing a birefringent wedge could be considered (see Section 2.11-3).

Another depolarization contributor is the birefringent annular amplifier optics. Results of a study conducted by OCLI indicate that the retardance induced by these annular optics is very close to zero. The system limit has been set at 0.38 degrees. The discussion of the optical coatings for these elements is found in Section 2.11.2.

The final contributor to the net phase retardation is the quarter wave mirrors. Each quarter wave plate consists of four mirrors, each with 22.5 degrees retardance, thus summing to 90 degrees total phase retardance. There are two sets to handle the two wavelength pairs of the HF spectrum. These turn the linearly polarized incoming light into circularly polarized light which is then focused into the SBS cell. The window to the SBS cell may contribute some additional phase retardance to the beam, but lacking any definition on the magnitude of this contribution, it is assumed to be small.

On the backward pass the quarter wave mirrors convert the initial P-state polarization from the oscillator into S-state. Once this is amplified on its second pass through the amplifier, most of it will be zeroth order S-state polarization which is directed off the grating rhombs into the BD and out the target path. The original S-state which passes through the grating rhombs on the forward pass, as well as that produced in the amplifiers, quarter wave plates, etc., will be turned into P-state and go directly back along the beacon path to the MO. Any first order S-state polarization will also travel along the beacon path. (This might arise from some of the P-state depolarized light on the second pass through the amplifier being further depolarized into S-state.)

Supplemented by the APACHE System Analysis Model (ASAM), a polarization study was conducted for the high-brightness SBL concept. As discussed in Section 2.3, the SBL system requirement to be satisfied is that the brightness of the target beam be reduced by less than 1% as a result of feedback to the M0.

The total system brightness sensitivity to oscillator power is shown in Figure 2.11-2. These calculations reveal that over a wide range of oscillator powers the system brightness is very insensitive to the oscillator performance (note the expanded scale). This is due to the self-healing nature of the oscillator-amplifier-SBS cell combination. A decrease in oscillator power reduces the power in the forward amplifier pass, leading to increased amplification in the return beam. The sensitivity at very low oscillator output is a result of the power at the SBS cell dropping below threshold. From these calculations, one finds that a 1% decrease in system brightness due to imperfect isolation corresponds to about a 50% drop in oscillator power, over a wide range of normalized powers encompassing the eventual design value calculated from ASAM. This sets the requirement for the allowable degradation in oscillator performance due to feedback. However, to provide margin it will be shown that the components in the SBL design provide substantially more isolation of the M0 than is required.

To assess what amount of feedback would cause the oscillator power to drop by 50%, use was made of two isolation analyses. An analysis of the ALPHA HEXDARR resonator is presented in Section 6 of Volume 1. This model, which was validated by direct comparison with results of isolation experiments, shows how the ALPHA performance would be affected by feedback. This analysis has been supplemented by recent work conducted by Science Applications Incorporated (private communication, 1989). Both these analyses assume that the frequency shifted modes returned to the M0 do not overlap those of the output beam. The results of both of these analyses are presented in Figure 2.11-3. A comparison between the two models shows good agreement, giving confidence to the results. Using these calculations, one finds that a 50% decrease in oscillator power due to feedback, corresponds to a feedback fraction of approximately  $10^{-2}$ . Thus, the

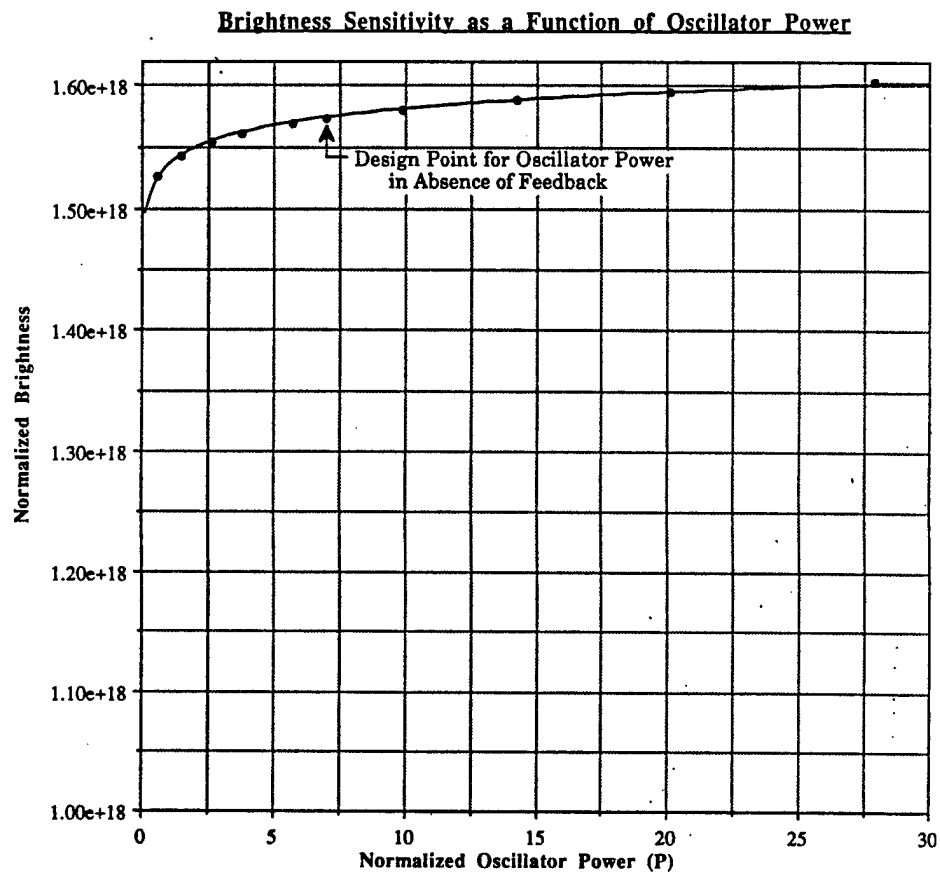


Figure 2.11-2. Brightness Sensitivity as a Function of Oscillator Power

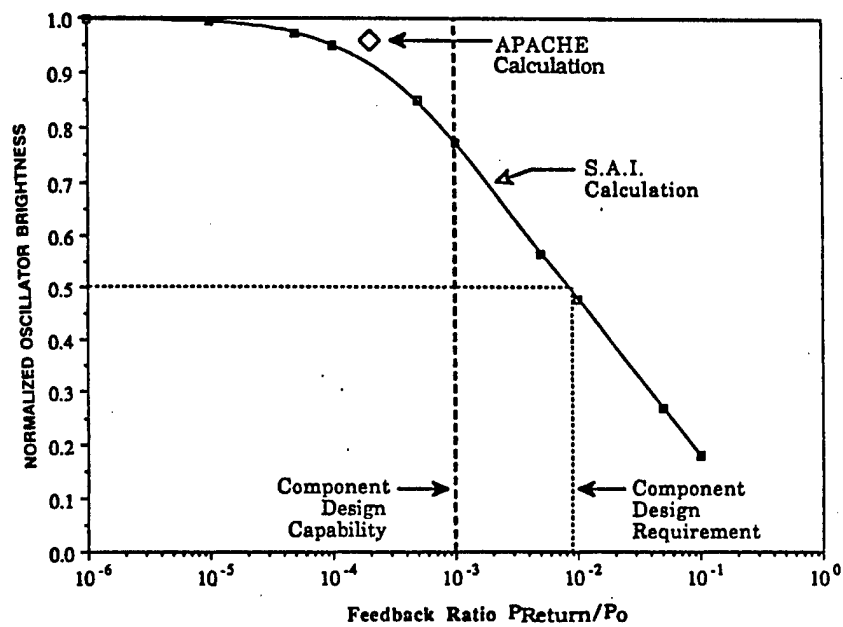


Figure 2.11-3. Isolation Analysis of ALPHA HEXDARR Resonator

requirement for the isolation components is that no more than 1% of the oscillator output be returned to the MO. The capability of the components in the design provide much more isolation than what is required. As will be shown, the current SBL design concept has a capability to isolate the MO to a level of  $10^{-3}$ .

The actual value of the return power is determined by the performance of the isolation components, specifically, the retardation error in the quarter wave optics, the grating extinction ratio and the amplifier optics retardation error (departure from zero retardance). The dependence of  $P_{\text{ret}}/P_0$  on these quantities is illustrated in Figure 2.10-4, which shows the sensitivity of the normalized oscillator return power as a function of the accuracy of the quarter wave plate. These results are calculated for a representative grating extinctions, obtained by modeling from the French Grating Codes (see Reference 1). The feedback fraction is quite sensitive to retardation errors, with a factor of five variation in power returned to the oscillator observed as a perfect retarder is degraded by 1 degree. However, the isolation performance is very insensitive to the extinction ratio of the grating. The effects of amplifier depolarization, shown in Figure 2.11-5 and seem to be similar to those for the QW optics.

In practice, the actual design value of  $P_{\text{ret}}/P_0$  is determined by the best achievable performance of the isolation optics, which turns out, in the present case, to provide plenty of extra margin in systems performance as well. The OCLI study presented in the next subsection and TRW calculations of grating extraction, yields the best achievable design values indicated by circles in Figures 2.11-4 and 2.11-5. These values in turn correspond to  $P_{\text{ret}}/P_0 \sim 10^{-3}$ , well within the systems-dictated requirement of  $P_{\text{ret}}/P_0 < 10^{-2}$ . The design values and certain of the assumptions used in the calculations are listed in Table 2.11-1.

The following sections describe the component design concepts to be used for the grating rhombs, quarter wave retardation mirrors, low birefringent annular optics and turning flats. a preliminary analysis of birefringent wedges is presented in Section 2.11-3. The wedge has not been included in the baseline conceptual design, since systems requirements can be satisfied using isolation components with the design parameters stated above.

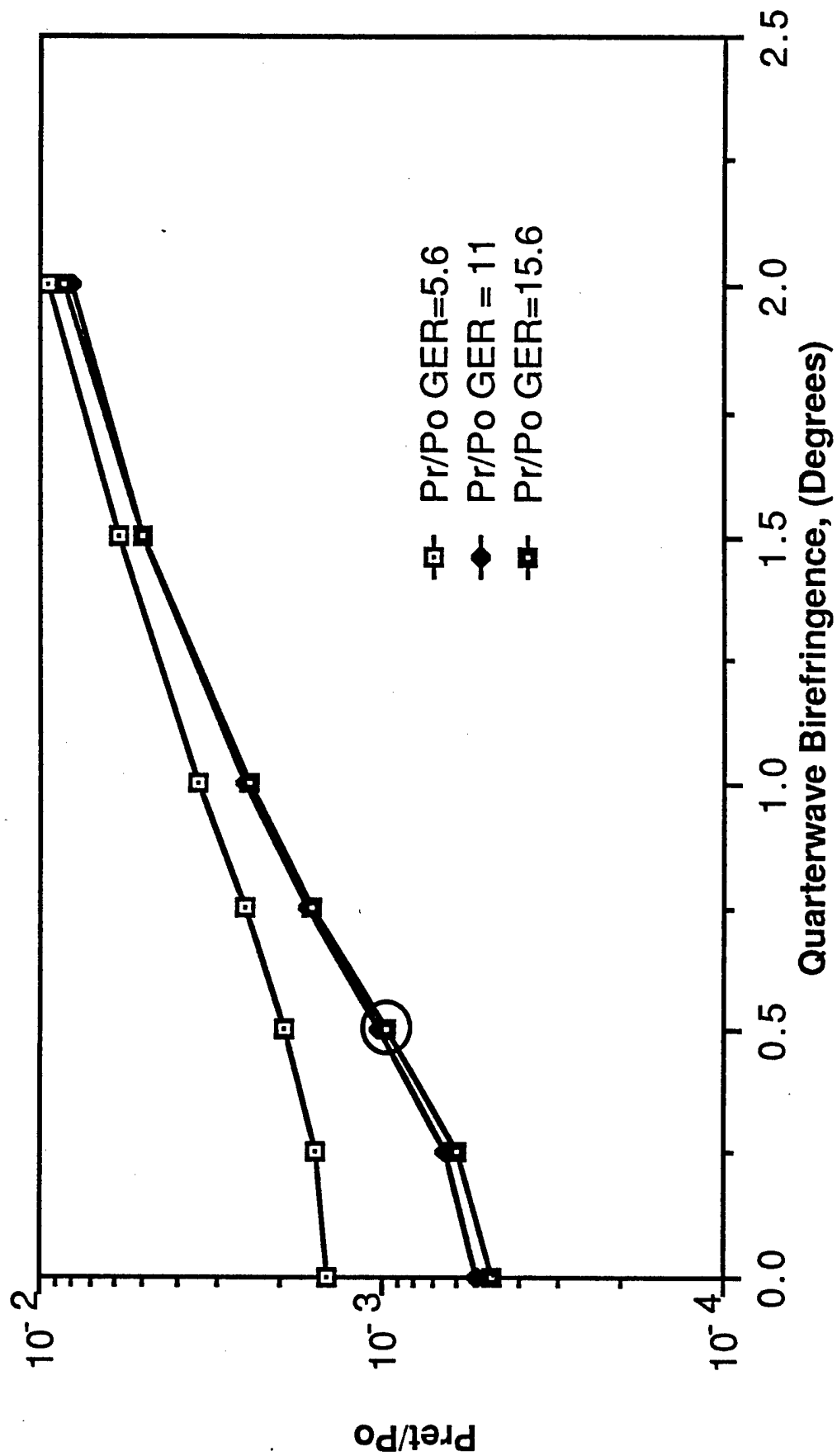


Figure 2.11-4. SBL Master Oscillator. Isolation as a function of errors in quarter wave retardance and grating extinction ratio (GER)

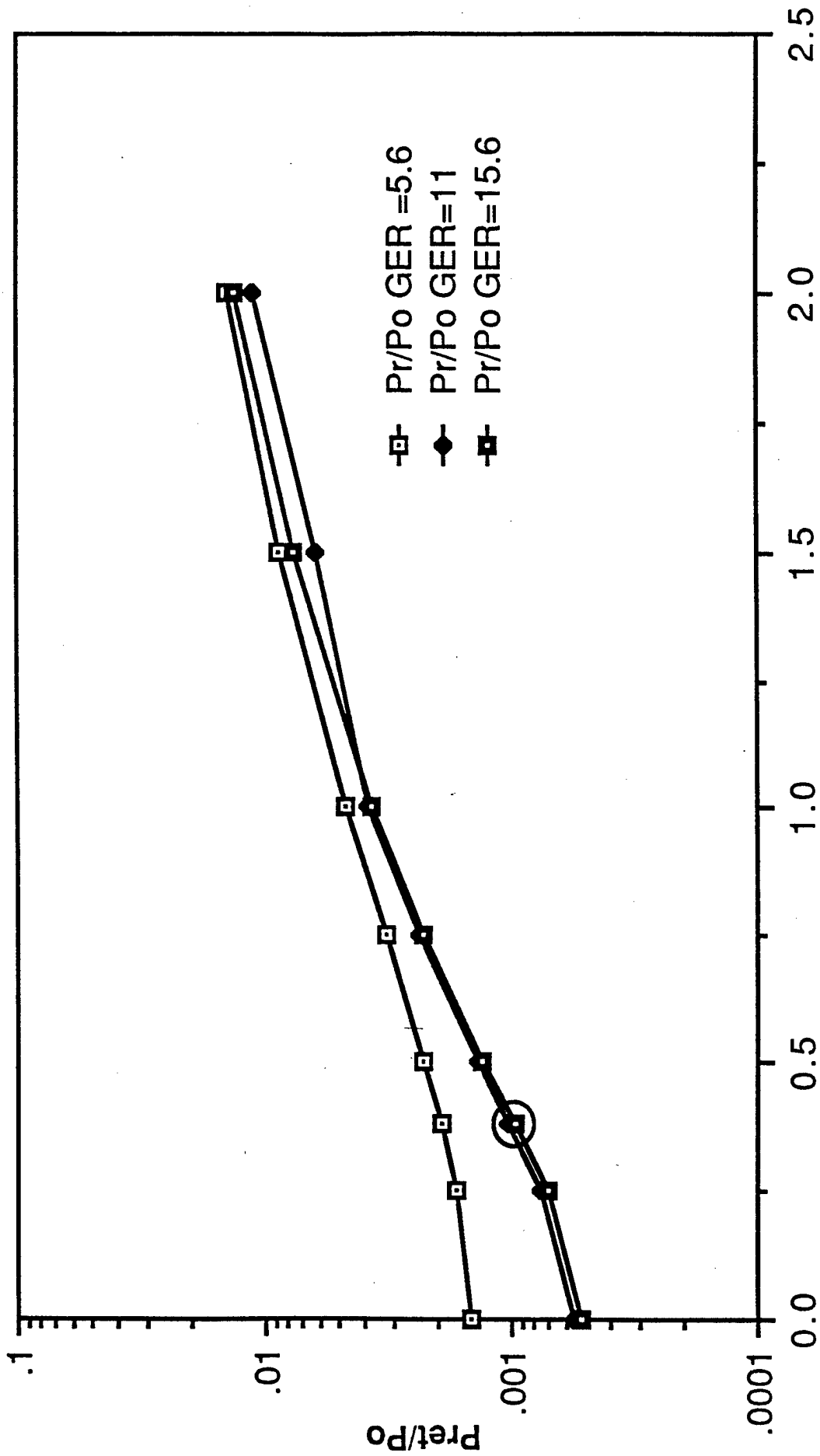


Figure 2.11-5. SBL Master Oscillator Isolation as a Function of Amplifier Birefringence and Grating Extinction Ratio (GER)



Table 2.11-1. Design Values for Isolation Components

Oscillator Output Polarization:	P-state: 98%
	S-state: 2%
Oscillator attenuation:	25%
Spatial Filter Power Loss:	0.4325
Beam director birefringence:	5 degrees
Grating efficiency — first order:	P-state 93.7%
	S-state: 8.4%
Grating extinction:	11:1
Amplifier birefringence:	0.38 degrees
Quarterwave plate accuracy:	0.5 degrees

#### Grating Rhombs

Calculations were performed using the French Grating Codes for the following specifications of sinusoidal-type gratings:

- Grating frequency: 600 lines/mm
- Groove depth: 0.55  $\mu\text{m}$
- Wavelength: 2.8  $\mu\text{m}$
- Incident angle: 60 degrees

The results yielded the following efficiencies:

- Zeroth order: P: 2.6%  
S: 90.0%
- First order: P: 93.7%  
S: 8.4%

From these results one sees that the first order extinction ratio is 11.1 per grating. Since there are four gratings, the extinction ratio goes as the fourth power. The reciprocal is used for calculations in ASAM, which gives a throughput factor of  $6.5 \times 10^{-5}$ . All of these grating specifications are considered to be within the state of the art in fabrication

techniques, an assertion to be experimentally verified as part of the APEX program. As previously noted, however, the system brightness sensitivity to variations in the grating extinction ratio is extremely low. Further information on the French Grating Codes, as well as the optimal requirements set on grating manufacture, are presented in Reference 1.

In the sections that follow, the results of an OCLI coating subcontract are reported, as well as the study on using a birefringent wedge to provide an additional MO isolation insurance option.

#### 2.11.2 Coatings for Quarterwave Mirrors and Birefringent

##### 2.11.2.1 Introduction

As discussed in the previous section, the MO must be isolated from detrimental feedback. If the optical train components were ideal, the grating rhombs would meet this requirement. However, the quarter wave mirrors and annular amplifier optics induce some depolarization in the beam. In an attempt to determine exactly how far from ideal these coatings are, OCLI performed a theoretical study of candidate coating designs for use in the APACHE optical system. Objectives of this study were to evaluate state-of-the-art, high-reflectance phase controlled thin film optical coatings as well as to investigate appropriate prototype techniques which might be applicable in the near term (2 to 5 years).

##### 2.11.2.2 Requirements

Listed below, in order of importance, are the three types of HF spectrum isolation component coatings that were studied:

1. Quarter wave mirrors: one or more mirrors working in series which convert linearly polarized light to circularly polarized light
2. Low birefringence annular optics: amplifier optics which provide zero net phase retardance after one complete pass through the entire amplifier cavity
3. Low birefringence flat: one or more mirrors working in series which have zero phase retardance over the entire HF spectrum.

The wavelength range could be treated as a whole, or discrete wavelengths could be split off and treated individually or as subgroups. Coating requirements are shown in Table 2.11-2.

Table 2.11-2. Coating Requirements

Parameter	Component Type		
	Quarterwave Mirrors	Low Brief Annular Optics	Low Brief Flats
Wavelengths	2.74, 2.78 2.87, and 2.91 $\mu\text{m}$		
Retardance (all wavelengths) (degrees)	90	0	0
Retardance uniformity (rms) (degrees)	0.5	0.5	0.5
Reflected wavefront distortion	1/20 (waves at 0.633 $\mu\text{m}$ )	1/20	1/20
Reflectance (all wavelengths)	>0.995	>0.995	>0.995
Damage fluence	>1 (J/cm <sup>2</sup> , 1 $\mu\text{m}$ pulse)	>1	>1
Damage integrity	>5 (kW/cm <sup>2</sup> 5 s)	>5	>5

A secondary requirements was that the reflectance at 0.633 or 0.647  $\mu\text{m}$  be greater than 0.80, thereby assisting with alignment of the assembled optical system.

OCLI's experience with multilayer dielectric enhanced metal films for mirror coatings provided the basis for the theoretical study. A reflector made by alternating layers of high-and low-refractive index dielectric materials over a metal undercoat will meet the high-reflectance requirements over the HF spectrum. As long as substrates can carry away small amounts of absorbed energy (i.e., cooled substrates), enhanced metal

mirrors survive high-power densities of continuous wave laser radiation. If the substrates are not cooled, then all dielectric coatings might have to be substituted.

#### 2.11.2.3 Design Considerations

While most predictions on coating deposition technology for 2 to 6 years in the future were based on existing data from both development and production coatings, some assumptions had to be made.

The wavelengths of interest (see Table 2.11-2) are at the edge of a broad absorption band for water. Enhanced reflection coatings for this application require very low absorption coating materials in their construction so as to reduce the heat absorbed by the mirror faceplate. Several investigations (Reference 2) have documented the typical absorption levels for the HF spectrum that have been obtained in thin-film materials deposited by conventional methods such as evaporation by resistance or electron beam heating. While low absorption should improve coating damage thresholds, the additional stringent phase controls might well compromise the power handling capabilities of the coatings, as phase compensating coatings frequently use a low refractive index material as the outer layer, instead of the high-index material normally used for high power.

Moisture might be present in the coatings in the form of water incorporated into the thin film during the deposition process or it may be absorbed into the coatings when they are exposed to the atmosphere. Absorption of incident laser energy by water can be reduced by choosing coating materials which are less susceptible to moisture take-up, and by using deposition methods which minimize the capture of moisture during the coating process.

Measured data shown in Figure 2.11-6 were used for preliminary selection of coating materials. Bulk absorption data have been included, where available, to illustrate the enormous differences which exist between the absorption in a thin film and its parent material. The "error bars" in this figure are not due to uncertainties in the experimental measurements but represent the range of values obtained from different thermal

deposition processes and different forms of source materials. There are some candidate materials for which no data exists; in these cases, best estimates were based on extrapolated data or similarity to other materials.

High absorption of some thin-film materials does not always preclude them from consideration in high-power applications. An example is a combination of SiO overcoating a metal layer. These two materials show the largest variation in measured absorption for both bulk and thin film form, but this combination, however, is physically durable and has survived high laser radiation levels despite the large absorption coefficients indicated in Figure 2.11-6. Many of the low-absorption materials shown, especially the fluorides, are unsuitable for enhanced reflector coatings due to their poor durability, tendency to absorb moisture, and high-film stresses.

Recent damage results have shown that some materials rarely used for HF laser applications may also be viable material candidates for this program. Specifically, several oxides exhibit good optical and mechanical properties for  $2.8\mu\text{m}$  coatings when deposited using ion assisted or ion bombardment techniques (see Table 2.11-3). These techniques consist of exposing the optical surface to directed energetic ions while the thin-film materials is being deposited. The energetic ions tend to improve the stoichiometry of the oxide, densify the resulting thin film, reduce the water content in films during deposition, increase control of coating stresses, and provide better film adhesion. One other benefit of using oxides is that such materials are known to survive a space environment.

The phase retardance requirements for this program complicate the coating design effort. Materials made available or more attractive as potential candidates through the use of ion assisted deposition processes might simplify the anticipated coating design problems. A broader selection of materials affords greater design flexibility and possible performance improvement over typical infrared materials.

Another consideration for the design of the particular coatings is the compatibility of the constituent materials with each other. Under normal deposition conditions, zinc selenide and thorium fluoride frequently fail the 24-hour humidity test. Other material combinations literally peel

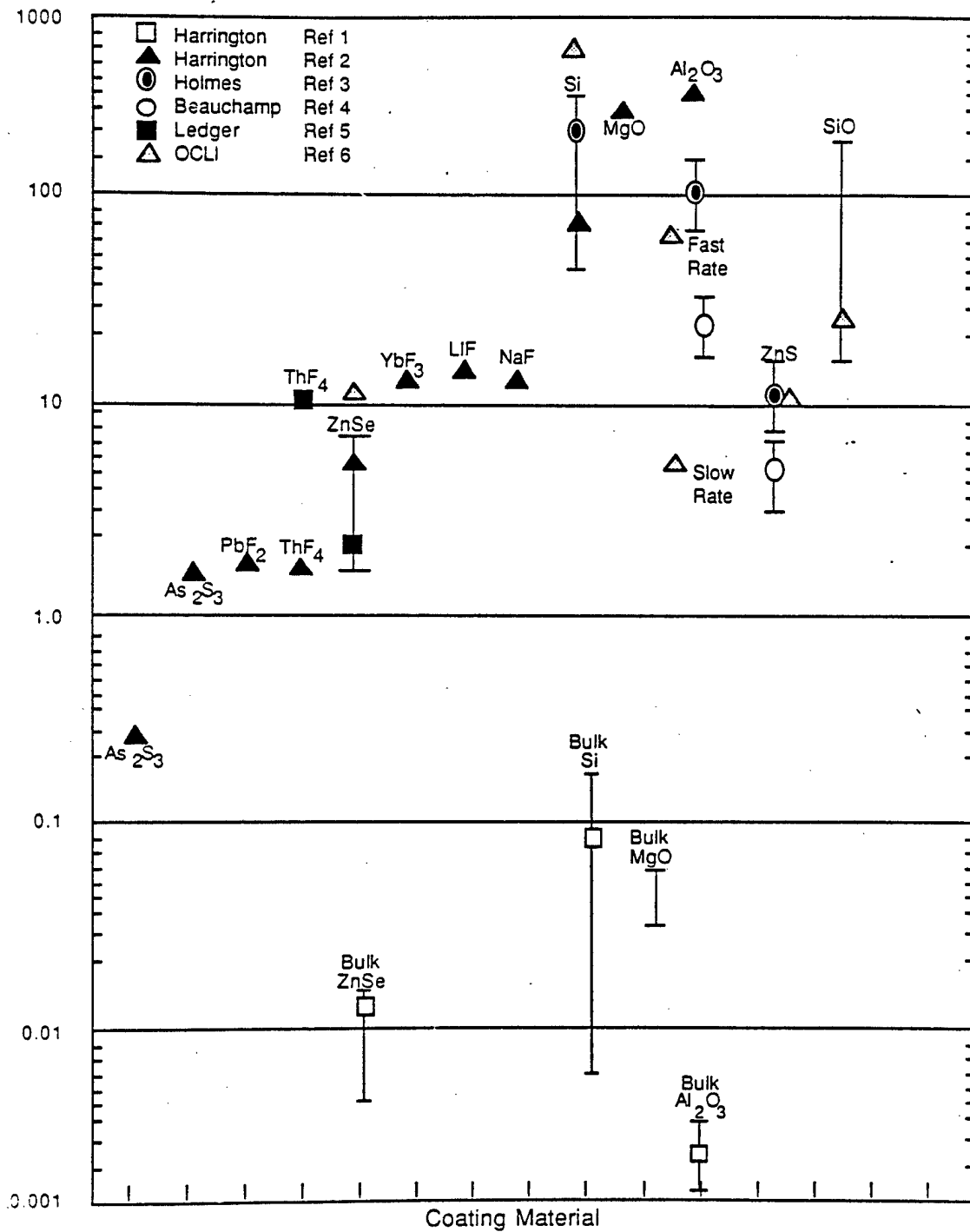


Figure 2.11-6. Bulk Material and Thin Film Absorption Coefficients at 9.2  $\mu\text{m}$  Wavelength

Table 2.11-3. Ion Assisted Deposition Test Results

IAD Materials	Stress Reduction (%)	Absorption Reduction (%)	Water Reduction	Index Change (%)
SiO <sub>2</sub>	90	30	Complete removal	+1
TiO <sub>2</sub>	70	60	Complete removal	+2
ZrO <sub>2</sub>	85	30	50	2.5

themselves off the substrate due to excessive stresses. Ion deposition processes have dramatically improved environmental and physical coating durability.

Several material combinations with relatively small index ratios were considered, but only the three that best meet the program requirements for quarter wave plates and annular birefringent optics are compared in this report for their advantages and disadvantages. Two design types for the birefringent flats are given, as well as a comparison of their advantages and disadvantages. The format used for presenting the results of this theoretical study is the same for each design, i.e., the reflectance and phase retardance for the nominal design is first, followed by the sensitivities of the reflectance and phase retardance to manufacturing variables. Two factors which enter into the manufacturability analysis are the centering of the design and the effects of random variations of layer thickness. Centering is the ability to place the thin film design at the correct wavelength. Random variations in layer thicknesses reflect the statistical nature of thin film deposition. Not all layers will be deposited at the theoretically correct thickness and it lies with the manufacturer to eliminate any systematic variations while minimizing the random variations.

In addition to manufacturing variables sensitivity, each design has been analyzed for dependence upon angle of incidence, effects of variations in absorption coefficients, and temporal variance. The latter typically

arises from absorption of moisture from the surrounding environment. If an optical system is used in a dry environment such as a vacuum, then these effects are minimal, but shifts can still occur in coatings when they are removed from the coating chamber and before they are measured in air. Process adjustments may be made by observing shifts with time of exposure, thereby optimizing performance. This analysis is similar to the centering errors mentioned above, but in this case, the wavelength shift is at least partially reversible.

The quarter wave plates are presented first as they are the first priority. These designs must provide a 90 degree phase shift upon reflection. Of secondary importance are the birefringence annular optics designs, which are to provide a 0 degree phase shift for a round trip through the annular optics systems. Finally, the coating designs for the low birefringence flats are presented. Here the phase retardance is to be kept at 0 degrees for a two mirror combination. Reflectance for all designs is to be maximized.

#### 2.11.2.4 Specific Theoretical Results

##### Quarterwave Mirrors (Recommended Design)

The reflectance and phase retardance of the Southwell design were modified for the APACHE program. For a single mirror, reflectance was too low and phase retardance was outside the 0.5-degree tolerance requirements. A smaller phase shift can be effected by several mirrors operating sequentially and this appears to be a more viable solution. For example, two mirrors could be used with each providing a 45-degree phase shift, or four mirrors could each provide a 22.5-degree phase shift summing to a total of 90-degree phase shift. The advantages include less phase retardance sensitivity to random variations in each of the layers, the mirrors can be coated in separated runs thereby allowing compensating corrections to be made on upcoming runs with necessitating rework, and mirrors can be angle tuned in pairs to optimize the phase performance of the four mirror set, without affecting the overall optical alignment. The



disadvantages are that more mirrors are required and hence the number of mirror mounts increases. It is believed that this added complexity in hardware is more than offset by the flexibility of the multiple mirror system and the decreased likelihood that mirrors will have to be reworked for noncompliance.

Three different designs are presented in order of preference. All designs use gold as the base metal layer, since it is nonreactive, thereby eliminating any concerns about chemical aging of the base metal reflector layer. The first choice combination of dielectrics for enhancing the gold reflectance is Si and SiO<sub>2</sub>. The theoretical performance curves for the nominal design show the reflectance to be a constant value of 99.6% across the four wavelengths. The phase retardance, shown in Figure 2.11-7, is constant at about 22.2 degrees. When manufacturing tolerances are included in the performance calculations, the results remain virtually unchanged.

When combined into a system of four mirrors, the resulting reflectance is the reflectance of one mirror taken to the fourth power, while the phase retardance is the algebraic sum of the four individual mirror values. Estimated phase retardance uncertainty will be the root sum squares of the standard deviations for each of the four coatings. From Figure 2.11-4 this appears to be about 0.25 degree per mirror, or  $(4 \times (0.25^\circ)^2)^{1/2} = 0.5^\circ$ . The reflectance and phase retardance performance requirements are thus met by this design.

The model shows that the reflectance variation is negligible and that phase changes almost proportionately with angle across the entire wavelength band of interest. This can be used advantageously with the four-mirror system to compensate for manufacturing variations. The effects of increased absorption are that reflectance is reduced while phase retardance remains unaffected. Thus, if moisture should enter the thin-film coating and increase absorption, the coatings will continue to function as designed with respect to phase. Moisture in the thin film would cause a wavelength shift, and this is addressed in the error budget analysis.

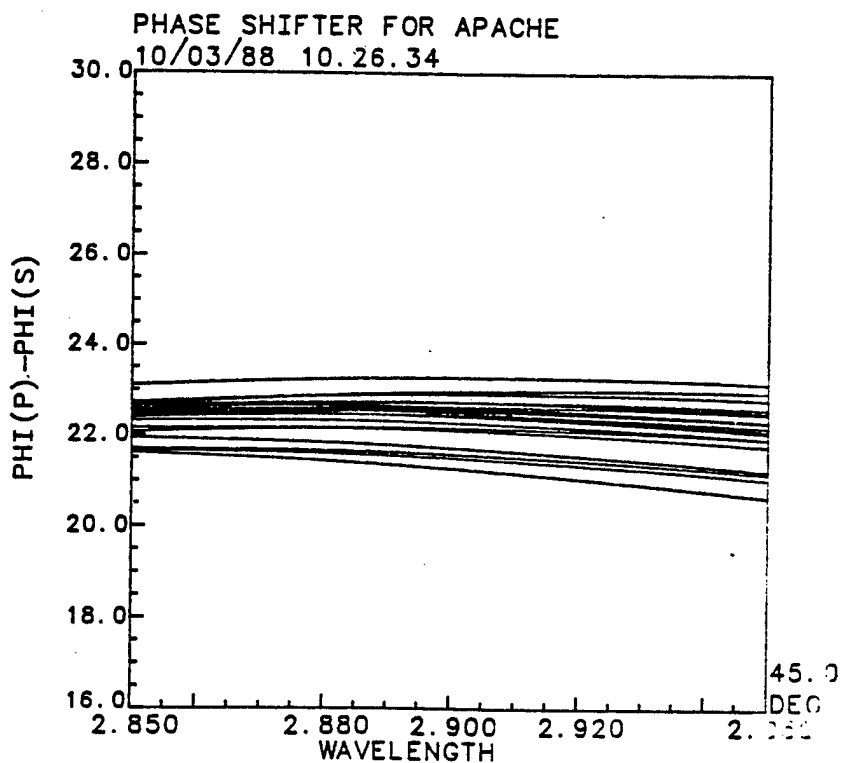
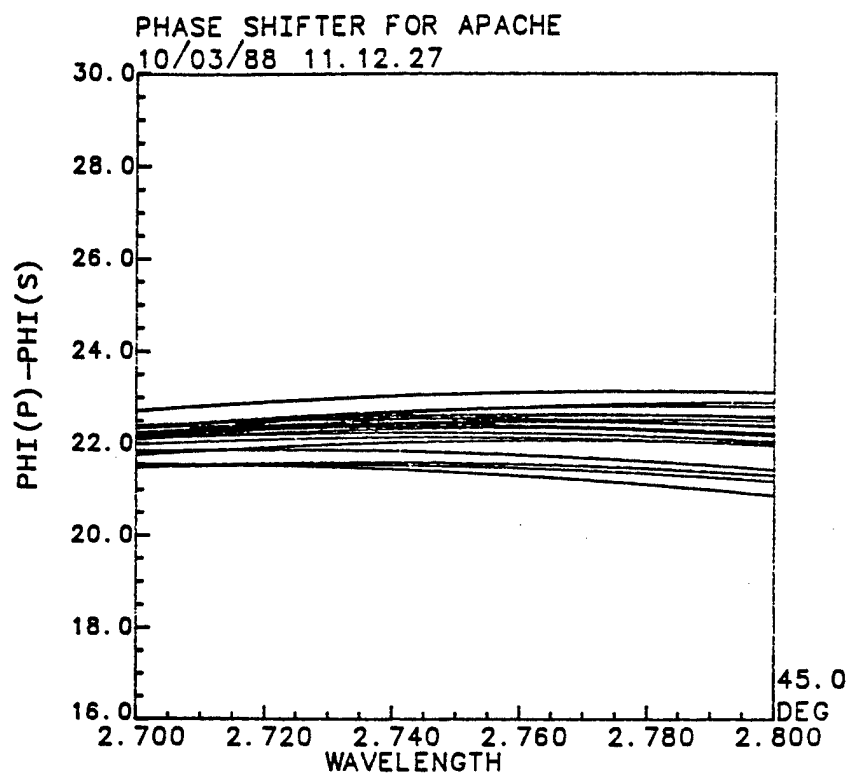


Figure 2.11-7. Phase Retardance Versus Wavelength: Recommended Design for 90-Degree Phase Retarder with Random Layer Variations

### Alternate Designs

One alternate design employs Si and SiO as the dielectric materials. This design does not have the advantage of the recommended plasma plating deposition method and is not suitable for deposition of SiO. While the layer thickness standard deviations would not increase if this design were to be deposited via conventional methods, the overall durability would be lessened. Secondly, use of conventional methods would probably result in higher absorption for the Si. Thirdly, the ratio of refractive indices is less than that of the recommended design. This results in slightly poorer theoretical performance for both reflectance and phase retardance with an equivalent number of dielectric layers. The lower index ratio reduces the bandwidth of the coating and also allows deeper electric field penetration into the coating, which, in turn, results in higher absorption.

The second alternative design used TiO<sub>2</sub> and SiO<sub>2</sub> as dielectric materials. Comparison of the theoretical performance of this third potential design candidate to the others shows even less likelihood of success. Although this design could be deposited with the recommended plasma plating technique, this combination has the lowest refractive index ratio of the three designs presented. Manufacturing tolerances for making successful coatings are reduced and spectral performance is marginal at best.

Table 2.11-4 shows a summary of the results. Best performance is given a value of 1 and worst a value of 3. In the case of equivalent performance, the values are averaged. Each design is ranked for several considerations. The recommended design has the lowest sum of rankings.

Table 2.11-4. Coating Design Comparison: Quarterwave Mirrors

Dielectric Combination	Deposit Method	Index Ratio	Durability	Layer Control	Absorption	Experience	Total
Si/SiO <sub>2</sub>	1.5	1	1	1.5	1	2.5	8.5
Si/SiO	3	2	3	3	3	1	15
TiO <sub>2</sub> /Si <sub>2</sub>	1.5	3	2	1.5	2	2.5	12.5

At first, the ranking of the first and second alternate designs may appear inconsistent with the statements made in previous paragraphs, but it must be kept in mind that theoretical performance depends greatly upon the index ratio of the coating materials.

The  $\text{TiO}_2/\text{SiO}_2$  design has inferior spectral properties when compared with the  $\text{Si}/\text{SiO}_2$  design, so the rankings were adjusted accordingly. These rankings reflect present capabilities and experience.

#### 2.11.2.5 Low Birefringence Annular Optics

The approach used for the low birefringence annular optics study was identical in concept to that proposed by Baumeister (Reference 2) and utilized successfully for the manufacture of the ALPHA resonator optics, with the exception that APACHE mirrors will be multilayer designs with much lower absorbances, thus complicating the design.

The APACHE amplifier mirrors have the same geometry as their ALPHA counterparts although the scale may be different. This means that the high-power radiation is incident upon each mirror over a range of angles. The incident angle varies uniquely with radius for each of six mirror surfaces; that is, for each radius on each annular mirror surface, there is a unique angle of incidence. The proposed designs for low phase retardance (or low birefringence) coatings must take this fact into account. The basic design concept for the system of six reflectors is that the net algebraic sum of phase shifts for the six mirrors (one round trip through the amplifier) is zero. Individual mirrors might cause a positive phase retardance, while other mirrors can compensate by introducing a negative phase retardance.

There are several interesting trade-offs involved with the proposed method. The most significant advantage is that the mirrors are not coated simultaneously because the design are different. Consequently, if phase performance is substandard, the subsequent coating run(s) can be modified to counteract this, thus avoiding the time and cost involved in repolishing and recoating the optics. Secondly, fewer layers are required to obtain the necessary phase control. Thirdly, nonzero phase retardance designs tend to be more tolerant of manufacturing variations than the strictly zero

phase retardance single coatings. A fourth advantage is that the simpler design recommended exhibits lower absorbance in general than the more complicated zero phase design concept while allowing less electric field penetration into the multi-layer coating, which, in turn, results in lower absorbance.

One disadvantage of the proposed concept is that more than one coating design is required. This is offset by the comparative simplicity of the compensating designs. Another disadvantage is that the zero phase retardance design has a high index material as the outermost layer, while the proposed negative phase retardance designs finish with a low-index layer, which tends to reduce the reflectance of the coating. Additionally, coating thicknesses on the various mirror surfaces will require masking for accurate control. Regardless of the selected designs, the masks will be different for the various surfaces.

For this application,  $\text{SiO}$  and  $\text{SiO}_2$  give the best theoretically performance, for the many of the same reasons given for the quarter wave mirrors. The reflectance of the positive slope design with random layer thickness variations stays constant at 99.92% across the wavelength range. (This nomenclature refers to the slope of the phase retardance as a function of wavelength.) Figure 2.11-8 shows the phase retardance of the positive slope design. For the corresponding negative slope design, the reflectance versus wavelength remains a constant at 99.7% across the four wavelengths of interest. Figure 2.11-9 shows the phase retardance of the negative slope, or compensating, design. It is assumed that the plasma plating deposition technique would be used.

When these two coatings are placed on the appropriate annular amplifier optics surfaces, the resulting overall phase retardance for the wavelengths in the HF spectrum is near zero. Figure 2.11-10 shows the net round trip phase retardance for six different positions (or rays) for each of the four HF wavelengths. The figure indicates the algebraic sum of phase retardance for the size surfaces (four positive and two negative slope coatings). Only the nominal designs are given.

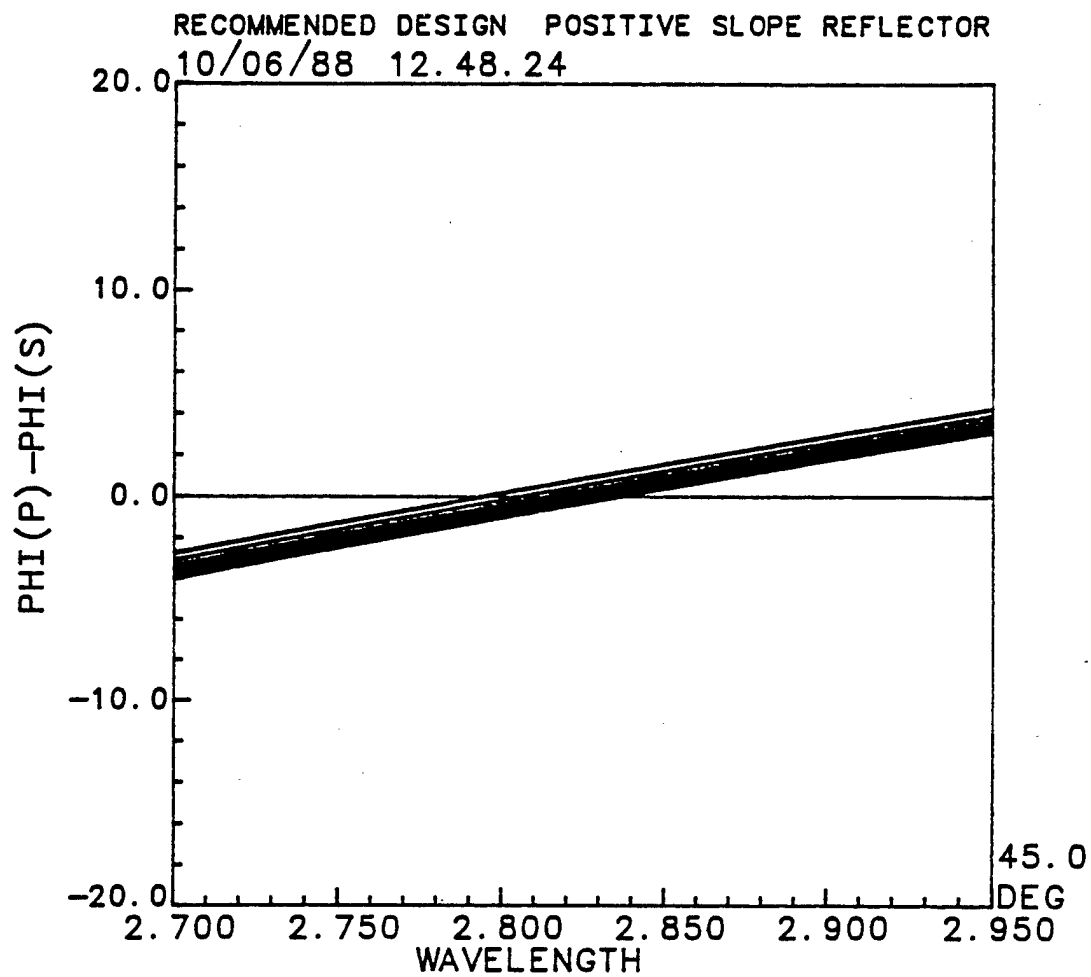


Figure 2.11-8. Phase Retardance Versus Wavelength: Recommended Design for Positive Slope Reflector for Annular Optics with Random Layer Thickness Variations

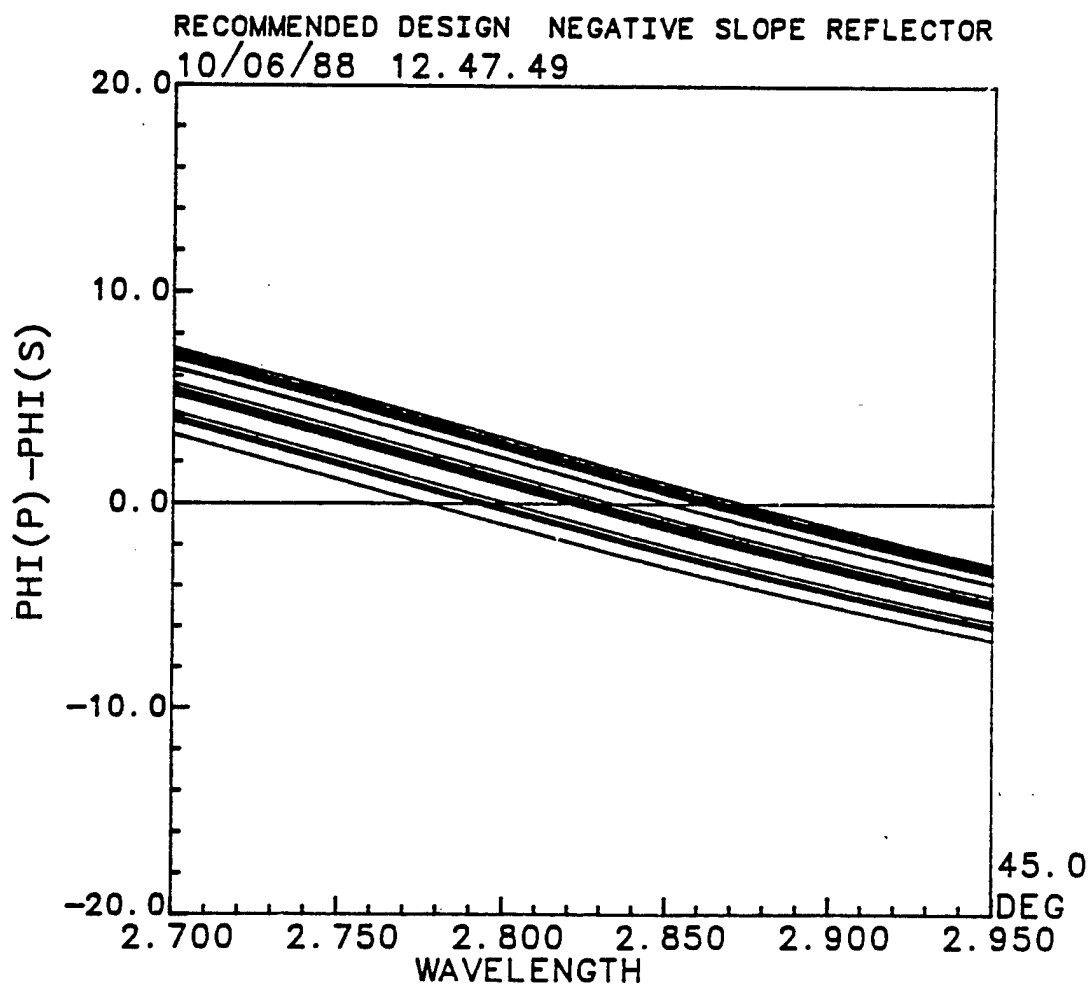


Figure 2.11-9. Phase Retardance Versus Wavelength: Recommended Design for Negative Slope Reflector for Annular Optics with Random Layer Thickness Variations

### Recommended Design

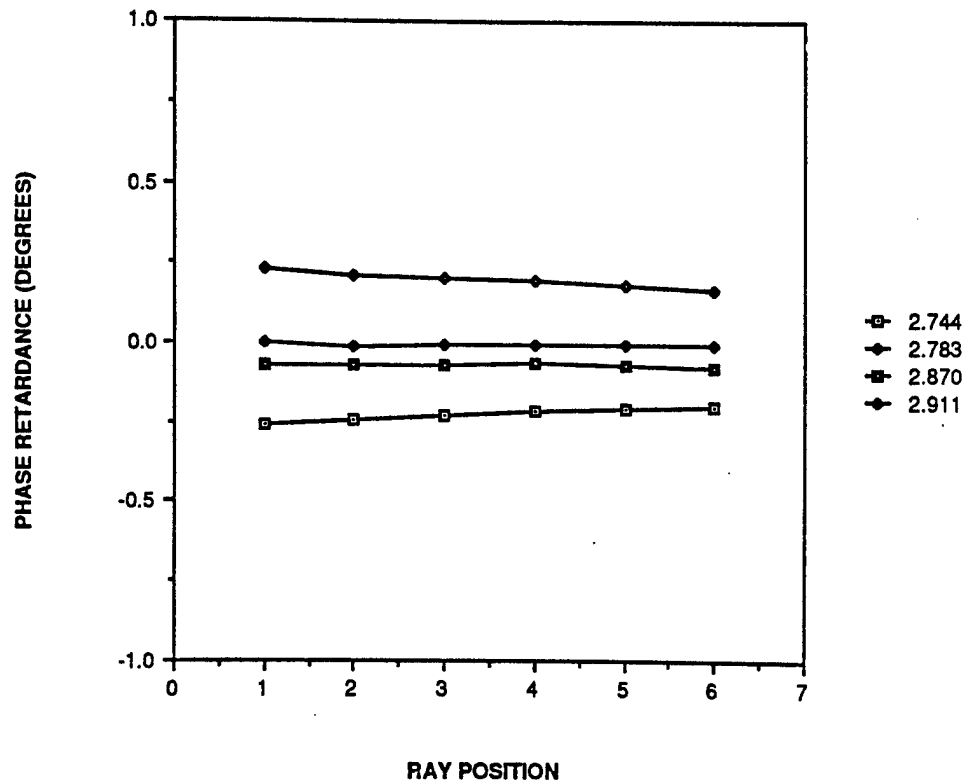


Figure 2.11-10. Net Round Trip Phase Retardance for Each of Six Position of Rays on the Amplifier Annular Optics — Recommended Design



As for the first alternate design, the same comments about comparative advantages and disadvantages discussed in the quarterwave mirror section apply.

A second alternate design employed a combination of ZnS and  $\text{Al}_2\text{O}_3$ . While these materials have been used successfully for ALPHA high reflectors, the theoretical performance is the worst of the three considered. In addition to the comparatively low index ratio, the precise layer thickness of zinc sulfide is difficult to control due to a temperature sensitive sticking coefficient. The overall phase retardance for the six mirrors was considerably less than that for the optimal design.

#### 2.11.2.6 Low Birefringence Flats

Compensatory coatings were selected as the best way to achieve low birefringence for flat optics also. With the compensating design method and the fairly high refractive index ratios available through ion assisted deposition methods, handling all four wavelengths with one coating was tractable for this design application. In a report by Powell and Fisher (Reference 2), theoretical and actual measured results were presented for both positive and negative slope designs. Discussed in this report are two designs differing primarily in constituent materials, which demonstrate clearly the benefits of using a material combination with a high ratio of refractive indices.

The first design alternate recommends a SiO and  $\text{SiO}_2$  combination. The reflectance for the positive slope design as a function of wavelength is constant at 99.93% over the HF spectrum of interest, and is not affected by random variations in layer thicknesses. The phase retardance versus wavelength corresponding to this ranges from -3.6 to +3.5 degrees as the wavelength increased from 2.70 to 2.95  $\mu\text{m}$  (it crosses the abscissa at approximately 2.827  $\mu\text{m}$ ). If the measurements of an actual coating indicate phase retardance performance to be less than anticipated, there is some chance of using angle tuning to save the mirrors. Increasing the absorption by a factor of two reduces the reflectance as expected but was found to have no effect on phase retardance.

The corresponding negative slope design using SiO and SiO<sub>2</sub> ranges from 99.7% at 2.70  $\mu\text{m}$  to 99.555 at 2.95  $\mu\text{m}$ , and the phase retardance versus wavelength ranges from 4.0 to -4.2 degrees as the wavelength increases. (It crosses the abscissa at approximately 2.835  $\mu\text{m}$ .) The most noteworthy properties of this coating are the reduced reflectance brought about because of the low-index outer layer required by the design, and the negative slope phase retardance provides a good match to the corresponding positive slope design.

Because of results reported by Decker (Reference 2), the alternate design chosen for the low birefringence flats application utilizes a titanium dioxide and silicon dioxide combination coating deposited via the plasma plating method. The recommended Si/SiO<sub>2</sub> design has an index ratio of about 2.36 while the TiO<sub>2</sub>/SiO<sub>2</sub> design has a ratio of approximately 1.51, which is about the lowest ratio possible for handling all four wavelengths with one coating.

The theoretical predictions of the coating performances for the alternate positive and negative slope designs show that the absorption coefficient for TiO<sub>2</sub> is lower than that for Si. The reflectance, however, for this design is significantly lower than that for the Si/SiO<sub>2</sub> design because the electric fields penetrate more deeply into the TiO<sub>2</sub>/SiO<sub>2</sub> coating. Increasing the number of layers in the alternate design does not enhance reflectance.

The lower index ratio results in increased slopes for the phase retardance versus wavelength. While the alternate designs do compensate for each other fairly well, the effects of random layer thickness variations on phase retardance are larger. Overall, the design for low birefringence flat mirror coatings demands as large an index as possible if it is going to be used over the entire wavelength range. If the decision is made to evaluate this type of coating separately for the two shorter and two longer wavelength pairs, the calculations can be obtained rather quickly.

### 2.11.3 Birefringent Wedge Design

As discussed in Section 2.11.1, the grating rhomb/quarter wave retardation concept does not provide perfect isolation of the master oscillator (MO). Residual depolarization from the amplifier optics, errors in quarter-wave retardation, and birefringence in optical coatings throughout the beam train cause power to leak back through the grating rhombs to the MO. Although the required level of isolation appears to be readily achievable using state-of-the-art retardation coatings and polarization sensitive gratings, much depends upon the tolerances to which these components can actually be fabricated. For this reason, it seemed prudent to investigate alternative concepts which might be employed to improve isolation capability should the need arise. One concept involves the use of a birefringent wedge. The MO is located a long distance away from the sources of depolarization with a spatial filter (beacon mirror) in between. A birefringent wedge placed in the beam path could be designed to introduce sufficient tilt to cause the depolarized part of the beam to miss the MO entirely on its return path. The objective of this task, therefore, was to develop a conceptual design of a component that could be used as a backup isolation concept. The design problem is two-fold. First, one must establish the optical requirements for the wedge to ensure that the return beam misses the MO. Second, since the birefringent wedge will be a transmissive optic, one must establish if the design will be able to withstand the optical fluence.

#### 2.11.3.1 Optical Design

There are five potential sources of residual feedback (which are listed below, together with information that tells how they might be effectively eliminated) into the MO on the backward pass. (See Figures 2.11-11 and 2.11-12). Refer to Flow Chart in Figure 2.11-11:

1. The MO puts out a beam of P polarization state. The forward pass through the amplifier generates a small component of S polarization due to the slight residual birefringence in the amplifier medium. It is coaligned with the P state beam. A pass through the birefringent wedge (BW) will induce slightly different angles in the two polarization states, which will then pass through the  $\lambda/4$  plate and into the SBS cell. On its second

pass through the amplifier, it will be P state. Any depolarization of this component will be into the S state, which is the polarization state of the target beam. However, the angle will be  $\Delta\theta$  above the optical axis; whereas, the target beam will be at  $-\Delta\theta$ . When the S component of the beam exists the amplifier on this backward pass, it will pass through the beacon but miss the MO by an angle  $\Delta\theta(=\theta_S - \theta_P)$ .

2. The imperfect  $\lambda/4$  plate produces some residual depolarization which feeds back along the beacon path. This will leak into the MO and, as such, constitutes the system limit.
3. The backward pass of the beam through the amplifier will again produce some depolarization of the outgoing P polarization state. This S component will be coaligned with the output target P state beam at an angle  $-\Delta\theta$ , and it will pass through the beacon and miss the MO.
4. At the grating rhombs a small amount of the target beam will leak through and return along the beacon path toward the MO. This too will pass through the beacon, but miss the MO by  $-\Delta\theta$ .
5. The grating rhombs might also convert some of the incident target beam to P state polarization upon reflection, which would pass through the grating rhombs (as they are designed to pass P state, but not S) and return along the beacon path to the MO. It will, however, be at an angle equal to that of the target beam, and it will miss the MO by  $-\Delta\theta$ .

The minimum amount of tilt induced by the birefringent wedge which ensures that the depolarized beam on the return pass will miss the MO is readily calculated. Using the SBL physical dimensions and accounting for the telescope magnification, this is computed to be:

$$\theta_{\min} = 25 \mu\text{rad}$$

In this calculation, a safety factor of two has been used to ensure success in missing the MO.

A second consideration relates to correction of aberrations within the amplifier. If too much tilt is introduced by the birefringent wedge, the path of the return beam within the amplifier will be displaced relative to that of the incident beam. If this occurs, aberrations accumulated on the incident path will not be well-corrected on the return pass. Using as

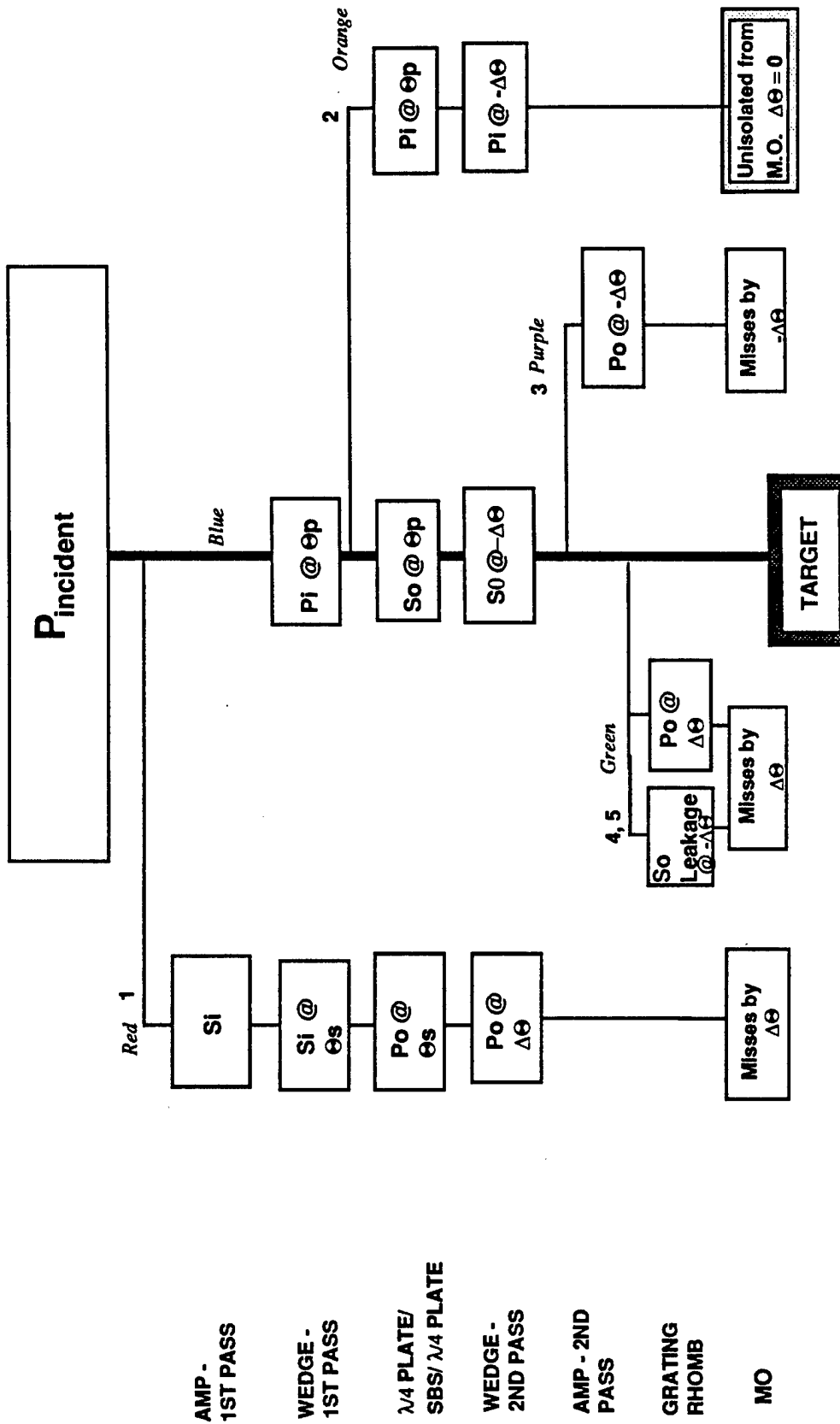


Figure 2.11-11. Flow Chart of Target and Unwanted Polarization Through the Apache System with Birefringent Wedge in Place

So = leakage through grating rhomb.

Po is created by grating misalignment to  $\lambda/4$  plate.

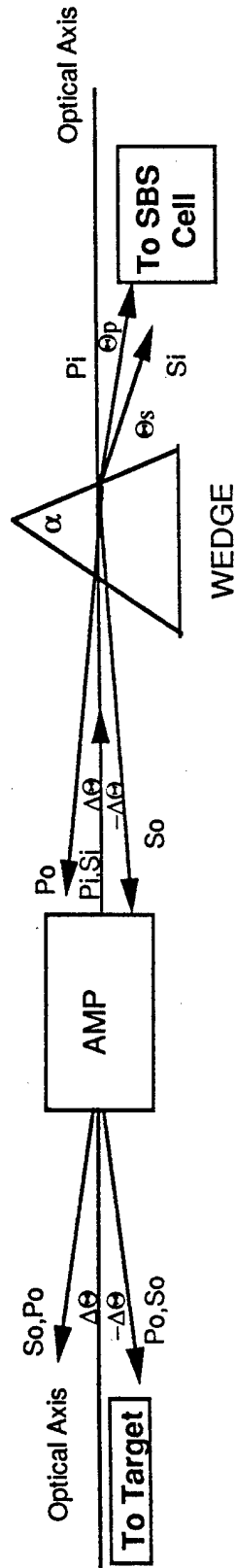
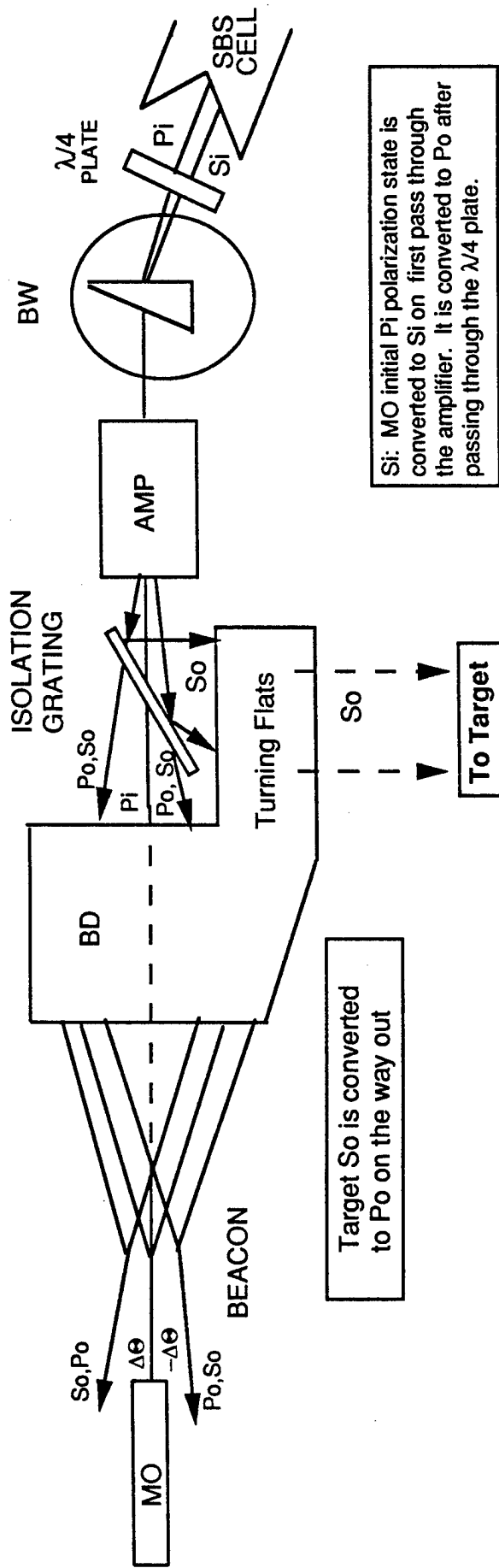


Figure 2.11-12. Birefringent Wedge Isolates the Master Oscillator from Amplifier Depolarization Leakage

criterion that the displacement in the return beam shall be everywhere smaller than 10% of the laser mode width, the maximum tilt acceptable tilt angle is

$$\theta_{\max} = 28 \mu\text{rad}$$

Since these numbers are almost the same, a nominal value of 25  $\mu\text{rad}$  has been used.

To establish the design of the birefringent wedge, the material to be used must be specified. Two candidates have been considered, viz., Sapphire and  $\text{MgF}_2$ . For Sapphire, the difference in index between the fast and the slow axis is 0.008.  $\text{MgF}_2$  is slightly more birefringent, with an index difference of 0.0104. Using 25  $\mu\text{rad}$  as the desired tilt displacement, one computes the wedge angle for the two materials as:

$$\alpha(\text{Sapphire}) = 1.56 \text{ mrad}$$

$$\alpha(\text{MgF}_2) = 1.2 \text{ mrad}$$

An examination of temperature sensitivity for these two materials revealed that these wedge angles are applicable over a wide range of temperatures. Wavelength sensitivity was also examined. Over the range of the HF spectrum, it was found that the wedge angle required to produce the 25  $\mu\text{rad}$  tilt varies by an insignificant amount.

Using the optical design requirements, a thermal/mechanical analysis was performed to define a design concept which could withstand the high-power laser fluences while providing the desired optical performance. A summary of the results is presented in Table 2.11-5. For reasons which will be discussed, Sapphire is chosen as the baseline material.

The approach used for selecting the birefringent wedge design was to choose a baseline configuration, select the appropriate materials, analyze, perform trade studies and redesign, if necessary, until all requirements were met. The baseline configuration was selected using the available technical experience in optical and structural design. The selected wedge design is shown in Figure 2.11-13. It is comprised of four components: substrate, heat-exchanger, bond material, and optical wedge.

Table 2.11-5. Birefringent Wedge Analysis Summary

Wedge material	Sapphire ( $\text{Al}_2\text{O}_3$ )
RMS birefringence (HF waves)	$76.5 \times 10^{-6}$
Maximum birefringent stress ( $\text{N}/\text{cm}^2$ )	-1078.0
RTV shear stress ( $\text{N}/\text{cm}^2$ )	18.0
Maximum surface distortion (cm)	$3.21 \times 10^{-4}$
Maximum wedge temperature (K)	353.7

The purpose of the substrate is to provide adequate support and dimensional stability to the wedge design. Molybdenum was selected for both the substrate and heat exchanger plates because it is the current state-of-the-art material used on cooled mirrors. It has excellent mechanical properties, high thermal conductivity, and low thermal expansion. The heat exchanger design would be a two-pass system sized to remove 99.75% of the absorbed beam energy. The first pass would remove 95.0%, and the second pass, 4.75%. The plates would be furnace brazed to the molybdenum substrate.

The birefringent wedge material selected for the baseline design was  $\text{Al}_2\text{O}_3$ . It is a high-quality crystal available in large sizes having low volumetric absorption. An antireflective front face coating and a multilayer dielectric back-face coating would be applied to the wedge. The  $\text{Al}_2\text{O}_3$  wedge is bonded to the heat exchanger plates with an enhanced thermal conductive RTV silicon rubber. This permits the transmission of absorbed heat without highly restraining thermal growth.

The dimensions of the baseline birefringent wedge design are shown in Figure 2.11-13. The sapphire wedge thickness was 0.1 to 0.1333 cm across the diameter of the wedge. This corresponds to a wedge angle of 1.655 mrad. The thinner the wedge material is, the less energy is absorbed. This in turn reduces the stresses and distortions in the sapphire, the strains in the bond material, and the size of the heat exchanger and substrate. The availability of the sapphire wedge with the appropriate optical qualities must still be determined.



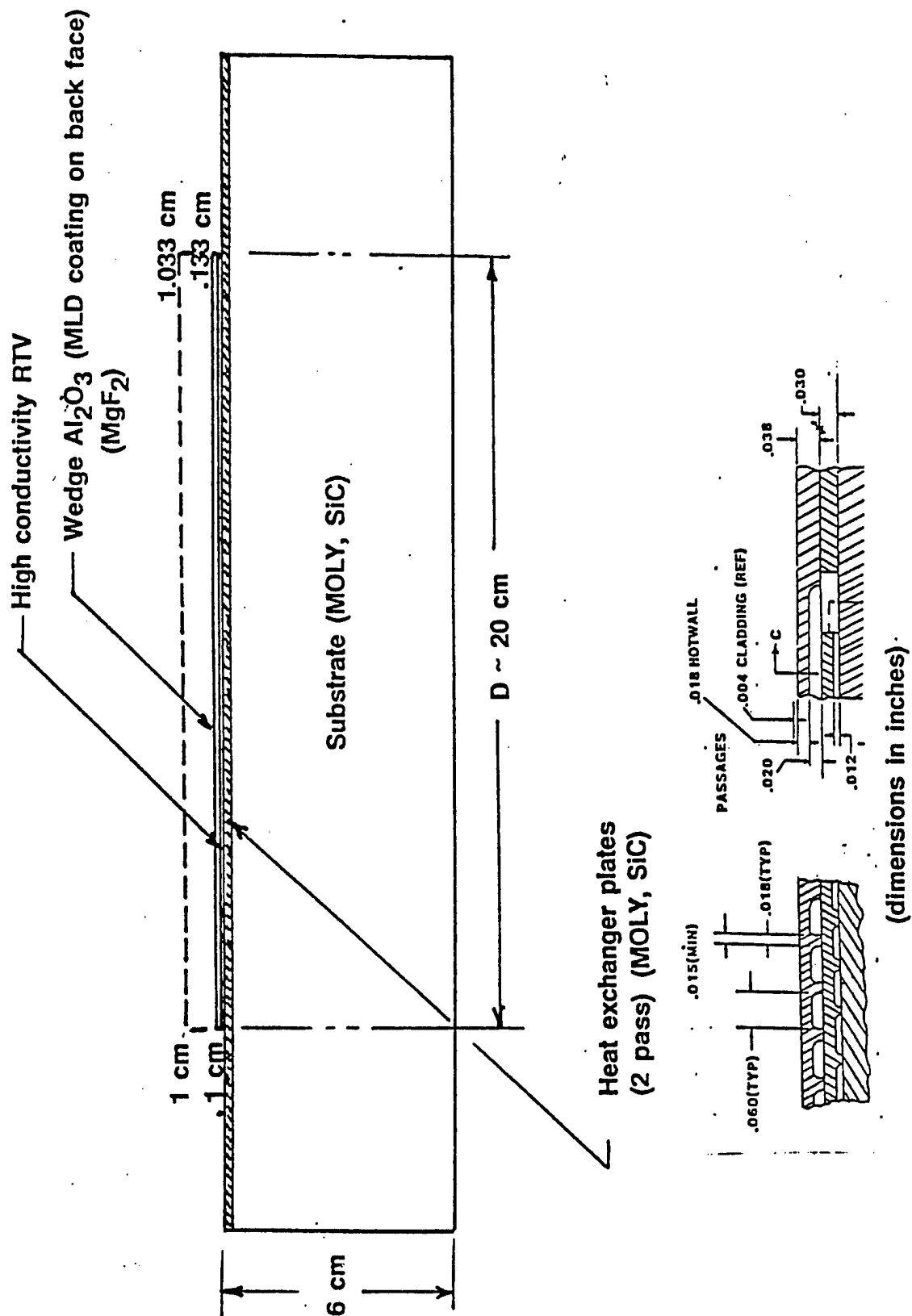


Figure 2.11-13. Birefringent Wedge Design

The thermal and stress characteristics of the characteristics of the birefringent wedge design were analyzed using the NASTRN FEM code. The solid element model was developed to perform the thermal analysis and the stress/distortion analysis simultaneously. The model is a 30-deg slice made up of 210 solid elements. The surfaces of the sapphire wedge contain heat flux elements to allow for surface energy absorption. Volumetric heat absorption takes place in the solid elements of the sapphire wedge.

The assumed beam power distribution and absorption characteristics of the sapphire wedge are as follows: the front face AR coating has a surface absorption coefficient (SAC) of 0.001; while the back face MLD coating has a SAC of 0.002; the volumetric absorption coefficient (VAC) of sapphire is 0.00015/cm; and the beam profile was assumed to be a flat top with a power level of 5000 kW.

Since the scaling laws are linear in the range of interest, the results may be adjusted up or down for different power levels.

The total energy absorbed in the wedge and removed by the heat exchanger plates was 6343 W. A peak temperature of 353.7 K was calculated on the front face of the sapphire. The temperature drop through the sapphire and RTV was 4.4 K and 46.4 K, respectively. The coolant temperature was taken as 300 K.

The computed stresses and distortions developed in the sapphire wedge are shown in Figure 2.11-14. The radial compressive stress in the middle of the plate is a maximum ( $804.5 \text{ N/cm}^2$ ) at the center and decreases to zero at the edge. The stress is due to the action of the RTV which partially restricts the thermal expansion of the sapphire.

The bending stress developed in the plate follows a semisinusoidal path out to the edge of the plate, due to the temperature drop through the plate. Normally a plate would assume a spherical shape; however, the RTV restricts movement normal to the surface and results in the radial wave pattern. The surface distortions show a similar pattern except that they are out of phase with the bending stress.

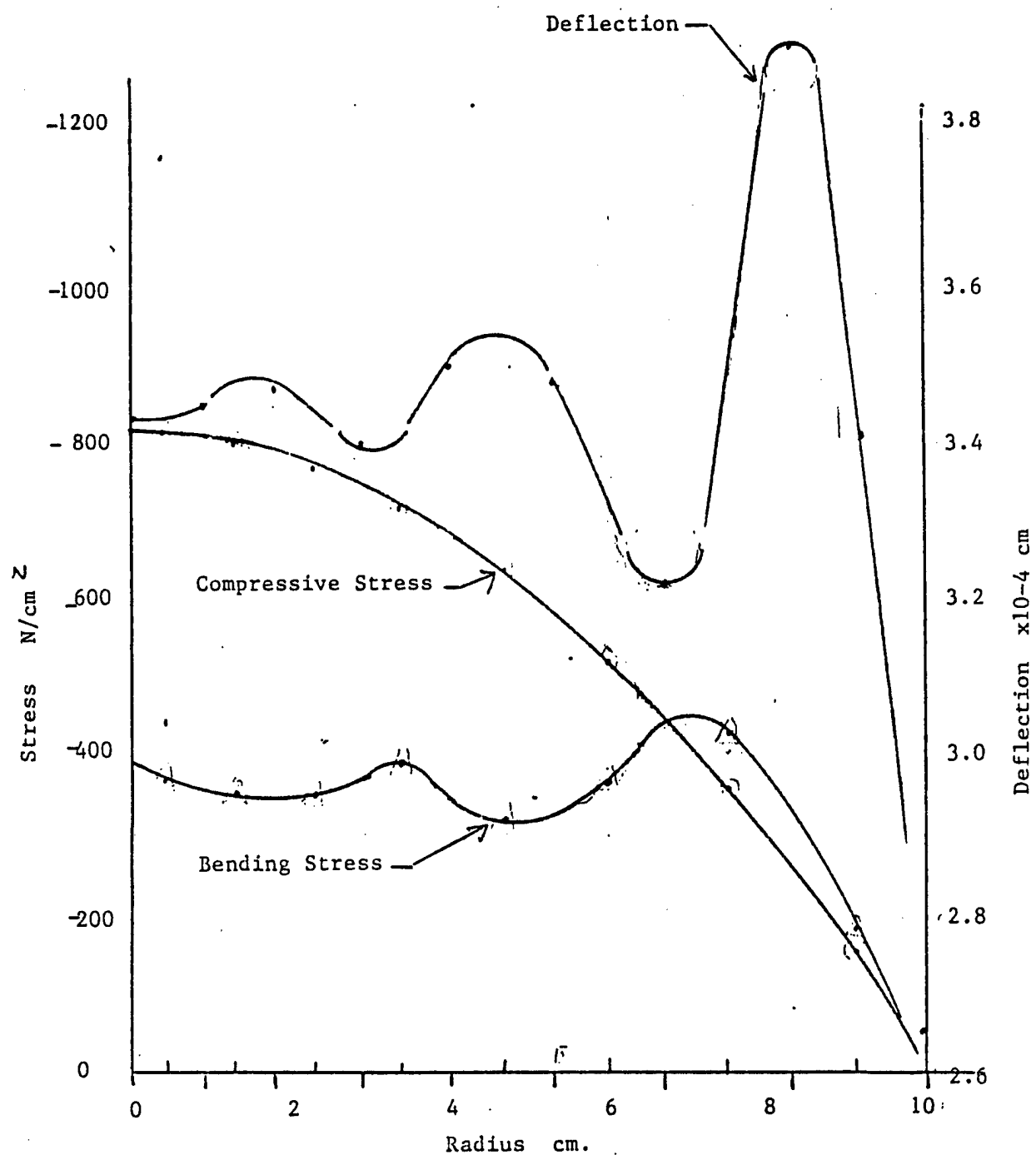


Figure 2.11-14. Birefringent Wedge Design with AR Coating

The value of the stress induced RMS birefringence ( $\eta$ ) was determined from the equation

$$\eta = \bar{A} \left\{ \sum_{N=1}^8 \left[ \frac{1}{2} (S_t + S_b) dA \right]^2 \right\}^{1/2} \quad (2.11-1)$$

where

$K = 1.58 \times 10^{-6}/N/cm^2$ ,  $A$  is the area of the plate, and  $dA$  is the incremental area.  $S_t$  and  $S_b$  refer to the stresses in the two wedge layers, and

$$S_t = S_1 - S_2$$

is the difference in principal stresses for each element layer. The RMS birefringence of the plate, averaged over the surface of the plate, was calculated to be  $76.5 \times 10^{-6}$  waves. This value was determined to be within the budget allocated for the birefringent wedge design.

References:

1. Phased Array Laser System (PALS) Final Report, Alvin D. Schnurr, TRW, Inc., 9 July 1986.
2. Advanced Phased Array Chemical High Energy Laser Program (APACHE) APEX Final Report, OCLI Advanced Products Division Subcontract Final Report SDRL No. 06, 10 October 1988.

### 3. OPTICAL MODELING AND ANALYSIS

#### 3.1 INTRODUCTION

This section describes the principal optical modeling and analyses efforts performed in support of the design of the APACHE SBL. Several new models were formulated to address unique aspects of the APACHE SBL, while existing models, generally with some modifications, were used where appropriate. The optical modeling was concentrated in five main areas:

First, an optical design of a phase conjugate beam director was formulated, using the Code V optical design code; optimization performed with this model yielded a design form which displayed excellent performance over the required instantaneous and steered fields of view for the SBL.

Second, the ASAP optical propagation code was used to model the performance of the beam director for an aberrated segmented primary mirror, and for departures of the beacon from its nominal position. The results demonstrated that the APACHE beam director displays excellent wavefront correction over a wide range of applicable parameters.

Third, the amplifier modeling section describes analyses of the bidirectional amplifiers in APACHE, accomplished using adaptations of existing amplifier codes, as well as a simplified single-gain sheet model developed under the present program. The key characteristic displayed by the calculations is a "self-healing" of the amplifier, resulting in high output powers whenever the input power is above a modest value required to reach saturation, and exceed the SBS threshold.

Fourth, the SBS cell was modelled using the BRIWON code, which facilitated the prediction of SBS cell output characteristics as a function of the characteristics of the conjugation medium and the input beam properties.

Fifth, an end-to-end APACHE optical propagation model (APOPM) was developed, consisting of several individual modules for the propagation within a specific subsystem, plus a set of interfaces which connect the modules. Significant progress was made during the APACHE Program in implementing APOPM, including successfully exercising the modules both individually, as well as in certain combinations, and performing representative calculations using the model.

## 3.2 BEAM DIRECTOR DESIGN

### 3.2.1 Introduction and Background

The goal of the APACHE beam director (ABD) optical design effort is the realization of an optical system design which utilizes optical phase conjugation to remove optical wavefront aberrations from an outgoing beam. Primary sources of aberration in the APACHE system include induced distortions, surface misfigure, and segment misalignments of the ABD's large segmented primary mirror. Designs based on optical phase conjugation are alternatives to the use of outgoing beam wavefront sensors and actively controlled primary mirrors.

#### 3.2.1.1 Operational Definition of APACHE Beam Director Optical System

The ABD consists of a two-channel, all-reflective optical system, with a single shared, segmented primary mirror common to both optical channels as indicated in Figure 3.2-1. A linearly polarized probe beam from a master oscillator is sent to a small remote beacon mirror. The spherical wavefront returning from the beacon mirror is collected by the primary mirror, and is processed by the remaining beacon channel optical elements. The beacon channel optics demagnify and collimate the beacon beam, send it through several fold and steering mirrors, and then through a polarization isolation grating rhomb to the amplifier and phase conjugation subsystems. In designing the beam director, the latter subsystems are treated as a unity amplification conjugator which reverses all incoming ray direction cosines and also reverses the signs of all optical path lengths (OPLs).

The amplifier/conjugator outgoing beam is then linearly polarized in a plane perpendicular to the incoming-beam polarization plane by quarter-wave plates. A polarization sensitive grating is used to direct the return beam to the target-channel optics. From there the energy is directed to the segmented primary mirror, which in turn directs the now near-collimated beam of energy toward a distant target.

The beacon channel is used to "read" segmented primary mirror aberrations. These aberrations are returned by the phase conjugator to the segmented primary mirror through the target channel as inverse wavefront

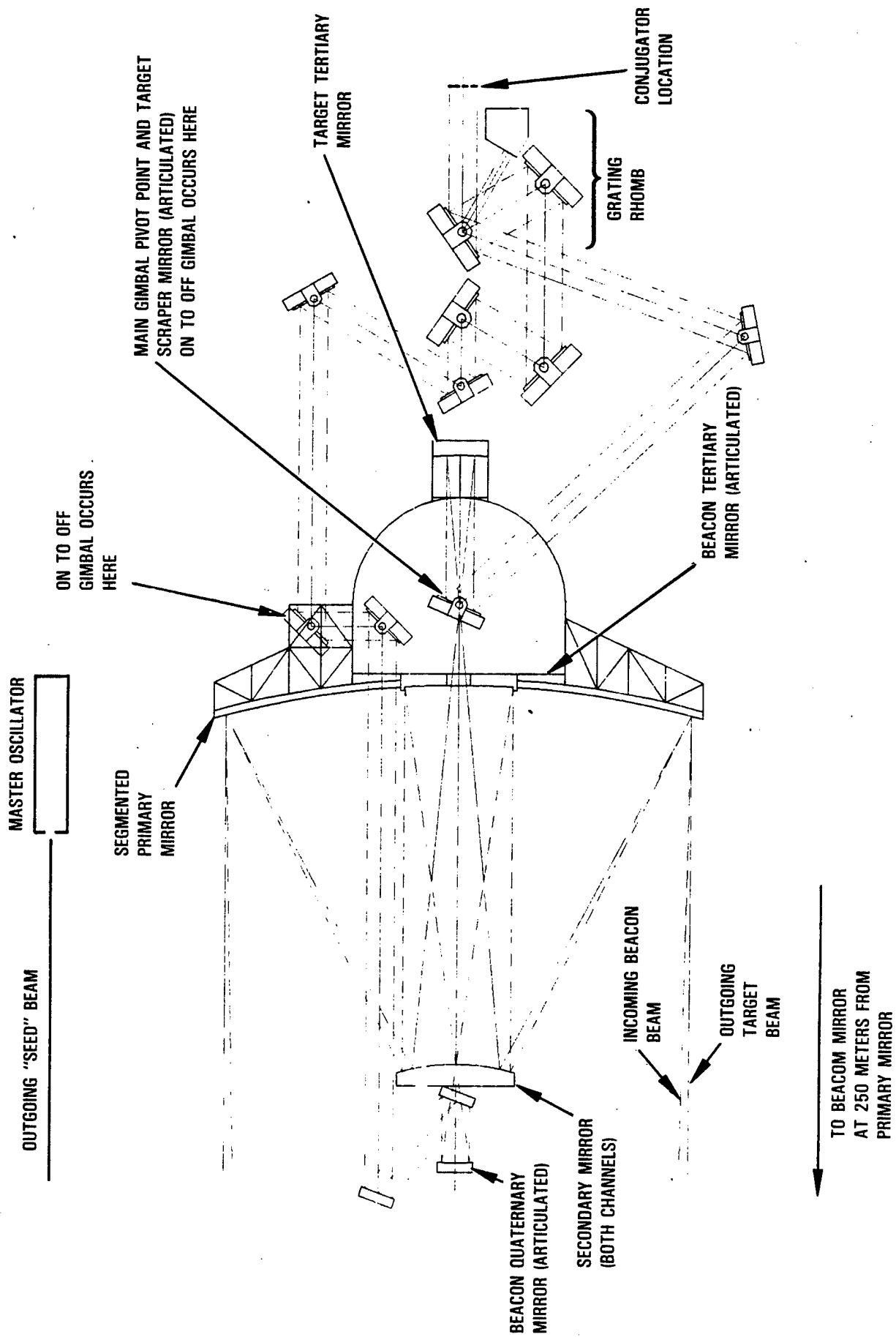


Figure 3.2-1. APACHE Beam Director (ABD) Optical Subsystem Schematic

phase differences. This phase conjugation technique passively neutralizes many of the degrading effects on the outgoing wavefront due to segmented primary mirror aberrations. The wavefront correction is partial rather than complete because the beacon is not at the same optical position as is the target. Also, it is not possible to optically relocate the beacon at the target position without the use of a transmissive or diffractive optical element nearly as large as the primary mirror, which is simply impractical. The beacon and target channels must therefore possess significantly different optical conjugates.

The discussion below addresses some of the unique requirements and challenges facing the design of a phase conjugate beam director. And then, later in this and the following sections, the discussion demonstrates how the BD design formulated under the APACHE Program successfully overcomes these difficulties, providing excellent wavefront correction performance over a wide range of applicable parameters.

One major challenge facing the phase conjugate BD optical designer is that the two channels of the optical system are used at significantly different optical conjugates. Thus, the aberrations impressed on the phase distribution of the beacon channel will not, in general, be the same as the aberrations encountered in the target channel. In fact, the aberrations resulting from segmented primary mirror imperfections or induced deformations are sensed in the beacon and target channels with an angular disparity, which is directly related to the difference between the beacon and the target positions relative to the primary mirror. The BD design formulated for APACHE takes into account and successfully provides a means of correcting this disparity.

In addition to different sensing of aberrations, the beacon and target channels have different transfer mechanisms that needed to be accounted for in the present design. The aberration theory developed by Buchdal ("Optical Aberration Coefficients, Dover Pubs, 1968) indicates that for systems which possess optical aberrations beyond the third-order (only the simplest systems possess only third-order aberrations), optical aberration contributions from an optical surface are made up of two parts. The first part, known as the intrinsic part, arises at an optical surface and is wholly related to the optical surface characteristics and the paraxial ray



data at that surface. The second part, known as the transferred part, is made up of a complex summation of lower-order aberrations from previous surfaces and from the current surface. The exact mix of summed aberrations varies for each specific aberration.

The challenge facing the phase conjugate design is how to make the aberration transfer mechanism of each of the two ABD optical channels as similar as possible. Moreover, the dissimilarity in the optical aberration transfer mechanisms of each channel depends on the difference in the positions of the beacon and the target with respect to the primary mirror. To compensate for this difference, nonshared, channel-specific optical elements are required. The incoming probe beam, after sampling the perturbed segmented primary mirror will be aberrated in its transmission through the beacon channel to the phase conjugator. Correspondingly, the transmission from the phase conjugator to the segmented primary mirror on the target channel contains aberrations. Even after the design has been optimized by making the two paths as similar as possible, some small residual aberration will always persist due to the inherent dissimilarity between the two paths, thereby, limiting the resolving power of the telescope.

As indicated below, an optical design has been implemented which overcomes the disparities between the two channels and achieves an impressive degree of wavefront correction. This is accomplished by placing the beacon at a sufficient distance from the segmented primary mirror (25 primary mirror diameters for the F/1 primary mirror) that conjugation fidelity is retained to a useful level, as discussed later in this section and in Section 3.3.2.

### 3.2.2 Optical Design Analysis and Results

This section describes the development of a design concept for the ABD and the optimization of this design using Code V; tolerancing and performance analyses were accomplished using the ASAP code, and are described separately in Section 3.3. To avoid classification issues, only the results of a 10-meter analysis are discussed.

As part of the trade study culminating in the current design for the ABD, several optical designs involving both on- and off-axis three-mirror anastigmat (TMA) design forms for the required wavelength, field of view, and afocal magnification were considered. Table 3.2-1 summarizes the key specifications and goals driving the ABD design. The afocal magnification was limited to ~17x by fluence considerations for the high-power optics in the system and by amplifier size considerations.

In performing the trades leading to the current design, the intrinsic dissimilarity between the target and beacon channels, based upon the difference in the conjugate positions of the target (near infinity) and the beacon (located 25 primary mirror diameters from the primary), was taken into consideration. Since these two channels could not have identical designs, an effort was made to devise the simplest two-channel optical system, with the smallest possible number of optical elements, which

Table 3.2-1. ABD Design Specification Goals

Parameter	Goal	Design
Primary mirror F/#	1.0	1.0
Pupil magnification	~17	16.7
Aperture stop location	On primary mirror	On primary mirror
Beacon position (units of primary mirror dia.)	25	25
Target channel nongimbal FOV	XXX deg	XXX deg
Beacon channel nongimbal FOV	$\pm 0.025$ deg	$\pm 0.025$ deg
Double-pass nominal RMS OPD (waves HF)	$\leq 0.025$	0.015

achieved the required performance. The guidelines for the formulation of this new system included:

1. The primary mirror should be common to both channels. It should be the aperture stop for both the target and the beacon channels. This aperture stop should be reimaged in each channel to a real-image exit pupil located at or near the conjugator location.
2. The secondary mirror should be a common element to both channels.
3. The entire system should not self-obscure, and the maximum linear obscuration should be in the neighborhood of 25%.
4. The mass of optically powered, on-gimbal optical elements behind the primary mirror should be minimized.
5. The two channels should take advantage of the difference in conjugate positions between the target and the beacon as the mechanism to optically separate the channels.

Consideration of these guidelines lead to a layout of the form illustrated in Figure 3.2-2. The operative approach in the design of an essentially on-axis ABD can be best understood by analyzing the operation of each of the two channels separately.

#### 3.2.2.1 Operation of the Beacon Channel

In the ABD design the master oscillator/beacon is represented as a point source located 25-primary-mirror diameters to the left of the segmented primary mirror. A diverging cone of beacon energy is collected by the F/1.0, parabolic segmented primary mirror and is sent to a hyperbolic secondary mirror. This energy is "collimated" to first order as it leaves the secondary mirror. This "collimated" beam is sent to the beacon aspheric tertiary mirror which focuses the energy back through a small hole in the secondary mirror. The exact focus lies behind the secondary mirror, inside a smaller hole cut into the beacon steering/scrapper mirror.

This beam now diverges to the beacon aspheric quaternary mirror which produces a highly corrected, collimated, beam demagnified by a factor of 16.7. The secondary mirror and the beacon tertiary and beacon quaternary mirrors also act to produce a high-quality, demagnified image of the

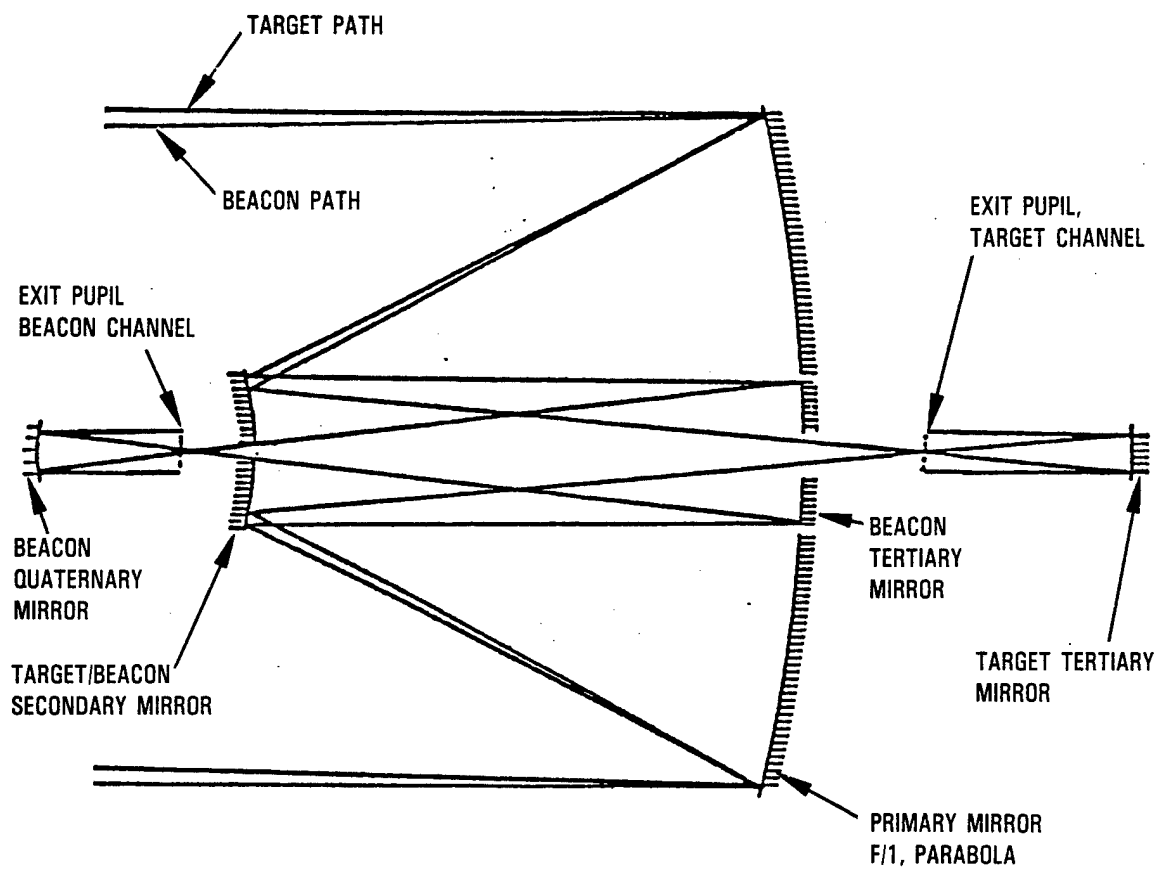


Figure 3.2-2. Starting Point Concept for Current ABD Design

segmented primary mirror at the beacon steering/scrapper mirror. This pupil imagery plays a vital role in the phase conjugation process by assuring that the wavefront tilt introduced by errors on the primary mirror maps into the amplifier/phase conjugator in the same way for both the beacon channel and the target channel. As illustrated in Figures 3.2-1 and 3.2-2, from the beacon steering/scrapper mirror the collimated beam is sent through a series of on- and off-gimbal steering/fold mirrors, through a beam derotation device to a polarization-isolation grating rhomb, and then into the amplifier/phase conjugator portion of the system.

#### 3.2.2.2 Operation of the Target Channel

To begin the target channel the beam that came from the beacon channel is reversed at the phase conjugator. All ray direction cosines are reversed (sign change), and optical path lengths are added in a negative sense when traversing the target channel. As this collimated and reversed beam leaves the phase conjugator/amplifier, its polarization plane is rotated by  $90^\circ$  using a set of quarter-wave plates. This change in polarization plane causes the target beam to traverse the alternate path available through the isolation grating rhomb. This isolation system is necessary to protect the master oscillator from seeing the amplified, outgoing beam. The target beam now traverses a different set of off- and on-gimbal fold and steering mirror, and hits the target conic tertiary mirror. The target tertiary mirror focuses the outgoing beam through a small hole in the target channel steering/scrapper mirror. The beam then diverges to the secondary mirror and then to the segmented primary mirror. The target channel optics act to focus (nearly collimate) the outgoing beam upon a target of choice. The target tertiary mirror and the secondary mirror also act to reimage the target channel steering/scraper mirror onto the segmented primary mirror with the same pupil mapping function as found in the beacon channel. As was mentioned earlier, this pupil imagery is critical to the operation of the ABD system phase conjugation.

### 3.2.2.3 Field of View and Field of Regard

Up to this point, the ABD system has been described as an on-axis system with the beacon and the target codirectional. In actual operation, however, the target and beacon will rarely be exactly coaxial.

The beacon channel has a field of regard which is defined by the maximum lateral excursions of the "free flying" beacon. A beacon channel field of regard of  $\pm 0.025$  deg, as measured from the segmented primary mirror position, sets the beacon stationkeeping requirements. As discussed in Section 2.6, this requirement is well within the capability of present day sensors and thruster control systems.

The beacon channel instantaneous field of view set by the optical performance limitations of the optical design form at  $\pm 0.01$  deg to  $\pm 0.002$  deg depending upon how far the beacon is decentered off-axis. Beacon mirror lateral motions beyond these values are tracked by the beacon channel optical system to actively maintain the required optical performance levels given in Table 3.2-1. Within the beacon channel optical train, the beacon tertiary mirror, and the beacon quaternary mirror perform this beacon tracking function. The beacon tertiary mirror tilts in two dimensions about its vertex, and the beacon quaternary mirror tilts in two dimensions and displaces in three dimensions to track the beacon mirror and maintain optical performance of the beacon channel. Since the required time scales for the tracking are driven by slow drift in beacon stationkeeping, these operations are expected to fall well within the capability of the sensing and control systems.

The target channel field of regard is set as a mission requirement by the minimum time to move from one target to the next. This field of regard is split between gimbaled and nongimbaled fields of regard. Only nongimbaled field of regard will be covered here. In order to minimize the time required for steering and to facilitate control, it is clearly desirable that the target channel optical train have only an optically flat steering mirror to redirect the target channel line of sight, and that target channel optical performance not depend on the position and angular pointing accuracy of a moving tertiary mirror.

In order to implement a design with a fixed tertiary, the beacon channel optical train was kept essentially the same, except that the collimated beam leaving the beacon quaternary mirror was no longer required to be centered over the hole cut in the beacon steering/scrapper mirror. This change and a similar change in the target channel allowed sufficient degrees of freedom to be opened in the design space so that the optical design form of the target channel could be changed to that of a classical, afocal, on-axis TMA, which would have excellent optical performance over the entire target channel nongimballed field of regard. Since access to the entire field of regard was not required at any one time in the ABD mission, it was possible to use a tilting and decentering flat steering/scrapper mirror. For any small instantaneous field of view within the field of regard, the single flat steering/scrapper mirror would direct output energy toward the target tertiary mirror in such a way that the reflected, focused energy would pass through the small hole in the steering/scrapper mirror, then pass to the secondary mirror, the segmented primary mirror, and on to the target.

Table 3.2-2 lists the RMS and P-V OPD wavefront performance of the ABD design. The design incorporates a "perfect" lens in the transverse aberration table output since Code V still does not deal directly with afocal systems.

#### 3.2.2.4 ABD Optical System Performance Evaluation

The ASAP optical propagation code was selected as the most efficient tool for modeling and analyzing the round-trip performance of the ABD system in the presence of primary mirror and beacon perturbations. The ASAP code is discussed briefly in Section 3.3, along with the results of performance analyses for the APACHE beam director. The correctibility of the ABD is found to be a complex function that depends sensitively on the particular perturbation applied to the primary mirror. Nevertheless, the analysis described below indicates that the APACHE BD design developed here performs extremely well over a wide range of applicable parameters for segment piston, tilt, and misfigure, as well as beacon misalignment.

Table 3.2-2. P-V and RMS OPD Wavefront Errors,  
Target and Beacon Channel. ( $\lambda = 2.9 \mu\text{m}$ )

Field Position	Target Channel		Beacon Channel	
	P-V ( $\lambda$ )	RMS ( $\lambda$ )	P-V ( $\lambda$ )	RMS ( $\lambda$ )
On-axis	0.050	0.015	0.008	0.002
Edge of field of view of channel	0.150	0.026	0.080	0.017



### 3.3 APACHE BEAM DIRECTOR ABERRATION AND MISALIGNMENT TOLERANCING ANALYSES

#### 3.3.1 Overview

In the previous section the performance of the APACHE beam director was described under the assumption that all the optics in the train were perfectly aligned and perfectly figured. In this section the results of tolerancing studies to quantify the effects of misalignment and misfigure on the optical performance of the BD are presented. The approach was to use Code V to compute the system aberrations due to misalignment of powered optics in the BD train, and to use the ASAP code to calculate the effects of primary mirror segment misalignment and misfigure, as well as beacon misalignment.

A major source of optical aberration in APACHE or any SBL system is expected to be segment misalignment and misfigure for the very large-aperture, multisegmented primary mirror in the BD telescope. Structural vibrations result in segment misalignments, and fabrication errors along with thermal distortion contribute to segment misfigure. To account for these effects, the ASAP model incorporates a multisegmented primary mirror, as illustrated in Figure 3.3-1. The concentric ring configuration for the segments was chosen so that a single ring of segments will feed one or more amplifiers. This configuration eliminates phase discontinuities along the radial direction in the amplifiers. Annular amplifiers with a narrow gain width, and thus a small radial  $F\#$  in the annular leg are sensitive to discontinuities in the radial direction. Discontinuities in the azimuthal direction are less important since the azimuthal  $F\#$  is large.

Another potential source of optical aberration particular to APACHE is departure of the beacon from its nominal position, coupled with a failure of the optics in the BD beacon and target channels to appropriately compensate for such motions; i.e., "tracking errors." For example, off-axis motion of the beacon is tracked by the beacon tertiary and quaternary mirrors, which articulate to compensate for changes in beacon angular position. Similarly, the beacon on-axis position, i.e., separation distance between the beacon and PM may also deviate from its initial

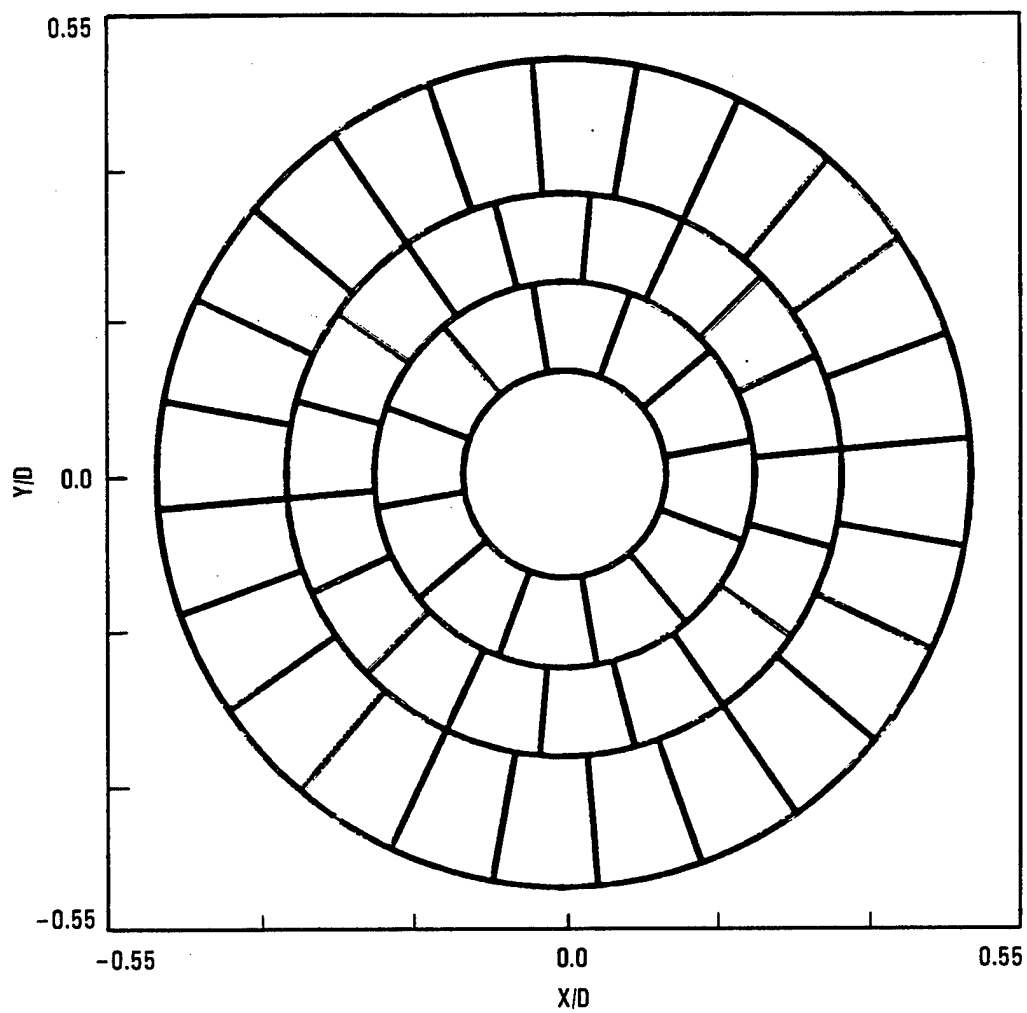


Figure 3.3-1. Segmented APACHE Beam Director

value. Optics in the beacon and target channels would then be articulated to compensate for such changes. Parameters of interest include mirror translations and rotations; deviations from prescribed values for these parameters leads to beam quality degradation. Moreover, when the excursions in beacon angular or on-axis separation distance become to large, even the "best" achievable articulation of the BD optics yield residual errors. In practice, the entire BD would gimbal for beacon or target motions outside the capture ranges of the articulated optics (see Section 2.6).

The tolerancing analyses performed under this program are described in the following subsections. Section 3.3.2 examines the effect of PM segment misalignments on ABD performance, while Section 3.3.3 addresses segment misfigure. In Section 3.3.4, the effect of misalignments of powered beam train optics on system performance is presented. Finally, the effects of beacon motion on ABD performance are analyzed in Section 3.3.5. These studies show that the APACHE system retains excellent wavefront correction capability over a wide range of applicable conditions for ABD alignment and misfigure.

### 3.3.2 Segment Misalignment

The objective of this analysis is to determine the wavefront correction capability of the APACHE BD when the segments of the primary mirror are misaligned relative to their nominal positions. The misalignment consists of piston (i.e., rigid displacement of the segment perpendicular to the surface of the aperture) and tilt (i.e., rigid rotations of the segment in two degrees of freedom about the nominal surface). Although in practice both piston and tilt are concurrent, it is nevertheless useful for the sake of analysis to consider them separately as well. An effective BD optical design must correct both piston and tilt; however, spatial filtering by the amplifier and limitations on the conjugability of tilt by SBS need also be considered in determining the end-to-end performance of the system.

For purposes of the present analysis, piston and tilt will both be expressed in terms of the physical displacement of the segment relative to

the fiducial PM surface; tilt is measured tip to tip on the segment. For a multisegmented mirror, a rms of piston and tilt is taken over all mirror segments. The displacements are expressed in units of HF waves.

While the ASAP model can be used to analyze any given set of segment misalignments, real mirrors are expected to be subject to random structural vibrations, which in turn induce random as opposed to deterministic misalignments of the segments. These are simulated here using random number generators to assign piston and/or tilt to the various segments. While it is also possible to take averages over multiple randomly generated configurations, it was deemed sufficient for the present purposes to use just a single configuration for each run, since the large number of segments facilitates averaging. Trial runs using a limited number of segments and averaging over multiple runs yielded results similar to a single run.

Various cases were run involving pure tilt or piston, as well as combinations of both. Also, cases were run for both 54 and 30 (inner two rings) active segments to determine the sensitivity of correctibility to the number of segments being conjugated.

A computational issue for the case of large tilt was the effect of rays near an edge "crossing" from one segment to another on the return pass. Such rays can contribute anomalously large OPD to the output beam, and would generally be eliminated or reduced via small gaps between the segments. However, diagnostic calculations performed for 18 segments with small gaps between segments displayed similar results to calculations in which the crossover rays were simply removed. For convenience, the latter approach was used in performing the calculations described below.

Results of the calculations for the current design are summarized in Table 3.3-1. The left-hand columns indicate the rms piston and tilt in HF waves of physical displacement. The right-hand columns indicate the output beam OPD when the full 54 segments are active. Incidentally, the design form itself contributes a residual error of approximately 0.005 waves rms, even when the system is perfectly aligned and figured. This is a consequence of the finite BD obscuration and the finite field of view over which the system must operate.

Table 3.3-1. APACHE Beam Director Correction of Random Piston and Tilt

Segment Physical Displacement rms Waves		Output OPD (rms Waves)	Correction Factor (CF)
Piston	Tilt	N = 54	
0.0	2.4539	0.01171	691
0.0	5.479	0.01802	608
8.54	0.0	0.03783	451
9.739	2.657	0.05516	---

$$N = \text{Number of active segments} = 54; \text{CF} = \frac{2 * \text{physical displacement}}{\text{output OPD}}$$

A measure of the correctibility of the ABD is the correction factor CF listed in the table. CF is the factor by which the OPD of the double-pass phase-conjugated output beam has been reduced relative to the single pass OPD (2 x physical displacement) of the misaligned segments. The present design form is seen to possess excellent correction capabilities for both piston and tilt in the regime of interest, i.e., excursions of several waves rms in tilt and/or piston.

Separate analyses were performed to determine the effect of the number of segments on ABD correctibility. Although some dependence on the number of segments was found at large values of piston ( 10 waves rms), the correctibility nevertheless remains high even with 54 active segments, as was indicated previously by the results in Table 3.3-1.

While CF is not expected to be constant over an extended range of input values, it is nevertheless instructive to display the ABD correctibility using a typical value of CF for a restricted range of piston

and tilts. If the effect of tilt and piston are assumed to be independent, then the following formula can be written:

$$(\text{output OPD})^2 = (2 \cdot \text{TILT} / \text{CFT})^2 + (2 \cdot \text{PISTON} / \text{CFP})^2$$

where CFT and CFP are the correction factors for tilt and piston, respectively. Using values from Table 3.3-1 of around 608 for CFT and around 451 for CFP, then for a mid-range of tilts and piston (~2-10) the plot of iso-output-OPD lines in piston and tilt space illustrated in Figure 3.3-2 is obtained. Although this plot is not quantitatively accurate over an extended range, being based on only a few calculated points, it should nevertheless provide a useful approximation to the correctability for mid-values of piston and tilt.

The efficacy of wavefront correction using phase conjugation is demonstrated graphically in Figures 3.3-3 and 3.3-4. The large input values of piston and tilt at the PM result in significant wavefront error of several waves at the conjugator plane. However, the APACHE BD effectively reduces this error to a small fraction of a wave after traversing the BD double pass.

### 3.3.3 Primary Mirror Misfigure

PM segment misfigure may be due to fabrication errors, thermal distortion induced by the HEL output beam, and/or structural vibrations. The ASAP model is capable of simulating any given distribution of surface misfigure over the various segments. In order to simplify the analysis and reduce run time, we carried out calculations assuming sinusoidal misfigures of varying amplitude and spatial frequency in the radial direction over the full PM aperture. Calculations were also carried out for specific distributions of sinusoids. Random distributions of misfigure on the various segments, and combinations of radial and azimuthal variations, involve complicated and costly calculations that we believed were best postponed to later work.

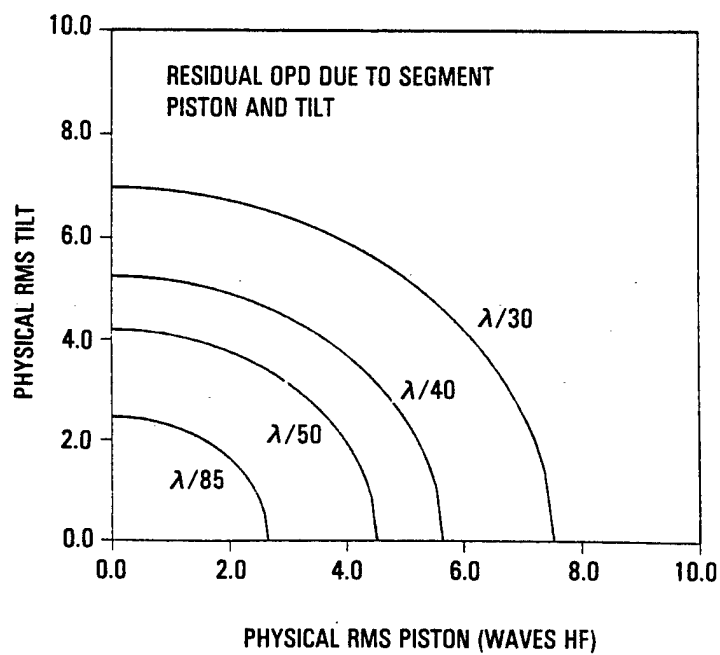
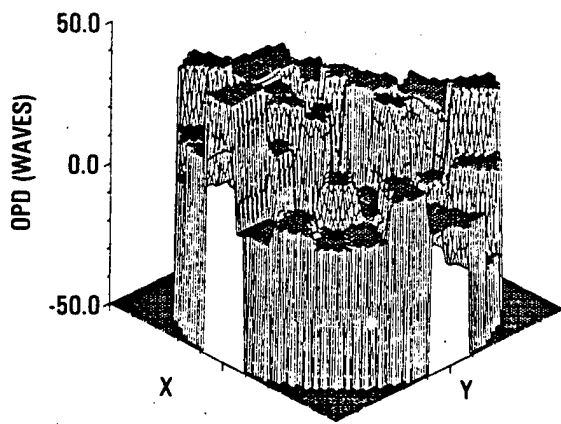


Figure 3.3-2. Tile and Piston Error Correction

#### OPD AT THE CONJUGATOR

PISTON ERROR = 8.54 WAVES (50 x 50)  
P-V = 68.80300 RMS1 = 14.49446



#### OPD OF DOUBLE PATH BEAM

PISTON ERROR = 8.54 WAVES (50 x 50)  
P-V = 0.30234 RMS1 = 0.03783

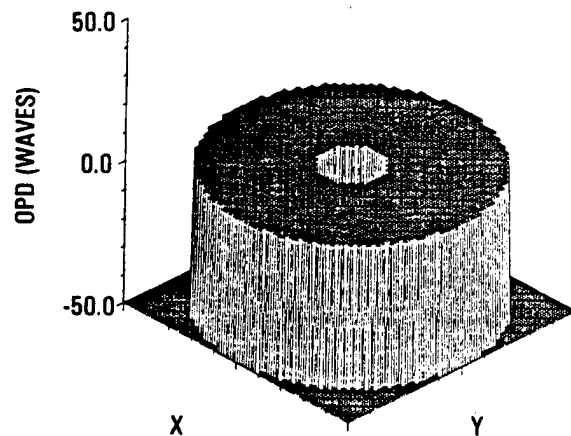
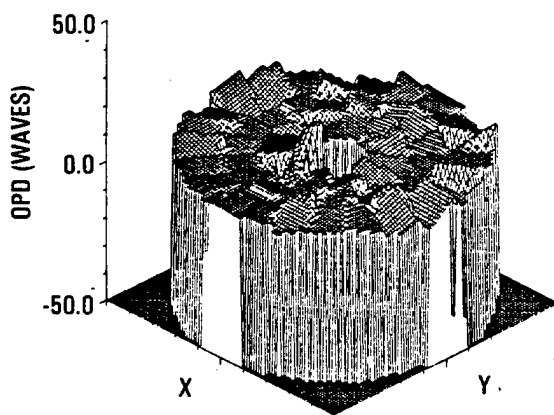


Figure 3.3-3. Piston Error Correction



OPD AT THE CONJUGATOR

TILT ERROR = 5.5 WAVES (50 x 50)  
P-V = 25.50150 RMS1 = 2.3304



OPD OF DOUBLE PATH BEAM

TILT ERROR = 5.5 WAVES (50 x 50)  
P-V = 0.13327 RMS1 = 0.01802

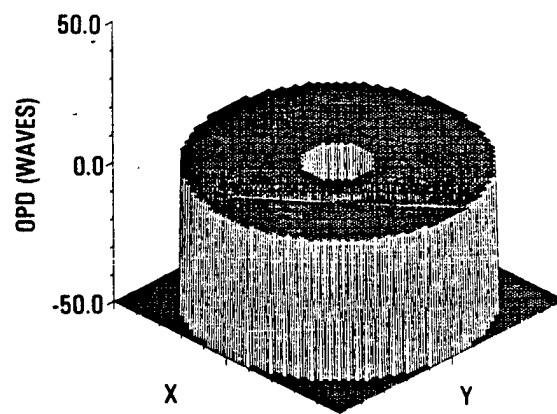


Figure 3.3-4. Tilt Error Correction

The sinusoidal distortions  $D_i$  are expressed as:

$$D_i = 1/2 A_i \cos (2\pi f_i r)$$

$A_i$ : peak-to-valley misfigure (3.3-1)

$f_i$ : spatial frequency

Different combinations of amplitude  $A$  and spatial frequency  $f$  were used in the calculations. The spatial frequency is expressed either as a number of cycles across the aperture diameter, or in units of cycles per meter.

Calculations of output OPD versus input misfigure were performed for a variety of candidate BD optical designs, and the results used to assess each design's ability to correct misfigure. The best overall performance was obtained with the current baseline design and is described as follows.

Table 3.3-2 indicates the correctibility achieved for misfigures consisting of a single sinusoid of given amplitude and spatial frequency. The same information is displayed graphically in Figure 3.3-5 for the rms output OPD versus frequency, and in Figure 3.3-6 for the correction factor versus frequency. The results indicate that the baseline APACHE BD design provides excellent correctibility of misfigure over a considerable range of amplitudes and frequencies. Interestingly, the correction factor varies weakly with amplitude over the range 0.18 to 0.7, so CF essentially becomes a function of spatial frequency (sf) alone. For low values of spatial frequency, CF becomes very large, approximately 40 at 1 cyc/m and rising rapidly below 1. For large spatial frequencies, CF declines to more modest but still impressive levels, eg, 10 for sf=4 cyc/m.

Ray spot diagrams illustrate the correction achieved with a phase conjugate return beam. Figure 3.3-7 indicates a set of equally spaced, parallel rays from the beacon incident at the PM aperture. When the PM is misfigured, the rays form a distorted pattern on the subsequent optics; the ray pattern at the conjugator for a typical case is indicated in the figure. Once the return beam has traversed the target path, the phase of the output beam from the primary has been corrected and it again displays a uniform, undistorted pattern of rays similar to that of the input.

Table 3.3-2. APACHE Beam Director Correction of Primary Mirror Misfigure (Design D)

Input Misfigure			Output OPD			Correction Factor (CF)
P-V (Waves)	RMS (Waves)	Frequency (Cycles)	Number of Rays (NxN)	RMS (Waves)	(BQ)	
0	0	0	50 x 50	0.005662	1.0006	----
1/2	0.1767	15	100 x 100	0.015496	1.0048	22.8
1/2	0.1767	25	100 x 100	0.022910	0.0104	15.4
1/2	0.1767	30	150 x 150	0.027135	1.0146	13.0
1	0.3535	10	75 x 75	0.019431	1.0075	36.4
1	0.3535	15	100 x 100	0.028453	1.0143	24.8
1	0.3535	25	100 x 100	0.043343	1.0378	16.3
1	0.3535	30	150 x 150	0.051868	1.0545	13.6
1	0.3535	40	200 x 200	0.068563	1.0972	10.3
2	0.7070	15	100 x 100	0.051624	1.0540	27.4
2	0.7070	25	100 x 100	0.086032	1.1573	16.4

$$CF = \frac{2 \times \text{RMS physical misfigure}}{\text{RMS OPD (out)}}$$

In general, mirror misfigure will consist of a distribution of sinusoids of variable amplitude, sf and phase. In order to analyze the ABD performance in the presence of a broad spectrum of optical misfigure, a representative distribution of the following form was chosen to simulate fabrication errors of large optical segments:

$$\text{Surface Distortion} = 1/2 \sum_{i=1}^{n=11} A_i \cos (2\pi f_i r + \phi_i)$$

$A_i$ : peak-to-valley misfigure (3.3-2)

$f_i$ : spatial frequency

$\phi_i$ : random phase shift

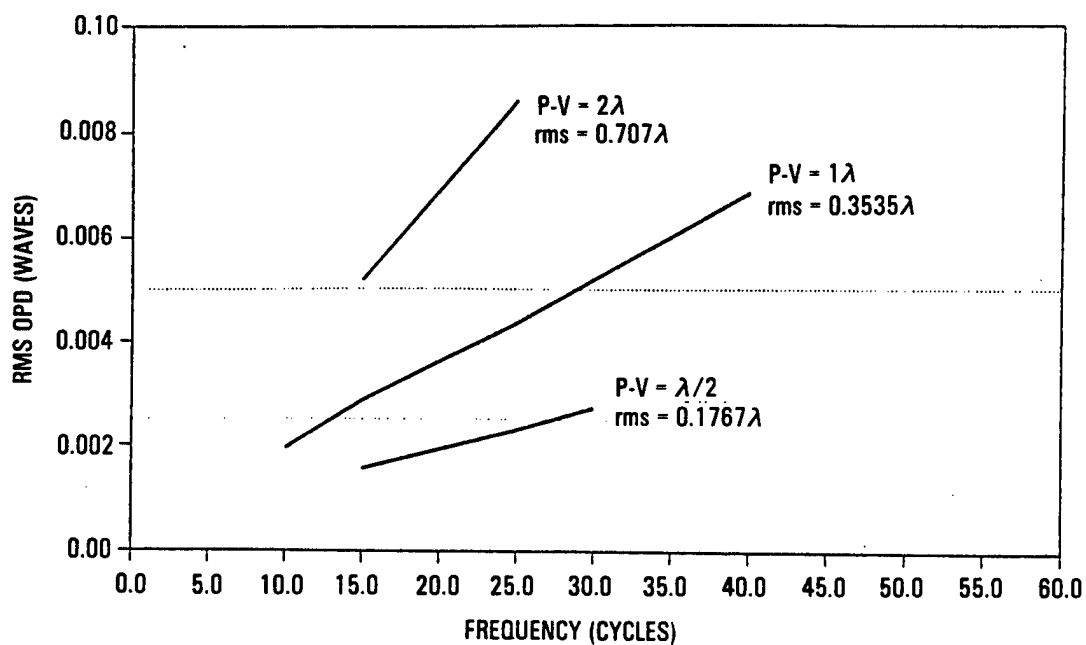


Figure 3.3-5. Residual RMS OPD for the Misfigured Primary

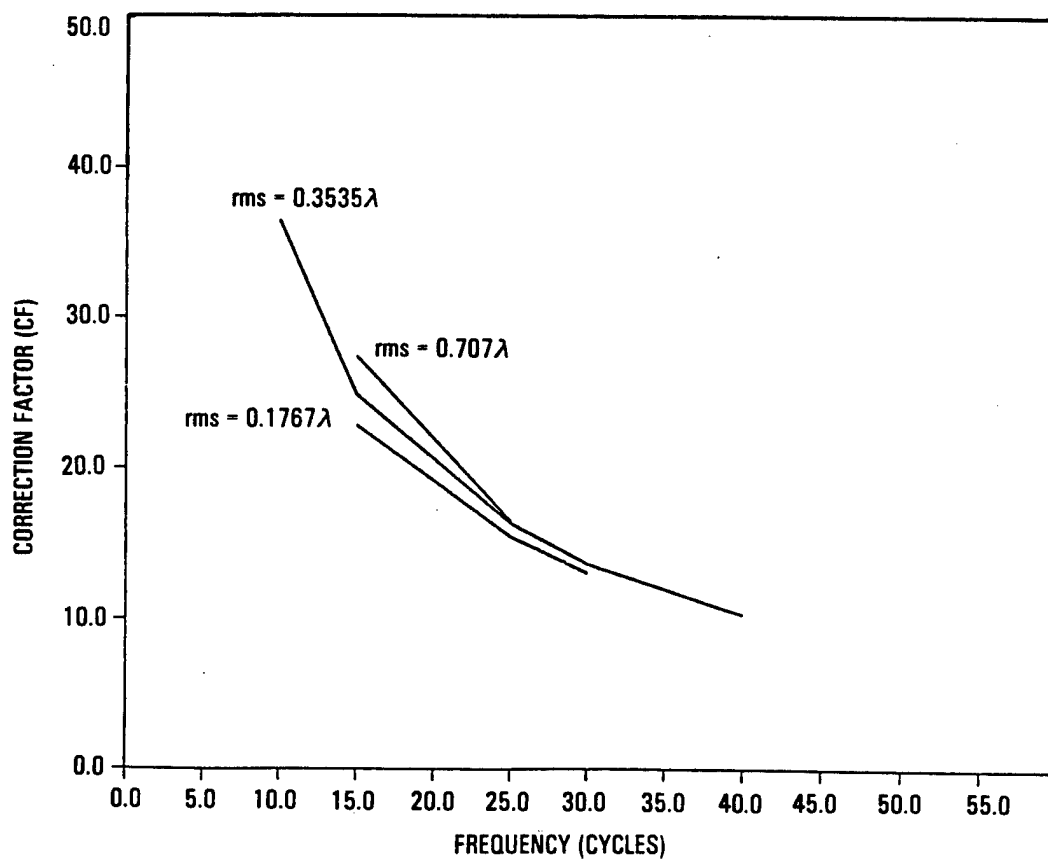
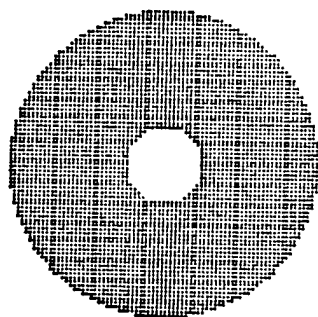
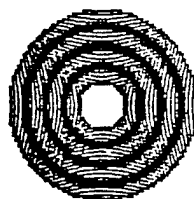


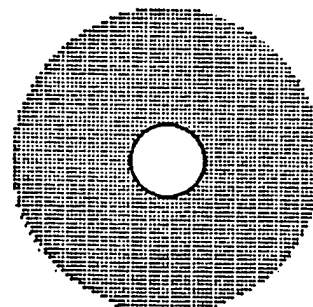
Figure 3.3-6. Correction Factor for the Misfigured Primary



INCOMING TO THE PM



TO THE CONJUGATOR



TO THE TARGET

Figure 3.3-7. Ray Spot Diagram for the Primary Misfigure

The amplitudes  $A_i$  were assumed to fall off as  $1/f$ , yielding the distribution illustrated in Figure 3.3-8. Calculated results for a misfigure amplitude of approximately 0.4 waves rms are indicated in Figure 3.3-8 and 3.3-9. The badly distorted wavefront at the conjugator is cleaned up after the return pass through the BD; the corresponding misfigure correction factor is almost 30. Thus, the APACHE BD is expected to perform well for a range of representative misfigure distributions.

#### 3.3.4 Misalignments of ABD Beam Train Optics

The effect of misalignments of the powered optics on ABD performance was evaluated as part of the trade studies carried out early in the ABD design process. As such, the results presented here should be viewed as preliminary and will require further refinements later.

The effect on wavefront quality using representative values of tilt, decenter, and despacing of the four powered optics in the ABD beam train are indicated in Table 3.3-3. The tolerances on the optics deduced from this analysis are comparable to those given in the literature for adaptive optics beam control systems, and are therefore considered to be reasonable.

#### 3.3.5 Beacon Misalignment

As indicated previously, the BD optical system is designed to operate over a range of beacon and target positions through articulation of the various optics in the BD beacon and target channels. Departures from the optimal articulations will result in degradation of BD performance. Beacon angular misalignments may be parametrized in terms of deviations in the beacon tracking angle. In addition, the beacon on-axis separation distance could depart from its nominal value. The calculations described below were conducted for the simplest initial configuration, where both the beacon and target directions lie on-axis (perpendicular to the PM). Calculations of performance were carried out as a function of both on-axis and angular deviations in beacon position from its nominal value for this configuration.

As will be demonstrated below, beacon off-axis and on-axis displacements introduce tilts and focus, respectively, in the outgoing beam OPD. In practice, both tilt and focus correction would be implemented in the target path to compensate for tilt and focus aberrations

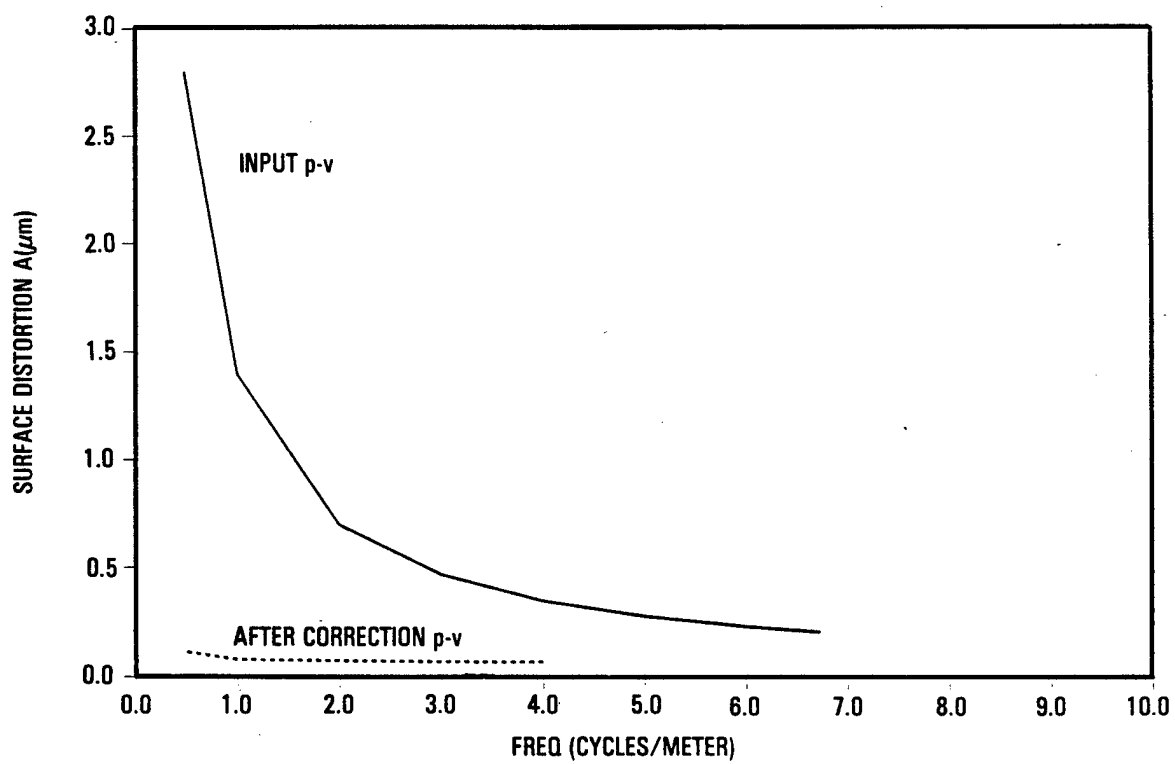
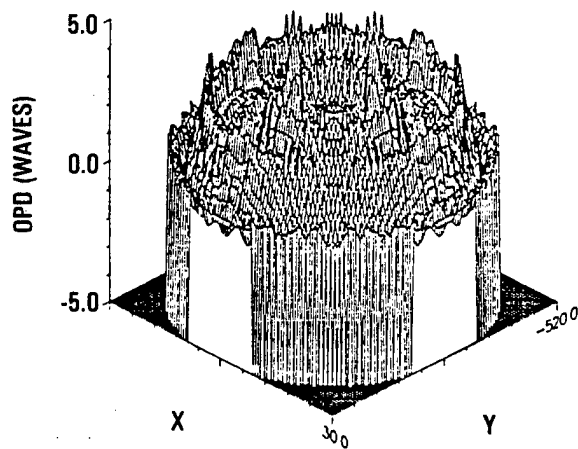


Figure 3.3-8. Misfigured Surface Correction

OPD AT THE CONJUGATOR

P-V=1.7219 WAVES (100 x 100)  
P-V = 4.68691 RMS1 = 0.97484



OPD OF DOUBLE PATH BEAM

P-V=1.7219 WAVES (100 x 100)  
P-V = 0.13236 RMS1 = 0.02858

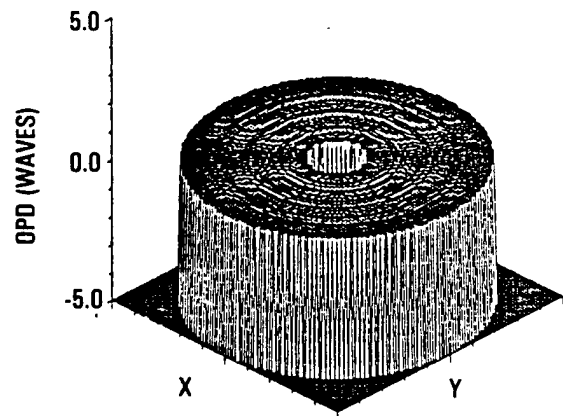


Figure 3.3-9. Correction of Primary Misfigure Spectrum



Table 3.3-3. Impact of Misalignments on Beam Director Wavefront Quality

<ul style="list-style-type: none"> <li>• Misalignments used as 1 SIGMA numbers to generate wavefront errors</li> <li>• Total is RSS of all contributors</li> <li>• <math>RSS = 1/20 \lambda</math></li> <li>• Wavefront errors in parenthesis</li> </ul>			
	Tilt	Decenter	Despace
Secondary	10 $\mu r$ (0.017 $\lambda$ )	100 $\mu m$ (0.015 $\lambda$ )	20 $\mu m$ (0.016 $\lambda$ )
Beacon Tertiary	10 $\mu r$ (0.016 $\lambda$ )	50 $\mu m$ (0.015 $\lambda$ )	10 $\mu m$ (0.014 $\lambda$ )
Beacon quaternary	440 $\mu r$ (0.008 $\lambda$ )	200 $\mu m$ (0.017 $\lambda$ )	10 $\mu m$ (0.014 $\lambda$ )
Target tertiary	440 $\mu r$ (0.010 $\lambda$ )	1000 $\mu m$ (0.012 $\lambda$ )	50 $\mu m$ (0.017 $\lambda$ )

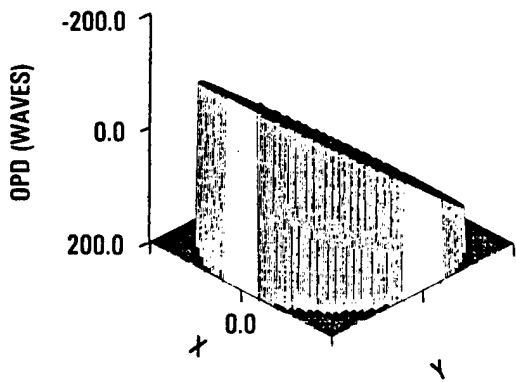
arising from a variety of sources (beacon displacement, birefringent wedge, unconjugated optics, etc). Thus, only higher order aberration residuals are primary concerns for BD performance.

The effect on BD performance of on-axis beacon displacements from nominal was calculated using the ASAP model. The calculations indicate that the excess OPD is primarily focus; the residual with focus removed remains less than 0.02 waves rms over a range of  $\sim \pm 10$  cm. Thus, BD performance is found to be relatively insensitive to on-axis displacements of the beacon.

Off-axis beacon displacements result in large tilts in the outgoing beam, as illustrated in Figure 3.3-10. However, once tilt has been removed, the residual OPD decreases significantly, as indicated in Figures 3.3-10 and 3.3-11. Figure 3.3-11 indicates that the residual remains below 0.02 waves rms for beacon angular displacements up to 160  $\mu rad$ . Companion analyses indicates that beacon excursions of this magnitude fall well within the capture range of the anticipated beacon-BD sensing and control system.

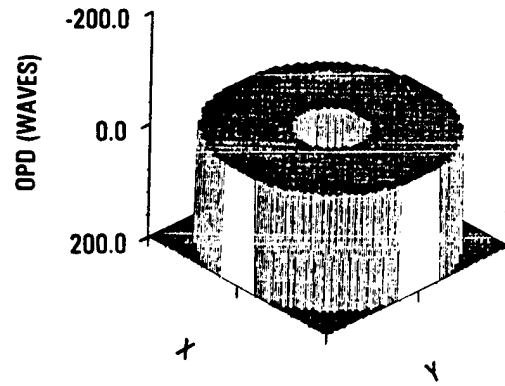
Thus, the ABD system is seen to provide excellent wavefront correction over a significant range of beacon misalignments.

OPD OF DOUBLE PATH BEAM  
OFF AXIS BEACON BEAM  
Y = 2.2 (CM) (50 x 50)  
P-V = 298.06000 RMS = 79.88948



(A) TILT NOT REMOVED

OPD OF DOUBLE PATH BEAM  
OFF AXIS BEACON BEAM  
Y = 2.2 (CM) (50 x 50) TILT REMOVED  
P-V = 0.04344 RMS = 0.01033



(B) TILT REMOVED

Figure 3.3-10. Double-Pass OPD for Off-Axis Beacon Displacement

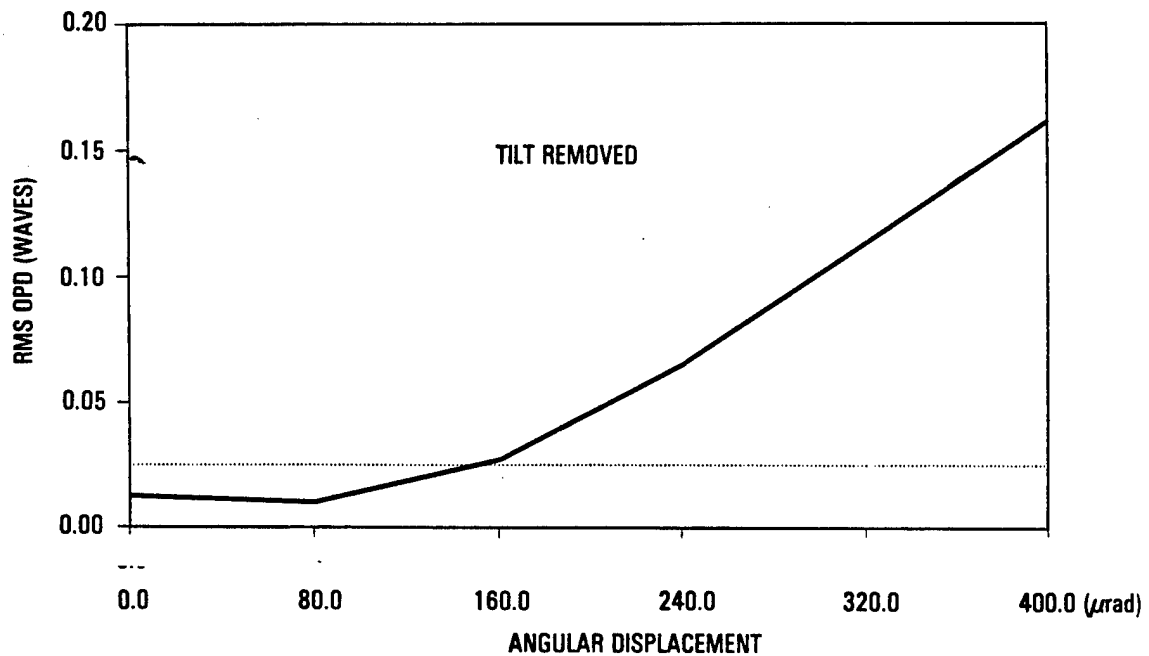


Figure 3.3-11. Sensitivity of OPD to Beacon Off-Axis Displacement

### 3.4 AMPLIFIER MODELING AND ANALYSIS

#### 3.4.1 Introduction

Phase conjugate SBLs require a double-pass configuration to passively correct wavefront aberrations from the primary mirror and from the optics in the amplifier and phase conjugator beam trains. Thus, the amplifiers that provide the power for the phase conjugated SBL are designed to operate in a bidirectional configuration. Seed power is provided by an oscillator whose (spatially-filtered) output samples the aberrations of the primary mirror (PM), is transmitted through the beam director, and then split into six concentric power rings, each incident at one of the six amplifiers in the system. The input beam to each is amplified by traversing the HF gain medium, and the resulting output field is then sent to the phase conjugator. A phase conjugated field of lower intensity (the phase conjugation reflectivity is less than unity) and of lower frequency (by  $\sim 107$  MHz) is returned to the amplifier. This return field experiences a second pass through the amplifier in a direction opposite to the first pass. Both the first pass and the second pass fields act to saturate the gain medium. The return, or second pass, field is output by the amplifier, coherently recombined with the output from the other amplifiers, and directed through the target path of the beam director. Since the return pass target beam is the (amplified) phase conjugate of the input beam, the PM aberrations sampled on the inward pass are removed on the output, resulting in a high-quality beam being directed to the target.

In the following, various aspects of amplifier modeling, design, and gain physics are discussed. First, a brief description of amplifier and oscillator codes used to support the analyses and design effort is presented. Next, the key elements of the annular amplifier concept used in APACHE are described. This is followed by a brief discussion of the gain model physics for bidirectional amplifiers. Finally, an example of the predicted output characteristics of the bidirectional amplifier is presented.

### 3.4.2 Amplifier and Oscillator Models (Codes)

Four principal codes were used for analyzing amplifier and oscillators in the APACHE system, namely CLAM, LFCM, AMP1GS and CROQ. Each of these codes is described briefly below.

The Chemical Laser Amplifier Model (CLAM) is a one-dimensional ("filamentary") model of an HF laser amplifier which includes the modeling of multiple longitudinal modes. The code predicts amplifier extraction efficiency and longitudinal mode intensities. The gain model is described in detail in Bullock, D. L., et al, Advanced Chemical Laser Optics Study (ACLOS) Final Report, AFWL-TR-82-54, Air Force Weapons Laboratory, Kirtland Air Force Base, NM, July 1982. It includes the effects of frequency-dependent gain, multiple longitudinal modes, and velocity cross-relaxation. The return pass through the amplifier may be frequency-shifted, as in the case when an SBS cell is used. The results from CLAM are used to anchor the one-gain-sheet AMP1GS model. In addition to CLAM, a companion code called ANOM (developed under the ACLOS program) models oscillators as opposed to amplifiers.

The Large Fresnel-number Conjugate Mopa (LFCM) code is a two-dimensional laser amplifier model. The fields are one-dimensional. The gain model is a " $g_0$ - $I_{sat}$ " model (although a detailed HF gain model is available in the version called SAM -- Slice Amplifier Model). The one-dimensional field slice propagates via fast Fourier transform (FFT) through the amplifier, with a user-specified number of gain sheets. The LFCM code gives predictions of amplifier extraction efficiency, amplified spontaneous emission (ASE), and phase conjugation and gain medium effects on beam quality (BQ). As discussed in Section 3.6, LFCM has been used to model the bidirectional amplifiers in the APACHE end-to-end optical propagation model (APOPM). In this model, LFCM is coupled on the input end to the ASAP model of the BD, and on the first-pass output to the BRIWON code for the SBS phase conjugator.

The AMP1GS (amplifier one-gain-sheet) model designed to run on a personal computer using the software tk!Solver. It is a one-dimensional, one-gain-sheet, " $g_0$ - $I_{sat}$ " model which uses the concept of average gain and

average intensity over the gain length to give an estimate of the amplifier extraction. It predicts the trends in power-to-phase conjugator and power output as a function of amplifier gain length and amplifier input power. A simple model for the effects of SBS-frequency-shifted return is included. AMP1GS is used to model the bidirectional amplifier in the APACHE Systems Analysis Model (ASAM), as discussed in Section 4.2.

The Cylindrical Resonator Optical Quality (CROQ) code predicts the performance of ALPHA-like HF cylindrical oscillators, and could be modified to apply to certain aspects of amplifiers as well. It is a three-dimensional, physical-optics code with detailed (rotational nonequilibrium) HF kinetics and an approximate fluid mechanics model. This code was used extensively on the ALPHA program to predict resonator performance. Those results have been used on APACHE to anchor the approximate gain model and resonator performance parameters contained in the CLAM, LFCM and AMP1GS codes.

#### 3.4.3 Amplifier Conceptual Design

The APACHE amplifier, part of which is indicated schematically in Figure 3.4-1, is based on a cylindrical gain generator analogous to the one used in the ALPHA resonator. This design facilitates a large gain volume, which is determined by both the diameter of the gain generator as well as its length. In a linear, as opposed to a cylindrical, device the volume is determined by the height of the gain generator. Since the mode width is small (2.5 to 5.0 cm), a large gain volume implies a large aspect ratio; such amplifiers encounter difficulties with mirror fabrication, as well as unequal diffraction (due to very different Fresnel number ( $F\#$ ) in the two mirror dimensions).

Note that the amplifier design used in the present discussion involves two passes through the gain region in each direction. In subsequent work under APEX, we plan to analyze alternative amplifier designs involving a single pass through the gain region in each direction. Such designs appear advantageous for increasing the  $F\#$  of the amplifier and thereby reducing gain-phase effects. The physics and amplification characteristics, however, would be expected to remain similar to these discussed here.

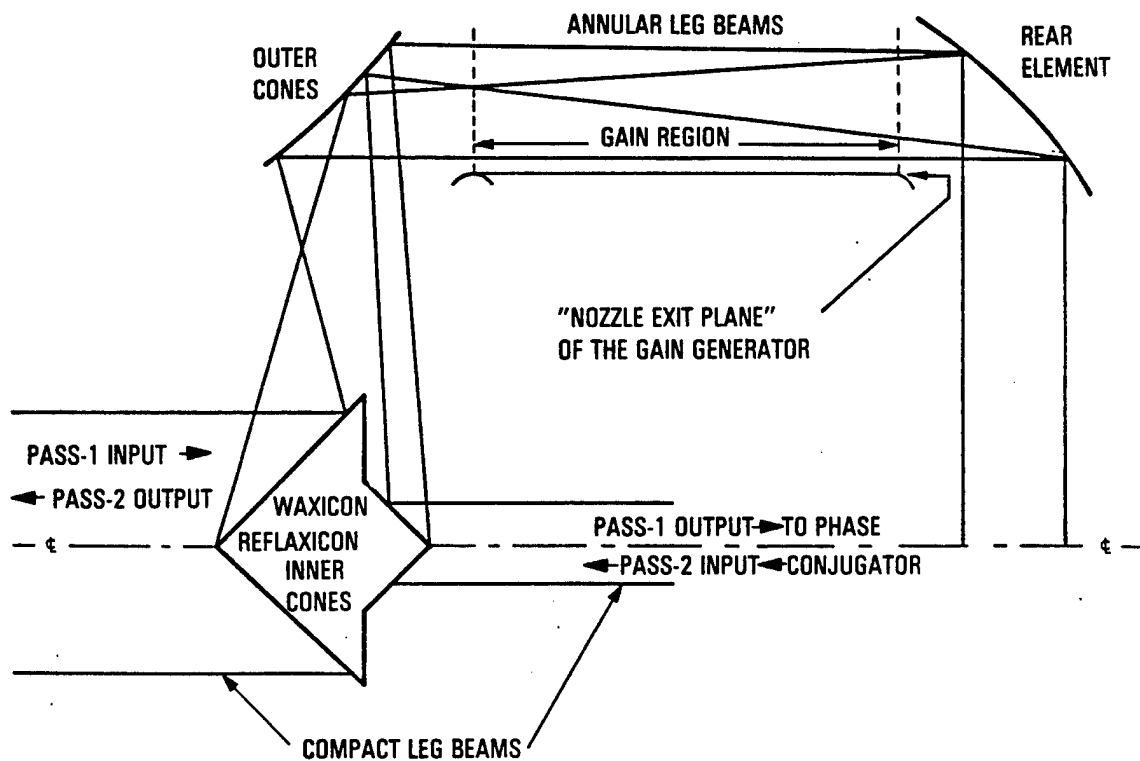


Figure 3.4-1. Schematic of Beam Path Through Amplifier Annular Leg

Within the APACHE SBL concept, each amplifier receives an input beam in the shape of a doughnut. (The doughnut varies in size for each amplifier because the beam coming from the BD is split into six concentric rings which feed six amplifiers). The input doughnut is increased in size by an axicon, so that its inner diameter is slightly larger than the diameter of the amplifier gain generator.

The amplifier possesses a rear cone and two axicons, similar to the ALPHA resonator. On one side of the gain generator are the two axicons, and on the other side is the rear cone. The beam on the first pass through the amplifier enters the annular leg via the reflaxicon outer cone, expands as it passes through the gain medium, hits the rear cone, is reflected across the rear cone, then gets smaller as it passes through the gain medium and returns to the waxicon outer cone.

The beam then gets changed from a doughnut to a circle by the waxicon. The spectral lines of the amplifier's pass-1 output are separated. Each spectral transition has six fields from the six amplifiers combined and sent to a phase conjugation cell. The fields from the phase conjugators retrace their paths, and the return field (containing all spectral transitions, each having been subject to its phase conjugate reflectivity and fidelity) enters the amplifier at the waxicon for the beginning of pass 2.

Pass 2 through the amplifier retraces path 1 through the annular region, exiting the amplifier at the reflaxicon. Figure 3.4-1 shows a slice through half of an amplifier, with arrows indicating the paths in the annular leg of pass 1 and pass 2.

#### 3.4.4 Amplifier Gain Physics

This section discusses the physics involved in the gain models used to analyze the APACHE amplifiers. The gain as a function of frequency is Doppler broadened in a Gaussian shape due to the velocity spread of the gaseous particles. The Doppler half-width at half maximum is given by:

$$\Delta\nu_D = \nu_0 [2kT \ln 2 / (Mc^2)]^{1/2} \quad (3.4-1)$$

where  $\nu_0$  is the line center frequency,  $k$  is Boltzman's constant,  $T$  is the temperature,  $M$  is the molecular mass, and  $c$  is the speed of light.  $\Delta\nu_D$  will be about 205 MHz in the APACHE amplifiers.

The oscillator cavity will have a number of longitudinal modes which lase because the gain for them will be above threshold. The longitudinal mode spacing is  $c/L$  for a ring laser, where  $L$  is the cavity length. For example, if the oscillator is a ring with a 25-m resonator length, the longitudinal mode spacing will be 12.0 MHz. Figure 3.4-2 shows the intensities of the longitudinal modes and the resonator as a function of frequency for an ALPHA oscillator, calculated using ANOM (i.e., the oscillator version of the CLAM code).

The threshold gain is given by the gain-equals-loss condition:

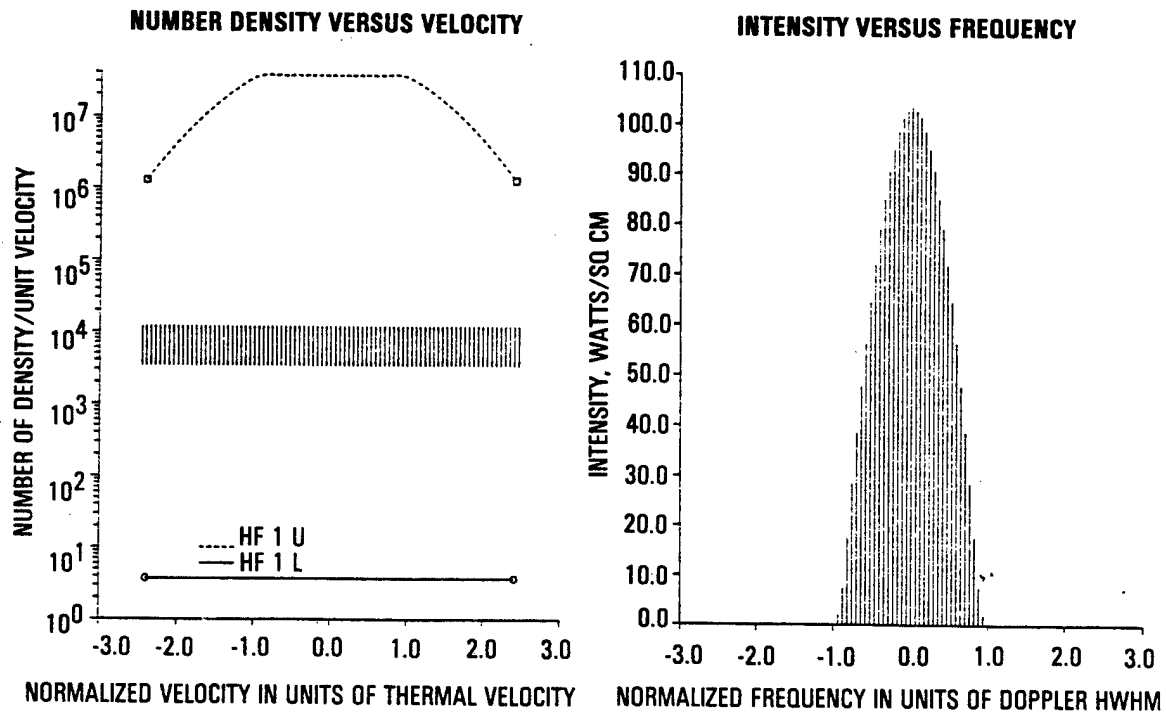
$$\text{round-trip-gain} * \text{feedback fraction} = 1$$

$$\exp(2g_{th}L_{gain}) * (1/Mag^2) = 1 \quad (3.4-2)$$

In the example of Figure 3.4-2, the small-signal gain peaks at about 0.02, whereas the threshold gain is 0.0055. The lasing modes have pulled the gain down to the threshold value. The modes are so closely spaced that "hole burning" is not visible -- the gain appears flat at threshold. The longitudinal modes near line center have higher intensities than those farther from line center because the small signal gain near line center is farther above threshold.

The amplifier also has a Doppler-broadened gain curve. In the amplifier, the longitudinal modes from the oscillator will have access to the gain at their frequency. In a two-way amplifier with no frequency shift of the return (pass 2) intensity, the longitudinal mode distribution in frequency space about the line center frequency would be close to symmetric (exactly symmetric if the longitudinal modes are symmetric about line





DOPPLER HWHM = 205.2 MHz  
 LORENTZ HWHM = 7.1 MHz

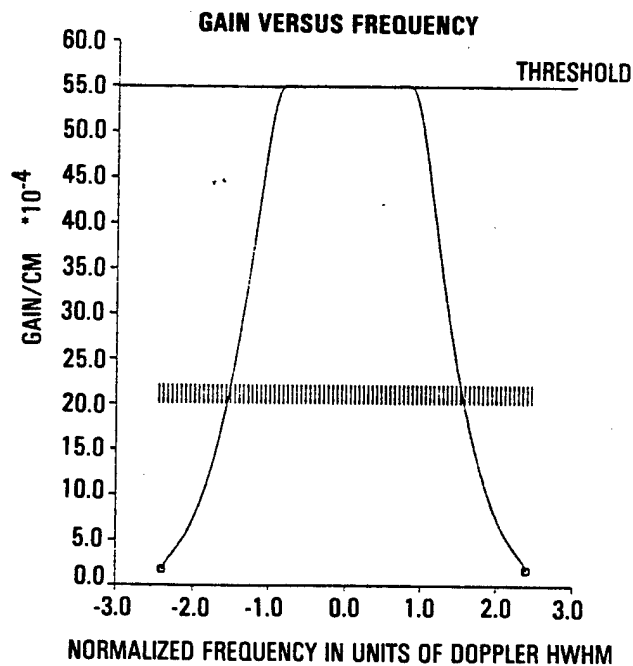


Figure 3.4-2. ALPHA Sized Oscillator

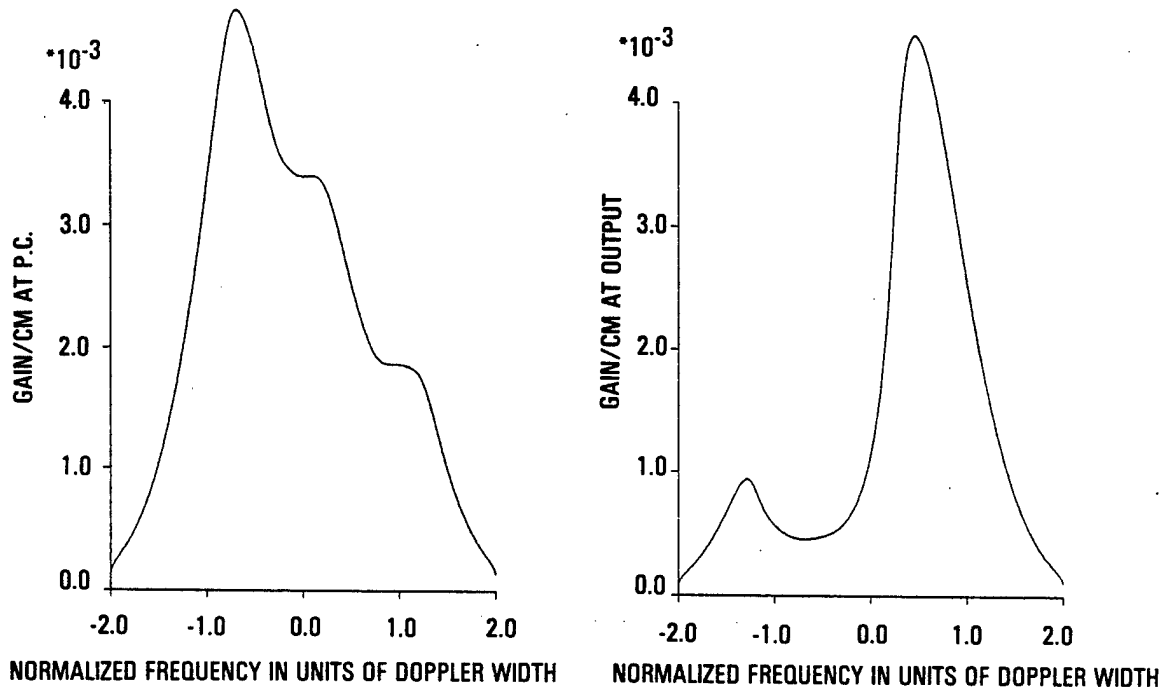
center). The pass-1 modes and the pass-2 modes would see the same gain, and the "hole" burned in the gain would be symmetric about the line center frequency. This can be seen in the no-shift-case gain curves of Figure 3.4-3, calculated using the CLAM code. In this case, the pass-1 amplification would exactly equal the pass-2 amplification.

Note that there are unused gain "wings." The amplifier has no "threshold gain" condition; its gain saturation is determined by the intensities of the longitudinal modes coming from the oscillator. Although a longer-gain-length oscillator would have lasing longitudinal modes farther from line center, and thus a better utilization of the amplifier gain, such an oscillator would also have lasing on more spectral transitions. On balance, having fewer transitions gives more efficiency in a system which must have a separate phase conjugation volume for each transition to be returned through the amplifier.

In a two-way amplifier with a -107 MHz frequency-shifted return from the phase conjugator, the return longitudinal modes would see gain over a different frequency range than the pass-1 longitudinal modes. Figure 3.4-3 shows the gain curves for this case. Figure 3.4-4 shows the pass-1 output and pass-2 output longitudinal modes for the cases of a frequency-shifted and non-frequency-shifted return, calculated using the CLAM code. Notice that the pass-1 modes in the frequency-shifted case have a higher peak intensity than those in the no-frequency-shift case. Also note that the pass-1 below-line-center modes are generally at a higher intensity than the above-line-center modes in the frequency-shifted case. These phenomena are due to the fact that in the frequency-shifted case, half the pass-1 modes see very little competition for the gain from the pass-2 modes, while the other half of the pass-1 modes see far more competition for the gain from the pass-2 modes than they would see for a not-shifted set of pass-2 modes (for the case modeled).

A mode at frequency (relative to line center) of  $+\Delta\nu$  propagating in the  $+z$  direction will see the same gain as a mode at frequency  $-\Delta\nu$  propagating in the  $-z$  direction. In Figure 3.4-3 the gain curve at the phase conjugator side of the amplifier (pass-1-output side) is shown from

**FREQUENCY SHIFTED RETURN (-107 MHz): GAIN VERSUS FREQUENCY AT P.C. AND OUTPUT**



**RETURN NOT FREQUENCY SHIFTED:**

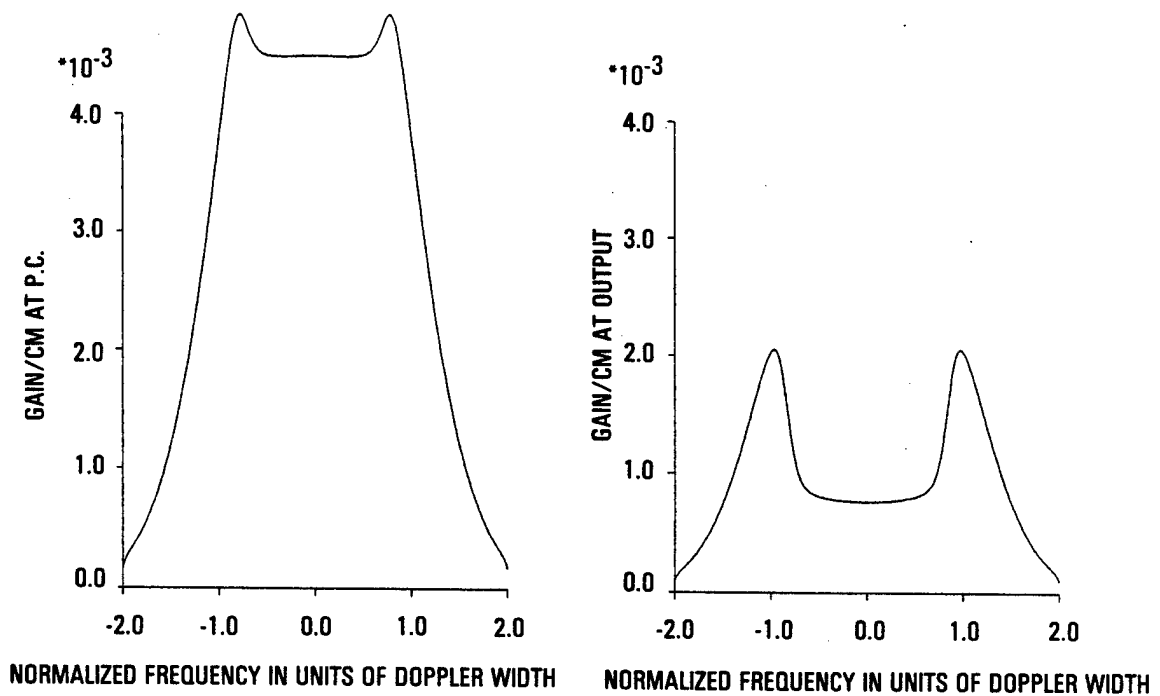
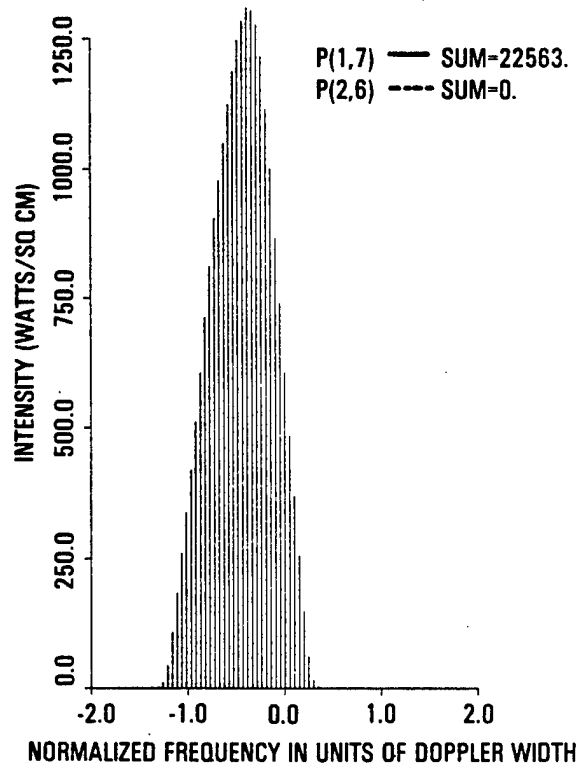
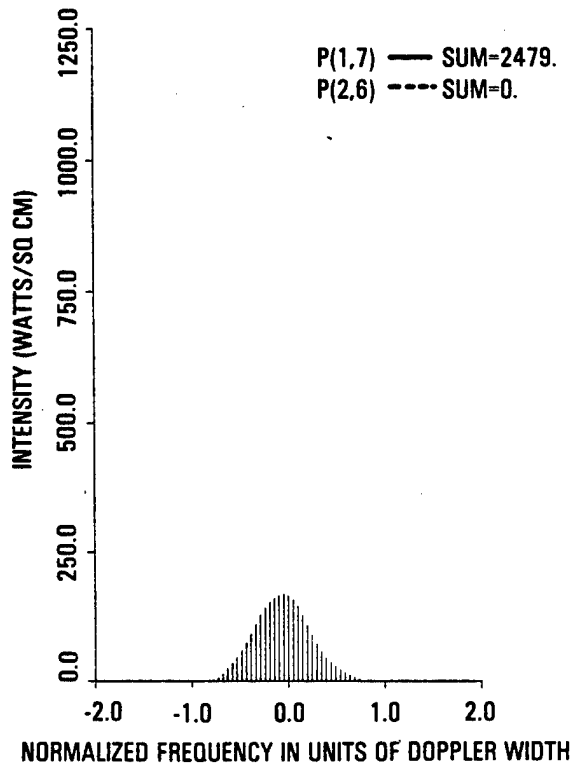


Figure 3.4-3. Two-Way Amplifier with Input from Oscillator with 200-cm Gain Length

# **FREQUENCY SHIFTED RETURN (-107 MHz): TO-P.C. AND OUTPUT INTENSITIES**



## **RETURN NOT FREQUENCY SHIFTED:**

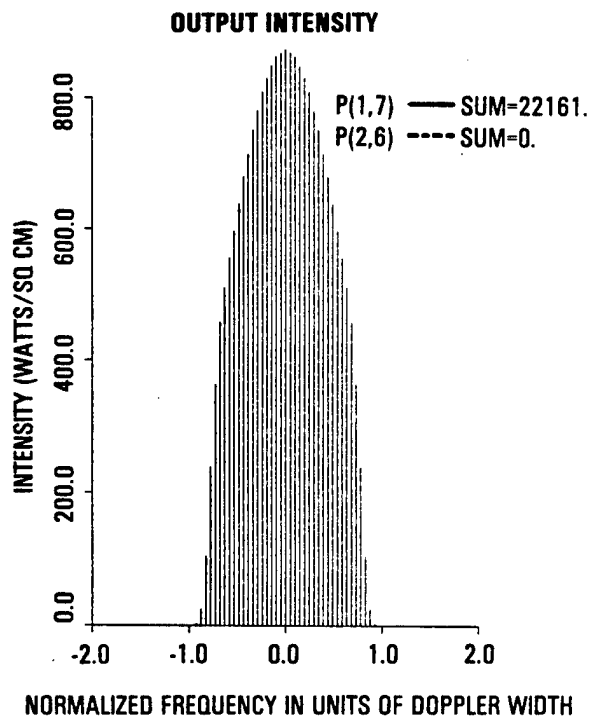
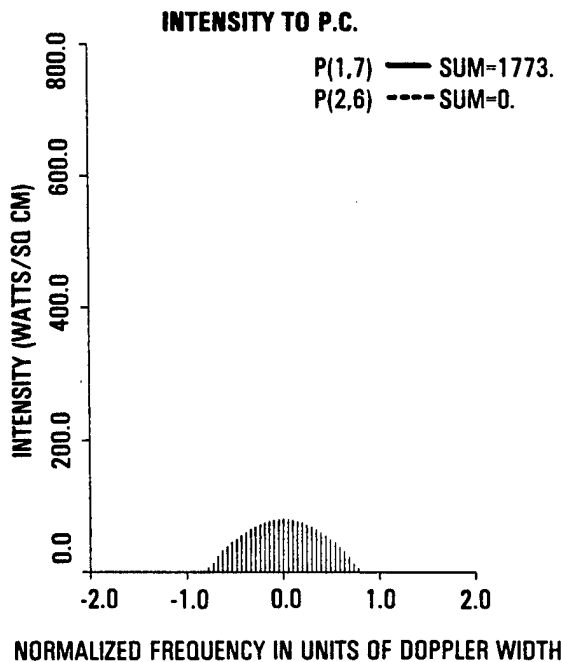


Figure 3.4-4. Two-Way Amplifier with Input from Oscillator with 200-cm Gain Length

the perspective of the pass-1 beam coming towards the observer. The pass-2 (return) modes will thus tap into gain on the positive frequency side of the plot. The gain at the amplifier output is essentially saturated by the pass-2 modes, since the pass-1 input modes are about 200 times less intense than the output modes.

Figure 3.4-5 shows the pass-1, pass-2, and overall (2-way) amplification as a function of frequency shift of the return modes, again calculated using the CLAM code. The overall amplification is related to the one-way amplifications by:

$$\text{Amp(overall)} = \text{Amp(pass 1)} * \text{Amp(pass 2)} * \text{SBS reflectivity.}$$

(The SBS reflectivity in this study was 0.5.) For SBS frequency shifts up to slightly more than half the Doppler halfwidth, which includes the case of a 107-MHz downshift, the two-pass amplification is approximately equal to that for the case of no frequency shift. This is due both to more gain being available to many of the pass-1 modes and to enough gain being available to the pass-2 modes to provide reasonable amplification.

#### 3.4.5 Amplifier Performance--Calculated Results

In this section results of calculations obtained using AMP1GS, and taking into account the dependence of SBS reflectivity on input power, are presented. One finds that the amplifier output power is relatively insensitive to the input power. Figure 3.4-6 shows normalized output power as a function of normalized input power, with the output power varying less than 10% for an input power variation of over two orders of magnitude.

This result implies that for a system with an SBS input power well above threshold, a drop in oscillator brightness (due, for example, to feedback of amplifier output through the oscillator isolation subsystem) will cause only a small drop in system output power.

The amplifier is self-healing. A smaller input gives less power to the SBS phase conjugator, which gives a smaller SBS reflectivity which gives less return signal to compete with the pass-1 signal at the phase-

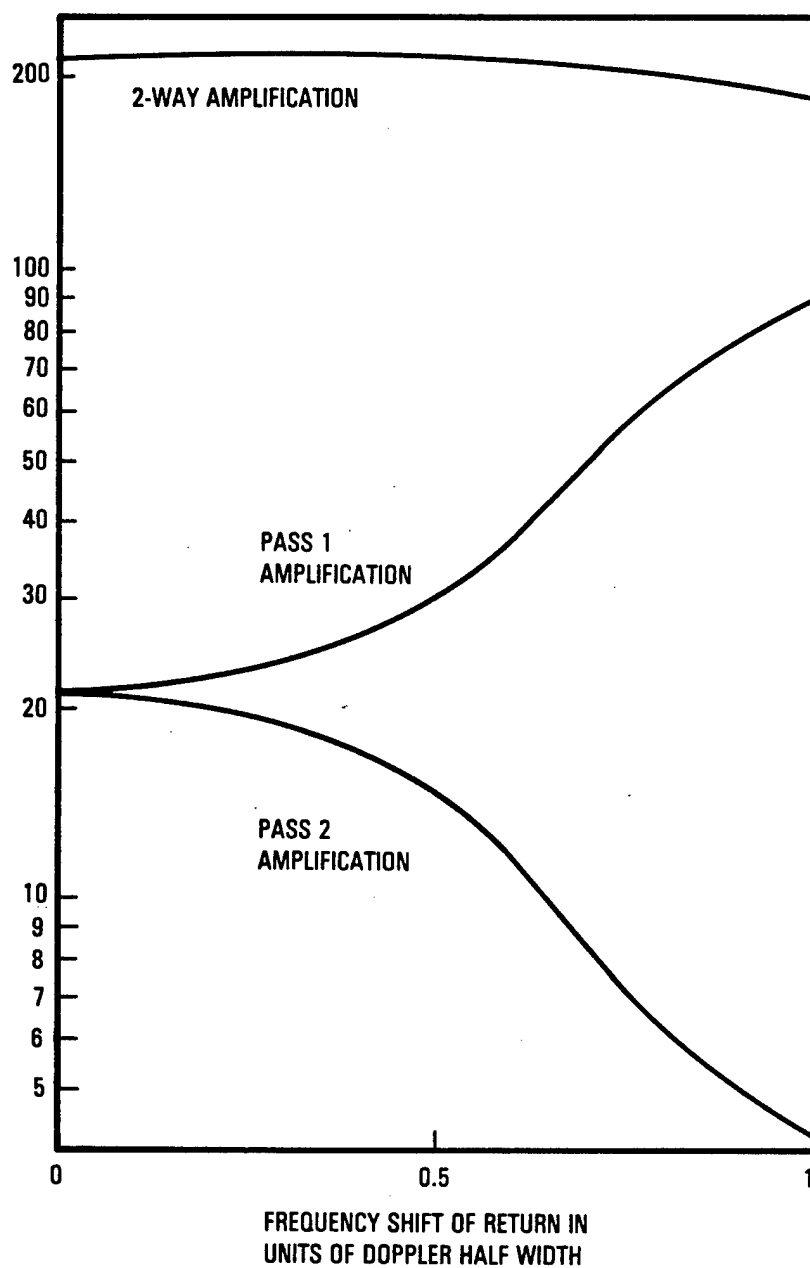
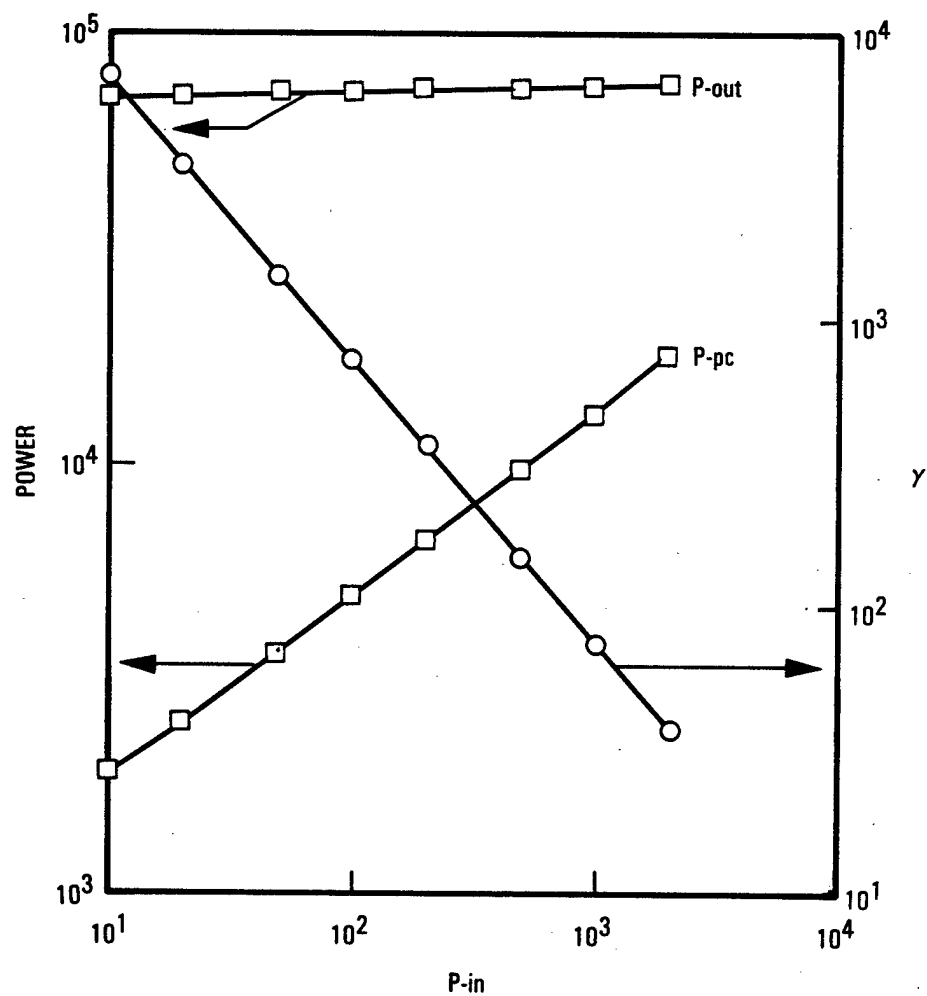


Figure 3.4-5. Input Intensity Amplification Versus Frequency Shift of Return



$P_{in}$  = INPUT POWER TO AMPLIFIER  
 $P_{out}$  = NORMALIZED ROUND-TRIP AMPLIFIER OUTPUT POWER  
 $P_{pc}$  = NORMALIZED POWER TO PHASE CONJUGATOR  
 $\gamma$  = ROUND-TRIP AMPLIFICATION

Figure 3.4-6(a). Normalized Roundtrip Amplifier Output Power, Normalized Power to Phase Conjugator, and Roundtrip Amplification Versus Input Power to Amplifier

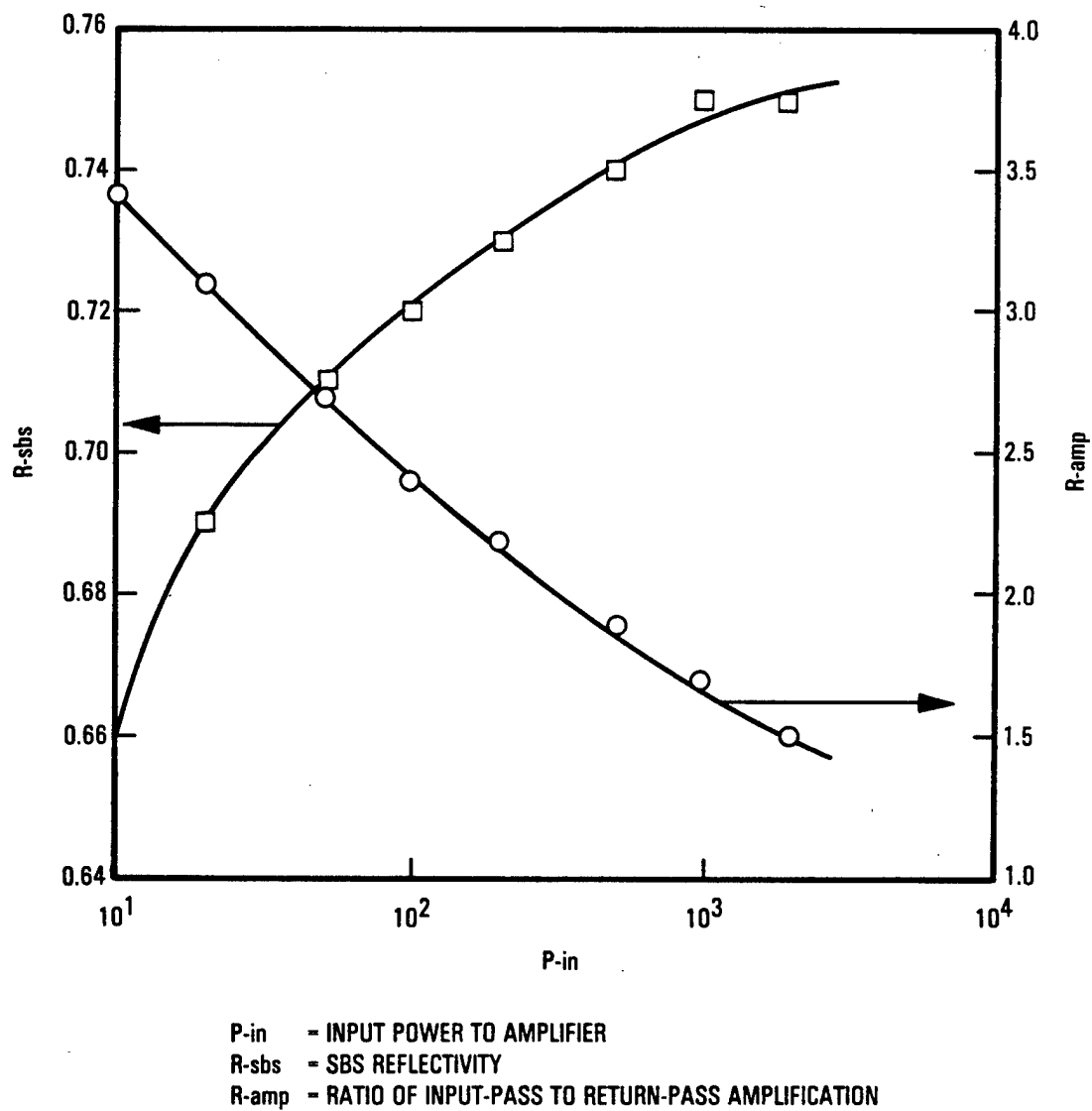


Figure 3.4-6(b). SBS Reflectivity and Ratio of Input Pass to Return Pass Amplification Versus Input Power to Amplifier



conjugator end of the amplifier, which leads to a larger pass-1 amplification.

The SBL amplifiers will yield nearly the same output, even though the input drops, as long as the power to the SBS cells have sufficient margin above threshold.

### 3.5 BRIWON MODEL OF STIMULATED BRILLOUIN SCATTERING

#### 3.5.1 Applications

The BRIWON code is one element of the end-to-end propagation model and simulates the effects on the field of imperfect stimulated Brillouin scattering (SBS) phase conjugation. The input (pump) field is the output of the amplifier that has been propagated to the location of the focusing lens of the SBS cell. The phase-conjugate output (Stokes) field is calculated by the BRIWON code and, in the end-to-end model, is propagated back to the position of the amplifier.

As part of the end-to-end model or as a stand-alone code, BRIWON is used in parametric studies to relate the effects on the Stokes field to the strengths of aberrations, either internal or external to the SBS cell. The types of external aberrations modeled correspond to tilt, piston, or misfigure errors on the beam director mirror, or, indeed, any departure from an ideal field due to any optical elements in the end-to-end model; in addition, the effects of random phase variations due to turbulence (as would occur in an aerowindow of the SBS cell, for example) may be calculated. Internal to the cell, the aberrations modeled result from absorption by the flowing gas, leading to thermal blooming, and from the motion of the gas and acoustic grating, leading to grating convection effects. Geometrical parameters ( $F\#$  of the focusing lens and SBS cell length) and physical parameters, e.g., pump power, wavelength, SBS medium, flow velocity, absorption coefficient, and self-focusing, all may be varied. Multiple foci, a configuration which will effect a reduction of threshold, is also modeled.

Used as a stand-alone code, BRIWON provides two measures of the effectiveness of phase conjugation: conjugation fidelity, a number which is a correlation coefficient between the input pump field and the output Stokes field; and beam quality, which measures the focusability of the Stokes field after it has again passed through any aberrators internal to the cell or at the focusing lens. As an element of the end-to-end code, in which aberrations are introduced upstream of the SBS cell, BRIWON provides only the conjugation fidelity number as a meaningful measure of the effectiveness of the conjugation process.

### 3.5.2 Physical SBS Model

#### 3.5.2.1 The Standard Model

The coupled differential equations for density, temperature, and electromagnetic field, which form the basis of the BRIWON code, were derived for the general case of a flowing medium. For a stationary medium, Kaiser and Maier (Reference 3.5-1) derived coupled differential equations for the density and temperature fluctuations from the Navier-Stokes equation, the energy transport equation, and the equation of continuity, assuming the slowly varying amplitude approximation and strong damping of the acoustic waves. These differential equations were solved (the details are given in Section 3.5.5) and the phonon amplitude expressed in terms of the product of pump and Stokes fields. The solution was then generalized to the case of a medium flowing uniformly in a direction transverse to the propagation direction, which, when combined with the steady-state electromagnetic field equations for the pump and stokes fields, lead to the following equations:

$$\frac{\partial}{\partial z} E_L - \frac{i}{2k_L} \frac{\partial^2}{\partial x^2} E_L + \frac{a}{2} E_L - i \frac{n_2 k_L}{2n} (|E_L|^2 + |E_S|^2) E_L = G |E_S|^2 E_L \quad (3.5-1)$$

$$\frac{\partial}{\partial z} E_S + \frac{i}{2k_S} \frac{\partial^2}{\partial x^2} E_S - \frac{a}{2} E_S + i \frac{n_2 k_S}{2n} (|E_L|^2 + |E_S|^2) E_S = G^* |E_S|^2 E_L^* \quad (3.5-2)$$

where the pump field is assumed to be propagating in the +z direction, the Stokes field in the -z direction, and the gain G is given by:

$$G(x, z, u) = g F(x, z, u)$$

$$g = \frac{g_0}{1 + (\Delta\omega/\Gamma)^2} [-(g_r^{\text{elec}} + g_r^{\text{abs}}) + i(g_i^{\text{elec}} + g_i^{\text{abs}})] \quad (3.5-3)$$

where

$$\begin{aligned}
 g_o &= \frac{k^2 \gamma^e \omega_L}{32\pi c n \rho_0 \omega \Gamma} \\
 g_r^{abs} &= \frac{n a c \beta_T v^2 (\Delta \omega)}{c_p \omega \Gamma} \\
 g_i^{abs} &= \frac{n a c \beta_T v^2}{c_p \omega} \\
 g_r^{elec} &= \frac{\gamma^e}{2} \\
 g_i^{elec} &= - \frac{\gamma^e (\Delta \omega)}{2 \Gamma}
 \end{aligned} \tag{3.5-4}$$

The function  $F(x, z, u)$  is unity for a nonflowing medium but otherwise is a function of the field amplitude and the flow velocity  $u$  (Equation 3.5-51). In these equations the following quantities are defined:

- $k$  = acoustic wave propagation vector.  $k = k_L + k_S \approx 2k_L$
- $\omega$  =  $\omega_L - \omega_S$  = frequency of the acoustic wave
- $v$  = phonon velocity
- $\gamma^e$  = electrostrictive coupling coefficient
- $c$  = the speed of light
- $n$  = the index of refraction
- $n_2$  = nonlinear index of refraction
- $\beta_T$  = the coefficient of thermal expansion

- $C_p$  = specific heat at constant pressure
- $\gamma$  = the ratio of specific heats
- $\alpha$  = linear absorption coefficient
- $\rho_0$  = ambient density.

We have defined  $\Delta\omega = \omega - \omega_B$ , where  $\omega_B$  is the Brillouin frequency  $\omega_B = k_B v = 2\omega_L v n/c$ , and assumed that  $\omega - vk \sim \Delta\omega$ ,  $\omega \sim \omega_B$ ,  $\Gamma/\omega \ll 1$ , and  $\Delta\omega/\omega \ll 1$ . The terms in  $g$  are the real and imaginary parts of the absorptive and electrostrictive gains.  $\Gamma$  is a weighted average of the Brillouin and Rayleigh line widths

$$\Gamma = \frac{1}{2} [\Gamma_B + (\gamma - 1) \frac{1}{2} \Gamma_{RL}] \quad (3.5-5)$$

The electromagnetic field equations are in their scalar form so that polarization effects, if any, will be ignored. In addition, there is no explicit dependence in these equations on the second traverse ( $y$ ) coordinate so that the description of the wave-optics is basically two dimensional. However, since the gain depends on the intensity in the medium, it is important to account for the increased intensity in the cell due to focusing in the  $y$  direction. To this end, the BRIWON code adjusts the pump and Stokes intensities at each  $z$  position to correspond to quasi-geometric focusing in the  $y$  coordinate. The intensity and phase changes within the cell as the field propagates from a plane  $z_0$  to  $z = z_0 + \Delta z$  may be derived from the differential equations, assuming no diffraction or absorption. One obtains, as an energy conservation equation

$$I_L - I_S = I_L^0 - I_S^0 \quad (3.5-6)$$

where the zero superscript denotes quantities at  $z = z_0$ , and  $I$  is the intensity. In addition, the pump and Stokes intensities are (for zero flow velocity)

$$I_L = \frac{(I_L^0 - I_S^0) I_L^0}{I_L^0 - I_S^0 e^{-\Phi_0}} \quad (3.5-7)$$

and

$$I_S = \frac{(I_L^0 - I_S^0) I_S^0 e^{-\Phi_0}}{I_L^0 - I_S^0 e^{-\Phi_0}} \quad (3.5-8)$$

and the corresponding phase changes are

$$\phi_L - \phi_L^0 = -\frac{1}{2} \Gamma(G) (I_L^0 - I_S^0) \Delta z + \frac{\Gamma(G) + \Delta}{2R(G)} \ln \left[ \frac{(I_L^0 - I_S^0) e^{-\Phi_0/2}}{I_L^0 - I_S^0 e^{-\Phi_0}} \right] \quad (3.5-9)$$

$$\phi_S - \phi_S^0 = -\frac{1}{2} \Gamma(G) (I_L^0 - I_S^0) \Delta z + \frac{\Gamma(G) + \Delta}{2R(G)} \ln \left[ \frac{(I_L^0 - I_S^0) e^{-\Phi_0/2}}{I_L^0 - I_S^0 e^{-\Phi_0}} \right] \quad (3.5-10)$$

where

$$\Phi_0 = -2 (I_L^0 - I_S^0) \Delta z R(G) \quad (3.5-11)$$

and  $R(G)$  and  $\Gamma(G)$  are the real and imaginary parts of the gain  $G$ . The generalization of these equations to a nonzero flow velocity are derived in Section 3.5.5. An iterative method is used in BRIWON to solve the differential equations, as described in Section 3.5.3.

### 3.5.2.2 Thermal Blooming

In general, the absorption coefficient  $\alpha$  is taken to be zero since the iterative solution of the equations is not fully implemented for  $\alpha = 0$ ; thus, stimulated thermal Brillouin scattering (STBS) is not modeled. However, the effect on the fields of changes in index of refraction due to

local heating of the absorptive SBS medium is modeled. Since we are considering only steady-state solutions, thermal blooming in the "long-time" regime is considered. The phase change over a propagation step of length  $\Delta z$  is

$$\Delta\phi = \Delta n \Delta z k_0 \quad (3.5-12)$$

where

$$\Delta n = \left( \frac{\partial}{\partial T} n \right)_p \Delta T \quad (3.5-13)$$

and  $\Delta T$  is the total accumulated temperature rise at the current  $x$  position of a volume element moving in the  $+x$  direction with velocity  $u$

$$\Delta T = \frac{a}{\delta C_p} \int_{-\infty}^x \frac{(I_L + I_S)}{u} dx' \quad (3.5-14)$$

and the change in index of refraction with temperature is

$$\left( \frac{\partial}{\partial T} n \right)_p \triangleq - \frac{(\epsilon - 1)(\epsilon + 2)}{6n} \beta_T \quad (3.5-15)$$

where  $\epsilon = n^2$ . The phase change in Equation 3.5-12 is applied to the pump and Stokes fields as a phase screen at each incremental propagation step within the cell.

### 3.5.2.3 Cell Turbulence

The possibility of using aerowindows in the cell motivated the modeling of turbulent layers at the front and/or back of the cell. As before, a two-dimensional geometry is assumed in which the  $z$  direction is the direction of propagation of a field incident on the turbulent layer,

and the  $x$  direction is the flow direction of the gas stream. The change in phase on passing through the layer is

$$\phi(x) = k_0 \int_{-\Delta z/2}^{\Delta z/2} \Delta n(x, z') dz' \quad (3.5-16)$$

where  $\Delta z$  is the thickness of the turbulent layer and  $\Delta n$  is the deviation from the mean of the index of refraction;  $k_0$  is the free-space wave number,  $2\pi/\lambda$ . The autocovariance function of the phase is

$$\begin{aligned} B_\phi(\xi) &= \langle \phi(x) \phi(x + \xi) \rangle \\ &= k_0^2 \int_{-\Delta z/2}^{\Delta z/2} \int_{-\Delta z/2}^{\Delta z/2} \langle \Delta n(x, z) \Delta n(x + \xi, z') \rangle dz dz' \quad (3.5-17) \\ &= k_0^2 \Delta z \int_{-\Delta z}^{\Delta z} [1 - |z'|/\Delta z] B_n(\xi, z') dz' \end{aligned}$$

where  $B_n(\xi, z)$  is the two-dimensional autocovariance function of the index of refraction; see Papoulis (Reference 3.5-2) for the transformation of the double integral.

The measured one-dimensional power spectral density of the index of refraction for shear flows is of the form (Batt, Taylor, References 3.5-3 and 3.5-4).

$$S_n(k) = \frac{C_0}{1 + L^2 k^2} \quad (3.5-18)$$

where  $C_0 = \langle \Delta n'^2 \rangle L/\pi$ ,  $L$  = the correlation length, and  $\langle \Delta n'^2 \rangle$  is the mean-square deviation from the mean of the index of refraction across the thickness of the layer. The corresponding one-dimensional autocovariance function is its Fourier transform



$$\begin{aligned}
B_n(\xi) &= \int_{-\infty}^{\infty} e^{iK\xi} S_n(K) dK \\
&= \frac{\pi C_0}{L} e^{-|\xi|/L}
\end{aligned} \tag{3.5-19}$$

One choice for a two-dimensional autocovariance function  $B_n(\xi, \eta)$  which is symmetric in  $\xi$  and  $\eta$  and which has the above form for  $\eta = 0$  is

$$B_n(\xi, \eta) = \frac{\pi C_0}{L} \exp\{-(\xi^2 + \eta^2)^{1/2} / L\} \tag{3.5-20}$$

Alternative forms have been suggested (Reference 3.5-5). Substituting this expression into the integral for the phase autocovariance function and taking its Fourier transform gives the phase PSD:

$$S_\phi(K) = 4k_0^2 C_0 \frac{L^2}{A^4} \left[ \beta K_1(\beta) - 1 + \frac{\beta}{2} \int_0^\beta K_0(u) du \right] \tag{3.5-21}$$

where  $A = (1 + K^2 L^2)^{1/2}$ ,  $\beta = A\Delta z/L$  and  $K_0$  and  $K_1$  are modified Bessel functions of order 0 and 1. The limiting form for large  $\beta$  may be shown to be

$$S_\phi(K) = \frac{k_0^2 \Delta z L^2 \langle \Delta n^{12} \rangle}{(1 + K^2 L^2)^{3/2}} \tag{3.5-22}$$

The general form of the phase PSD (Equation 3.5-21) is used in the BRIWON code to generate, by standard harmonic synthesis methods (Reference 3.5-6), realization of the normally distributed random phase across the SBS cell. The phase aberration is applied as a phase screen to the pump and Stokes fields at any location within the cell; up to two such screens may be used within the cell, although in the case of turbulence due to flow in an aerowindow, the screen locations are necessarily at the front and back boundaries of the SBS cell.

### 3.5.3 Code Implementation

The BRIWON code assumes that a specified pump field is present at a lens which focuses the field into a cell containing the SBS medium. The free-space paraxial wave equation in the  $x, z$  coordinates is used to propagate the field to the front of the cell where its value is fixed as a boundary condition on the unknown pump field within the cell. An initial guess at the Stokes field at the front of the cell is also assumed. The cell itself is divided into  $NZ$  sheets and on each sheet there are  $NX$  transverse sample points at which the fields are to be evaluated. For a nonflowing medium, the field (Equations 3.5-1 and 3.5-2 with  $F(x,z,0) = 1$ ) are solved by an iterative method in which the fields are propagated on successive round-trips through the cell until a consistent set of solutions to the pump and Stokes field equations are obtained. On the first iteration the initial guess at the Stokes field is propagated backwards from the front of the cell to the rear, in step with the forward-propagating pump field. This is done in order to estimate the effect of the Stokes field on the depletion of the pump on the first pass through the cell. At the rear of the cell a boundary condition is applied to the Stokes field, i.e., that  $E_S$  is a noise field with random amplitude and phase normalized to an assumed power level (this is an approximation to the actual situation of scattering of the pump field by random fluctuations throughout the medium, providing the source for the Stokes field). This field is then propagated step-wise to the front of the cell, in the presence of the pump field from the previous pass. On the second and subsequent round-trips through the cell, the pump field is evaluated at each cell point on going from front to back, using the Stokes field calculated on the previous pass. The process is repeated until the fields duplicate themselves on successive passes (to within a specified error).

The propagation of the fields from one sheet at  $z = z_0$  to the next at  $z_0 + \Delta z$  is done in two steps. To account for diffraction effects, the field at  $z_0 + \Delta z$  is first obtained at all  $x$  points by using free-space propagation of the field at  $z_0$ . Using the diffracted field as a new

initial value at  $z_0$ , the effect of the medium at  $z_0 + \Delta z$  is then accounted for by modifying the amplitudes according to Equations 3.5-7 and 3.5-8 (noting that  $G$  is constant for  $u = 0$ ) and the phases by Equations 3.5-9 and 3.5-10. In addition, at each sheet a phase screen is applied to represent the effects of internal aberrations, if any, as in the case of thermal blooming. All free-space propagation steps are carried out using an FFT propagation algorithm.

For a flowing medium the procedure is the same except for including the effects of the gain on the fields on going from  $z_0$  to  $z_0 + \Delta z$ . Now the gain  $G$  is no longer constant but depends on the complex fields themselves through the function  $F(x, z, u)$ . Thus the intensity equations (Equations 3.5-64 and 3.5-65 of Section 3.5.5) and the phase equations (Equations 3.5-68 and 3.5-69) contain the unknown amplitudes and phases on the right-hand sides of the equations through the function  $\Phi$ . A direct solution is not possible; therefore, these equations are solved iteratively for every  $x, z$  point in the cell. For small  $\Delta z$ , the integral appearing in the function  $\Phi$  may be approximated by a 2-point trapezoidal integration

$$\int_{z_0}^{z_0 + \Delta z} R[G(x, z', u)] dz' \approx \frac{\Delta z}{2} \{R[G(x, z_0, u)] + R[G(x, z_0 + \Delta z, u)]\} \quad (3.5-23)$$

where  $R(G)$  denotes the real part of  $G$ . The first term contains (through the function  $F(x, z, u)$ ) the fields at the current  $z_0$  position, which are known. The second term contains the pump and Stokes fields at the new position  $z_0 + \Delta z$ , which are unknown. (Actually, the function  $F$  contains the integral of  $E_L E_S^*$  over all  $x$  points at  $z = z_0 + \Delta z$  upstream of the current  $x$  point. The equations are solved for each  $x$  beginning with the most upstream point and moving downstream. Thus all values of  $E_L E_S^*$  in the integrand are already known except for the value at the upper end-point of the integral. The integral itself is evaluated numerically using a 12-point Gauss-Laguerre integration algorithm. The starting fields for the iterative solution of these equations at  $(x, z_0 + \Delta z)$  are their values at  $(x, z_0)$ . Twelve iterations or less are normally adequate for a solution.

The iterative solution of the intensity and phase equations at each point in the cell and on each round-trip pass through the cell increases considerably the amount of computation (and cost) required for modeling SBS with grating convection. An algorithm was therefore introduced which tests whether the current cell point lies well outside the diffracted pump beam and whether the pump intensity is small. If so, the grating convection calculation is skipped. This procedure resulted in a significant reduction in computation time with no change in the numerical results.

The iteration procedure is continued until the reflectivity remains constant to within a specified fraction (typically  $10^{-4}$  to  $10^{-5}$ ) of its value. On convergence, the Stokes field at the front of the cell is propagated back to the focusing lens, any aberrations which were applied to the pump field at the lens are reapplied to the Stokes, and the resulting field is propagated to a focus where the power contained in buckets of increasing area in the focal plane is calculated. A search for "best focus" is also carried out by removing an amount of tilt and focus from the near field which maximizes the power in a bucket whose size is that of the diffraction-limited spot of the incident pump field (a "Q = 1" bucket). The square root of the ratio of the power in a Q = 1 bucket of the incident pump field, which is defined to be the reference field, to that of the Stokes, is the beam quality value reported by the code. The printed output of BRIWON also contains values of reflectivity (the ratio of output Stokes to input pump power), pump power at the rear of the cell--which is generally equivalent to threshold power, and conjugation fidelity--defined by a correlation integral between pump and Stokes fields at the focusing lens

$$CF = \frac{\int E_L E_S dx}{\{\int |E_L|^2 dx \int |E_S|^2 dx\}^{1/2}} \quad (3.5-24)$$

where the integrals extend over all space. In addition, if aberrations are applied, statistical measures of the aberration (e.g., rms phase) are

calculated, and a Fourier series decomposition of the Stokes phase is reported.

The reduction of threshold by focusing the pump and Stokes fields several times within the cell, with the focal points suitably separated, was modeled by assuming a tandem arrangement of SBS cells. The pump field leaving the back of one cell is propagated to the near field and refocused into the next cell. Similarly, the Stokes field leaving the front of one cell is propagated to a near-field lens and is refocused into the preceding cell. The boundary conditions for the fields are now specified for the pump at the front of the first cell and for the Stokes at the rear of the last cell. The iteration procedure in BRIWON for solving the coupled field equations then requires the propagation of the pump and Stokes through all cells on each iteration.

Extensive graphical output is provided by the code. Data to be plotted is set up by BRIWON, while a postprocessor plot code, B1PLOT, generates whatever plots are requested by the user. Plot data is provided for the following two-dimensional plots: iteration history of reflectivity and conjugation fidelity, power in the pump and Stokes fields as a function of longitudinal (z) coordinate in the cell, conjugation fidelity as a function of transverse distance from the optic axis, and the pump and Stokes intensity profiles at the front of the cell, the rear of the cell, the focusing lens, and the focal plane within the cell; far-field intensity profiles are provided for the input pump, output Stokes (corrected and uncorrected for best focus), and transmitted pump. Power-in-the-bucket as a function of bucket size is plotted, and, if random aberrations are specified, the particular phase realization generated is plotted, along with its power spectral density and the theoretical PSD from which it was generated. In the form of three-dimensional (isometric) and/or contour plots one has the options of plotting, as a function of x and z cell coordinates, the pump and Stokes intensity and phase as either linear or logarithmic plots. Most of the above graphical output is available for each cell of a multicell (i.e., multifocus) configuration.

#### 3.5.4 Numerical Results

The BRIWON code has been exercised extensively to model the SBS process for a range of pump powers, flow velocities,  $F\#$ , cell geometries, and aberrators. Results relevant to particular experiments are summarized in the appropriate sections of this report, but to illustrate some of the graphical output of the code Figures 3.5-1 through 3.5-3 are included for a representative case. The case corresponds to an input pump power of about four times threshold,  $F/30$ , wavelength of  $2.8 \mu\text{m}$ , and an SBS medium of 40 atm Xe. The Figure 3.5-1 shows, on both linear and log scales, the depletion of the pump power as the beam progresses from the front to the rear of the cell, and the corresponding development of the Stokes power, from back to front. The pump at the focusing lens is 12th-order hypergaussian with a flat phase; its intensity and phase are shown as the solid lines on Figure 3.5-2, along with that for the returned Stokes. Similar field plots, but at the front of the SBS cell are shown in Figure 3.5-3. Figures 3.5-4 and 3.5-5 are isometric plots of the pump and Stokes intensities within the cell as a function of the transverse and longitudinal spatial coordinates. As a separate calculation, both the input pump and output Stokes fields at the focusing lens are also propagated to a focus for beam quality calculations. Figure 3.5-6 shows the far-field intensity distribution of the input pump and the corrected Stokes ("corrected" meaning after a search for best focus). Figure 3.5-7 shows the corresponding power-in-the-bucket values as a function of the dimensionless far-field coordinate  $Q$ , from which the  $Q = 1$  beam quality number is derived.

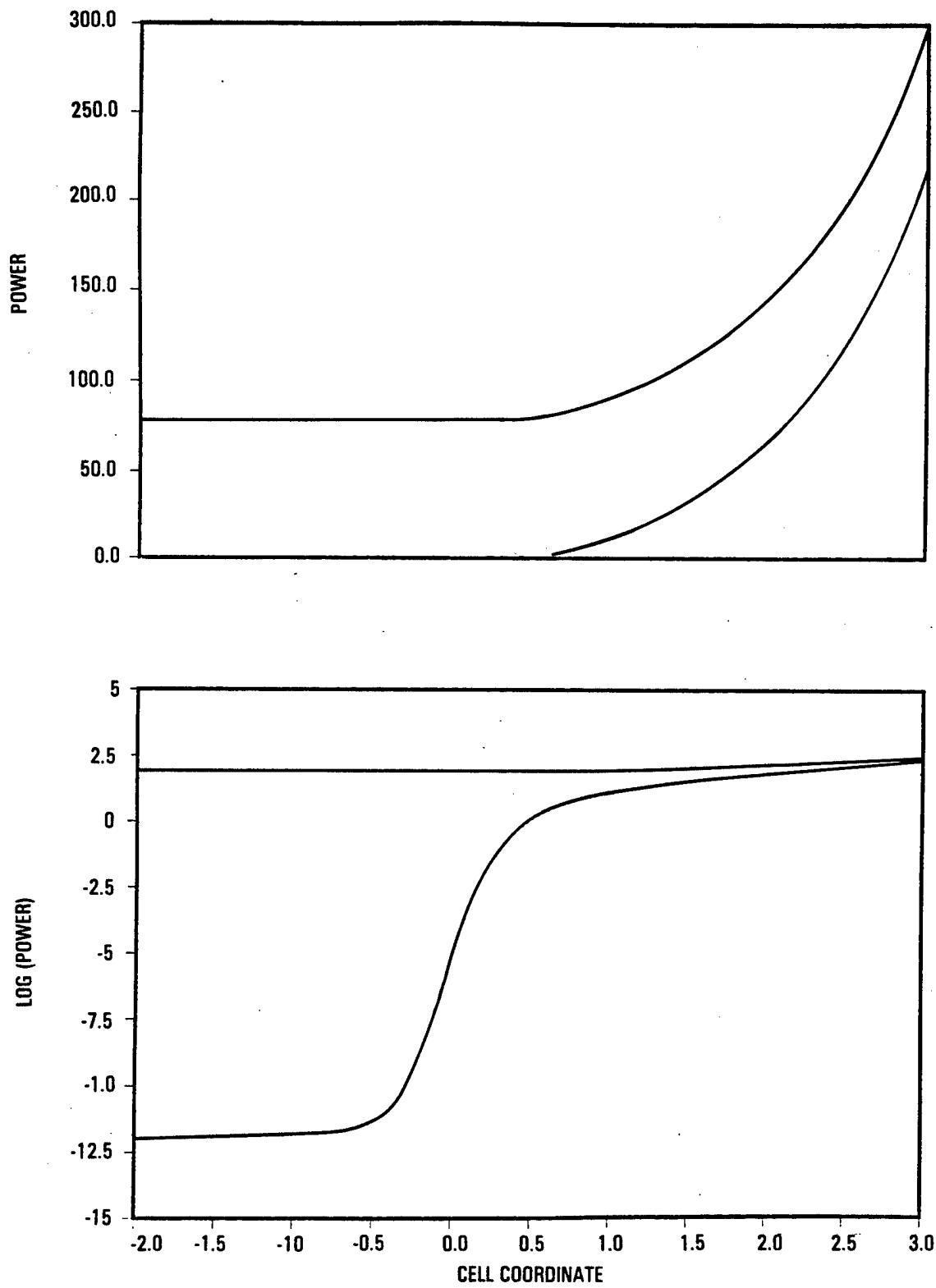


Figure 3.5-1. Power Throughout the Cell

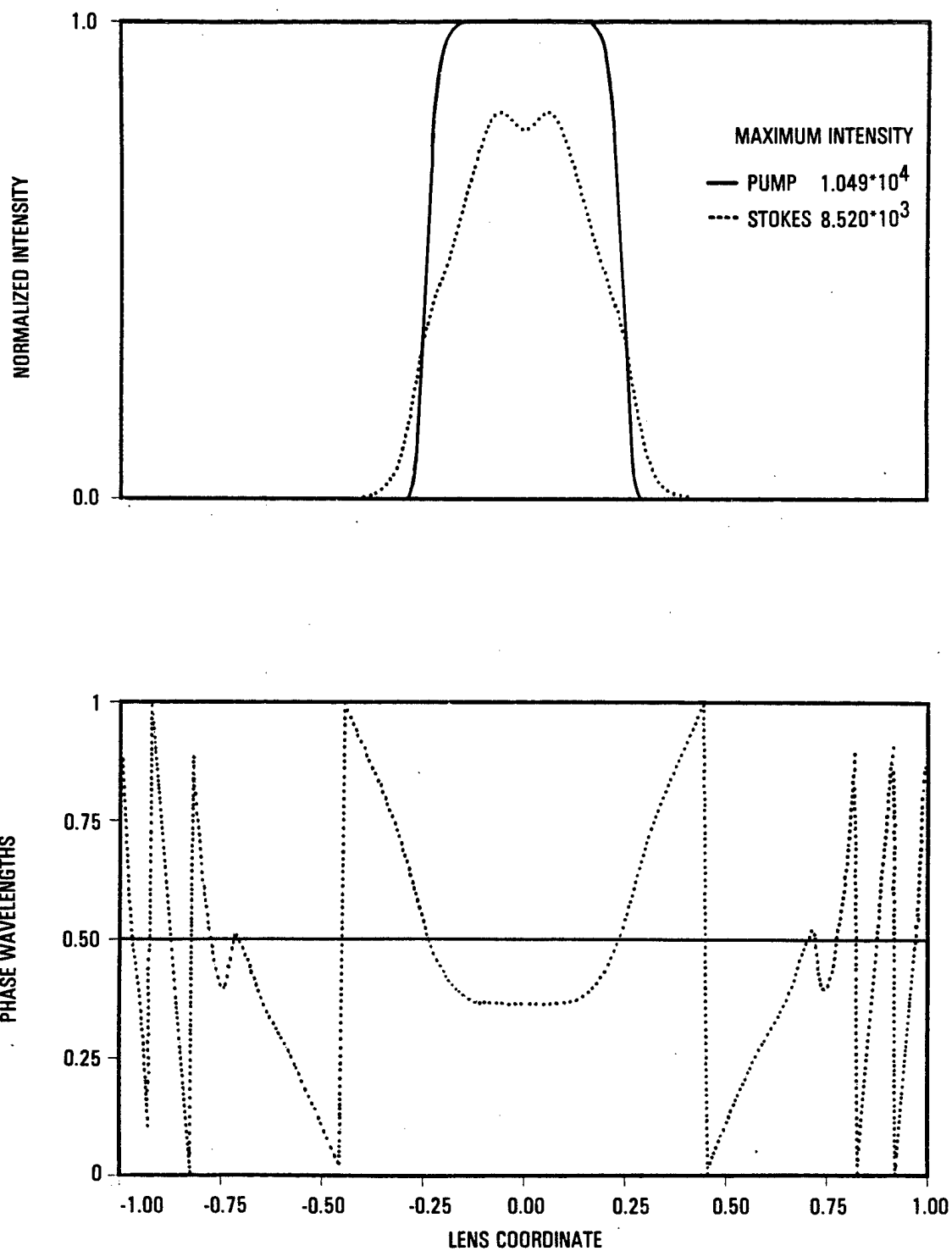


Figure 3.5-2. Fields at the Entrance/Exit



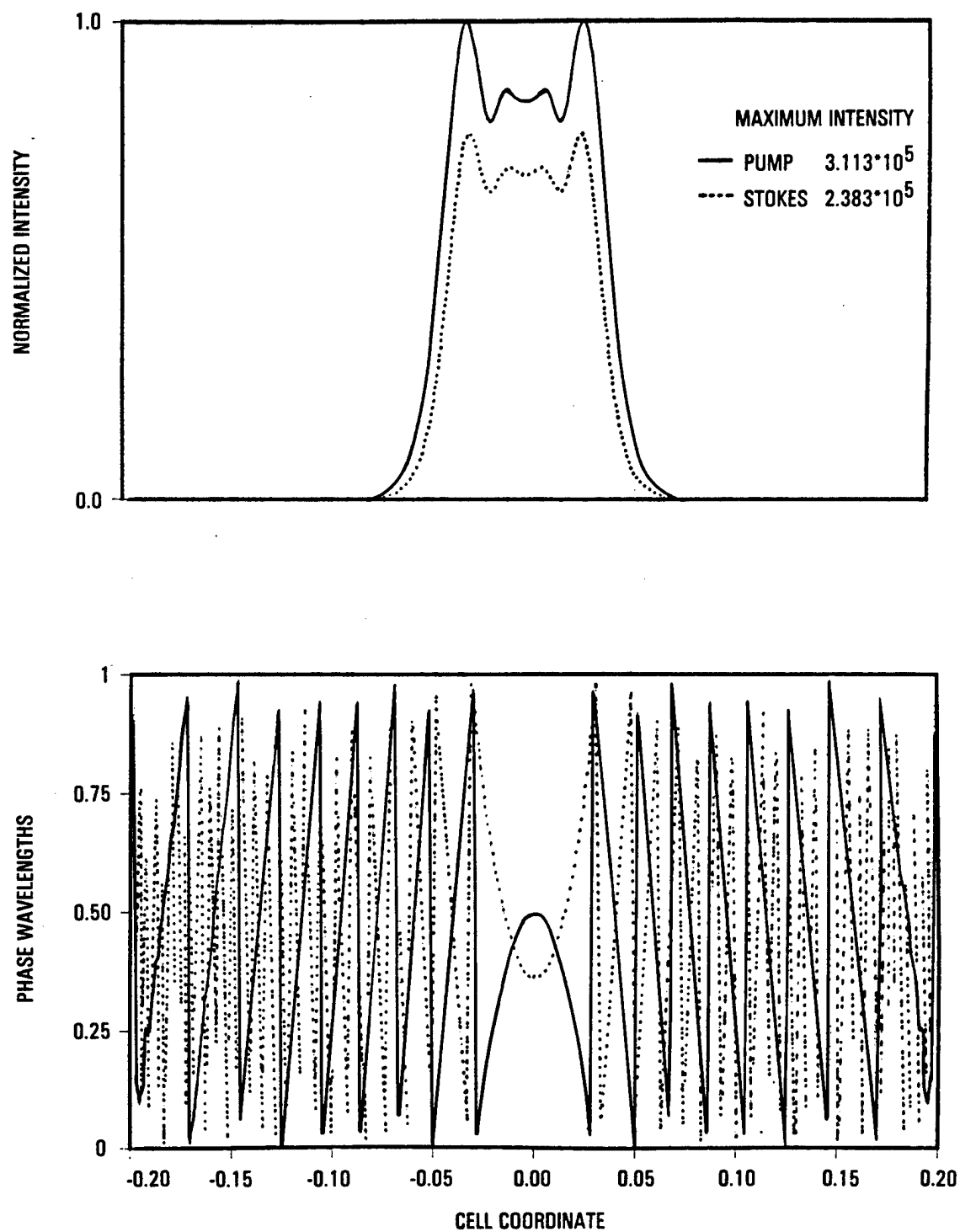


Figure 3.5-3. Fields at the Front of the Cell

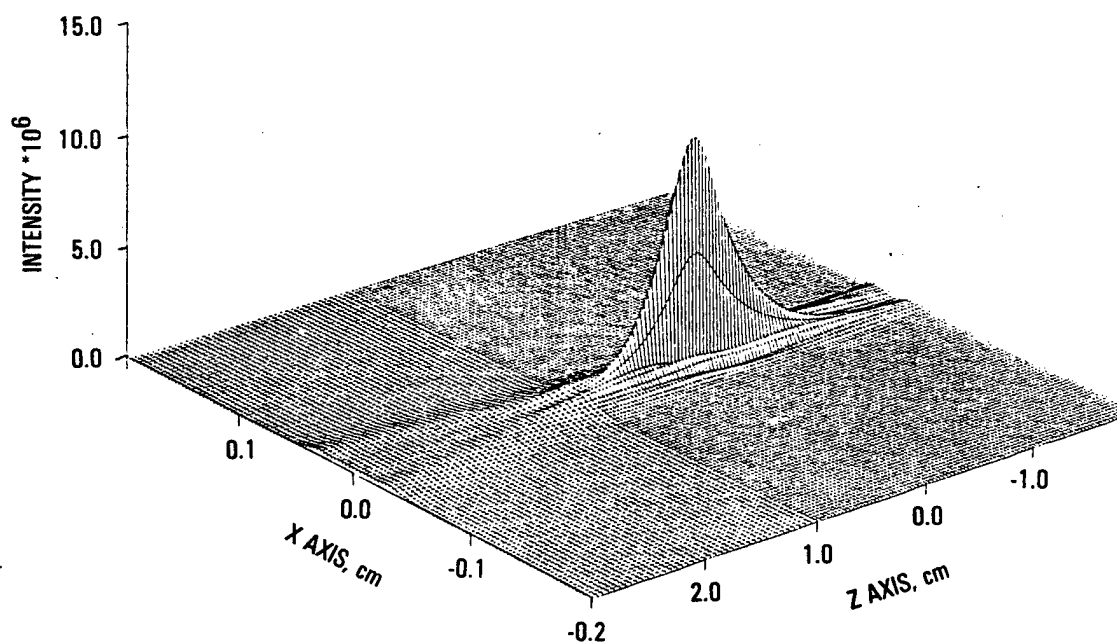


Figure 3.5-4. Pump Field in the Cell

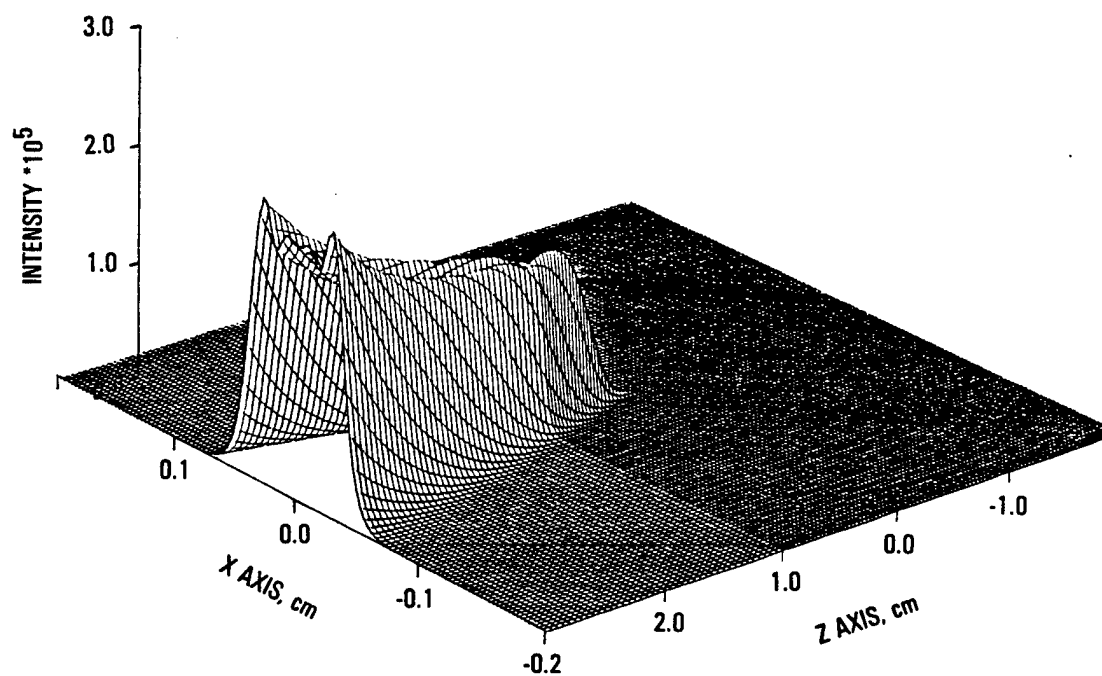


Figure 3.5-5. Stokes Field in the Cell

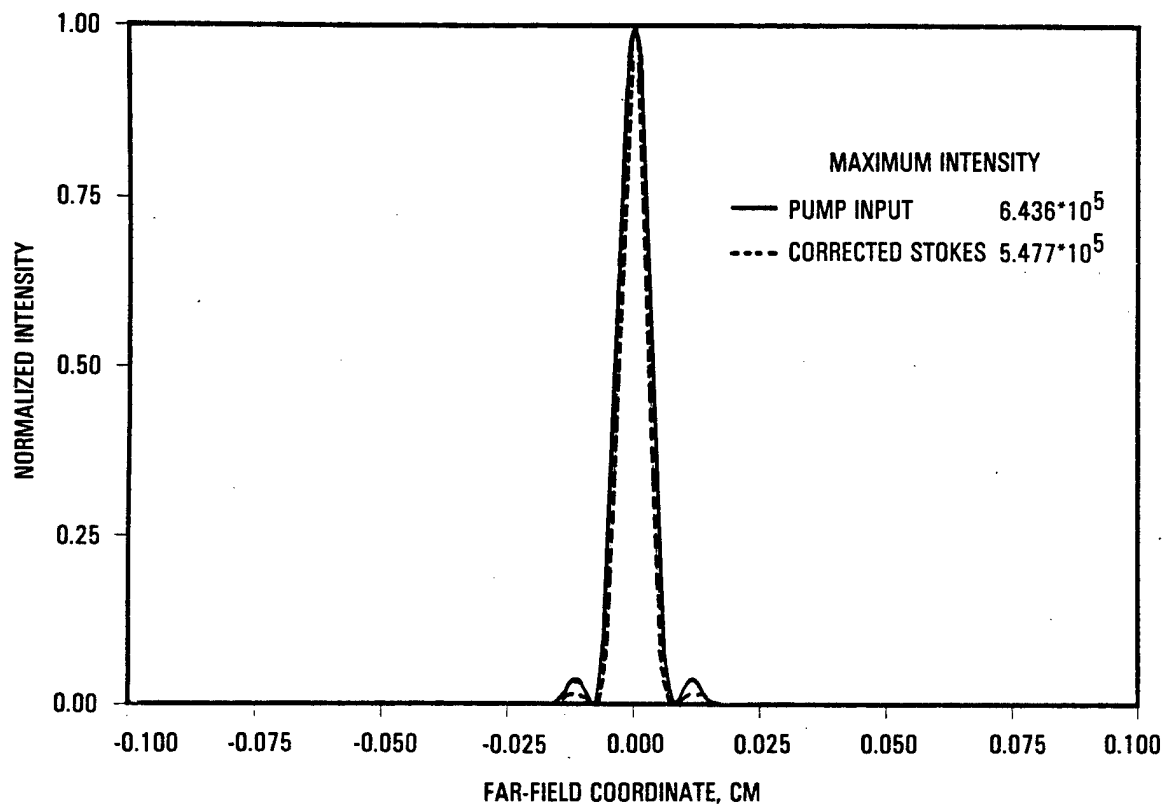


Figure 3.5-6. Far-Field Intensity

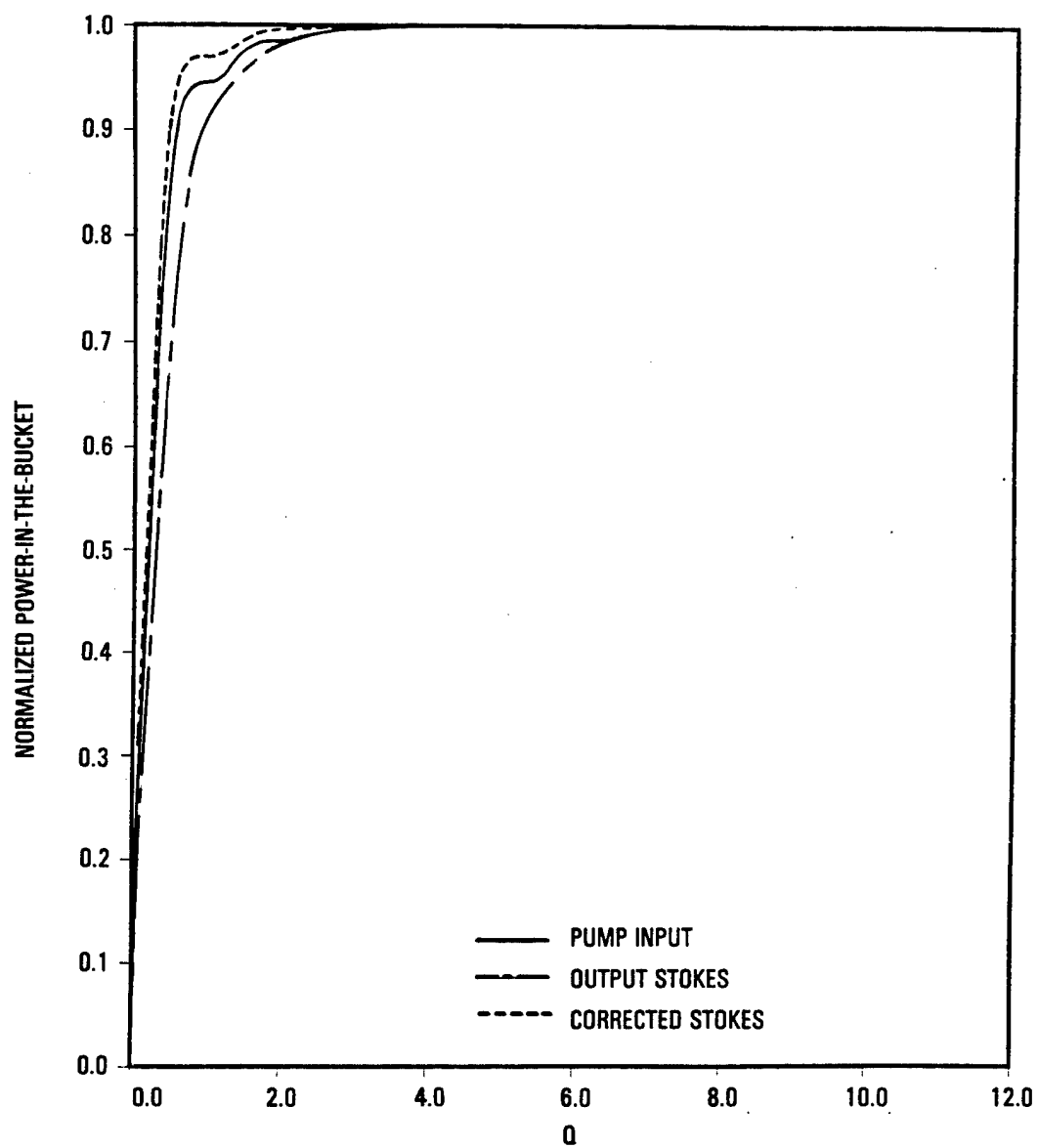


Figure 3.5-7. Far-Field Power

### 3.5.5 Derivation of Equations

The coupled differential equations for density, temperature, and electromagnetic field, which form the basis for the BRIWON code, were derived for the general case of a flowing medium. The starting point of the analysis was Equations (56) and (57) of the Kaiser and Maier article [Reference 3.5-1] for the density and temperature fluctuations in the SBS medium, which are derived therein from the Navier-Stokes equation, the energy transport equation, and the equation of continuity, assuming the slowly-varying amplitude approximation. In addition, strong damping of the acoustic waves was assumed, and the variation of the dielectric constant with temperature at constant density was neglected. These equations may be written as

$$-\frac{\partial^2 \rho}{\partial t^2} + (2i\omega - \Gamma_B) \frac{\partial \rho}{\partial t} + \left( \omega^2 + i\omega\Gamma_B - \frac{v^2 k^2}{\gamma} \right) \rho - \frac{v^2 k^2 \rho_0 \beta_T}{\gamma} T = -\frac{\gamma^e}{8\pi} k^2 E_L E_S^* \quad (3.5-25)$$

for the density variation,  $\rho$ , and

$$\frac{\partial T}{\partial t} + (-i\omega + \frac{1}{2}\gamma\Gamma_{RL})T - \frac{\gamma - 1}{\rho_0 \beta_T} \left( \frac{\partial \rho}{\partial t} - i\omega\rho \right) = \frac{nca}{4\pi\rho_0 c_v} E_L E_S^* \quad (3.5-26)$$

for the fluctuations,  $T$ , from the steady-state temperature. In these equations the following quantities are defined:

- $\rho$  = amplitude of the density wave
- $T$  = amplitude of the temperature wave
- $k$  = acoustic wave propagation vector.  $k = k_L + k_S \simeq 2k_L$
- $\omega = \omega_L - \omega_S$  = frequency of the acoustic wave
- $v$  = phonon velocity
- $\gamma^e$  = electrostrictive coupling coefficient
- $c$  = the speed of light
- $n$  = the index of refraction

- $\beta_T$  = the coefficient of thermal expansion
- $\gamma$  = the ratio of specific heats
- $C_V$  = the heat capacity at constant volume
- $\alpha$  = linear absorption coefficient
- $\Gamma_B$  = the spontaneous Brillouin linewidth
- $\Gamma_{RL}$  = the Rayleigh linewidth
- $\rho^0$  = ambient density.

The linewidths are given in terms of the material parameters by

$$\Gamma_B = \frac{\eta k^2}{\rho^0} \quad (3.5-27)$$

$$\Gamma_{RL} = \frac{2\gamma_T k^2}{\rho^0 c_p}$$

where  $C_p$  is the specific heat at constant pressure,  $\gamma_T$  the thermal conductivity, and  $\eta = \frac{4}{3}\eta_S + \eta_B$ , where  $\eta_S$  and  $\eta_B$  are the shear and bulk viscosities of the medium, respectively.

For simplicity, Equations 3.5-25 and 3.5-26 are rewritten in the form

$$-\frac{\partial^2 \rho}{\partial t^2} + a_1 \frac{\partial \rho}{\partial t} + a_2 \rho - a_3 T = C_1 H(t) \quad (3.5-28)$$

$$\frac{\partial T}{\partial t} + b_1 T - b_2 \frac{\partial \rho}{\partial t} + b_3 \rho = C_2 H(t),$$

where  $H(t) \equiv E_L E_S^*$ . These equations are then Laplace transformed, assuming initial conditions  $\rho(0) = 0, T(0) = 0, (\frac{\partial \rho}{\partial t})_0 = 0$ , leading to the algebraic equations in the Laplace transform variable  $s$

$$(-s^2 + a_1s + a_2)L\{\rho\} - a_3L\{T\} = c_1L\{H(t)\} \quad (3.5-29)$$

$$(s + b_1)L\{T\} - (b_2s - b_3)L\{\rho\} = c_2L\{H(t)\}.$$

Eliminating  $L\{T\}$  and solving for the transform of the density, we obtain

$$L\{\rho\} = \frac{[c_1(s + b_1) + c_2a_3]L\{H\}}{(-s^2 + a_1s + a_2)(s + b_1) - a_3(b_2s - b_3)} \quad (3.5-30)$$

The denominator, a cubic in  $s$ , has roots,  $s_1, s_2, s_3$ , in terms of which the density is

$$\rho(t) = L^{-1} \left[ \frac{c_1s + b_1c_1 + c_2a_3}{(s - s_1)(s - s_2)(s - s_3)} \right] * H(t) \quad (3.5-31)$$

where the  $*$  operator represents the convolution of the two functions of time. Now, assuming  $s_1 \neq s_2 \neq s_3$ ,

$$L^{-1} \left[ \frac{c_1s + a_0}{(s - s_1)(s - s_2)(s - s_3)} \right] = \sum_{n=1}^3 \frac{(c_1s_n + a_0)}{q(s_n)} \exp\{s_nt\} \quad (3.5-32)$$

where

$$q(s_n) = \left[ \frac{(s - s_1)(s - s_2)(s - s_3)}{s - s_n} \right]_{s=s_n} \quad (3.5-33)$$

and

$$a_0 = b_1c_1 + c_2a_3. \quad (3.5-34)$$



Performing the convolution then gives the solution for  $\rho$

$$\rho(t) = \sum_{n=1}^3 \frac{(c_1 s_n + a_0)}{q(s_n)} \int_0^t e^{s_n(t-t')} H(t') dt' \quad (3.5-35)$$

Now, if  $\omega \approx vk$  and  $\Gamma_B, \Gamma_{RL} \ll vk$ , then approximate solutions to the cubic in Equation 3.5-30 may be shown to be

$$s_1 = i(\omega - vk) - \Gamma$$

$$s_2 = i\omega - \frac{1}{2} \Gamma_{RL} \quad (3.5-36)$$

$$s_3 = i(\omega + vk) - \Gamma$$

where  $\Gamma \equiv \frac{1}{2} [\Gamma_B + \frac{1}{2}(\gamma - 1)\Gamma_{RL}]$ . The values for the quantities  $q(s_n)$  are then

$$q(s_1) = -2ivk(-ivk + \frac{1}{2} \Gamma_{RL} - \Gamma)$$

$$q(s_2) = (vk)^2 + (\Gamma - \frac{1}{2} \Gamma_{RL})^2 \quad (3.5-37)$$

$$q(s_3) = q(s_1)^*$$

and for  $a_0$

$$a_0 = \frac{k^2}{8\pi} \left[ \gamma e^{i\omega - \frac{1}{2} \gamma \Gamma_{RL}} + \frac{2nc\alpha\beta_T v^2}{c_p} \right] \quad (3.5-38)$$

We consider next the case in which the medium is moving with constant  $u$  in the  $+x$  direction. For steady-state conditions the partial derivatives with respect to time in Equations 3.5-25 and 3.5-26 are simply replaced by  $u$  times the partial derivative with respect to  $x$ . We choose an origin of  $x$ -coordinates such that  $x = 0$  lies outside the region of illumination by the pump field. With boundary conditions  $\rho(0) = 0, T(0) = 0, \left(\frac{\partial \rho}{\partial x}\right)_0 = 0$ , the Laplace Transform solution is the same as before, with  $t$  replaced by  $x/u$ . Thus, Equation 3.5-35 becomes

$$\rho(x) = \sum_{n=1}^3 \frac{(c_1 s_n + a_0)}{q(s_n)u} \int_0^x e^{s_n(x-x')/u} H(x') dx' \quad (3.5-39)$$

where  $H(x)$  is the steady-state value of  $E_L(x)E_S(x)^*$ . For convenience, we redefine the  $x$ -coordinate so that its origin lies within the pump beam and extend the integral to  $-\infty$ . Defining the integral in Equation 3.5-39 to be  $I_n(x)$  and the quantities  $F_n$  and  $D_n$  to be

$$F_n = - \frac{s_n}{u} \frac{I_n}{E_L E_S^*} \quad (3.5-40)$$

and

$$D_n = - \frac{c_1 s_n + a_0}{q(s_n) s_n} \quad (3.5-41)$$

the density function may be written as

$$\rho(x) = \left[ \sum_{n=1}^3 D_n F_n \right] E_L E_S^* \quad (3.5-42)$$

In the limit of zero velocity,  $F_n \rightarrow 1$ , and

$$\rho(x) \rightarrow E_L E_S^* \sum_{n=1}^3 D_n \quad (3.5-43)$$

Using the properties of the Laplace transform of rational fractions, the sum of this equation may be shown to be

$$\sum_{n=1}^3 D_n = \frac{i \frac{k^2}{4\pi} \left[ \frac{n c a \beta_T v^2}{\gamma C_v} + \frac{1}{2} i \gamma e^{\omega} - \frac{1}{4} \gamma \gamma \Gamma_{RL} \right]}{\left[ \omega^2 + i \omega \Gamma_B - v^2 k^2 \right] \left[ \omega + \frac{1}{2} i \gamma \Gamma_{RL} \right] + \frac{1}{2} i (\gamma - 1) \Gamma_{RL} v^2 k^2} \quad (3.5-44)$$

For  $\omega \sim vk$  and  $\Gamma_{RL}/\omega \sim \Gamma_B/\omega \ll 1$ , which is the case for Xe at 40 atm, then the real parts of the exponentials in the integrals  $I_n$  are of the same order of magnitude but  $I_2$  and  $I_3$  contain a rapidly oscillating phase term as well. The main contributions to  $I_2, I_3$  will be from the interval  $0 \leq x - x' \leq u/\omega$ , over which the remainder of the integrands are approximately constant. Thus,  $F_2$  and  $F_3$  are of order unity. If  $E_L E_S^*$  does not change rapidly on the interval  $0 \leq x - x' \leq u/\Gamma$  (which for 40 atm Xe,  $\lambda = 2.8\mu$ ,  $F\# = 30$ , and  $u = 10$  m/s is about 1/40 of the diffraction-limited spot size), then  $F_1$  is also of the order of magnitude of unity. On the other hand, the coefficients  $D_2$  and  $D_3$  are smaller than  $D_1$  by a factor of order  $\Gamma/\omega$ . Thus, of the three terms in the sum in Equation 3.5-42 only the first need be retained, and  $\rho(x)$  becomes

$$\rho(x) = D_1 F_1 E_L E_S^* \quad (3.5-45)$$

The steady-state differential equations in  $x$  and  $z$  for the Stokes and pump fields, including absorption and self-focusing, are

$$\frac{\partial}{\partial z} E_S + \frac{i}{2k_S} \frac{\partial^2}{\partial x^2} E_S - \frac{a}{2} E_S + i \frac{n_2 k_S}{2n} (|E_L|^2 + |E_S|^2) E_S = \kappa^* E_L \rho^* \quad (3.5-46)$$

$$\frac{\partial}{\partial z} E_L - \frac{i}{2k_L} \frac{\partial^2}{\partial x^2} E_L + \frac{a}{2} E_L - i \frac{n_2 k_L}{2n} (|E_L|^2 + |E_S|^2) E_L = \kappa E_S \rho \quad (3.5-47)$$

where the pump field is assumed to be propagating in the +z direction, the Stokes field in the -z direction, and  $\kappa = i\omega_L \gamma^e / (4cn\rho_0)$ . The electromagnetic field equations are in their scalar form so that polarization effects, if any, will be ignored. In addition, there is no explicit dependence in these equations on the second transverse (y) coordinate so that the description of the wave-optics is basically two dimensional. However, since the gain depends on the intensity in the medium it is important to account for the increased intensity in the cell due to focusing in the y direction. To this end, the BRIWON code adjusts the pump and Stokes intensities at each z position to correspond to quasi-geometric focusing in the y coordinate. Specifically, the size of the beam,  $Y(z)$ , in the y direction is taken to be  $Y(z) = [(z/F\#)^2 + Y(0)^2]^{1/2}$  where z is measured from the focal plane and the  $F\#$  is that for the y direction (which need not be the same as for the x direction). The "size of the beam" at the focus,  $Y(0)$ , may be specified by the user; its default value is  $\lambda F\#$ .

Substituting for  $\rho(x)$ , using Equation 3.5-45, defining the pump gain G to be the coefficient of  $|E_S|^2 E_L$  on the right-hand side of Equation 3.5-47, evaluating  $D_1$  with Equations 3.5-41 and 3.5-36 through 3.5-38, then leads to the following expression for the gain

$$G(x, z, u) = g F(x, z, u) \quad (3.5-48)$$

$$g = \frac{g_0}{1 + (\Delta\omega/\Gamma)^2} \left[ - (g_r^{\text{elec}} + g_r^{\text{abs}}) + i (g_i^{\text{elec}} + g_i^{\text{abs}}) \right]$$

where

$$\begin{aligned}
 g_0 &= \frac{k^2 \gamma^e \omega_L}{32 \pi c n \rho_0 \omega \Gamma} \\
 g_r^{\text{abs}} &= \frac{n a c \beta_T v^2 (\Delta \omega)}{c_p \omega \Gamma} \\
 g_i^{\text{abs}} &= \frac{n a c \beta_T v^2}{c_p \omega} \\
 g_r^{\text{elec}} &= \frac{\gamma^e}{2} \\
 g_i^{\text{elec}} &= - \frac{\gamma^e (\Delta \omega)}{2 \Gamma}
 \end{aligned} \tag{3.5-49}$$

and the function  $F(x, z, u)$  is given below. We have defined  $\Delta \omega = \omega - \omega_B$ , where  $\omega_B$  is the Brillouin frequency  $\omega_B = k_B v = 2 \omega_L v n / c$ , and assumed that  $\omega - v k \neq \Delta \omega, \omega \neq \omega_B, \Gamma / \omega \ll 1$ , and  $\Delta \omega / \omega \ll 1$ . The terms in  $g$  are the real and imaginary parts of the absorptive and electrostrictive gains.  $\Gamma$  is a weighted average of the Brillouin and Rayleigh line widths

$$\Gamma = \frac{1}{2} \left[ \Gamma_B + (\gamma - 1) \frac{1}{2} \Gamma_{RL} \right] \tag{3.5-50}$$

The effect of the flowing medium appears solely in the gain terms and is contained in the function  $F(x, z, u)$ , which is, explicitly,

$$F(x, z, u) = - \frac{s_1}{u} \frac{\int_{-\infty}^x \exp\{s_1(x - x')/u\} E_L(x', z) E_S^*(x', z) dx'}{E_L(x, z) E_S^*(x, z)} \tag{3.5-51}$$

where

$$s_1 = i(\omega - vk) - \Gamma$$

$$\approx i\Delta\omega - \Gamma$$
(3.5-52)

Physically, the integral in  $F(x, z, u)$  represents a superposition of all density fluctuations (phonon gratings) upstream from the current  $(x, z)$  point, each exponentially weighted by the time required to flow to the point  $x$  relative to the phonon decay time  $1/2\Gamma$ . Clearly, if the flow velocity  $u$  approaches zero, the function  $F$  has the limiting value of 1 and the equations reduce to their usual form. In that case, the gain  $G$  is given simply by  $G = g$  which, for a homogeneous medium, is constant.

We consider next the energy conservation equation and also derive the expressions for the change in the amplitude and phase of the fields with  $z$ , assuming no diffraction. Dropping the second derivatives with respect to  $x$  in Equations 3.5-46 and 3.5-47 and forming from Equation 3.5-48 the quantity  $E_S^* \frac{\partial}{\partial z} E_S + E_S \frac{\partial}{\partial z} E_S^*$  and from Equation 3.5-47 the quantity  $E_L^* \frac{\partial}{\partial z} E_L + E_L \frac{\partial}{\partial z} E_L^*$  and subtracting the resulting two equations, we obtain the differential equation

$$\frac{\partial}{\partial z} (|E_L|^2 - |E_S|^2) = -\alpha (|E_L|^2 + |E_S|^2)$$
(3.5-53)

if  $\omega_L = \omega_S$ . This equation simply states that a change in the pump intensity in an interval  $dz$  is accounted for by a corresponding change in the Stokes intensity (propagating in the opposite direction) less the amount of energy absorbed by the medium. Note that this result is general and applies to any dependence of the density  $\rho(x)$  on  $E_L$  and  $E_S$ . In particular, it holds for the case of a flowing medium for which  $\rho(x)$  is given by Equation 3.5-39. For the special case of no absorption the previous equation simplifies to

$$\frac{\partial}{\partial z}(|E_L|^2 - |E_S|^2) = 0 \quad (3.5-54)$$

which, when integrated from  $z_0$  to  $z = z_0 + \Delta z$ , has the solution

$$|E_L|^2 - |E_S|^2 = |E_L^0|^2 - |E_S^0|^2 \quad (3.5-55)$$

It must be emphasized that this equation as well as all other equations derived from the field equations (Equations 3.5-46 and 3.5-47) strictly apply only to the case of collimated propagation in the  $z$  direction, since the second derivatives in  $x$  and  $y$  (appearing in the original Laplacian, have been dropped). For any other case (e.g., for the common situation of focused beam), one or both of these derivatives must be retained, although the equations of this report will be approximately correct for sufficiently small step sizes  $\Delta z$ .

We next form, from Equations 3.5-46 and 3.5-47, the quantities  $\frac{1}{E_S^*} \frac{\partial}{\partial z} E_S^*$  and  $\frac{1}{E_L} \frac{\partial}{\partial z} E_L$ , again dropping the second derivatives with respect to  $x$  and assuming no absorption by the medium. Adding and subtracting the resulting two equations then leads, respectively, to the equations

$$\frac{\partial}{\partial z} \ln(E_L E_S^*) = (G + 2i\Delta) (|E_L|^2 + |E_S|^2) \quad (3.5-56)$$

and

$$\frac{\partial}{\partial z} \ln \left( \frac{E_S^*}{E_L} \right) = G(|E_L|^2 - |E_S|^2) \quad (3.5-57)$$

where  $\Delta$  is defined to be the coefficient of the intensity in the self-focusing terms in Equations 3.5-46 and 3.5-47, i.e.,

$$\Delta = \frac{n_2 k_L}{2n} \quad (3.5-58)$$

Eliminating  $G$  from the last two equations results in

$$\frac{\partial}{\partial z} \ln(E_L E_S^*) = \frac{|E_L|^2 + |E_S|^2}{|E_L^0|^2 - |E_S^0|^2} \frac{\partial}{\partial z} \ln \left( \frac{E_S^*}{E_L} \right) + 2i\Delta(|E_L|^2 + |E_S|^2) \quad (3.5-59)$$

Integrating Equation 3.5-57 yields the expression

$$\frac{E_S^*}{E_L} = \frac{E_S^{0*}}{E_L^0} \exp \left[ (|E_L^0|^2 - |E_S^0|^2) \int_{z_0}^z G(x, z', u) dz' \right] \quad (3.5-60)$$

where  $G(x, z, u)$  is given by Equation 3.5-48. Taking the absolute square of this equation, we have

$$\frac{|E_S|^2}{|E_L|^2} = \frac{|E_S^0|^2}{|E_L^0|^2} e^{-\phi} \quad (3.5-61)$$

where

$$\phi = -2(|E_L^0|^2 - |E_S^0|^2) \int_{z_0}^z R(G(x, z', u)) dz' \quad (3.5-62)$$

and  $R(G)$  denotes the real part of the function  $G$ . Using the energy conservation equation, we then obtain the Stokes intensity at  $z$  in terms of the pump and Stokes intensities at  $z_0$  (and in terms of the grating convection integral appearing in  $\phi$ )

$$I_S = \frac{(|E_L^0|^2 - |E_S^0|^2) |E_S^0|^2 e^{-\phi}}{|E_L^0|^2 - |E_S^0|^2 e^{-\phi}} \quad (3.5-63)$$

or, denoting intensities by  $I$ ,

$$I_S = \frac{(I_L^0 - I_S^0) I_S^0 e^{-\phi}}{I_L^0 - I_S^0 e^{-\phi}} \quad (3.5-64)$$



Similarly, for the pump intensity at position  $z$  we have

$$I_L = \frac{(I_L^0 - I_S^0)I_L^0}{I_L^0 - I_S^0 e^{-\phi}} \quad (3.5-65)$$

The effect of the gain on the phases of the fields can be found by substituting  $E_L = |E_L| \exp(i\phi_L)$  and  $E_S = |E_S| \exp(i\phi_S)$  into Equations (3.5-56) and 3.5-57), taking the imaginary parts, and adding and subtracting the resulting equations. For the change in the pump phase in from  $z_0$  to  $z$  we find

$$\phi_L - \phi_L^0 = \frac{1}{2} \int_{z_0}^z (I_L + I_S - I_L^0 + I_S^0) \text{Im}(G) dz' + \Delta \int_{z_0}^z (I_L + I_S) dz' \quad (3.5-66)$$

while for the Stokes phase

$$\phi_S - \phi_S^0 = -\frac{1}{2} \int_{z_0}^z (I_L + I_S - I_L^0 + I_S^0) \text{Im}(G) dz' + \Delta \int_{z_0}^z (I_L + I_S) dz' \quad (3.5-67)$$

Since the absorption coefficient has been assumed to be zero, we may use Equation (3.5-55) so that the phase changes become

$$\phi_L - \phi_L^0 = \int_{z_0}^z I_S \text{Im}(G) dz' + \Delta \int_{z_0}^z (I_L + I_S) dz' \quad (3.5-68)$$

$$\phi_S - \phi_S^0 = -\int_{z_0}^z I_L \text{Im}(G) dz' + \Delta \int_{z_0}^z (I_L + I_S) dz' \quad (3.5-69)$$

where  $\text{Im}(G)$  is the imaginary part of the function  $G$ .

For a stationary medium  $F(x,z,u)=1$  and the imaginary part of the gain is many orders of magnitude smaller than the real part. However, for a flowing medium  $F(x,z,u)$  is complex with an imaginary part comparable to its real part. The imaginary part of  $G$  can then be comparable in magnitude to  $R(G)$  and the phase changes in Equations (3.5-68) and (3.5-69) can be relatively large, particularly for the Stokes field for which the imaginary part of the gain is multiplied by the pump intensity.

These equations simplify considerably for the case of zero flow velocity. Integrating Equation (3.5-56) from  $z_0$  to  $z$  (noting that  $G$  is

constant for  $u = 0$ ), expressing the complex fields in terms of their amplitudes and phases, taking the real and imaginary parts of the equation, and then eliminating the integral of  $|E_L|^2 + |E_S|^2$ , provides an expression for  $(\phi_L - \phi_L^0) - (\phi_S - \phi_S^0)$ . The same procedure applied to Equation (3.5-57), and using Equation (3.5-55), yields an equation for  $(\phi_L - \phi_L^0) + (\phi_S - \phi_S^0)$ . One then finds that

$$\phi_L - \phi_L^0 = -\frac{1}{2} \text{Im}(g)(I_L^0 - I_S^0) \Delta z + \frac{\text{Im}(G)+\Delta}{2R(G)} \ln \left[ \frac{(I_L^0 - I_S^0)e^{\phi^0/2}}{I_L^0 - I_S^0 e^{-\phi^0}} \right] \quad (3.5-70)$$

$$\phi_S - \phi_S^0 = -\frac{1}{2} \text{Im}(G)(I_L^0 - I_S^0) \Delta z + \frac{\text{Im}(G)+\Delta}{2R(G)} \ln \left[ \frac{(I_L^0 - I_S^0)e^{-\phi^0/2}}{I_L^0 - I_S^0 e^{-\phi^0}} \right] \quad (3.5-71)$$

where

$$\phi^0 = -2(I_L^0 - I_S^0)\Delta z R(G) \quad (3.5-72)$$

and Equations (3.5-64) and (3.5-65) have been used. In contrast to Equations (3.5-68) and (3.5-69), these expressions for the phase changes involve only the intensities at the initial position  $z_0$ .

### 3.5.6 References

- 3.5-1 W. Kaiser and M. Maier, "Stimulated Rayleigh, Brillouin and Raman Spectroscopy," Laser Handbook, Volume 2, F.T. Arecchi and E.O. Schulz-Dubois, eds., North-Holland Publishing Co., 1972.
- 3.5-2 A. Papoulis, Probability, Random Variables, and Stochastic Processes. McGraw-Hill, New York, 1965.
- 3.5-3 R.G. Batt, "Turbulent Mixing of Passive and Chemically Reacting Species in a Low-Speed Shear Layer," J. Fluid Mech., 82, (1), p. 53-95, 1977.
- 3.5-4 S. Taylor, "Relevance of PSD Used in BRIWON to Model Turbulent Index Variations," TRW IOC AP-1556, 31 May 1988.
- 3.5-5 M. Litvak, "Laser Scatter from Xe-He Interface," TRW IOC AP-1554, Revision A, 28 June 1988.
- 3.5-6 Dennis L. Knepp, "Multiple Phase Screen Calculation of the Temporal Behavior of Stochastic Waves," Proc. IEEE, 71, (6), p. 722-737, 1983.

### 3.6 APACHE OPTICAL PROPAGATION MODEL (APOPM)

#### 3.6.1 Introduction and Background

This section describes the development of an optical propagation model called APACHE Optical Propagation Model (APOPM), which simulates wavefront propagation through an APACHE SBL. During the APACHE Program, the individual modules making up the model, as well as key interfaces between the modules, were developed, debugged, and exercised for representative test cases. Certain additional enhancements of the existing interfaces are still required to achieve full integration between the modules. These code-related enhancements are planned to be pursued during follow-on efforts.

APOPM was implemented to analyze optical propagation in the APACHE system, and to determine the optical performance associated with various designs and operating conditions. The model is intended to facilitate the design of both prospective APACHE SBL systems, as well as subscale experiments aimed at demonstrating wavefront correction of amplified laser beams using phase conjugation. To this end, a model was formulated which could both be used to simulate the end-to-end propagation of an input field through the whole APACHE system, as well as separately analyze the propagation and performance within one or more subsystems. The model incorporates propagation through key APACHE subsystems and components, including the beam director and its multisegmented primary mirror, the bidirectional amplifiers, and the SBS phase conjugation cell. Moreover, the model needed to accommodate a variety of configurations and brightness levels, as well as a wide range of parameter variations and input conditions.

Implementation of a fully three-dimensional wave optics model, although desirable, was not practical for a variety of reasons. First, an appropriate three-dimensional code for SBS phase conjugation was not available. Second, for the conditions of interest to APACHE, three-dimensional wave optics codes appeared to require long run times, limiting their usefulness for the extensive parametric studies required. Moreover, many conditions of interest, such as misfigured and misaligned

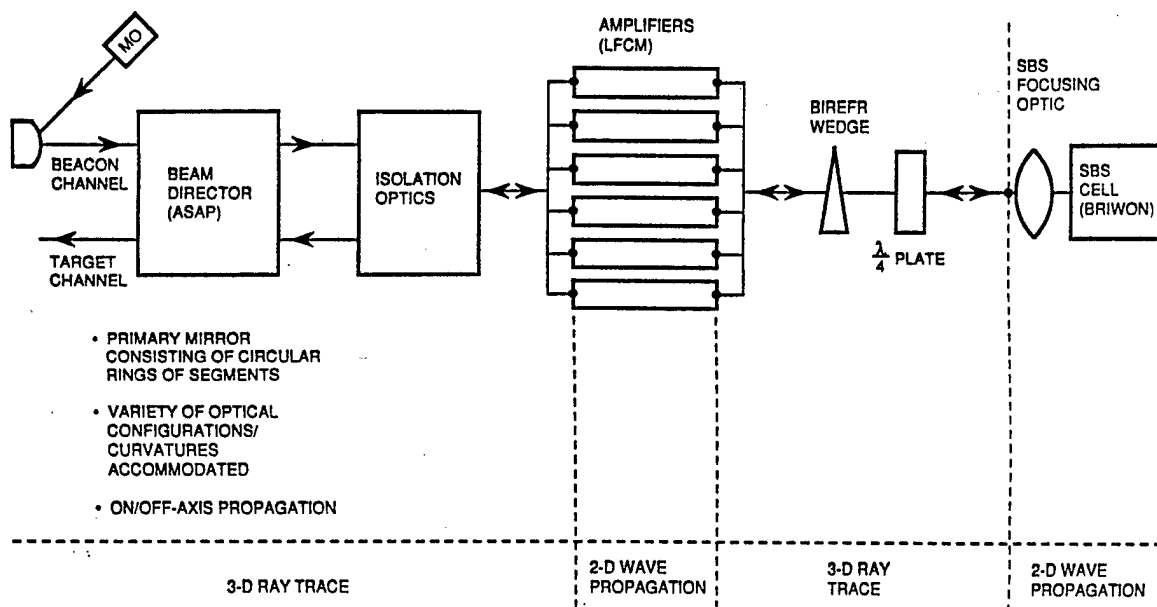
multisegmented mirrors were not conveniently modelled using existing wave optics codes. Third, an ASAP ray trace model of the APACHE beam director had already been developed and applied successfully to diagnose beam director design; it was desirable, therefore, to take advantage of this well-established capability.

Below we present an overview of APOPM describing the structure and content of the model, followed by a brief description of the code development efforts performed for APOPM. Finally, representative results obtained using the bidirectional amplifier module are described.

### 3.6.2 Overview of APOPM

In view of the above considerations, the APOPM model was constructed as a modular combination of three-dimensional and two-dimensional codes for individual APACHE subsystems, as indicated schematically in Figure 3.6-1. In particular, a three-dimensional ASAP ray-trace model was chosen to model the APACHE beam director (which was designed off-line using Code V); a two-dimensional wave optics model of the phase-conjugate amplifier (the LFCM code) was chosen for the bidirectional amplifiers; and a two-dimensional wave optics model, the BRIWON code, was selected for the SBS cell. The master oscillator (MO) was not included because the MO output is spatially filtered by the beacon. Thus, MO and beacon beam quality effects, including deviations from nominal beacon position, are most conveniently incorporated via the ASAP model of the BD. Propagation through other portions of the beam train, including beam dividing and combining optics for the amplifiers, and various isolation subsystem components such as gratings, retardance plates and birefringent wedges, can straightforwardly be incorporated into APOPM using the ASAP code. For simplicity, detailed propagation through these portions of the system has been omitted from the initial version of APOPM implemented under the current program.

When using APOPM to simulate end-to-end propagation, we start with a spherical probe wave emanating from the beacon which floods the primary mirror. In principle, it is also possible to add aberrations to the incoming probe beam, but this is generally not appropriate since the beam



June 89-D-2

Figure 3.6-1. APACHE Optical Propagation Model

quality of the spatially filtered probe can be assumed to be very good. The beam incident on the primary is propagated through the BD using the ASAP model of the APACHE BD. This model incorporates a multisegmented primary mirror and a monolithic secondary, plus a number of other smaller beam director optics, as discussed in detail in Section 2.7. Random or deterministic aberrations can be applied as misfigure and/or misalignments to the various segments and optical elements in the BD. The aberrated beam is successively demagnified and propagated through the BD, eventually exiting at the polarization-separation grating. On the input leg, the low-power beam traverses the optics in the beacon channel, distinct from the high-power path traversed by the return beam. The ASAP code propagates rays through the BD; however, by exercising an option in ASAP, we can also obtain the output beam in the form of a field (intensity and phase), as required for input to LFCM. This is illustrated in Figure 3.6-2 for the case of a spherical wave input to the beam director. The figure displays the phase profile at the output from the beam director propagating toward the amplifier, and a one-dimensional cut through the phase profile, which can be used as input to LFCM.

The two-dimensional field from the BD is used as input to the LFCM amplifier model, which provides a two-dimensional simulation of propagation through a cylindrical, ALPHA-type laser amplifier. Any line through the two-dimensional beam profile may be selected for the propagation through LFCM.

Transformations between the annular and compact legs (via the LFCTOA and LFATOC interface codes described below) are used for the input and output of the bidirectional amplifier to account for the cylindrical geometry. The wave is subsequently propagated through the gain region in either direction using the two-dimensional LFCM code with the appropriate magnification. Plane and distributed aberrations from the amplifier optics or gain medium can be incorporated using phase screens.

After the incoming beam from ASAP (low-power probe) has been propagated through the amplifier, it becomes the input to the SBS cell. The output from the SBS cell provides a reverse-pass beam through the

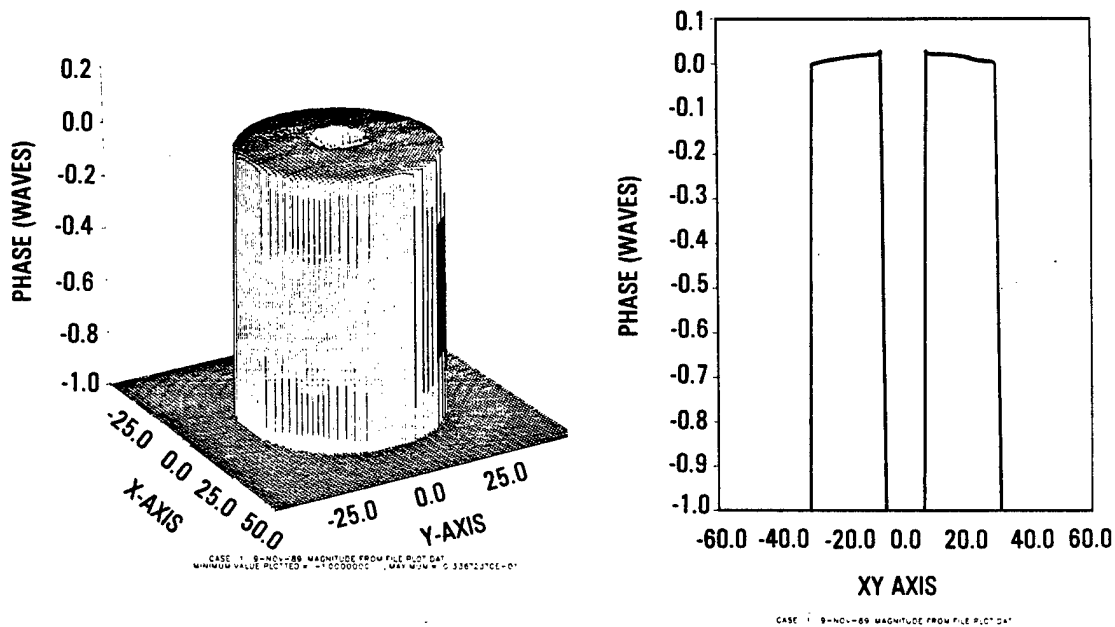


Figure 3.6-2. Beam Intensity and Phase Distributions Computed by ASAP as Input to LFCM Code



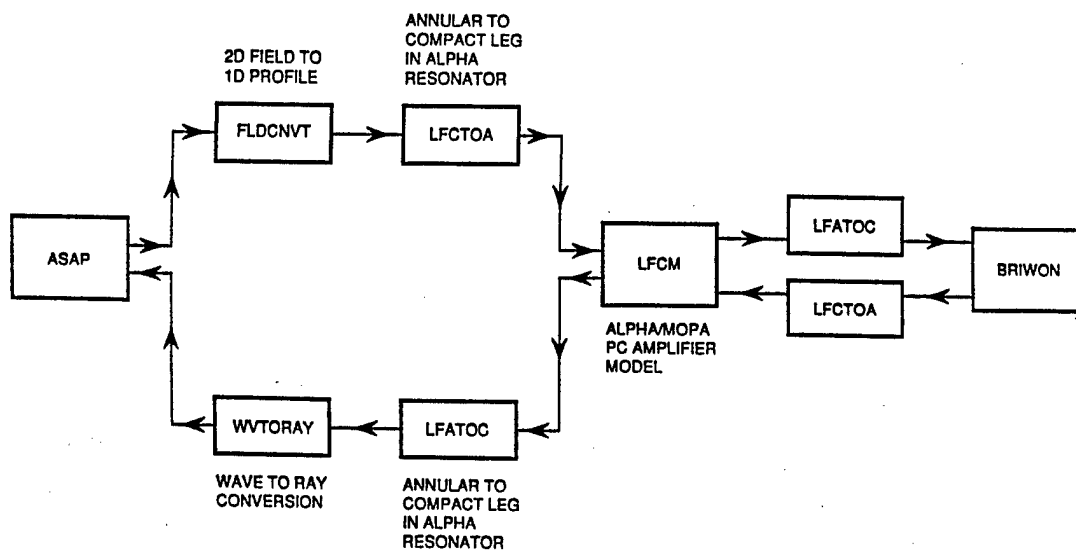
amplifier, which eventually becomes the high-power beam to the target. The bidirectional gain distribution is used to calculate the field going to the SBS cell. The return from the SBS cell is then used for the return wave propagating through the gain region, an approximation which is suitable for the high conjugation fidelity regime of interest here.

The BRIWON SBS model, through LFATOC, directly accepts, as input, the field output from the amplifier model. A variable focus can be applied to the incoming wave, simulating the effect of the focussing optics in front of the SBS cell. Various fundamental parameters describing the SBS medium are input to the code. Generally, BRIWON is used to model SBS under quasistatic conditions, although certain effects such as turbulent layers and grating convection can be simulated as well. The field output from BRIWON, through LFCTOA, is used directly as input to the amplifier in the return direction, as indicated above. Examples of results obtained using the BRIWON SBS module are presented in Section 3.5.

Several options are available for creating a return beam from the one-dimensional amplifier output to propagate through the beam director target path. For example, for circularly symmetric BD aberrations, the one-dimensional field may be used directly to generate the two-dimensional return wave. Alternatively, a two-dimensional propagation could be performed with ASAP for the target path, and the performance gauged using the corresponding cut through the two-dimensional profile created from the beacon path. Finally, cuts in different directions can be used as inputs to LFCM and BRIWON, and used to reconstitute a pseudo-two-dimensional return wave for the BD target channel.

### 3.6.3 APOPM Code Development

Three codes have been written (FLDCNVT/FLDCVT2/FLDCVT3) to read the files output by ASAP and to produce a field file which can be read by the program LFCTOA. A second file is produced which can be read back into ASAP to test the wave-to-ray conversion routine. The logic chart for the amplifier codes on the incoming path to the SBS cell and the return path back to ASAP is given in Figure 3.6-3. LFCTOA reads a one-dimensional field file, and transforms the coordinates and intensity distribution



June 89-D-5

Figure 3.6-3. Amplifier Code Logic Chart

according to the waxicon/reflaxicon to outer cone transformation in an ALPHA-type amplifier. LFATOC makes the opposite transformation. Both use geometrical ratioing of areas instead of wave optics propagation. LFCTOA produces an input to LFCM, both at the BD end (using the field produced by ASAP) and at the phase conjugator end (using the field output by BRIWON). Since ASAP is a ray trace code that does not require guard bands, LFCTOA was modified to read the file produced by FLDCNVT (or FLDCVT2 or FLDCVT3) and apply a guard band needed by the Fourier transform routines in LFCM.

The LFCM code, a two-dimensional wave optics amplifier code, was previously modified to model the ALPHA resonator geometry and two-level kinetics appropriate to an HF gain medium. This gain model does not include the frequency dependence of the gain, and thus cannot predict the change in gain saturation due to the SBS shift. It does, however, account for the gain saturation resulting from the presence of both incoming and SBS return waves. This code was used with the current APACHE design parameters to represent the phase-conjugated HF amplifier in the end-to-end model and to perform trade studies on the effects of the gain/conjugation interaction. On the incoming path, LFCM is run with perfect phase conjugation in order to simulate, in an approximate way, the gain saturation due to the overlapping incoming and return fields. The field going to the phase conjugator is then input to LFATOC. LFATOC performs the transformation from the outer cone to the waxicon/reflaxicon. LFATOC assumes that the field from LFCM is half of the actual field in the annular leg and combines this half with its mirror image to give the output in the compact leg. The resulting field is then input into BRIWON, a two-dimensional wave optics code, which computes the field of the SBS return beam. This is run through LFCTOA to give the field in the annular leg of the resonator on the phase conjugator side. Using the original input beam into the amplifier, LFCM is then run with the actual SBS return calculated by BRIWON instead of perfect phase conjugation. The beam output from the amplifier on the return path is once again converted by LFATOC to the compact leg.

Code modifications to ASAP were made to read an input field from the file created by LFATOC and create the corresponding ray grid. The flux of each base ray on the grid is modified according to the intensity information given by the input field with linear interpolation for grid points lying between input points. Since LFCM and BRIWON have one transverse dimension, circular symmetry is assumed to create the two dimensional grid. The procedure used here is the same as that used by ASAP to create initial intensity profiles for the user-specified options offered by the program. The OPD information from the input field is then used to create a surface with point-to-point sag corresponding to half the OPD. After the intensity is set, the rays are reflected from this surface and thus acquire the desired phase information. The ray grid may then be traced back through the optical train to the beam director.

#### 3.6.4 Phase Conjugate Amplifier Parameter Studies

Studies of the preliminary design for the APACHE amplifier were conducted primarily in three areas. These areas consisted of (1) adjusting the gain saturation to reflect that produced by a return beam with an SBS shift; (2) varying the number of gain sheets and evaluating differences in output power and intensity distribution; and (3) assessing the ability of the amplifier design to correct aberrations of varying amplitude and spatial frequency in the presence of gain.

To account for the effect of the SBS shift on gain saturation, the SBS reflectivity was varied to yield a power to the SBS cell, and MOPA output power in agreement with predictions of the APACHE systems model, which includes the effect of the SBS shift. These calculations used a top hat intensity profile, gain length of 6.7 m, mode width of 2.6 cm, small signal gain of 0.038 per cm, and the same injected power used in the systems model. The case was first run without gain to determine the required guard band and mirror sizes. The mirrors were set to twice the geometric mode width, and the MOPA output wavefront after perfect conjugation was corrected to within 0.01 waves. The gain was turned on, and with intensity reflectivities of 0.61, 0.42, and 0.16, the MOPA output powers were very close to that of the systems model, varying little with SBS reflectivity.

This effect has been observed previously and is due to the fact that the gain on the return pass, which is less saturated, compensates for the loss at the SBS cell. The powers to the SBS cell for these three cases were 0.8 MW, 0.962 MW, and 1.59 MW, respectively. The latter was closest to the values of the systems model.

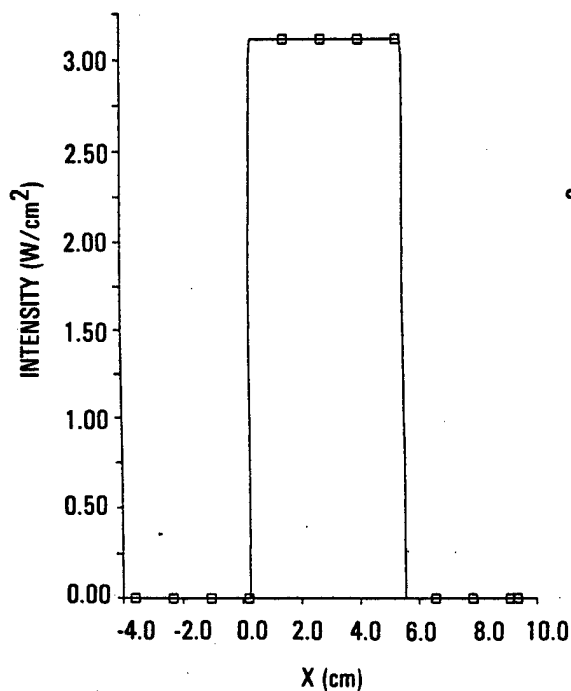
To verify these power levels and the effect of this amplifier design on the intensity and phase profiles in the presence of gain, the number of transverse points and gain sheets were increased to 256 and 8, respectively. The results were the same to within 5%.

Finally, phase conjugation correction of applied aberrations in the amplifier was evaluated. A collimated geometry with 5.2-cm mode width, overall gain length of 6.7 m, and small signal gain of 0.038 per cm was tested. The cases were run with 256 transverse points and four gain sheets. The mirror diameters were 2.75 times the geometric mode width.

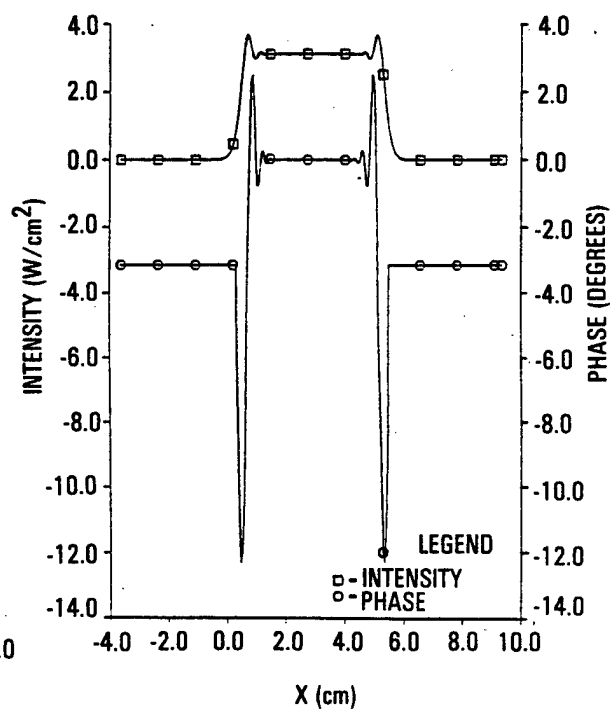
Typical results of the calculations are illustrated in Figures 3.6-4 and 3.6-5. Figure 3.6-4 illustrates results obtained for an unaberrated input field without gain. The field incident to the amplifier is indicated in (a), the field exiting the amplifier toward the SBS cell in (b), and the field output from the amplifier on the return pass in (c) [note the scale on the phase plot]. As expected, the field emerges from the amplifier with negligible changes for this case.

Figure 3.6-5 shows the corresponding sequence of curves for the case of an input field subjected to a two-cycle aberration of magnitude 0.32 waves, with the amplifier gain switched on. In this instance, the intensity is amplified and spatially modulated after the first pass through the amplifier. After the return pass, most of the applied aberration has been corrected (the residual is less than a fortieth of a wave), and the intensity further amplified.

(A) INPUT FIELD WITHOUT ABERRATION VS X



(B) COMPLEX FIELD INPUT TO P\* VS X



(C) MOPA OUTPUT COMPLEX FIELD VS X

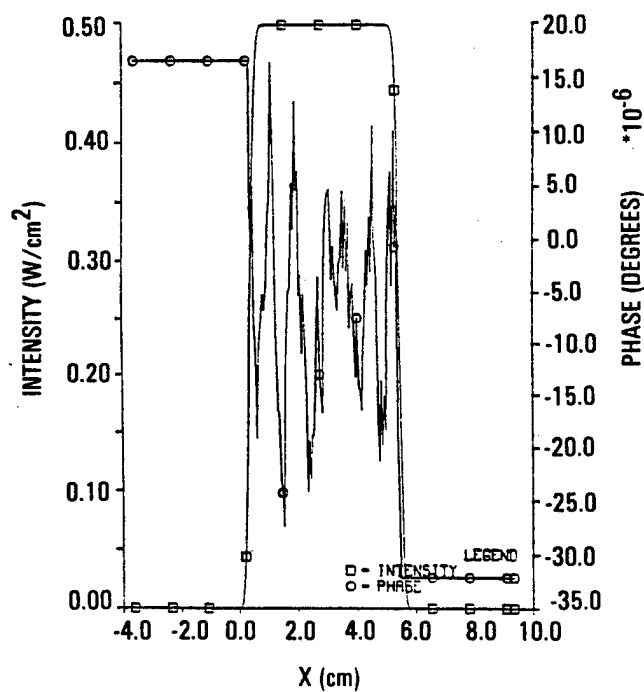
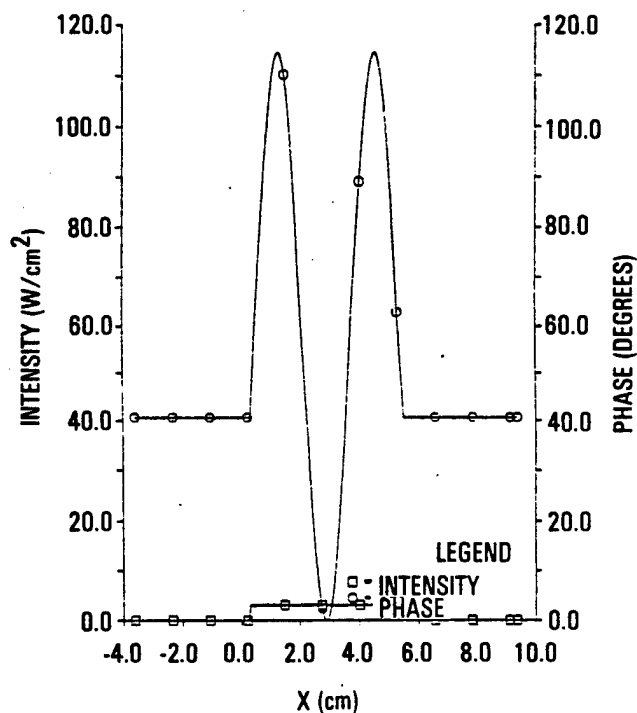
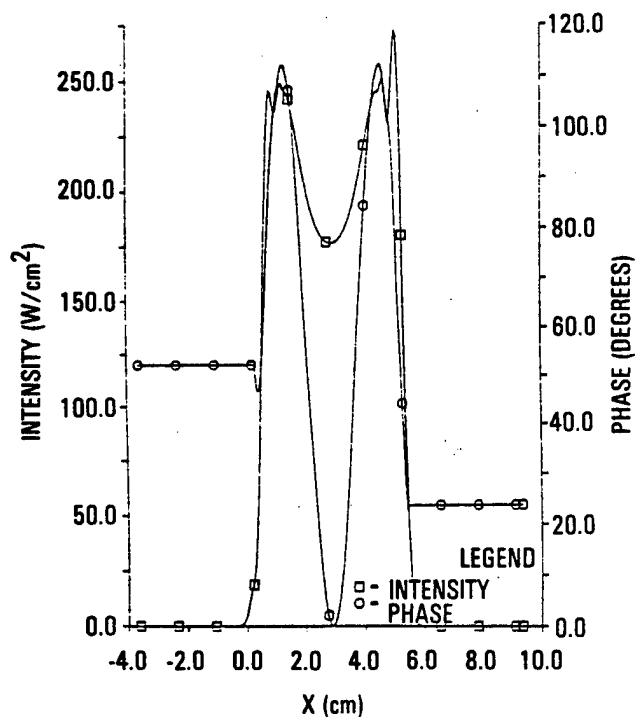


Figure 3.6-4. Examples of APOPM Code Calculations; Bare Cavity, No Input Aberration

(A) INPUT FIELD WITH ABERRATION VS X



(B) COMPLEX FIELD INPUT TO P\* VS X



(C) MOPA OUTPUT COMPLEX FIELD VS X

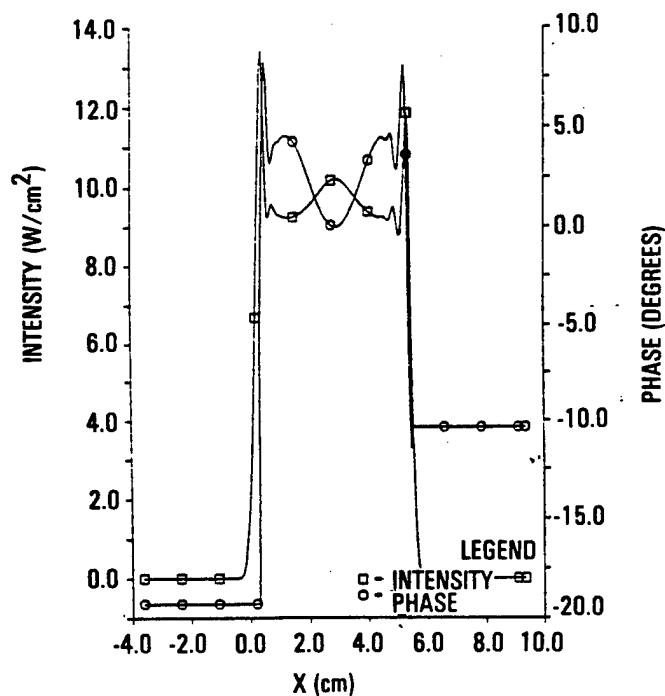


Figure 3.6-5. Examples of APOPM Code Calculations; with Gain, 2 Cycles of Aberration Superposed on Input Beam

## 4. ASAM MODEL

### 4.1 BACKGROUND AND OBJECTIVES

The APACHE Systems Analysis Model (ASAM) is used to relate systems level measures of performance such as total brightness, cost, and weight to subsystem and component parameters such as oscillator and amplifier sizes, SBS threshold and polarization subsystem isolation efficiency, for example. The model serves as a focal point for incorporating the technology development (experiments and analysis) into a single tool to support design. The model is intended to provide an efficient tool for assessing performance and selecting design parameters, which complements rather than replaces more detailed fundamental models and experimental data from which the simplified relationships in the model are drawn.

The ASAM contains of a set of relationships which specify the effect of various subsystem and component performance parameters on system level quantities such as brightness, cost, or weight. The calculation of brightness is complicated by nonlinear relationships between input and output powers and/or beam qualities for certain subsystems. Consider, for example, the effect of an initial amount of feedback to the master oscillator, which leads to a series of power changes throughout the SBL system starting with the MOs output itself, followed by the amplifier's output, the SBS cell output power and beam quality (BQ), and so forth. The new feedback power will, in general, differ from the initial value. In this instance, ASAM determines the self-consistent solution for both the oscillator output and the corresponding feedback power for a given size oscillator.

The model possesses several strata of input parameters at increasing levels of detail. For example, the isolation system performance may be parametrized at the subsystem level by just a single branching ratio between power transmitted along the target channel to that fed back through the beacon channel. At the component level, this branching ratio depends on various parameters such as grating rejection efficiency, quarter wave plate retardance error, excess amplifier retardance, and so forth. The parametrization process could be carried even further, e.g., expressing



grating efficiency in terms of line spacings and groove depths. The ASAM provides a context for parametrization at these varying levels of detail, although in most instances it will not be efficient to use the most fundamental levels of detail available within the model. Rather, the model is often most conveniently used with each subsystem parametrized in terms of just a few top-level characteristics or measures of performance, such as oscillator output power, amplifier length, SBS threshold, and so forth.

As used in the APACHE Program, ASAM actually consists of three separate submodels to calculate brightness, weight, or cost, which could also be merged for convenience, as required. The brightness model essentially traces power and BQ through the APACHE system using analytically derived or experimentally inferred functional relationships between their input and output values for each subsystem or functional element. As currently configured, aperture and jitter do not pertain at the subsystem level; rather, specific values for systems jitter and primary mirror aperture are selected when using the model.

In the following subsections, we review the key relationships contained in the systems model and their origins. In these sections, the following nomenclature will be utilized:

- $P_o$  = MO power without feedback
- $P_r$  = Return power feedback to MO
- $P_{mo}$  = MO power output in the presence of feedback
- $P_{amp}$  = Output power from amplifier (double-pass)
- $P_{th}$  = Threshold power for SBS (single line)
- $N_{th}$  = Number of times above threshold in SBS cell
- = Input power to SBS for single line/ $P_{th}$  for that line.

#### 4.2 BRIGHTNESS MODEL

In ASAM, the brightness is given in terms of the following variables

$$B = \frac{PA}{\lambda^2} \frac{1}{BQ^2} \frac{1}{\left[1 + \frac{\sigma_j^2}{\sigma_d^2}\right]} (1 - \epsilon^2)^T \quad (4.2-1)$$

where,

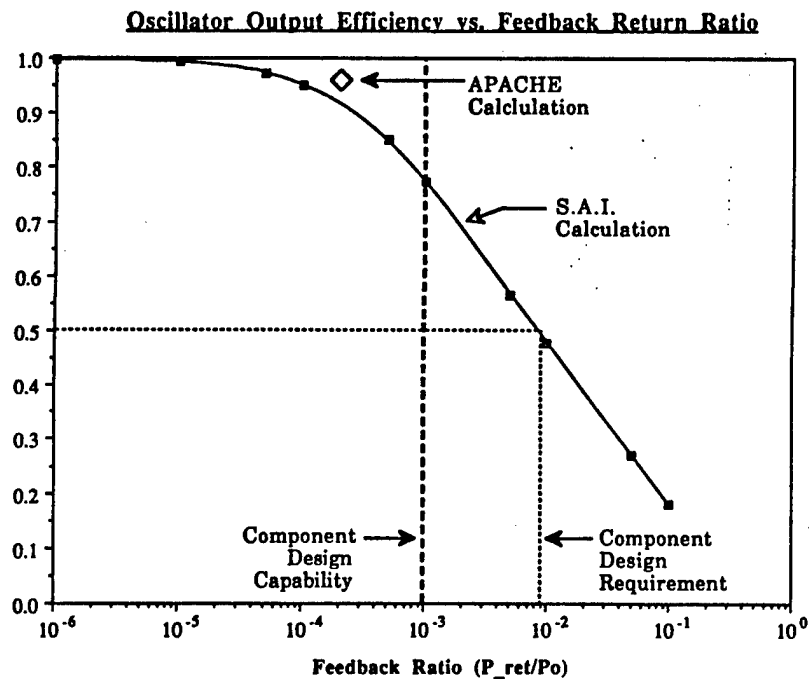
- P = Power out of device
- A = Area of primary mirror
- $\lambda$  = Wavelength
- BQ = System beam quality
- $\sigma_j$  = Beam spread due to jitter
- $\sigma_d$  = Beam spread due to diffraction
- $\epsilon$  = Linear obscuration ratio
- T = Transmission function

The functional relationships used in ASAM for power and BQ in each subsystem or functional element are summarized below.

#### 4.2.1 Master Oscillator

At the top level, the master oscillator subsystem performance is specified by (a) the oscillator output power  $P_o$  in the absence of feedback; (b) the return power leaking backward through the beacon channel,  $P_r$ ; and (c) the reduction in oscillator output power as a function of the return ratio  $P_r/P_o$ . Since the MO output power  $P_{mo}$  depends on the return power, which itself depends on the output power, a transcendental relationship determines the value of  $P_{mo}$  corresponding to a given  $P_o$ . Note that strictly speaking, both the output power and BQ of the MO are influenced by feedback. The output power  $P_{mo}$  in the present formulation is more appropriately interpreted as the brightness at the spatial filter in the far field of the oscillator, which depends on both near-field power and BQ.

The model used in ASAM to specify degradation due to isolation is based on a ring resonator code calculation by SAIC, which yields the relation illustrated in the figure below. This analysis is consistent with similar modeling conducted by TRW on the ALPHA HEXDARR resonator. The TRW model was validated by direct comparison with experiments, as discussed in Section 6 of Volume I. The calculation shows a degradation of about 20% for a return ratio of  $10^{-3}$  and 50% for  $10^{-2}$ .



Nonisolated Feedback Power/Oscillator Power

#### 4.2.2 Beacon Mirror and Spatial Filter

ASAM currently assumes that the spatial filter can be adjusted to yield a wavefront of specified beam quality  $BQ=1.005$  (cf. Section 2.2). Thus, the only other effect of the spatial filter is a reduction in the incident power by some specified amount, chosen as 63.5% in our calculations. Thus, the spatial filter enhances BQ at the cost of a reduction in transmitted power. However, as long as the amplifier is saturated and power at the SBS cell is above threshold, this reduction in power has a negligible effect on systems performance.

#### 4.2.3 Beam Director

Since the beam director consists of two nonequivalent channels (beacon channel for the input, target channel for the output) and due to the fact that the beacon and target are at different conjugates, the correction of primary mirror aberrations is imperfect. The correctibility of the APACHE beam director has been calculated under a variety of conditions such as primary mirror segment piston, tilt and misfigure, and beacon tracking angle misalignment, using the ASAP model discussed above (cf. Section 3.3). Certain of these relations have been already been incorporated in ASAM, and others can easily be added as required.

ASAM also allows the BQ degradation due to unconjugated optics to be specified, along with the power attenuations corresponding to each channel. In addition to the incoming power in the beacon channel and the outgoing power in the target channel, ASAM also keeps track of the feedback power leaking through the isolation system and propagating backwards along the beacon channel to the MO. The amount of power fed back is determined by the isolation subsystem.

#### 4.2.4 Bidirectional Amplifier Subsystem

ASAM accommodates an equal division of the incoming power from the beam director into N amplifiers; N=6 is the current choice for the high brightness SBL. ASAM uses a simplified single gain sheet amplifier model called AMP1GS discussed in Section 3.4 to calculate the output power from the amplifier on the forward and reverse passes. The forward pass power depends on the return pass power from the SBS cell, so the amplifier model must calculate a self-consistent solution to the amplifier plus SBS cell power equations. As currently configured, the amplifier model keeps track of four separate laser lines. While detailed inputs of fundamental quantities can be made to the amplifier model, generally the amplifier is parametrized in terms of just a few top-level characteristics such as a gain coefficient and gain length and width.

The outputs from the amplifiers are summed to simulate the beam combining implemented prior to focusing into the SBS cell.

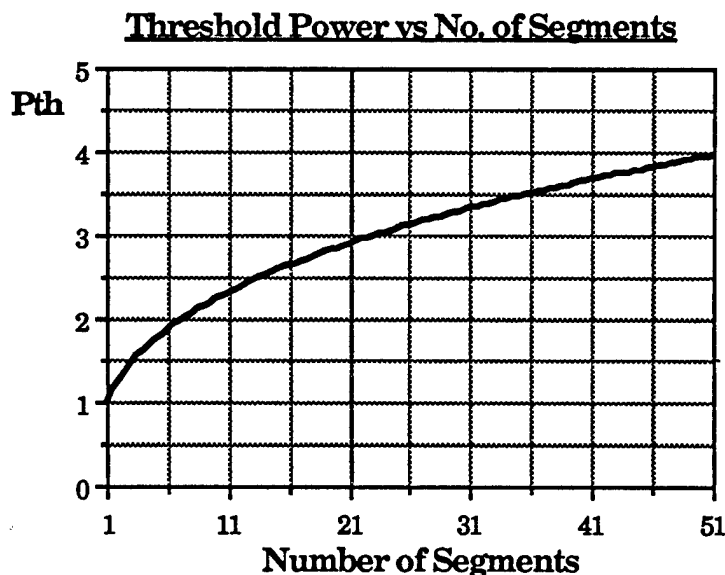
Amplifier BQ is not calculated by ASAM, but any additional BQ budgeted for gain-phase interactions or other mechanisms can be specified as an input to be tracked by the model.

#### 4.2.5 SBS Subsystem

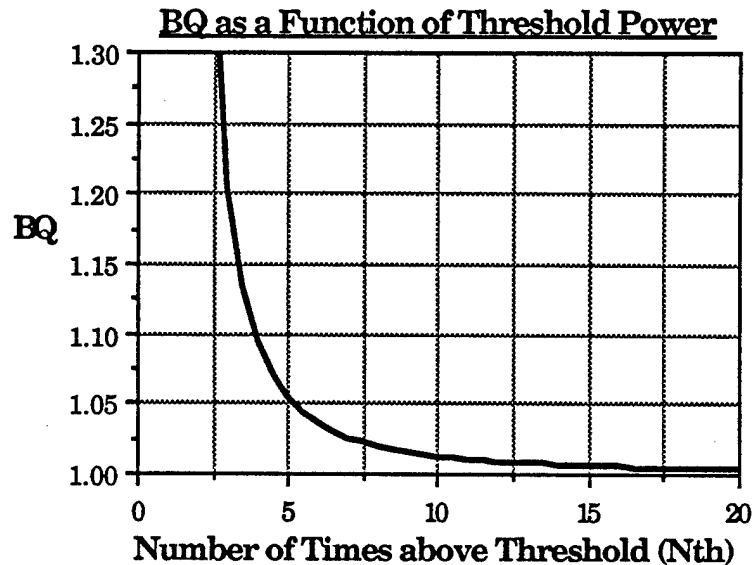
The response of the SBS cell is determined by the input beam characteristics as well as the properties of the conjugation medium. The reflected power from the SBS cell is zero for input powers below some threshold value  $P_{th}$ , and increases linearly above threshold; a slope efficiency of 0.9 would be typical. However, the threshold power is itself a function of the input beam phase, so the SBS return power depends on both the power and BQ of the input beam to the SBS cell.

The independence of threshold on input beam quality has been modeled based on the results of array alignment experiments conducted under APACHE (cf. Section 6. in Volume I). Essentially, this experiment indicated that for multisegmented mirrors with  $M$  randomly misaligned segments, the threshold increased as  $M^{0.35}$  as shown in the plot below. Moreover, the threshold increased linearly with increasing (correlated) beam tilt  $T_1$ .

The beam quality of the SBS output beam is also affected by both the conjugating medium and the input beam characteristics. Conjugation fidelity is influenced by many factors, including, for example, the purity and uniformity of the medium, and thermal and flow induced fluctuations. Beyond these factors, a principal influence on output beam quality is the number of times above threshold  $N_{th}$  of the incoming beam power. The degradation of SBS output beam BQ as a function of threshold is shown in the plot below.



Number of Segments



Number of Times above Threshold (Nth)

This relation represents an approximate parametrization based on results obtained from the RSELE program, where it was observed that for good SBS fidelity one must be approximately three times above the SBS threshold. The actual functional relationship used is ad hoc and was simply chosen to represent a decrease in fidelity as the input power is diminished. This formulation needs to be updated as more data becomes available.

#### 4.2.6 Isolation Subsystem

As mentioned previously, the isolation system performance can be parameterized at the top level in terms of a single branching ratio between power delivered to the target channel and power leaking back through the beacon channel towards the MO. At a more detailed level, ASAM relates this branching ratio to its underlying causes, i.e., retardance in amplifier optics leading to polarization mixing, retardance errors in the quarter waveplate, and grating performance parameters (leakage of unwanted polarization through the polarization sensitive grating rhombs).

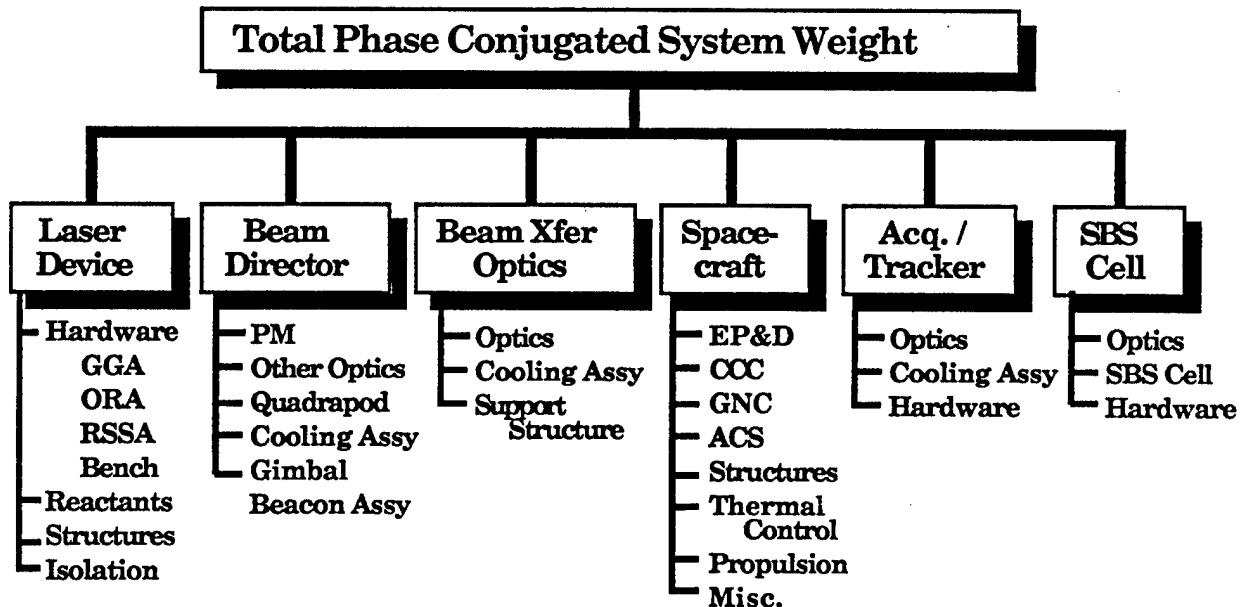
ASAM also incorporates an additional power attenuator ("neutral density filter") between the MO and beacon, which is used to enhance MO isolation. Since the input power to the amplifier is sufficiently above saturation, reductions in the incoming power have relatively little effect on the amplifier output. However, any power leaking back towards the MO will be significantly attenuated, thereby enhancing isolation.

Examples of calculations of brightness as a function of various subsystem parameters, obtained using ASAM, are presented in Section 5.2 on system resiliency.

### 4.3 COST AND WEIGHT MODEL

#### 4.3.1 Weight Model

A subset of the ASAM is the weight model which calculates the total phase conjugated SBL weight. As shown in the figure below, this total system weight is synthesized from the weights of its various subsystems, namely the laser device subsystem, the beam director subsystem including the beacon subsystem, the beam transfer optics, the acquisition/tracker subsystem, the SBS cell subsystem, and the spacecraft subsystem. Some of the primary weight scaling parameters for each of these systems are described below.



Total Phase Conjugated System Weight

The laser device weight is comprised of hardware weight, reactant weight, and structure weight associated with both the oscillator and amplifiers. The hardware refers to all the hardware associated with the GGA, EMA, ORA, RSSA, and bench assemblies, and the weight scales primarily with the power of the device as derived from actual ALPHA data. The reactants refer to the reactants required by the GGA, with the weight scaling with runtime, power, and the individual reactant flow rates based upon equations developed from actual ALPHA data and HYLTE nozzle technology. The structure refers to the support structure used to hold the various components to the spacecraft, and the weight scales as a percentage of the total hardware and reactant weight based upon TRW estimates. Additionally, the weight of the isolation optics, i.e., the four quarter waveplates and the four grating rhombs, are added to the laser device weight.

The beam director weight is comprised of the weight associated with the optics including both the primary mirror and the beam train optics, the quadrapod structure, the cooling assembly, and the gimbal. The primary mirror weight scales with diameter based upon a detailed analysis done by ORA. The quadrapod structure refers to the four struts which hold the secondary mirror to the primary mirror, and the weight scales with the PM diameter and F#. Based upon TRW and vendor estimates, the beam train optics weight scales with the optics diameter which in turn is a function of the telescope magnification. All the optics are cooled, with the cooling assembly weight scaling as a function of power and runtime from the RSSA weights. The gimbal (gas bearing) weight was estimated taking into account the beam director weight and slew rate.

The beacon weight consists of the weight of the mirror assembly and the spacecraft assembly. The mirror assembly consists of the mirror itself, the cooling assembly, and the support structure. For the optics and cooling assembly, the weight scaling parameters are exactly as described above. Additionally, the spacecraft and structure weight scales as a percentage of the total weight based upon TRW estimates.



The beam transfer optics refer to the optics which transfer the beam from the beam director to the amplifier and back. The weight for the optics, cooling assembly, and support structure all scale in the same manner as previously discussed. This is also the case for the target acquisition and tracker subsystem which consists of optics and sensors which locate the target and keep track of its position.

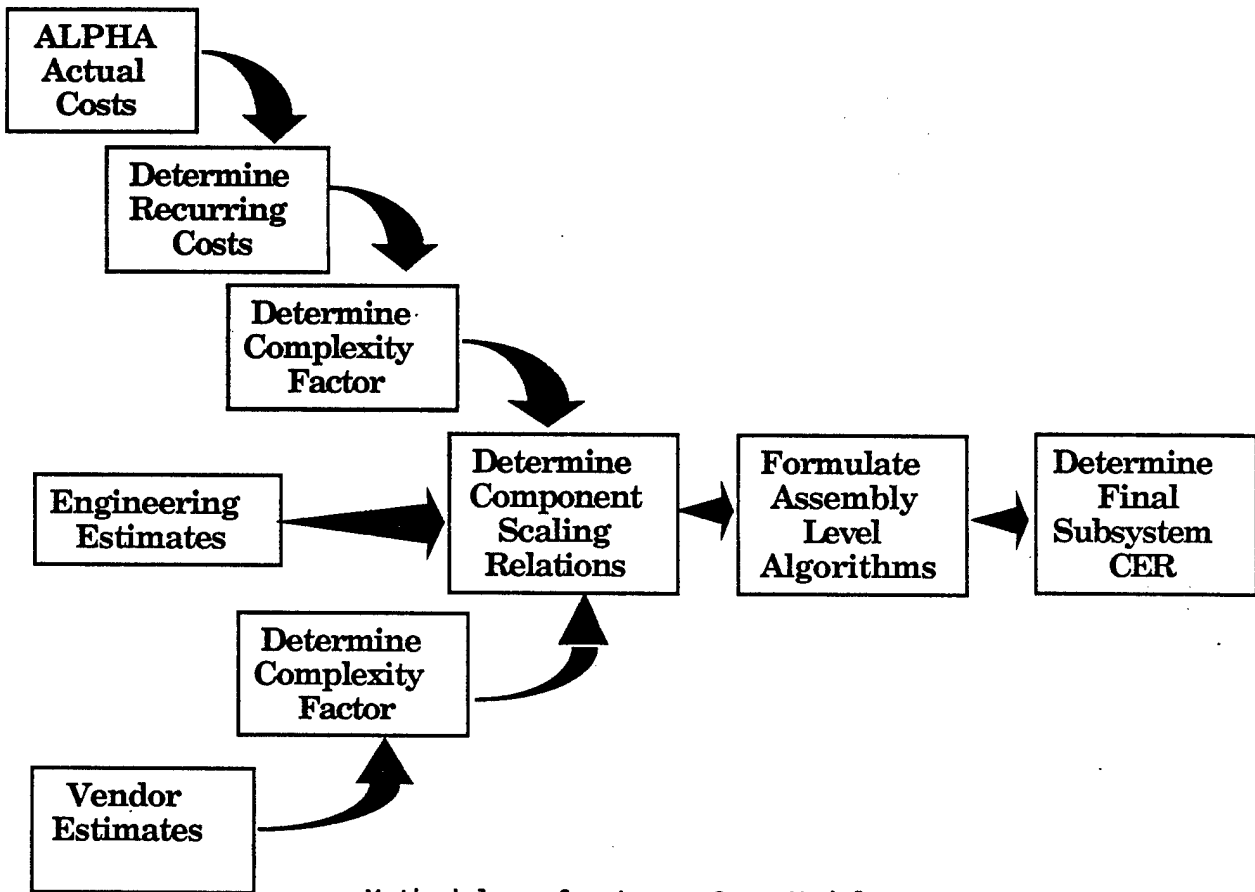
The SBS cell weight consists of the weight of the cell itself, the weight of the focusing mirrors, and the weight of the hardware associated with a flowing gas cell configuration. The SBS cell assembly scales with the size of the cell as well as the total weight of the gases, while the optics scale with diameter as before.

The final component making up the system weight is the spacecraft itself. Basically, the spacecraft weight was obtained directly from a study done by LMSC on a similar type of SBL. Additionally, a contingency of 12% of the total system weight was added to the weight model to take into account any unforeseen weight contributions.

#### 4.3.2 Cost Model

The cost model is also a subset of the ASAM which calculates the total phase conjugated SBL cost. As before, the total system cost is comprised of the individual costs of its various subsystems. All the subsystems outlined in the weight model are also covered in the cost model with the addition of launch and management costs. Again the primary cost scaling parameters for each of these subsystems are described below.

The laser device cost takes into account the same elements as above, namely the hardware costs (GGA, ORA, etc.), the reactant costs, and the support structure costs. The methodology involved in developing the laser device cost estimating relationships (CERs) is shown in the figure below. For the hardware and fluid costs, the TRW device model, which was based upon actual ALPHA data, was again utilized. The support structure costs scale with fluid and hardware weight based upon an algorithm developed by LMSC. In fact, all the structure costs for all the subsystems in this model scale with weight using this same cost algorithm. Also, the cost of the isolation optics are added to the laser device cost.



Methodology for Laser Cost Model

The beam director costs consists of the same components as previously described. Again, the primary mirror costs scale with diameter based upon analyses done by ORA. The beam train optics costs scale with the optics diameter based upon TRW and vendor data. The cooling assembly costs are scaled down from the RSSA costs. The quadrapod structure and gimbal structure use the LMSC structural cost algorithm.

The beacon cost consists of the mirror costs and spacecraft costs. The mirror costs scales with diameter based upon TRW estimates, while the spacecraft cost scale with weight based upon a propulsion system model developed by LMSC.

The beam transfer optics and target acquisition/tracker costs scale as one expects: the optics costs scale with diameter, the cooling assembly scales from RSSA costs, and the structure scales with weight using the LMSC cost algorithm.

The SBS cell most depends on the cost of the optics, gases, and flowing cell hardware. The optics scale with diameter based upon TRW and vendor estimates; the gases scale as a function of cost per unit weight; and the hardware scales with weight based upon the LMSC propulsion system model.

The launch cost is based on a cost per unit weight and is consistent with the one used by LMSC. The management costs consist of program management costs, system engineering costs, integration and testing costs, quality assurance costs, and some miscellaneous costs. These costs were based upon a percentage of the total system cost based upon estimates from TRW and LMSC.

As before the spacecraft cost was obtained from LMSC. Additionally, a cost contingency of 12% was added to the total system cost to take into account any other missing costs.

## 5. SBL SYSTEMS EFFECTIVENESS

### 5.1 INTRODUCTION

A major focus of the APACHE SBL design effort was the effectiveness of the phase conjugation design concept when incorporated into a deployed system, taking into account the realities associated with manufacturing, launching, deploying and maintaining a highly complex weapons system. Toward this goal, a study was conducted to assess how the incorporation of phase conjugation in an SBL impacts the effectiveness of the SBL in a system sense. The systems effectiveness study addressed how phase conjugation affected items such as optics manufacturability, control system complexity, fabrication schedule, system cost and weight, and resiliency. This last term relates to the sensitivity of system performance to deviations in subsystem design parameters from nominal values.

In order to quantitatively assess how system effectiveness is influenced by phase conjugation, it was desirable to compare two equivalent systems, side-by-side, one based on phase conjugation and the other using (active) adaptive optics (AO) for device cophasing and beam control. A concept developed under the USAF Space Division's SBL System Architecture Study was used as a representative AO SBL design for systems effectiveness comparisons with the APACHE phase conjugate SBL concept.

The subject of systems effectiveness is extremely broad in scope, involving a wide range of system parameters and prospective figures of merit. In order to keep the scope of the APACHE study at a tractable level, only those areas felt to have the largest impact on system effectiveness were considered. Thus, the systems effectiveness study was restricted to the following areas:

- Systems resiliency
- Primary mirror cost and weight
- Laser device cost and weight.

The results of effectiveness analyses performed for these areas are reported in the following sections.

The work described here represents an initial attempt to quantify how phase conjugation impacts SBL fabricability and operation in a realistic environment. Although preliminary in nature, the results of this study surfaced several areas where phase conjugation eases fabrication and control requirements by relaxing optical and mechanical tolerances. Further work is planned for APEX on systems effectiveness, which will build on the initial efforts developed under APACHE and described below.

## 5.2 SBL SYSTEMS RESILIENCY STUDY

### 5.2.1 Background and Introduction

The term "resiliency" is used here to describe the ability of an SBL system to maintain a viable level of overall performance despite degradations in the performance of individual subsystems or components. Subsystem degradation may be due to a variety of factors. First, the performance may be substandard due to manufacturing defects and/or the failure to meet design tolerances. Second, performance can degrade due to improper handling, storage, transportation and/or installation. Third, performance may become degraded as a result of stresses and vibration incurred during launch. Fourth, performance may degrade due to environmental effects, both on the ground as well as in space. Fifth, degradation may occur due to aging, both in use as well as in a dormant mode. Sixth, degradation may be incurred due to threats during engagement, e.g., EMP and soft x-rays accompanying nuclear blast. In the present work, no attempt is made to assess the probability that any of these conditions will occur, resulting in degradation of SBL functional elements. Rather, the present analysis only addresses what happens to total systems performance when the performance of a particular subsystem or component has degraded by a certain amount for whatever reason, without specifying the particular causes for the subsystem degradation.

#### 5.2.1.1 Brightness as a Gauge of Systems Performance

Various criteria can be invoked with which to gauge overall systems performance. The most useful and direct for SBL system performance is the total systems brightness, i.e., the brightness of the output beam to the target. We therefore take the resiliency of an SBL system to be its

ability to retain total systems brightness despite degradation in subsystem or component performance. The output beam brightness may be expressed in the form:

$$B = B_0 * P * A * f_1 * f_2 / BQ^{**2} \quad (5.2-1)$$

where B is the output beam brightness, B<sub>0</sub> is a constant (its value need not be specified since only normalized brightnesses will be used here), P is the total power of the output beam, A is the primary mirror aperture area, BQ is the net beam quality of the output beam, and f<sub>1</sub> and f<sub>2</sub> are factors accounting for jitter and obscuration. The emphasis in the present study will be to compare system performance for a phase conjugate SBL with one based on adaptive optics, as a function of variations in subsystem parameters. The latter variations ultimately affect the power or beam quality terms in the systems brightness. While there are also potentially significant differences between the resiliency of a representative A0 and an APACHE SBL system with respect to jitter, a detailed analysis of jitter-related phenomena was judged to be beyond the scope of the present effort. Moreover, it is convenient to perform the analysis assuming equal aperture areas and obscurations in the two systems. Although these could be allowed to differ in more sophisticated studies of system resiliency, nevertheless, the results would be expected to remain qualitatively similar.

#### 5.2.1.2 Degradation Sources, Mechanisms and Subsystem Performance Parameters

Degradations may be described by specifying the functional element (i.e., subsystem or component) and the type of degradation involved. For example, the master oscillator (MO) is a functional element which is subject to various types of degradation, such as increased BQ, decreased power, and/or increased jitter. The functional element together with the type of degradation (e.g., MO BQ) will be referred to as a "degradation source." Associated with any given degradation source are any number of degradation mechanisms or causes. Thus, as an example, MO BQ can degrade due to deterioration of the optical coatings in the MO, which results in thermal distortions of the MO optics.

In the analysis which follows, each degradation source will be represented by a single parameter. In some cases, such as MO BQ, the degradation source and the parameter selected for its measure (i.e., BQ) are identical. On the other hand, in the case of oscillator isolation, return power to the MO is the parameter selected for the analysis. Resiliency is measured by degradation in total systems brightness as the applicable parameter deviates from its design value or design tolerance. Should the brightness of system A turn out to be highly sensitive to deviations in MO BQ from its design value, then it would not be considered resilient with respect to this source of degradation. On the other hand, if system B's brightness is entirely insensitive to increases in MO BQ, then system B is highly resilient with respect to degradations in MO BQ.

For the initial resiliency study, approximately twenty degradation sources applicable to either one or both SBL systems (i.e., APACHE and adaptive optics) were investigated. For each degradation source, we attempted to identify the single simplest and most physically transparent independent parameter; brightness was then calculated as a function of that parameter for use in the resiliency analysis. For simplicity, interaction effects between different mechanisms were neglected (with some exceptions) in the initial analyses conducted here.

#### 5.2.1.3 Calculation of the Sensitivity of Brightness to Subsystem Parameters

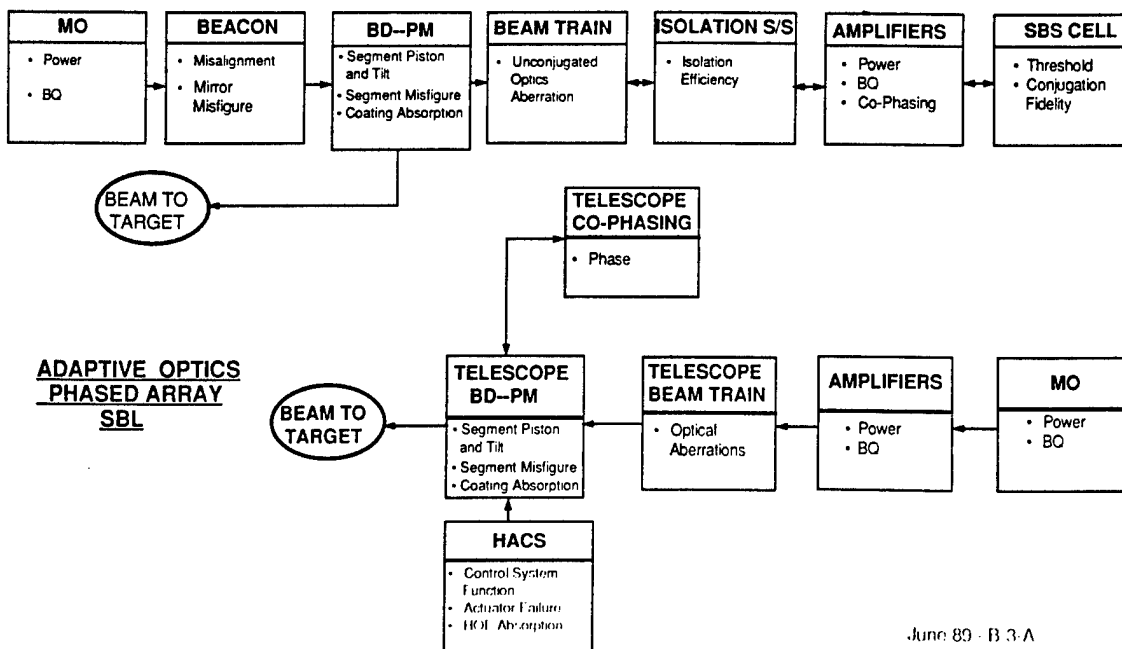
The dependence of brightness on the applicable parameter for a given degradation source was calculated using simple analytic formulae whenever possible, or through the use of various models and codes where more detailed calculations were required. For example, several of the resiliency calculations required the use of the APACHE optical propagation model (Section 3.6), while others required use of the APACHE Systems Analysis Model (Section 4). In other instances, specialized models were formulated to facilitate the analysis, as will become evident from the discussion below.

#### 5.2.1.4 Degradation Sources Selected for the Present Study

The degradation sources selected for the present analysis are summarized in Figure 5.2-1. They are also lumped under the various



## APACHE SBL



### BEAM DIRECTOR

- o PM SEGMENT PISTON
- o PM SEGMENT TILT
- o PM SEGMENT MISFIGURE
- o PM SEGMENT COATINGS
- o HOLOGRAPHIC OPTICAL ELEMENTS
- o TELESCOPE/AMPLIFIER OUTPUT COPHASING
- o ABERRATION CONTROL SYSTEM CORRECTABILITY
- o FINE FIGURE ACTUATOR FAILURE

### BEACON

- o BEACON TRACKING ANGLE
- o BEACON MIRROR MISFIGURE

### BEAM TRAIN OPTICS

- o OPTICAL ABERRATIONS

### AMPLIFIERS

- o BEAM QUALITY
- o POWER (GAIN)

### SBS CELL

- o CONJUGATION FIDELITY
- o THRESHOLD

### MASTER OSCILLATOR

- o BEAM QUALITY
- o POWER
- o ISOLATION EFFICIENCY

Figure 5.2-1. SBL Degradation Sources

functional elements of each system, and indicated in block diagram form in the figure. While certain degradation sources such as MO BQ and segment misfigure, for example, are common to both AO and APACHE, others are particular to only one. For example, HOE absorption is particular to the AO system, while SBS threshold is particular to APACHE.

A more detailed summary of the degradation sources and their associated parameters considered in the resiliency study is presented in Table 5.2-1. The table lists functional elements, degradation sources applicable to each functional element, some examples of corresponding degradation mechanisms, the associated parameter for each degradation source, and which system(s) the degradation applies to. More detailed discussions of each degradation source will be presented in conjunction with the analyses described below.

#### 5.2.1.5 Mathematical Definition of Resiliency and Associated Figure of Merit

Consistent with the above discussion, resiliency is defined as follows: Resiliency is the deviation in a component or subsystem performance parameter from its design value or design tolerance, which causes the total system's brightness to degrade by some fixed percentage relative to its design value. The above definition for resiliency is illustrated graphically in Figures 5.2-2 and 5.2-3.

As depicted here, resiliency is quantitatively determined by how much the performance of a subsystem or component can deviate from its design value before appreciable degradation (between 5-20% in brightness, say) occurs in total systems performance. To provide a nondimensional measure of this resiliency, a figure of merit is defined as the ratio of the subsystem degradation (labeled B in the figure) to the original design value (A). As an example, if the systems performance is insensitive to variations in the subsystem parameter (case 1 in Figure 5.2-3), the figure of merit will be large relative to unity. However, if small deviations in the subsystem parameter significantly affect the total system's performance (see case 2), then the figure of merit is much less than unity. This

Table 5.2-1. Degradation Sources and Associated Parameters

Subsystem, Component or Functional Element	Degradation Source	Examples of Potential Degradation Mechanisms	Associated Parameter	Applicable To: AQ PC
Beam director Primary mirror Segments	Segment actuator Position errors: Piston Tilt	Sensor, controller or actuator malfunction	RMS (physical) piston RMS (physical) tilt	X X
	Segment misfigure Low spatial frequency	Thermal effects and structural vibrations	RMS surface misfigure	X
	Mid-spatial frequency	Thermal effects and structural vibrations	RMS surface misfigure	X
Primary mirror coatings	Coating absorption	Environmental effects and aging	Coating reflectivity	X
Holographic optical elements	HOE coatings absorption	Environmental effects and aging	Coating reflectivity	X
Amplifiers and/or phased array telescopes	Phase differences between amplifiers and telescopes	Sensor, controller or translation stage malfunction	RMS phase error	X
Hierarchical control system	Residual errors	Sensing, control system and/or figure actuator malfunction	Residual WFE	X
Figure actuators	Actuator failure	Aging	(Failure rate) x (Operation time)	X

Table 5.2-1. Degradation Sources and Associated Parameters (Continued)

Subsystem, Component or Functional Element	Degradation Source	Examples of Potential Degradation Mechanisms	Associated Parameter	Applicable To: AQ	Applicable To: PC
Beacon	Beacon-BD tracking angle misalignment	Sensor, controller or propulsion system malfunction	Tracking angle		X
Beam train optics	Mirror misfigure (is included with unconjugated optics)	Thermal distortion, vibrations	RMS wavefront error		X
	Optical aberrations	Vibration-induced misalignment and thermal distortions	RMS wavefront error	X	X
	Beam quality	Thermal distortion and dynamic misalignments	BQ	X	X
Amplifiers	Power	Improper gas flow or mixing	Gain coefficient	X	X
SBS subsystem	Conjugation fidelity	Improper gas flow, gas contamination	BQ		X
	SBS threshold	Same as amplifiers	Threshold		X
Master oscillator	Beam quality		BQ	X	X
	Power		Power	X	X
Polarization isolation S/S	M0 power degradation due to power return	Retarder or grating coatings degradation	M0 return power		X

- Resiliency is quantified in terms of a resiliency parameter and figure of merit (FOM)
  - Resiliency parameter  $\equiv B$
  - $$\text{FOM} \equiv \frac{\text{Resiliency Parameter}}{\text{Design Tolerance}} = \frac{B}{A}$$
  - $\text{FOM} \gg 1 \Rightarrow \text{Resilient to degradation in component performance}$
  - $\text{FOM} \ll 1 \Rightarrow \text{Sensitive to subsystem performance}$

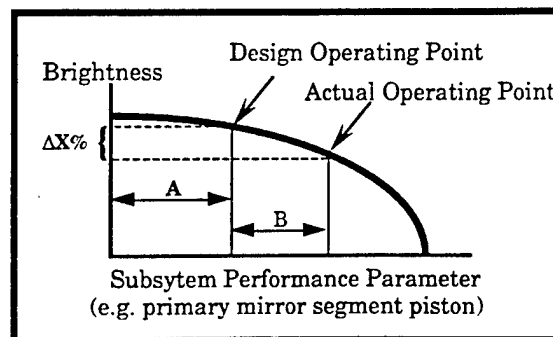


Figure 5.2-2. Resiliency Definition

- The resiliency is a measure of how close the design point is to the knee of the performance curve

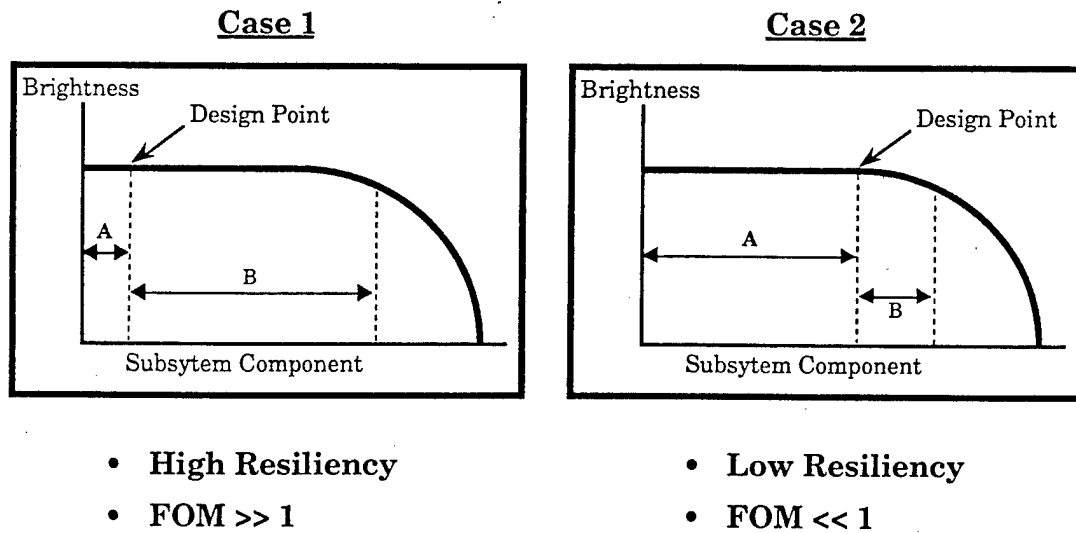


Figure 5.2-3. Resiliency Examples

figure of merit provides a useful quantitative measure of the resiliency of the system to variations in the performance of any one of the many subsystems or functional elements comprising the system. As such, it also provides a useful means of quantitatively assessing how relaxation of tolerances achieved with phase conjugation affects systems resiliency.

It should be noted that for both APACHE and AO, the majority of the subsystem design specifications required as inputs to the resiliency analysis are in fact classified numbers. In order to be able to present the results of this work in an unclassified format, certain key pieces of data had to be removed from the resiliency charts, and are presented instead in a separate classified appendix to this report. In particular, the actual value used for the brightness degradation in the present analyses will not be specified in the unclassified discussion below. Furthermore, all of the FOM values will be normalized by an unspecified factor. The normalized values of the FOMs still provide a useful gauge of relative performance, although their absolute values are meaningless. The complete set of design values, the value for the brightness degradation percentage, and the (unnormalized) FOM values are all given in the classified appendix.

Table 5.2-2 provides a summary of the resiliency values and normalized figures of merit calculated in the present study, for the degradation sources listed in Table 5.2-1. The derivation of these quantities will be described in some detail below. In the meantime, the conclusions deduced from the calculated results are summarized in Table 5.2-3. The phase conjugate system is observed to be sensitive to only two degradation sources, while the AO system is sensitive to at least five. Moreover, the sensitive degradation sources in the APACHE case involve primarily passive elements which are unlikely to degrade further, in contrast to the AO system, where the majority of the sensitive degradations involve active systems which are subject to degradation over time and must, moreover, maintain extremely tight tolerances.

Table 5.2-2. System Resiliency Summary (Classified design values appear in Addendum). Low resiliency degradation sources identified by boxes around figure of merit.

Subsystem or Functional Element	Degradation Source	Units	Adaptive Optics			Phase Conjugation		
			Design Value	Resiliency Parameter	Figure of Merit	Design Value	Resiliency Parameter	Figure of Merit
Beam director	Segment piston displacement	$\lambda$ (RMS)		0.014	0.35		11.10	2.22
	Segment tilt alignment	$\lambda$ (RMS)		0.017	0.62		2.7	2.70
	Segment surface misfigure							
	• Low spatial frequency	$\lambda$ (RMS)	HACS				0.75	1.70
	• Mid spatial frequency	$\lambda$ (RMS)		0.022	1.96		0.21	1.68
	Segment coating absorptivity	%		0.22	0.88		2.82	28.2
	HOE coating absorptivity	%		0.25	1.00	—	—	—
Aberration correction	Hierarchical Aberration Control System (HACS) residual	$\lambda$ (RMS WFE)		0.013	0.06	—	—	—
	Actuator reliability	Cycles*FR	Input values required			—	—	—
	SBS							
	• Conjugation fidelity	$\lambda$ (RMS WFE)	—	—	—		0.02	0.18
	• SBS threshold (TH/TH <sub>0</sub> )	(Ratio)	—	—	—		3.05	1.22
HEL device cophasing	Pathlength control	$\lambda$ (RMS WFE)		0.018	0.11	—	~cm's	Large
Beacon	Mirror surface misfigure	$\lambda$ VIS (P-V WFE)	—	—	—		0.67	0.91
Beam train optics (BTO)	Adaptive optics BTO		HACS			—	—	—
	APACHE BTO							
	• Conjugated optics	$\lambda$ VIS (P-V WFE per optic)	—	—	—		Large	Large
	• Unconjugated optics		—	—	—			
	— No DM						0.11	0.20
	— With DM						0.44	0.80
Amplifier	Beam quality	$\lambda$ (RMS WFE)	HACS				1.13	2.18
Master oscillator	Power (P <sub>0</sub> /P)	(Ratio)	—	Large	Large		2.74	1.10
	Beam quality	$\Delta$ BQ	HACS				4.30	3.60
	Isolation (P <sub>R</sub> /P <sub>R</sub> <sup>0</sup> )	(Ratio)	—	—	—		3.0	1.20



Table 5.2-3. SBL Systems Resiliency--Conclusions

PHASE CONJUGATED SBL		ADAPTIVE OPTICS SBL		
SYSTEM PERFORMANCE SENSITIVITY		SYSTEM PERFORMANCE SENSITIVITY		
SENSITIVE	RESILIENT	SENSITIVE	RESILIENT	UNCERTAIN
SBS FIDELITY	SEGMENT PISTON	SEGMENT PISTON	OSCILLATOR BQ	HOE COATING REFLECTIVITY
UNCONJUGATED OPTICS	SEGMENT TILT	SEGMENT TILT	OSCILLATOR POWER	ACTUATOR RELIABILITY
	SEGMENT MISFIGURE	COATING REFLECTIVITY	AMPLIFIER BQ	
	PATH LENGTH CONTROL	PATH LENGTH CONTROL	BEAM TRAIN ABERRATIONS	
	OSCILLATOR BQ	ABERRATION CONTROL SYSTEM		
	OSCILLATOR POWER			
	AMPLIFIER BQ			
	SBS REFLECTIVITY			
	ISOLATION EFFICIENCY			
	BEACON ALIGNMENT			

#### 5.2.1.6 Selection of Design Values

The design values for the subsystem performance parameters were taken directly from the wavefront error and power budgets for the two systems. Budgets were formulated using literature values derived from various sources for the AO system, including the Lockheed System 3 Phased Array Study, the Perkin-Elmer Advanced Beam Control System (ABCS) Study, and the Lockheed CDTI SBL System Architecture Study. The APACHE budget was chosen to yield the identical value for the total system brightness, assuming equal aperture, and residual jitter in both systems. The wavefront error and power budgets are tiered down in the form of a budget tree as indicated in Figure 5.2-4, with the classified values omitted from the chart. This and additional charts containing the classified values for the system error budgets are presented in the classified appendix to this report.

#### 5.2.2 Resiliency Analyses and Results

In this section, various degradation sources listed in Table 5.2-1 are discussed, and the calculations used to determine their resiliency are described and the results summarized. Although a large number of degradation sources were analyzed as part of this study, the analysis reveals that the resiliency of either system is dominated by degradations in relatively few subsystems or components. In the interest of brevity, the detailed discussion presented below is restricted to those degradation sources which substantially affect the resiliency of either system, as well as several others that are unique to APACHE alone. For those interested in the details surrounding the remaining degradation sources, a more comprehensive report ("APACHE Systems Resiliency Study," January 2, 1990, AP-1980) is available which covers the derivation of all of the resiliency values and FOMs listed in Table 5.2-2.

HOE coating degradation and actuator failure represent special cases where insufficient information was available to draw definitive conclusions at this time. Although the resiliency values listed in Table 5.2-2 indicate that the AO system is sensitive to HOE coating degradation, a highly simplified model of a linear grating was used to derive these

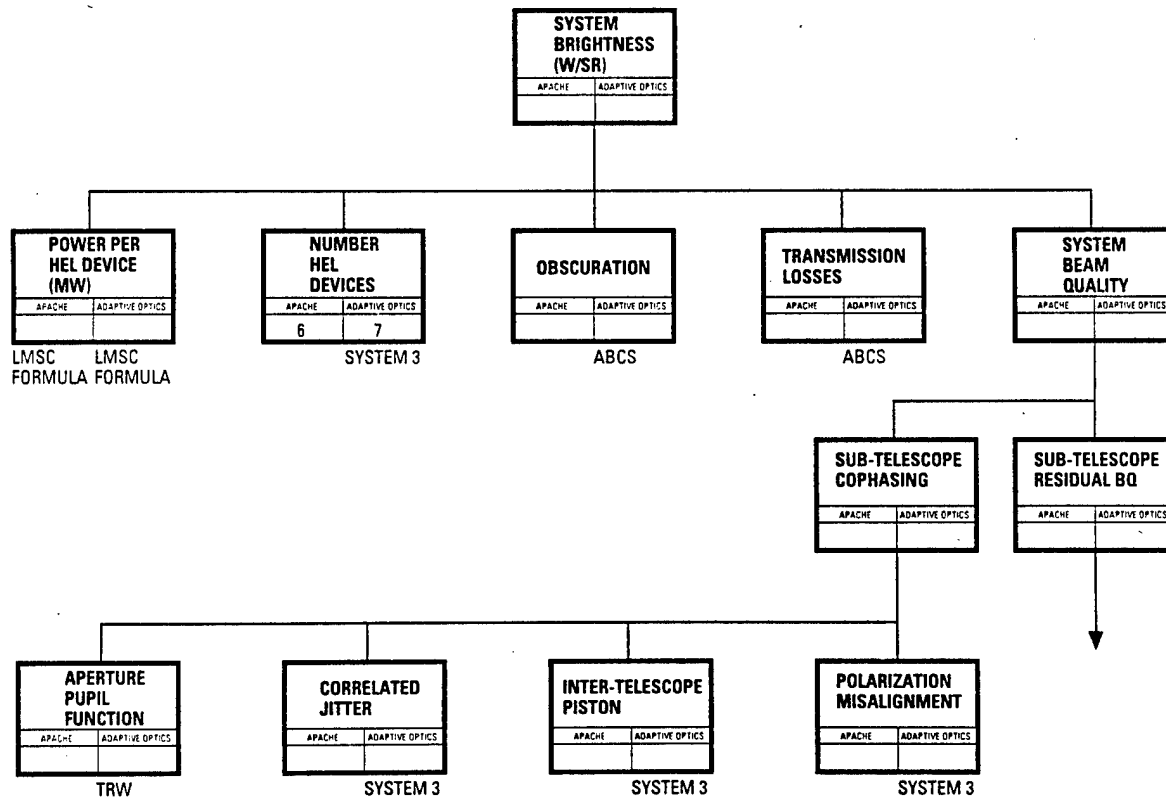


Figure 5.2-4. System Error Budget Begins with System Level Requirements

values. In actuality, the HOEs will likely consists of circular zone plates which are less sensitive to spot deflections, but could be sensitive to blurring, depending on the signal to noise and the details of the centroiding algorithm. In the absence of a detailed calculation accounting for these effects, the resiliency with respect to HOE coating degradation remains uncertain. Likewise, resiliency with respect to figure actuator failure remains uncertain due to a lack of reliable data on actuator failure rates. Thus, these two degradation sources require further study, and are therefore omitted from the detailed discussion presented below.

A quantitative criterion needs to be established indicating which FOM values denote resiliency and which sensitivity. The rule of thumb adopted here is that normalized FOMs above one indicate insensitivity to variations of the applicable parameter relative to its design value, i.e., indicate resiliency. However, FOMs less than or equal to one indicate sensitivity to subsystem performance degradation, and a lack of resilience.

#### 5.2.2.1 Beam Director

Various degradation sources occur in the beam director, including those associated with PM segment piston, tilt and misfigure; and PM segment coatings and HOEs. Below, resiliency to segment piston, tilt and coatings degradation is examined in detail.

##### 5.2.2.1.1 Resiliency to Primary Mirror Segment Actuator Position Errors (Piston and Tilt)

Large primary mirrors are subject to a variety of structural perturbations, especially following wide angle retargetting involving large slews. Both the AO and APACHE systems control the position of the PM segments using bipod actuators with 6 deg of freedom. Actuator position errors can result from a variety of potential degradation mechanisms, including segment phasing sensor malfunction, control system and computer errors, and actuator malfunction due, for example, to nonlinearity or hysteresis. The issue addressed here is the sensitivity of systems brightness to residual misalignment (piston and tilt) errors associated

with the control of the segment actuators in either system. As will be shown below, in the APACHE system phase conjugation is used to correct the residual segment position errors which were not further correctible in the AO system. The two degradation sources are segment piston and segment tilt, and the corresponding performance parameters are taken to be the RMS deviations from the design form, measured in HF waves of physical displacement.

Analysis Approach. For the AO system, segment piston and tilt errors result directly in degradation of the output beam quality. Marechal's approximation is used for the beam quality as a function of residual wavefront error (WFE), namely:

$$BQ = \exp [1/2 (2\pi * \text{RESIDUAL WFE})^2]$$

where the WFE is twice the physical segment displacement. Since the total systems brightness is inversely proportional to the square of the beam quality, the above expression can be used directly to calculate the AO system's resiliency to piston or tilt errors.

For the APACHE system, residual piston and tilt errors are corrected by phase conjugation. However, the correction is imperfect for several reasons, most importantly the nonequivalence of the beacon (low power) and target (high power) beam paths. To determine the finite correctibility due to the nonequivalent paths, calculations are performed using the ASAP model of the APACHE beam director (see Section 3.3). The results of the calculation are displayed in Figure 5.2-5; as shown here, the APACHE double pass design achieves excellent correction of both piston and tilt, with WFE correction factors of approximately 500 for piston and 200 for tilt. Thus, piston errors as large as five HF waves ( $\pm 15 \mu\text{m}$ ) induce just 1/50 wave of degradation in the performance of the phase conjugate system. The systems brightness can be calculated for a given value of piston or tilt error by applying the respective correction factor to obtain the residual WFE, and using the resulting value as the input to Marechal's approximation.

Another factor which must be taken account for the case of large tilts is the limited conjugability of separate beamlets in the focal region of the SBS cell. Thus, although the optical design of the BD accommodates large tilts, the correctibility is somewhat reduced due to the physics of the SBS process, as shown by the array alignment experiment discussed in Section 5.0 of Volume 1.

Results and Discussion. The results of the brightness sensitivity calculations for PM segment piston and tilt are displayed in Figures 5.2-6 and 5.2-7, respectively. As indicated, the roll-off due to tilt in the SBS process causes the brightness to degrade more severely than would be predicted by including only nonequivalent path effects. The results are displayed on a semilog plot because of the large differences in sensitivity between the APACHE and A0 systems. As expected, the A0 system must be held to tight optical tolerances (i.e., a small fraction of a wave) to prevent significant degradation in brightness. In contrast, the APACHE system can tolerate large amounts of piston and tilt, of the order of several waves, before suffering appreciable brightness degradation. This difference in sensitivity is exploited to significantly relax segment piston and tilt tolerances of the APACHE system.

The brightness degradation percentage and the piston and tilt design values used to calculate the resiliency are given in the classified appendix. Using these values, the resiliency to piston error (in terms of RMS physical displacement) is determined to be 11.1 waves for APACHE vs 0.014 waves for A0. For tilt, the results are a resiliency of 2.7 waves for APACHE vs 0.017 waves for A0. When translated to normalized FOMs, APACHE displays a FOM of 2.22 for piston and 2.7 for tilt, vs 0.35 for piston and 0.62 for tilt in the A0 system. Thus, APACHE is significantly more resilient than the A0 system with respect to segment piston and tilt errors.

Potential Mitigation. The A0 system's sensitivity to segment and tilt errors could be mitigated with enhanced sensing and control, additional segment actuators, and stiffer substructures. The penalty for this mitigation would be increased control system complexity and system weight.

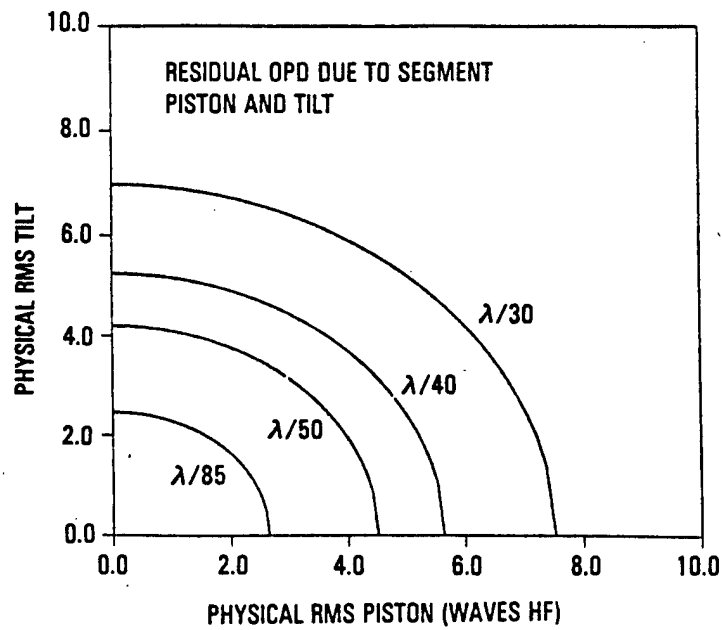


Figure 5.2-5. Residual OPD Due to Segment Piston and Tilt

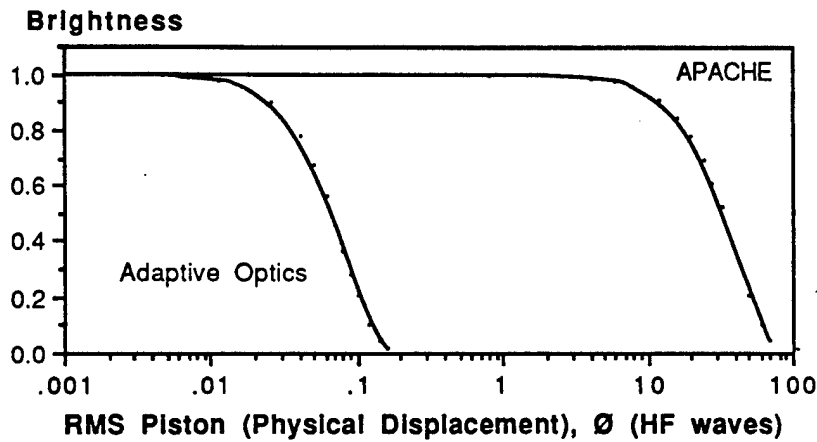


Figure 5.2-6. Brightness Sensitivity to Segment Piston Errors

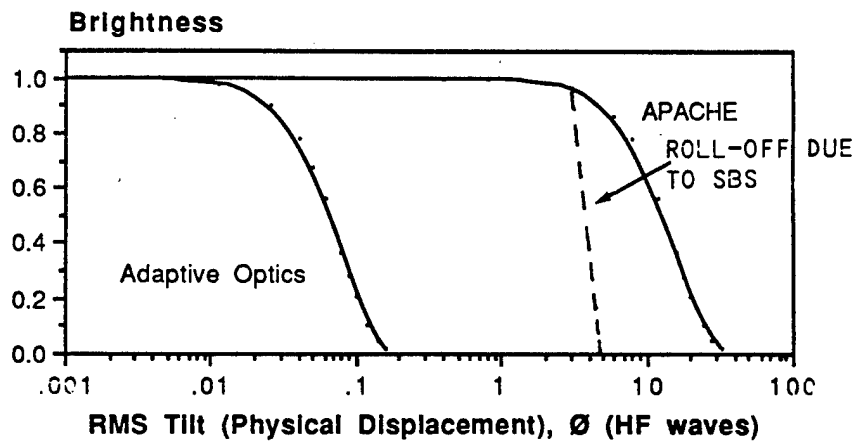


Figure 5.2-7. Brightness Sensitivity to Segment Tilt Errors

#### 5.2.2.1.2 Resiliency to Primary Mirror Segment Coatings Absorption

Both the AO and APACHE systems have high reflectivity coatings on the PM segments to prevent power losses and to minimize segment thermal distortion. Coatings absorption can degrade over the lifetime of the SBL due to environmental effects, engagement threats such as nuclear blast, and aging (operational or dormant). Coatings absorption induces thermal distortion via several mechanisms, primarily substrate CTE (coefficient of thermal expansion) variations and axial thermal gradients. Also, additional substrate thermal distortion may be induced by laser hotspots. A key factor determining the effect of increased coatings absorption on systems brightness is the spatial scale of the thermal distortion. Both systems correct low spatial frequency aberrations very well, while the correction of higher spatial frequencies is less effective. In close analogy to the segment misfigure, the AO system relies on the HACS and figure actuators to correct segment thermal distortion due to increased coatings absorption, while the APACHE system uses phase conjugation.

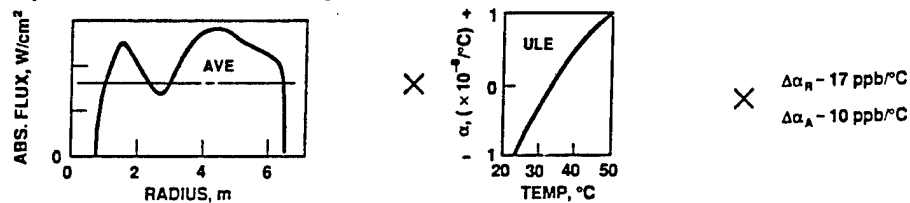
The nominal coatings reflectivity is assumed to be 99.8%, with the remaining 0.2% divided equally as 0.1% absorption and 0.1% scattering. The substrate material is assumed to be ULE. The parameter of interest is the coating absorptivity, which induces substrate thermal distortion, thereby degrading the BQ and brightness of the output beam to target.

Analysis Approach. The analysis of thermal distortion induced by coatings absorption begins with an examination of factors such as CTE uniformity within a boule and from boule to boule, the temperature dependence of the CTE, the laser beam profile, the faceplate thickness, and, for the AO system, the interactuator spacing and correctibility of the segment figure control. Several of the inputs are illustrated graphically in Figure 5.2-8. Four potential degradation mechanisms were analyzed in detail, namely, axial thermal gradients, global CTE nonuniformity, local CTE nonuniformity, and laser hotspots.

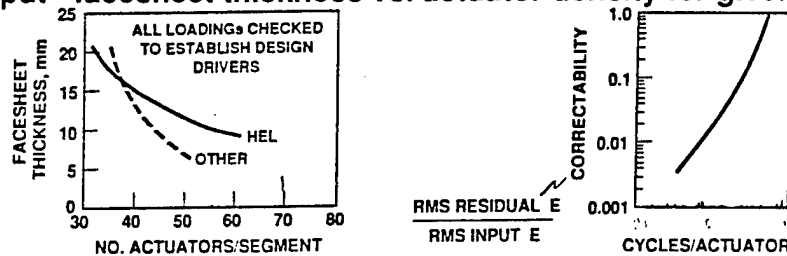
The results of the analysis are summarized in Table 5.2-4. All of the mechanisms except local CTE nonuniformity result in low spatial frequencies



- Key input - run time, absorption (EOL), material/laser characteristics



- Key output - facesheet thickness vs. actuator density for given WFE



- Sets facesheet thickness, actuator spacing, blank pedigree  $\rightarrow$  weight, cost

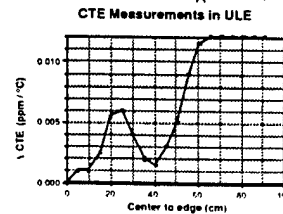
Figure 5.2-8. Thermo-Optics Drive Facesheet Thickness/Actuator Spacing

Table 5.2-4. Thermo-Optical Errors Primarily Due To ULE Variations in CTE

(steady-state, 99.8% reflectivity with 50% losses assumed due to absorption, 10 mm face, 3-meter tile)

ERROR TYPE	SURFACE ERROR ( $\mu\text{m}$ , PK)		CYCLES/ ACTUATOR	METHODOLOGY/ COMMENTS
	UNCORRECTED	CORRECTED (Conventional)		
$\Delta T_A$ - Axial Temp. gradient (0.82°C)	0.094	< 0.001	~1/12	Hand & computer models of faceplate gradients/bending as flexured from/restrained by R/S. $\alpha(T) \leq 0.03 \text{ ppm}/^\circ\text{C}$ (2.7 $\mu\text{m}$ unrestrained)
$\alpha_{A,R}$ - CTE Inhomogeneities*				
Global (0.015 ppm/°C)	0.376	0.004	~1/12	6.4°C soak (10.8 $\mu\text{m}$ unrestrained)
Local (0.010 ppm/°C)	0.116	0.116	1 - 4	Between actuators/flexures (driver - $\Delta \alpha_A \cdot \Delta T_S / t$ )
LVAG - HOT SPOT (lateral variation in $\Delta T_A$ )	0.012	0.001	~1/6	LVAG ~0.88 $\Delta T_A$ per HEL profile LVAG WFE ~1/8 $\Delta T_A$ effect (typ., TBR)
Maximum totals:	0.598 $\mu\text{m}$	0.122 $\mu\text{m}$		
		-0.017 $\lambda_{HF}$ RMS WFE		
Allowable RMS WFE ( $\lambda_{HF}$ )		Conventional SBL - 0.02 $\lambda$ APACHE - 0.14 $\lambda$		

\* Further  $\Delta \alpha$  control in production of boules TBR.



which are effectively corrected by the figure actuators of the AO system, as indicated in the table. Similarly, the correction factors for APACHE are very high ( $>40$ ) in this regime. Thus, both systems are insensitive to these mechanisms, so they will be neglected for purposes of the resiliency analysis. On the other hand, local CTE nonuniformities induce thermal distortion WFE of 0.017 waves RMS per 0.1% absorptivity, on spatial scales equal or less than an actuator spacing. This WFE is not correctible by the AO's HACS system, and therefore results directly in BQ degradation which we calculate using Marechal's approximation. The thermal distortion is assumed to be proportional to the absorptivity over the range of interest here.

For APACHE, on the other hand, phase conjugation provides significant correction of mid-sf thermal distortion, as indicated in Figure 5.2-9. The APACHE system brightness is calculated using a correction factor of 10 appropriate to spatial scales of 25 to 30 cm in the Marechal expression for BQ.

Results and Discussion. The sensitivity of brightness to PM segment coatings absorptivity is displayed for the two systems in Figure 5.2-10. The inability of the AO system to correct distortions with spatial scales less than an actuator spacing adversely affects the resiliency. On the other hand, APACHE is highly resilient to coatings absorption because phase conjugation effectively corrects distortions at these scales. The resiliency FOM for APACHE is 11.3, while for AO it is 0.88. Thus APACHE is an order of magnitude more resilient than AO with respect to coatings absorption.

Potential Mitigation. The sensitivity of the AO system to coatings absorption could be mitigated by higher densities of actuators, development of even more thermally homogeneous substrates, and development of lower absorption and very highly degradation resistant large-area HF laser coatings. The penalty for this mitigation would be increased cost, weight and technical risk for the control system, and increased cost and risk (especially with respect to water band absorption) for the coatings.

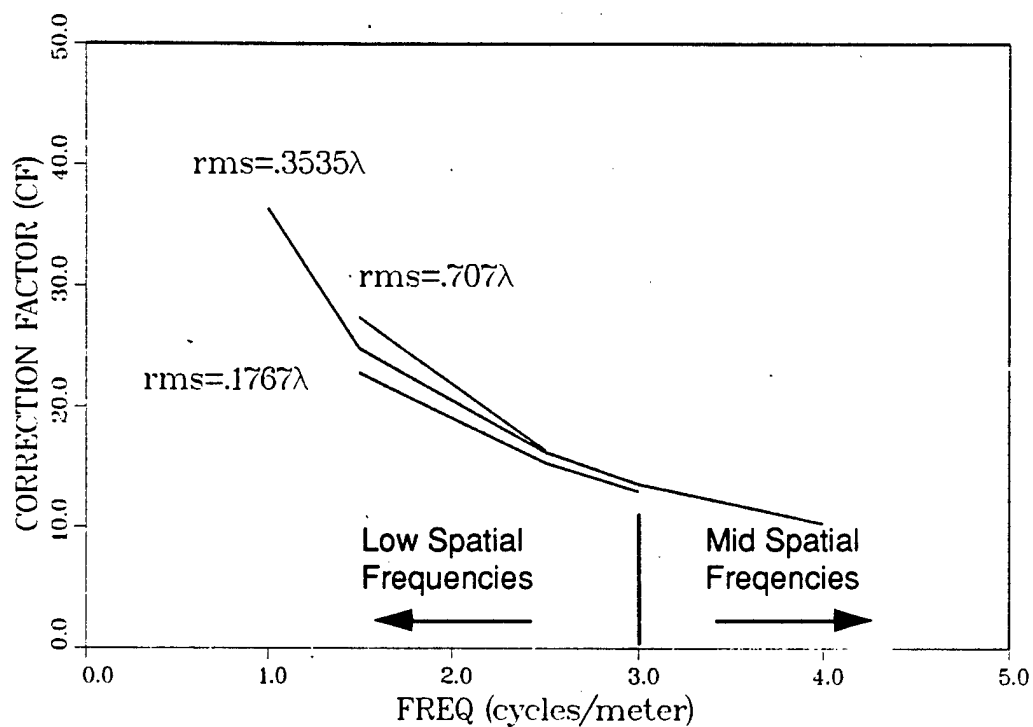


Figure 5.2-9. APACHE Aberration Correctability as Function of Spatial Scale

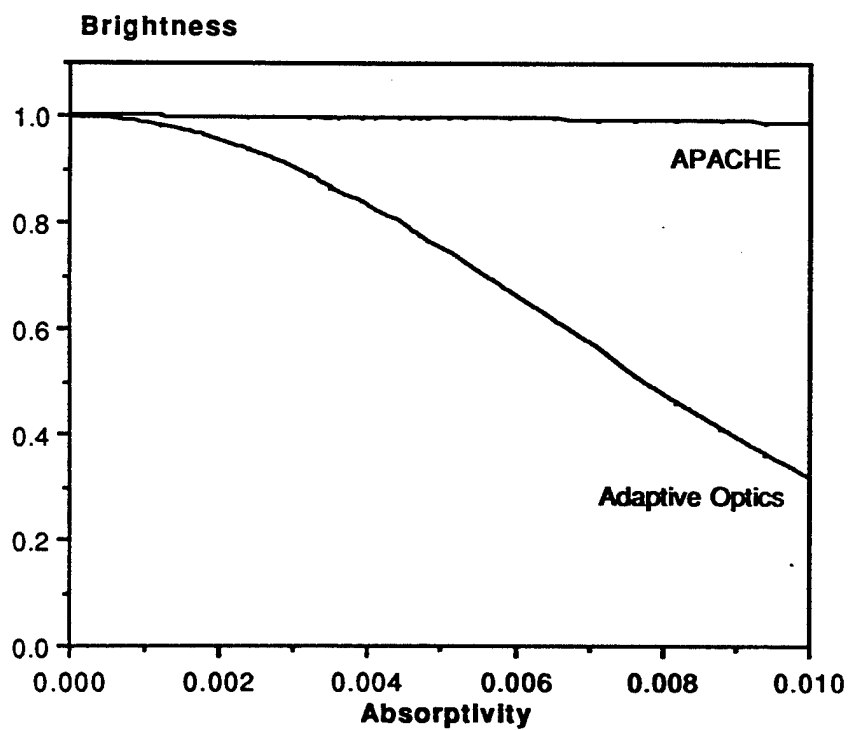


Figure 5.2-10. Brightness Sensitivity to Coating Degradation

#### 5.2.2.2 Aberration Correction

This category covers degradation sources directly related to wavefront correction, including the performance of the HACS and figure actuator failure for the AO system, and the performance of the SBS subsystem for the APACHE system.

##### 5.2.2.2.1 Resiliency to Hierarchical Aberration Control System (HACS) Residuals

The HACS is applicable only to the AO system, which uses active controls to correct wavefront errors in the outgoing beam. The HACS is intended to sense and correct wavefront aberrations originating in various parts of the AO system, including the master oscillator, amplifiers, optical beam train, and primary mirror segments (misfigure). When operating ideally in a closed loop sense, any magnitude and spatial and temporal distribution of aberrations falling within a given capture range of HACS figure actuator stroke, spatial bandwidth and temporal bandwidth would be reduced to some fixed value of residual wavefront error. In practice, departures from ideal behavior occur and the residual error may depend on the magnitude of the input aberrations as well as their spatial and temporal distributions. Thus, the performance of various deformable optics and aberration control systems will often be expressed in terms of correctibilities rather than fixed residuals.

Many potential degradation mechanisms can result in increased HACS residuals. For example, aberrations lying outside the capture limits of the stroke, temporal bandwidth and spatial bandwidth of the HACS will contribute to the residual. Moreover, increased residuals may be the result of both hardware and software errors, including wavefront sensor errors due to detector malfunction and electronic noise, computer errors, and figure actuator malfunction due to nonlinearity or hysteresis.

An analysis which attempts to realistically account for the complex behavior of an actual SBL HACS system is well beyond the scope of the present work. For this reason, the present analysis restricts consideration to just HACS residuals alone, whatever the origin. A more complete analysis at some later stage will need to address the dependence

of the HACS residuals on the magnitudes of the aberrations from various portions of the AO SBL system.

Analysis Approach. Within the simplified view of HACS behavior discussed above, the degradation in BQ, and therefore brightness, may be calculated directly as a function of the residual HACS WFE using Marechal's approximation.

Results and Discussion. Calculations of brightness sensitivity are indicated in Figure 5.2-11. As expected, the AO system brightness is sensitive to HACS WFE residuals, which are not further correctible and therefore translate directly into brightness degradation. The resiliency in RMS WFE is only 0.013 waves. The FOM is a very low 0.06, due to the tight design tolerances for the combined HACS residual associated with the myriad sources of SBL system optical aberrations handled by the HACS.

Potential Mitigation. Implementing redundant HACS functional elements, such as wavefront sensors, control loops, and figure actuators, is the most direct approach to mitigating the sensitivity of the AO system brightness to HACS residuals. However, the penalties in terms of complexity and cost of this subsystem are likely to be substantial.

Resiliency to SBS Conjugation Fidelity and SBS Threshold. The wavefront correction analogy to the HACS system of the AO concept, and the heart of the APACHE system is the SBS cell, where phase conjugation of the input pass beam occurs. The ability of the APACHE system to passively correct wavefront aberrations depends on the fidelity of the phase conjugation process. Degradation in conjugation fidelity translates directly into beam quality degradation in the output beam. Moreover, both fidelity as well as reflectivity are affected by the proximity of the input beam power to the SBS threshold; generally, power greater than three times threshold for the weakest laser line is considered desirable. The degradations apply only to the APACHE system, where SBS phase conjugation takes the place of the AO's HACS to effect wavefront correction.

The performance of the SBS cell can be degraded through various mechanisms. For example, contamination of the conjugating gas medium could

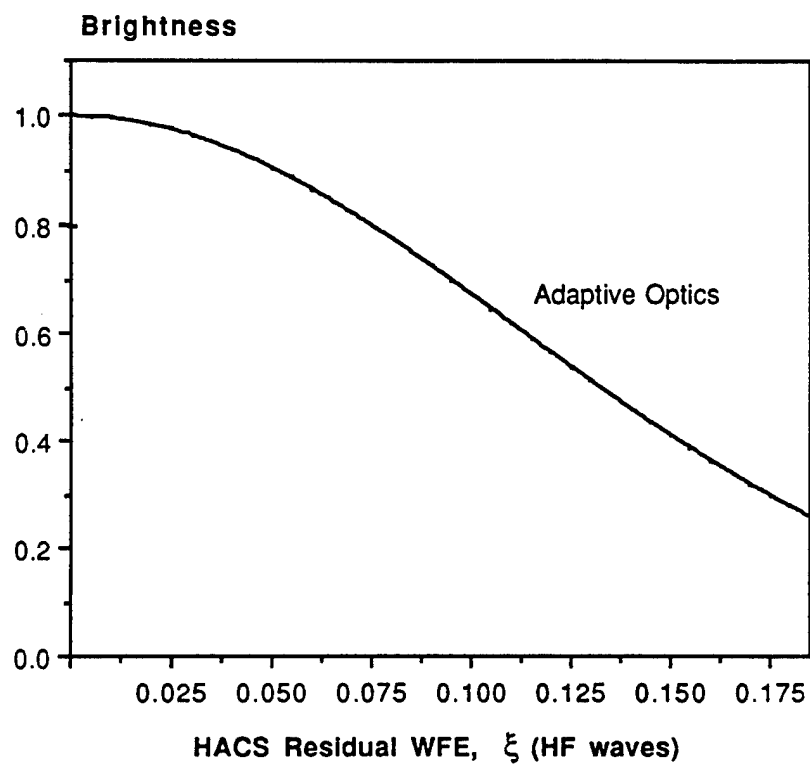


Figure 5.2-11. Brightness Sensitivity to HACS Residual

induce thermal blooming. Performance could also be affected by thermal inhomogeneities and nonuniform flow rates. Another potential cause of degradation in the conjugation fidelity is the nature of the input aberrations. For example, segment tilts which are too large conjugate poorly. This effect has already been taken into account in the analysis of segment tilt presented above, and was seen to be reasonably benign. However, aberrations from other sources such as the amplifiers may also effect conjugability, although quantitative relationships have yet to be established.

Analysis Approach. The sensitivity of brightness to excess BQ due to degradation of SBS conjugation fidelity is calculated directly from the systems brightness formula. The effect of SBS threshold on brightness was calculated using the APACHE system's analysis model. Among other things, the model accounts for BQ and reflectivity changes of the four principal HF laser lines at the SBS cell as a function of power in the weakest line, and for variable return power to the master oscillator and its effect on MO degradation.

Results and Discussion. Results of calculations for brightness sensitivity to SBS conjugation fidelity and SBS threshold are presented in Figures 5.2-12 and 5.2-13. The APACHE system is seen to be insensitive to moderate increases in the SBS threshold. The resiliency is greater than three, so that the threshold may increase by a factor of three before significant degradation occurs. The corresponding normalized FOM is 1.22, again indicating that APACHE is resilient to SBS threshold changes.

The SBS conjugation fidelity results indicate, as expected, that APACHE is sensitive to degradations in BQ during phase conjugation. The absolute resiliency is only 0.02 waves RMS of WFE, or  $\Delta BQ$  of 0.06. The FOM of 0.18 is well below one, indicating a lack of resiliency with respect to this degradation source. Thus, ensuring and maintaining the fidelity of the conjugation process is essential to the performance of the APACHE system. However, once the physics issues have been resolved, it is unlikely that the conjugation fidelity would degrade over time.



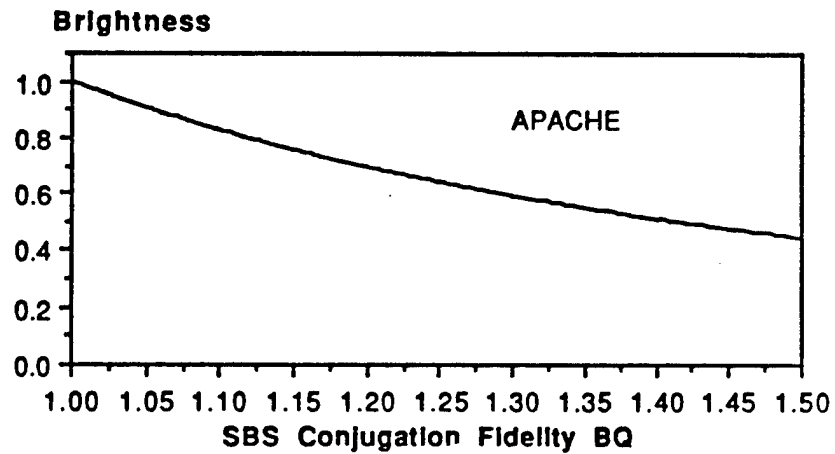


Figure 5.2-12. Brightness Sensitivity to SBS Conjugation Fidelity

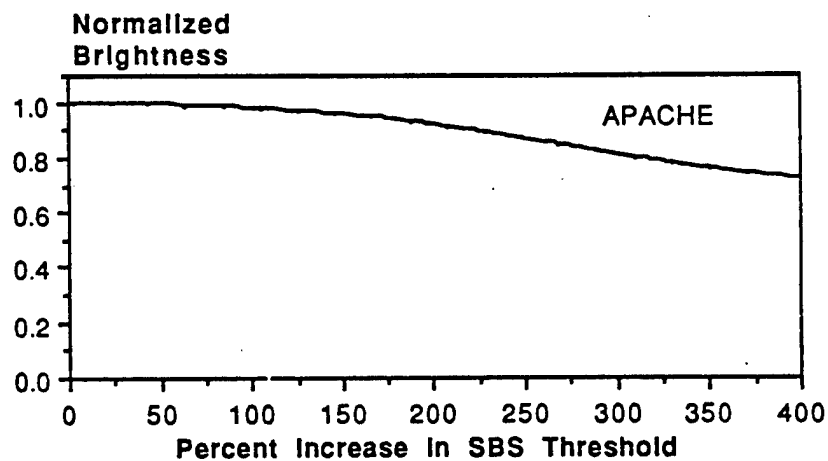


Figure 5.2-13. Brightness Versus Increase in SBS Threshold

Potential Mitigation. The sensitivity to conjugation fidelity can be mitigated with redundant gas supplies to guard against contamination, and by adjusting the flow velocity to reduce thermal effects. An entire redundant SBS cell is another alternative. A simple tilt corrector with coarse alignment tolerances could be used to prevent degradation of conjugation fidelity due to overly large tilts.

HEL Device and Telescope Cophasing Errors. Both the AO and APACHE systems considered here contain multiple devices (laser amplifiers) whose powers are combined to achieve the final high value of output beam power. However, the combining and cophasing of the separate devices is accomplished differently in the two systems. APACHE uses phase conjugation together with bidirectional propagation to both combine and cophase the outputs from six individual devices. The combined output is subsequently directed toward the target using a single telescope consisting of a multisegmented but single aperture primary mirror. The AO system, on the other hand, directs the output from each of seven devices to separate, segmented subtelescopes. The outputs from all of the subtelescopes are then mutually cophased to produce a coherent output beam directed toward the target.

The APACHE system is very insensitive to optical pathlength mismatch, which is extremely well corrected by phase conjugation.

In fact, the pathlength control requirements are set by the coherence lengths of the individual laser beams and by the small frequency shift of the return pass beam induced by the SBS process. The pathlength control requirement turns out to be several centimeters, which should be readily achievable.

The AO system requires active multispectral phase matching of individual subtelescopes concomitant with agile retargeting within a small fraction of a second. The technique used is the adjustment of the optical pathlength between pairs of telescopes using "optical trombones." The trombones are complex optomechanical devices in which cooled mirrors are translated over large distances (tens of centimeters), to meet tolerances of a small fraction of a wave. Moreover, the feedback control for the trombones is centered on a complex multiline fringe visibility

pattern which varies with laser power fluctuations, which complicates the path-matching problem. An example of a multiline interference pattern is illustrated in Figure 5.2-14.

The optical trombone system is subject to a variety of degradation mechanisms related to sensing, controls and mirror mechanical motion. For example, errors can result from changes in the multiline visibility due to the rapid temporal fluctuations of the HEL spectrum known to occur in HF lasers. Since edge sampling is used, errors can occur in sensing due to differences in the wavefront phase measured near the edge from that of the remainder of the subtelescope. Errors can also occur in the feedback control of the translation stages. Finally, the large distances which are rapidly traversed by the trombone hardware create opportunities for mechanical degradation, as well as backlash and hysteresis.

Analysis Approach. The dependence of brightness on the relative phase difference between N telescopes, taken from LMSC's System 3 SBL Study, is given by the expression:

$$B = N^2 \{ [1 + (N-1) \exp(-(2\pi\phi)^2)] / N \} \quad (5.2-3)$$

where  $\phi$  is the rms phase difference between adjacent telescopes. This formula indicates the well known result that N telescopes possess brightness proportional to  $N^2$  when perfectly phased, and to N when out of phase.

Explicit calculations are not required for APACHE, where subtelescope cophasing does not apply. Since the pathlength tolerances are within several centimeters, a perfect phase conjugator achieves perfectly coherent combination of multiple bidirectional amplifiers.

Results and Discussion. The sensitivity of brightness to pathlength control, i.e., cophasing errors, is indicated in Figure 5.2-15. APACHE is highly resilient to cophasing errors, since tolerances on the scale of centimeters are allowed, which are orders of magnitude more relaxed than optical tolerances. The AO system, on the other hand, is highly sensitive to cophasing errors, with a low absolute resiliency of 0.02 waves, and a FOM of 0.11. Thus, the AO system is not resilient to cophasing errors.

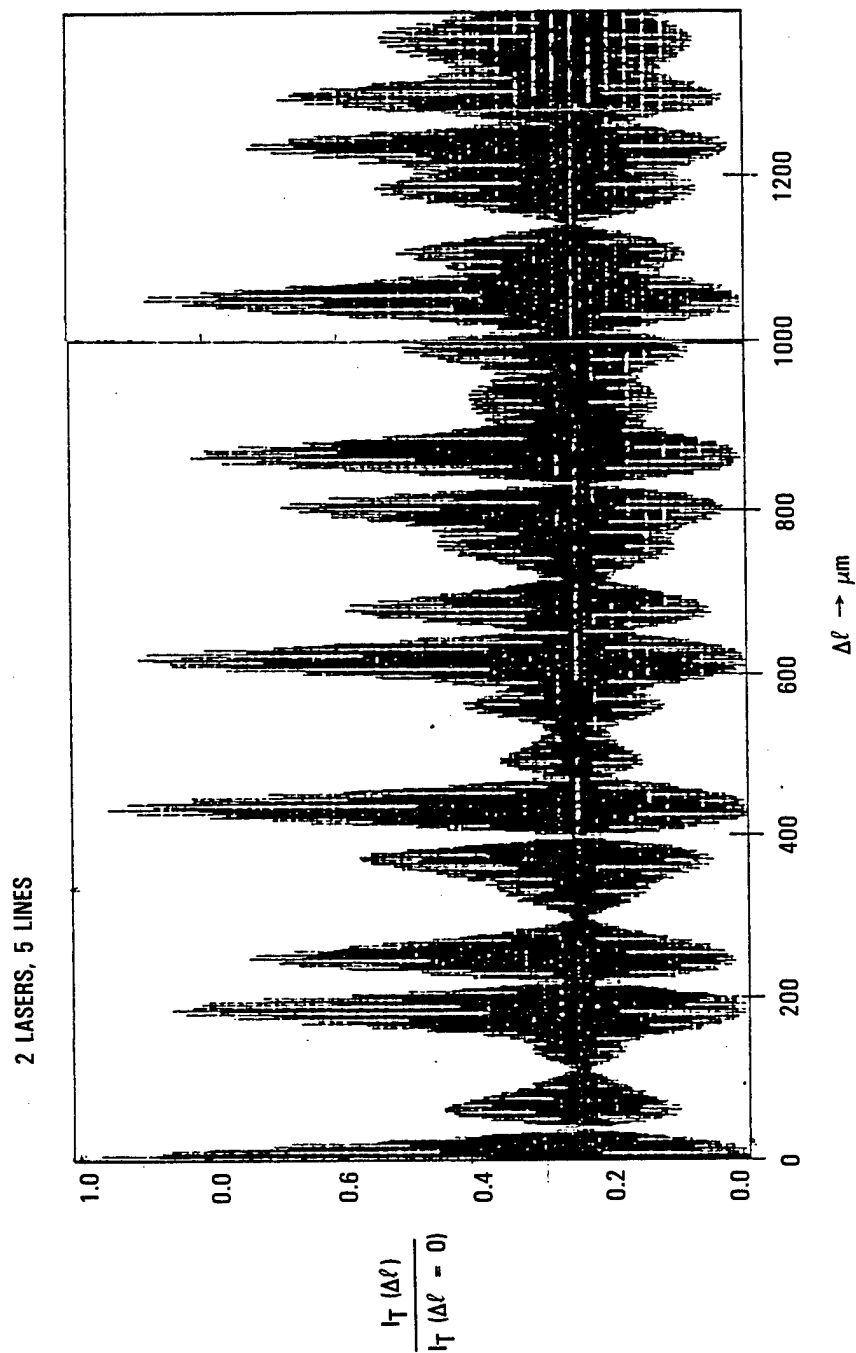


Figure 5.2-14. Edge Sensor Intensity vs Optical Path Difference

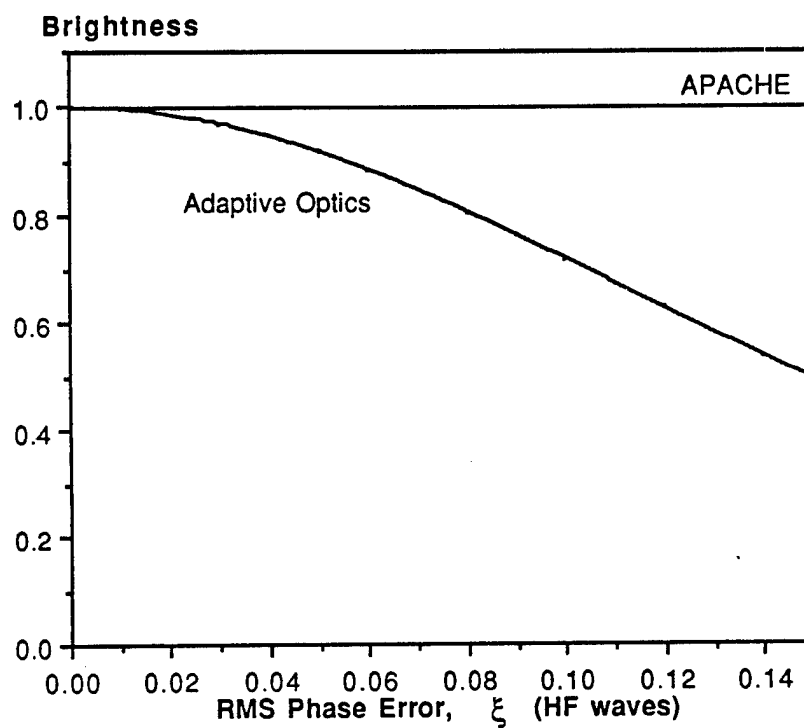


Figure 5.2-15. Brightness Sensitivity to Amplifier and Inter-Telescope Cophasing Errors

Potential Mitigation. One way to reduce the cophasing requirements for the AO system is to reduce the number of subtelescopes and devices, by increasing the device and/or aperture sizes. A trade study would be required to determine the feasibility of such an approach. Another mitigation aimed at reducing mechanical translation requirements is the development of specialized algorithms for rapid determination of multispectral phase maxima.

APACHE Beacon. APACHE uses a free-flying beacon to spatially filter the master oscillator beam and direct it toward the primary mirror. The beam from the beacon samples the aberrations on the primary, which are eventually corrected on the return (high-power) pass out to the target. Tracking sensors on the beacon and beam director are used to command the beacon position and the orientation of the beacon channel tertiary mirror located in the beam director. Optical aberrations originating at the beacon are important to systems performance since the beacon mirror is unconjugated. Two potential degradation sources are beacon mirror misfigure and beacon mirror tracking angle misalignment. Beacon misfigure errors may be considered as one of the contributors to the unconjugated optics aberrations discussed later in this section. In the following we discuss resiliency with respect to beacon tracking errors.

Resiliency to Beacon Tracking Angle. The beacon tracking optics on the APACHE beam expander are used for monitoring the position of the beacon, and commanding rotation of the beacon tertiary mirror to compensate for any angular misalignment of the beacon relative to the beam expander axis. The beacon tracking system helps to relax tolerances on beacon stationkeeping; the design value for tracking tolerance is  $40 \mu\text{rad}$ , well within the projected capability of the applicable sensing and control systems. Degradation of the sensing and control systems could result in tracking errors. These errors, which are primarily tilt, are measured by a shared aperture alignment focal plane array system and corrected by steering mirrors in the target channel, similarly to other line of sight errors. Slight degradations in brightness would be expected due to small residuals following compensation for tilt and focus errors.

The system will be less sensitive to deviations in on-axis beacon position errors which are, moreover, amenable to focus correction. Therefore, the present analysis is restricted to just angular misalignment effects.

Analysis Approach. The residual OPD due to tracking angle misalignment was calculated using the ASAP model of the APACHE beam director. The results are indicated in Figure 5.2-16, where the residual OPD is seen to be quite small ( $\pm 0.05$ ) up to about  $50 \mu\text{rad}$ , and to rise slowly thereafter.

The residual OPD calculated above can then be used directly in Marechal's approximation to determine the sensitivity of brightness to beacon tracking angle misalignment.

Results and Discussion. The brightness results plotted in Figure 5.2-17 indicate that the APACHE system is insensitive to beacon tracking errors. The absolute resiliency is  $150 \mu\text{rad}$ , nearly four times greater than the design tolerance. Thus, the APACHE concept is highly resilient to beacon tracking errors.

Resiliency to Beam Train Optics Aberrations. Both systems incur aberrations due to misalignments and misfigure of multiple beam train optics, for example, those used to transmit the beam from the amplifiers through the beam director to the primary mirror. Degradation mechanisms include thermal distortion due to coating degradation or inadequate heat exchanger flow, and misalignments due to dynamic structural vibrations. For the AO system, WFEs due to beam train optics aberrations are corrected by the HACS, along with WFEs from other sources in the system. The effect of the combined HACS residuals on AO system brightness was analyzed above, so a separate treatment of beam train optics aberrations is not required.

For APACHE, a major distinction exists between conjugated and unconjugated optics. For all practical purposes, beam train optics which are in common input and output path can be considered to be fully conjugated; the resiliency of APACHE to aberrations of these optics will be large and does not merit further quantification here. However, aberrations of optics which are not in the common path (or are sampled differently on

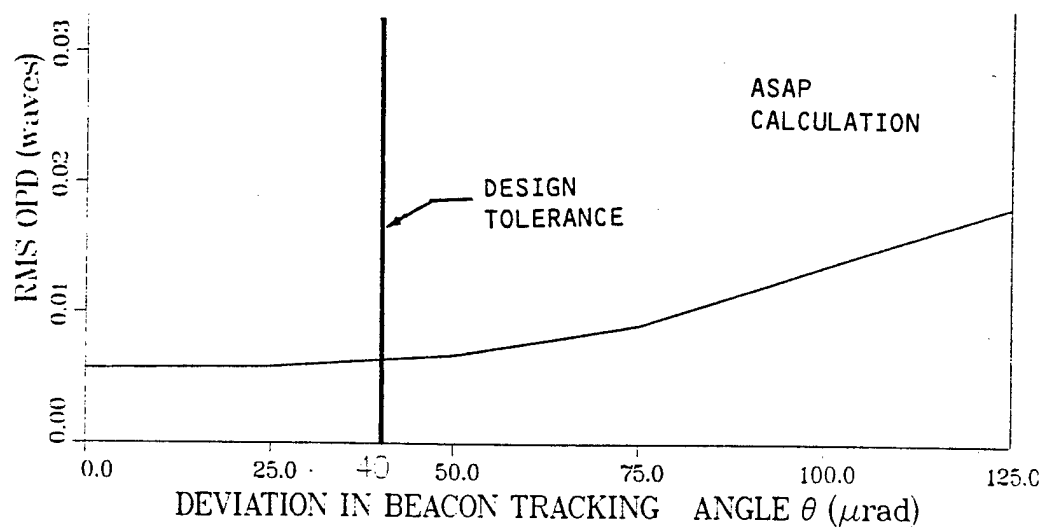


Figure 5.2-16. Residual OPD Due to Beacon Tracking Misalignment

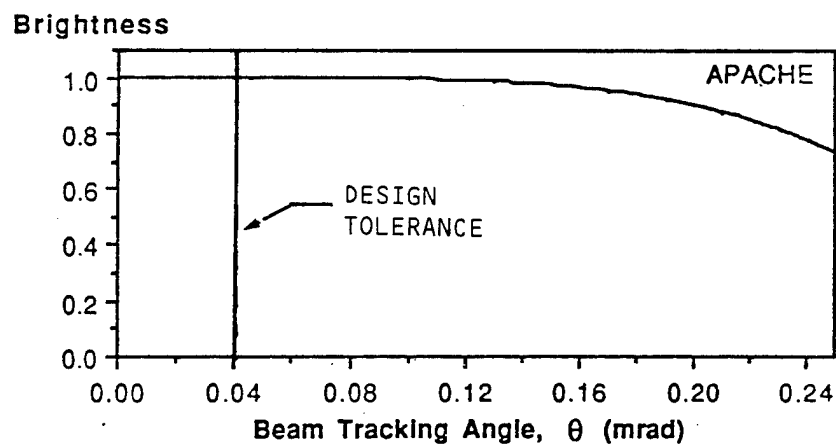


Figure 5.2-17. Brightness Sensitivity to Errors in Beacon Tracking Angle



the two passes) and therefore unconjugated, lead directly to degradations in systems brightness.

One option for correcting aberrations of unconjugated optics in the APACHE system is the implementation of a "simple" (i.e., low spatial and temporal bandwidth) deformable mirror (DM). The hybrid approach combining phase conjugation with a simple DM will be analyzed below in addition to only passive correction, since it may offer a simple, cost effective means of enhancing performance over the purely passive approach.

Analysis Approach. Without a DM, the brightness degradation may be calculated directly as a function of total WFE due to unconjugated optics using Marechal's approximation for BQ. It is also instructive to parametrize the brightness in terms of the WFE per unconjugated optic. For simplicity, we consider the case of uncorrelated aberrations, for which the net effect of errors due to different optics is given by the root sum of squares (RSS) of the individual errors. The current APACHE baseline has seventeen unconjugated optics, the majority of which are fixed turning flats. For the present calculations, we assume an identical WFE per optic and take the RSS over the seventeen optics. The case involving both correlated and uncorrelated aberrations can be formulated in a similar but somewhat more complicated fashion.

Various schemes can be invoked to sense the wavefront and command a DM to correct the excess WF aberration in the APACHE system. In contrast to the AO system, both the incoming and outgoing beams must be sensed and the appropriate deformation added to the outgoing wave to transform it to the exact conjugate of the incoming wave from the primary, rather than a flat wavefront. One of the fixed turning flats in the low power (beacon) channel may be used as a DM to effect the required wavefront deformation. One possible scheme for implementing the correction is indicated schematically in Figure 5.2-18. The incoming WF is sensed at the beacon quaternary and the outgoing WF at the target tertiary. In this configuration, only two optics in the train remain unconjugated, the secondary and the beacon tertiary. The brightness is calculated directly assuming perfect correction of conjugated optics, and uncorrelated and equal WFE for the two unconjugated optics.

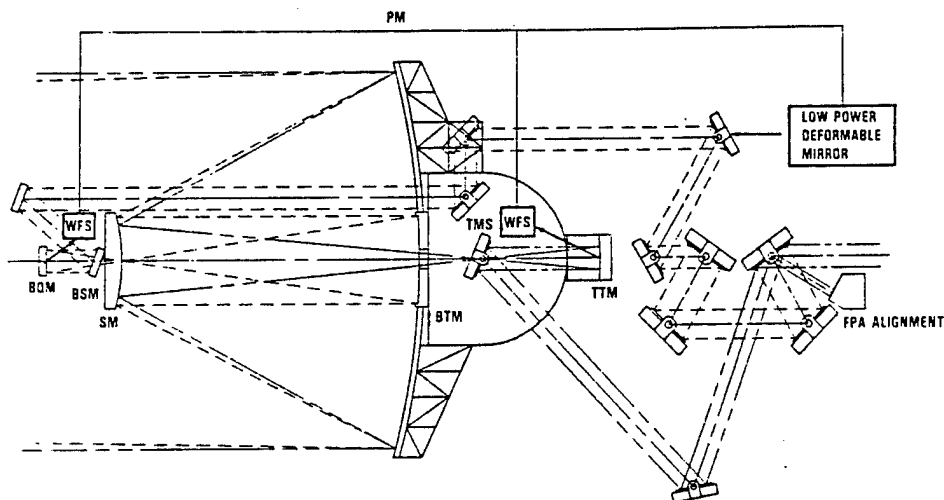


Figure 5.2-18. Resiliency to APACHE Unconjugated Optics

Results and Discussion. The sensitivity of APACHE system brightness to optical beam train aberrations is indicated in Figure 5.2-19. Without a DM, APACHE is highly sensitive to WFE from unconjugate optics, with absolute resiliency of 0.11 vis waves p-v, and a FOM of 0.2. This sensitivity is substantially reduced by the use of a low bandwidth DM, which increases the absolute resiliency to 0.44 vis waves p-v, and the FOM to 0.8. More detailed design analysis combined with a cost/benefit trade would be required to determine whether the use of such a DM is cost effective. In any case, it will be essential to maintain design tolerances on unconjugated optics in the APACHE system, despite the partial relief offered by a DM in the system.

APACHE Isolation Subsystem. The APACHE system brightness can be affected by leakage of power through the polarization isolation system into the beacon channel rather than the target channel. A certain fraction of this unwanted power returns to the MO, causing the MO output power to degrade. The parameter characterizing the performance of the isolation

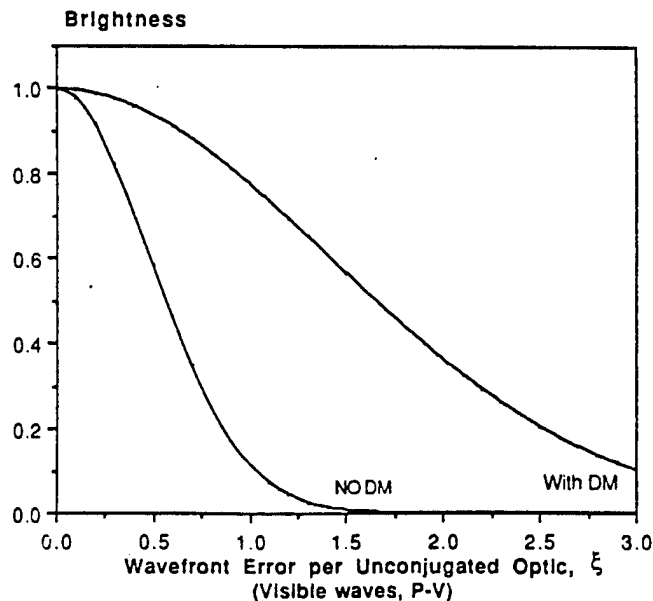


Figure 5.2-19. Brightness Sensitivity to Unconjugated Optics Aberrations

system is the fraction of output beam power incident on the grating which is returned toward the MO via the beacon channel.

Various mechanisms can contribute to the degradation of isolation system performance, including thermally induced birefringence and degradation of coatings used to control, retard and separate the polarization of beams transmitted through the APACHE system.

Analysis Approach. The APACHE Systems Analysis Model is used to calculate brightness as a function of isolation system performance, as measured by the fraction of power incident on the grating which is transmitted to the beacon channel. To determine the consequent MO power degradation, the model uses the results of the isolation analysis discussed in Section 2.11.

Results and Conclusions. The sensitivity of APACHE system brightness to degradations in isolation system performance is indicated in Figure 5.2-20. APACHE is seen to be insensitive to moderate increases in return power to the MO. The absolute resiliency in the ratio of return

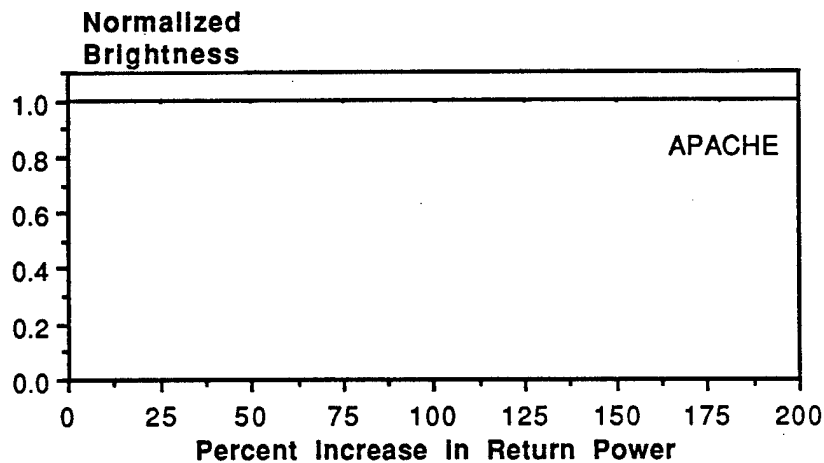


Figure 5.2-20. Brightness Versus Percent Increase in Isolation Factor

power relative to nominal is a factor of 3, and the normalized FOM is 1.2. Thus, APACHE is resilient to degradation in isolation subsystem performance.

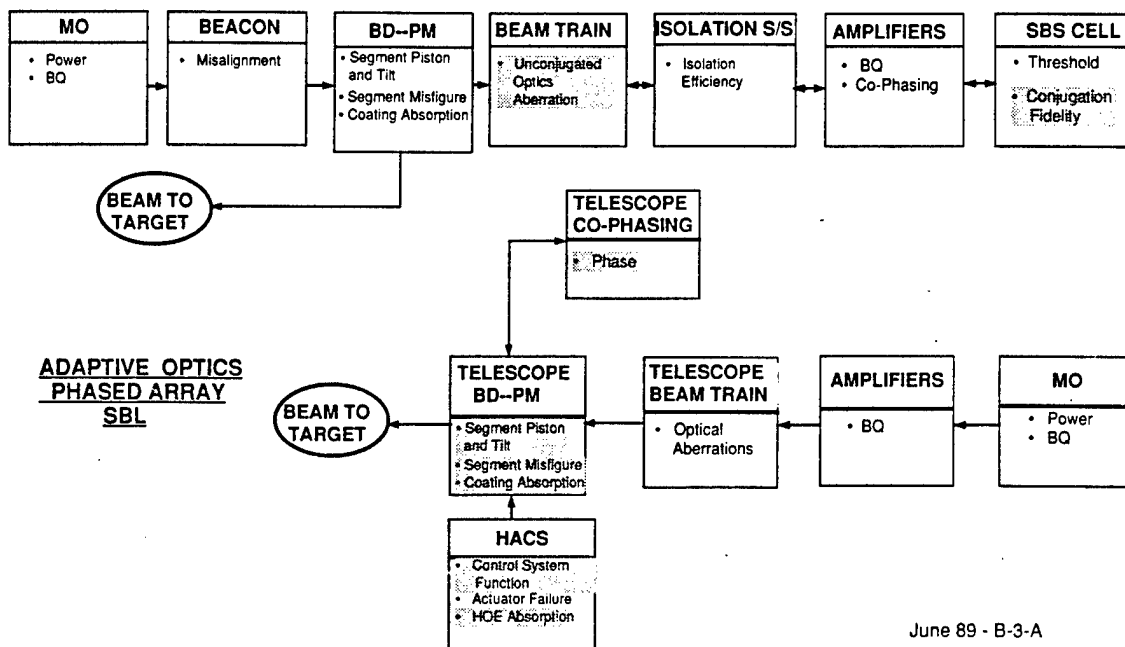
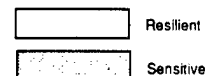
Potential Mitigation. The resiliency could be enhanced further by oversizing the MO, and by further attenuating the MO return through the use of birefringent wedges and neutral density filters.

### 5.2.3 Resiliency Study Summary and Conclusions

In the present study, we have identified a wide variety of potential degradation sources affecting the performance of key subsystems and components, for both AO and APACHE SBL systems. Resiliency was defined as the deviation in the corresponding subsystem parameter from its design value or tolerance, which results in a given percentage decrease in systems brightness relative to its design value. A corresponding FOM was defined as the ratio of the resiliency to the design value. The sensitivity of systems brightness to subsystem performance was analyzed and resiliency determined for each of the degradation sources in either system.

The results of the study are indicated qualitatively in block diagram form in Figure 5.2-21. The calculated values of absolute resiliency and normalized FOMs were summarized previously in Table 5.2-2, and the sensitive and resilient degradation sources for each system were listed in

## APACHE SBL



June 89 - B-3-A

Figure 5.2-21. Resiliency Summary

Table 5.2-3. The latter shows that the APACHE system is resilient to all of the degradation sources investigated other than unconjugated optics (beam train and beacon mirrors) aberrations and SBS conjugation fidelity. WFE from these sources directly degrade the output beam quality and therefore brightness. On the other hand, the AO system is sensitive to PM segment piston and tilt errors, segment coatings absorption, HACS residual errors, and device cophasing errors. Figure actuator failure and HOE coating degradation may also adversely affect AO system resiliency, but currently available input information was insufficient to draw quantitative conclusions. The only factor common to both systems for which the resiliency was nearly equal was amplifier power loss (catastrophic as well as noncatastrophic). For this reason, amplifier power loss is omitted in the systems resiliency comparisons.

Table 5.2-2 summarizes the results of the resiliency analyses and calculations, many of which were described in detail above. The design values for the degradation parameters, the value of percentage brightness degradation used to calculate the resiliency, and the normalization factor for the FOM are all given in the classified appendix to this report. The unclassified table presented here lists just the resiliency values and normalized FOMs for each degradation source in either system, organized by subsystem or functional element. The degradation sources to which the system is sensitive (i.e., nonresilient) are indicated by boxes in the FOM column. The further above unity that the normalized FOM is, the more resilient the system is to the degradation source in question; conversely, the lower the FOM is from unity, the less resilient the system. We consider the system to be resilient to a given degradation source only if the FOM exceeds unity. As indicated in Table 5.2-3, five items are sensitive for the AO and an additional two are uncertain at present; two items are observed to be sensitive for APACHE.

Although the relative resiliency expressed by the FOM is the primary criterion used here, the absolute resiliency is also important, since it represents potential for redesign and reoptimization. Obviously, a combination of both high absolute and relative resiliency is most desirable. From this standpoint, APACHE displays significant advantages

over A0 with respect to resiliency to segment piston error, segment tilt error, and segment coatings absorption. Formulation and analysis of potential strategies for exploiting this resiliency are deferred to future work.

In order to determine and compare composite resiliencies for the two systems, one must know the probability distributions for the departure of all subsystem performance parameters from their design values. In most cases, little information is available on which to base the choice of probability distribution or to fix the parameters of the distribution. Parametric analyses could, in principle, be carried out, but would be tedious due to the profusion of independent parameters requiring variation. The formulation and analysis of composite resiliency is therefore deferred until more information becomes available about the probabilities of various types of degradation. The analyses of individual degradation sources presented here can be used directly as inputs to such calculations.

In summary, the APACHE system is observed to be substantially more resilient to subsystem performance degradation than the A0 system. Not only is the likelihood of a successful mission significantly enhanced, but the increased resilience could also be potentially exploited to realize weight and cost savings for the APACHE system relative to the A0.

### 5.3 PRIMARY MIRROR COST AND WEIGHT

#### 5.3.1 Introduction and Summary

The relaxed optical design and fabrication tolerances afforded by the use of nonlinear optics will have a substantial impact on the cost to produce these optics and on their overall weight. In order to quantitatively assess how cost and weight are driven by design tolerances, a comparative study was conducted for the key components of two primary mirror assemblies. A generic 10-m mirror was considered, and a cost/weight comparison was made for a mirror designed for an SBL using adaptive optics versus an equivalent mirror designed for use in a phase conjugated system. The methodology begins with design requirements for the two systems, and considers costs and weight for the production of the raw boules used for the mirror facesheet, figuring and coating, figure and phase actuators, and the reaction and support structure, as indicated in Figure 5.3-1. This involved flowing error budget requirements all the way down to the control loops, to determine natural frequencies and structural sizes from which structural weights and costs could then be established. Primary mirror structural weights were found to be approximately 1.5 times those of the coated facesheet alone, while the costs were comparable.

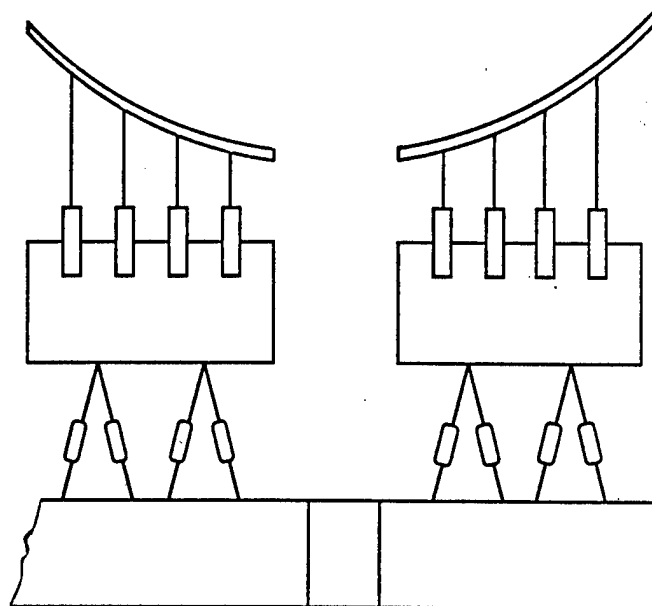
This work has helped us provide an independent check on primary mirror cost and weight, while bringing attention to the key design drivers for SBL primary mirrors. The analysis was performed for a generic 10-m primary mirror, which for an A0 system costs about \$64M and weighs about 4610 Kg ( $58 \text{ kg/m}^2$ ). A0 SBL costs are found to be 77% higher than for a phase conjugated APACHE SBL, while areal densities are nearly 84% higher. Specifically, phase conjugation reduces costs and areal densities by over 75% to \$36M and  $32 \text{ kg/m}^2$ , respectively. These results are summarized in Figure 5.3-2.

It should be noted here that these cost and weight savings for a phase conjugate system are probably conservative. No attempt has been made to capitalize on new design concepts or fabrication techniques which might be more applicable to the more relaxed tolerances afforded by the use of phase conjugation. These might include lightweight mirror construction using SiC



- **MAJOR COMPONENTS - 5 tier construction**

1. FACESHEET
  - A. SUBSTRATE
  - B. POLISHING
  - C. COATING
  - D. HOE's
2. FIGURE ACTUATORS
3. REACTION STRUCTURE
4. PHASING ACTUATORS
5. SUPPORT STRUCTURE



- **3 tier construction integrates reaction and support structure; uses combined figure/phase actuators**

Figure 5.3-1. HI-BRITE SBL Primary Mirror Assembly

- **Beam director cost and weight summary**

	APACHE	Adaptive Optics	Change
<b>Cost (\$M)</b>	36.06	63.97	77 %
<b>Areal Density (Kg/m<sup>2</sup>)</b>	31.66	58.38	84 %

- **Cost and weight savings spread across broad range of components and fabrication processes**

**FACESHEET**

<b>Substrate</b>	Reduced requirements for APACHE give ~10% less cost for thermal expansion pedigree/testing
<b>Polishing</b>	Reduced requirements for APACHE give ~16 less polishing cycles saving ~3.9 weeks or \$62 K / tile
<b>Coating</b>	Lower sensitivity to absorption variations in APACHE eases testing (~5%)
<b>HOE's</b>	707 ± in conventional SBL @ ~\$10K each; none in APACHE

**FIGURE ACTUATORS** 707 ± in conventional SBL @ ~\$2K each; none in APACHE

**REACTION STRUCTURE** 25 Hz APACHE will hold WFE budget vs. 40 Hz conventional SBL, saving ~3 Kg / m<sup>2</sup>

**PHASING ACTUATORS** Both shown @ 6 / tile. If reduced requirements for APACHE can lock adjacent tiles, save \$0.45M

**SUPPORT STRUCTURE** 10 Hz APACHE will hold WFE budget vs. 20 Hz conventional SBL, saving ~13 Kg / m<sup>2</sup>

Figure 5.3-2. Summary of Cost and Weight Results

foam, aluminum mirrors (as opposed to ULE), and deployable optics, to mention a few of the potential design alternatives. It should also be noted that further tile optimization may be possible, especially with respect to segment sizing and the use of three-tier construction. Three-tier approaches use integrated figure/phase actuators and a single combined reaction/support structure. If sufficient inventory and adequate breakage controls are available, costs may be reduced further in three-tier construction, as cost effective, larger segments can be used without any need to further thicken an intermediate reaction structure. And although we may have to thicken the integrated reaction/support structure slightly to carry dead weight increase caused by facesheet thickening, the increase is modest compared to the five-tier case. In the latter case, a thickness for the third power increase is required to compensate for the loss in reaction structure stiffness, which varies inversely as the fourth power of segment size. Three-tier construction offers less vibration isolation than five-tier construction, but this may prove acceptable, especially with the more forgiving phase conjugated approach.

We have intentionally chosen to compare the conventional and phase conjugated approaches using the current AO SBL five-tier baseline. Future comparisons could involve, for example, comparison of a five-tiered SBL with a three-tiered phase conjugated approach. Further, the AO SBL might possibly evolve to a three mirror beam expander (BEX) with reduced dynamics/slew, regardless of primary construction, while phase conjugated versions may not need this level of complexity. Again, we have used a conservative five-tier-to-five-tier mirror BEX comparison in the current study. This choice facilitates a like-kind comparison between the two systems, leaving for subsequent work the possibility of redesigning the primary mirror to exploit phase conjugation.

The cost and areal density breakdowns for a generic 10-m primary mirror, for the AO and APACHE SBL systems, are summarized in Figure 5.3-3 and 5.3-4. Note that structural costs are comparable to those for the coated facesheet. In the following subsections, the derivations of these costs and weights are provided for each of the items listed in the table.

	APACHE		CONVENTIONAL SBL		COMMENTS
	Cost	Areal Density	Cost	Areal Density	
FACESHEET					
Substrate	\$5.46 M	16.5 Kg/m <sup>2</sup>	\$6.07 M	22.0 Kg/m <sup>2</sup>	α Pedigree, T/O sets Th Current CCOS MLD Pedigree (5%) 1 between fig. act's  9/m <sup>2</sup> = 707  SBL @ 29.7 cm APACHE @ 23.2 cm SBL @ 6 / segment APACHE ≤ SBL SBL @ 47.1 cm APACHE @ 34.1 cm  } SBL @ 18.5 man-yr APACHE @ 12.5 man-yr  SBL @ 6 players x 4 yrs APACHE@4.5playersx4 yrs
Polishing	\$6.17 M	_____	\$7.11 M	_____	
Coating	\$4.80 M	_____	\$5.06 M	_____	
HOE's	N / A	_____	\$7.07 M	_____	
FIGURE ACTUATORS	N / A	_____	\$1.41 M	3.6 Kg/m <sup>2</sup>	
REACTION STRUCTURE	\$4.05 M	4.68 Kg/m <sup>2</sup>	\$7.82 M	9.04 Kg/m <sup>2</sup>	
PHASING ACTUATORS	\$0.55 M	< 0.14 Kg/m <sup>2</sup>	\$0.55 M	0.14 Kg/m <sup>2</sup>	
SUPPORT STRUCTURE	<u>\$8.96 M</u> 29.99	10.34 Kg/m <sup>2</sup>	<u>\$20.42 M</u> 55.51	23.6 Kg/m <sup>2</sup>	
ASSEMBLY (1%)	\$1.43 M	_____	\$2.12 M	_____	
TEST (0.5%)	\$1.07 M	_____	\$1.58 M	_____	
MANAGEMENT	\$3.57 M	_____	\$4.76 M	_____	
TOTAL-PRIMARY	\$36.06 M	31.66 Kg/m <sup>2</sup> 2485 Kg/m <sup>2</sup>	\$63.97 M	58.38 Kg/m <sup>2</sup> 4583 Kg/m <sup>2</sup>	

Figure 5.3-3. Cost and Weight Comparison - Generic 10-m Primary Mirror (solid 3-m petals)

Parameter	Cost (%)		Areal Density (%)	
	APACHE	AO	APACHE	AO
Facesheet				
Substrate	15.2	9.5	52.1	37.7
Polishing	17.1	11.1	--	--
Coating	13.3	7.9	--	--
HOE's	--	11.1	--	--
Figure Actuators	--	2.2	--	6.2
Reaction Structure	11.2	12.2	14.8	15.5
Phasing Actuators	1.5	0.9	0.4	0.2
Support Structure	24.8	31.9	32.7	40.4
Assembly	4.0	3.3	--	--
Test	3.0	2.5	--	--
Management	9.9	7.4	--	--
Total:	100.0	100.0	100.0	100.0

Figure 5.3-4. Cost and Areal Density by Percent for 10m Primary Mirror of APACHE and AO SBLs

Again, the results obtained for the APACHE SBL do not as yet fully reflect the potential benefits stemming from the greatly relaxed tolerances and enhanced resiliency of phase conjugated systems. Performance advantages provided by systems resiliency are described in Section 5.3.2.

Finally, the cost study reported here has dealt solely with replication costs. Very little has been done so far on assessing differences in development costs, on-orbit integration and checkout costs, and total life-cycle costs for the two design concepts. In fact, these differences are likely to be considerable due to substantial differences in the design complexity and system tolerances between adaptive optics and phase conjugated systems. For the present purposes, however, only replication costs were considered, in part to be consistent with a parallel cost estimation study presently underway within the Air Force's SBL Architecture Program.

In what follows, detailed descriptions of the methodology used in this cost study are presented. This methodology follows a "bottom up" cost approach for a multitier mirror assembly, which considers the fabrication costs associated with each major element in the assembly. As a roadmap for how these costs are developed, it will be instructive to refer to the data in Table 5.2-3, which presents the results in the same order as they are discussed in the text.

### 5.3.2 Summary of Fabricability Study Methodology

The costs and weights calculated here are tied to actual hardware costs (i.e., LAMP) and vendor quotes and surveys. The present results have also been cross-checked against several other sources in addition to LAMP. For example, we have used data from HALO, TEAL RUBY, HST, AOA, solar telescopes, radio telescopes, and various IR&D studies, as well as historical trend evaluations. This data has been updated to represent the current state of the art (SOTA) in all areas, with specific attention given to boule production (Corning, Schott, and Hereaus Amersil inputs), Computer Controlled Optical Surfacing (CCOS--EK and Itek inputs), optical coating (OCLI and Battelle inputs), and structures (Composite Optics, Inc. and Boeing inputs).

Our models are also generally consistent with the on-going GBL Producibility Study, but the APACHE effort extends the GBL study (which currently emphasizes just the facesheet), further down into the multitiered mirror substrate. As noted earlier, our current costs are for five-tier construction, since it is the current AO SBL baseline, as well as the design form closest to that used for LAMP, and thus represents the smallest extrapolation of our past experience.

To help focus the analysis presented here, we concentrate on selected aspects of the primary mirror that have not been treated previously (i.e., coatings, and reaction/support structures) or that require updating based upon the continuing evolution in the state of the art (i.e., polishing). Phase conjugation relaxes rms wavefront error tolerances from 10X to 35X as a function of the spatial frequency of the error involved; this helps ease polishing requirements and allows us to use thinner facesheets/structures or fewer actuators (see Figure 5.3-5). In order to be conservative, in light of HEL heating and the possibility of coating pits, we have chosen to use practical as opposed to theoretical values for wall thicknesses (see Figure 5.3-6). Our thicknesses are 7.5 to 10 mm, down from LAMP's 17 mm but well over the 3 mm faces which have been produced on pieces approximately 2.5-m in diameter, and substantially higher than the 1-mm section sizes where breakage can easily occur.

We have retained ULE fused silica as the material of choice for both conjugated and unconjugated designs in this study (driven by HEL run-time, absorption, and expansion/expansion homogeneity), though lighter and/or less expensive alternatives (e.g., aluminum) may ultimately prove feasible as well as advantageous for phase-conjugated systems.

### 5.3.3 Production Costs of Raw ULE Boules

Corning has provided us with component times to manufacture the raw ultra-low-expansion (ULE) fused silica glass (a representative low-expansion faceplate material), to grind the raw boules into hexes, to hex/stack seal and/or flow-out these boule assemblies into segment size pieces, and then to wire-saw cut, grind, slump, anneal, inspect, and ship the tiles. Given a representative three-furnace based production process, we find we can produce eighteen 3-m unpolished segments in 54 weeks, while

<u>PARAMETER</u>	<u>APACHE</u>	<u>SBL</u>	<u>DRIVER</u>
Allowable higher-order RMS wavefront error	~10x - 35x	x	Brightness and spatial frequency of error
Facesheet material (alternates TBD)	"ULE"	"ULE"	HEL run-time & coating absorption, low thermal expansion & high expansion homogeneity
Facesheet thickness ( and/or # of actuators)	7.5 mm	10 mm	Residual thermo-optical error, potential coating pits, & handling

Figure 5.3-5. Allowable Life and Facesheet Thickness




<u>System</u>	<u>Diameter</u>	<u>Face/Webs</u>
LAMP	~ 2.5 m	17 mm (solid)
IR & D	1.0 m	2 mm / 2 mm
IR & D	1.8 m	3 mm / 0.2 mm (broke)
HALO	~ 2.5 m	3 mm / 1 mm
		
Conventional SBL	3.0 m	10 mm (solid)
APACHE	3.0 m	7.5 mm (solid)

Figure 5.3-6. Manufacturing of Ultralite Facesheets

a single furnace gives three unpolished segments in 27 weeks. With costs/resources of about \$50K/boule and 3.7 workers/raw segment (at an average loaded cost of \$62/hr), raw tile costs are about \$0.4M each or \$57 K/m<sup>2</sup>. If we assume both a generic 10-m aperture and a nineteen 3-m-tile geometry (reasonable for the SBL baseline at its specific aperture size), and then subsequently take 79% of this cost as a reasonable percentage to allow for the full population of a generic 10-m mirror, then the primary mirror substrate cost becomes approximately \$6.07M or \$77 Km<sup>2</sup>.

At 7.5-mm facesheet thicknesses (set by expansion/HEL factors), APACHE facesheet areal densities are 16.5 kg m<sup>2</sup>, while those for 10-mm thick SBL facesheets are 22 kg m<sup>2</sup> (see the top data-line of Figure 5.3-3). Based upon prior expansion testing/blank selection, we estimate that there could be a 10% cost savings in the raw APACHE blanks (i.e., a net 10-m cost of \$5.46M for our conjugated configuration).

#### 5.3.4 Facesheet Polishing Costs

Recent CCOS advances have resulted in polishing cost reductions and we have extended our prior cost models to account for recent Itek and EK CCOS results and parametrics as a function of segment size. All relevant fabrication steps have been accounted for, assuming prior familiarization with tool working pressure and grit sizes. Specifically, our costs account for coarse generating both segment faces, flipping and mounting the segments (concave up), generating the required aspheric shapes in a numerically controlled mill, etching to relieve stresses, precision grinding, aspherizing via purely conventional but SOTA CCOS, edging, and final figure touch-ups based upon stress relief/springing and elimination of scratches. Further cost reductions may yet prove possible (e.g., through the use of flexible laps, variable pith size/spacing, and independent correction/smoothing laps) as research in this area progresses.

Our costs have assumed use of a solid facesheet. Lightweight facesheets can be made by frit bonding a core and facesheet, NC machining, air-pressure expansion, and joining of thin-walled tubing, or water jet milling. However, the thermo-optical errors for lightweighted facesheets tend to be larger than those for solid ones, and this issue requires

further consideration before a final design selection is made. Also, consideration must be given to any limits on facesheet thickness imposed by coating forensics, i.e., the impact of environmentally induced coating pits on local temperature increases and induced stresses.

The costs to make tiles by today's CCOS techniques is only a small fraction (1/3) of that which would have been predicted based upon early CCOS work (see Figure 5.3-7), where data points out to about 3 m are based upon actuals and the remainder of the figure is based upon extrapolation). This tends to make larger size blanks more attractive from the standpoint of polishing cost alone. However, as we shall see coating costs can rise rapidly depending on the technique used. Also, as tile diameters rise, reaction structure depths increase, and structural costs become as large as those for the current facesheet.

The advantages provided by larger segments are also offset by the potential cost/schedule impacts of glass breakage. Of course, we have less edge area with larger segments which is a plus. Conversely, smaller segments can be polished by a larger number of small optical shops, and have less need for actuation. This in-turn raises the question: At what size can tiles be made completely rigid? Initial data has been summarized on parametric costs and performance for 1-, 2-, 3-, 4- and 5-m tiles as a function of all primary components (substrate, polishing, coating, HOEs, actuators, structure, etc.). This data will enable us to further refine trades associated with segment size in future work.

A generic 3-m tile takes about 30 weeks to produce using current automated CCOS techniques (see Figure 5.3-8). To obtain this information, we have assumed a representative 0.8 convergence rate, although faster convergence rates are possible (rates relate to edge area and metrology accuracy). We also assume sufficiently low and controlled stress birefringence that should we choose to edge the blank post-polishing to "avoid" the difficulty in polishing an edge, the blank will hold its figure or require only minor touch up (see "scratches," below). The number of cycles/week, the number of cycles needed, and the size of the work crew all depend somewhat upon tile size (values for a generic 3-m tile are shown). These factors will be covered in future work related to tile optimization.

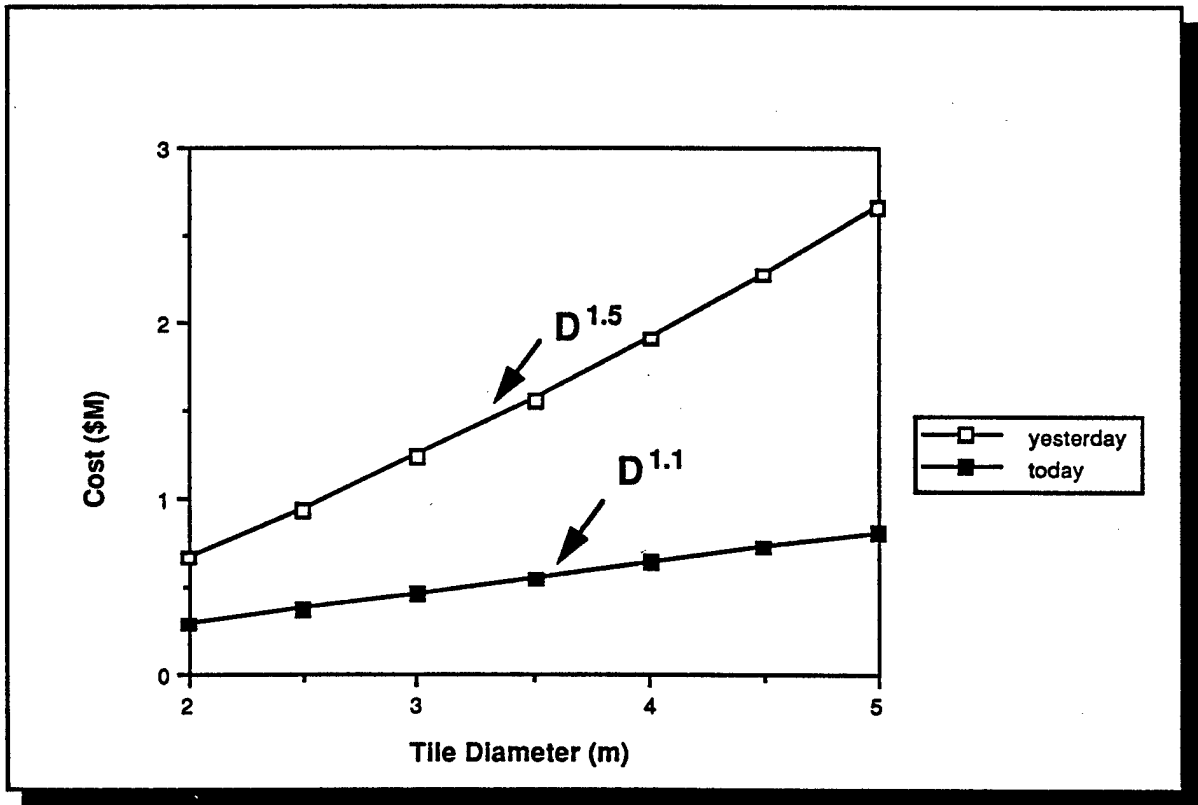


Figure 5.3-7. Cost Reductions Achieved Through Recent Advances in Computer-Controlled

## Single Shift Polishing Schedule

FABRICATION STEP	SCHEDULE
"Rough" grind and inspect	4.2 wks
Polish (77 cycles @ 4/wk.) 77.2 cycles 4.1 cycles/wk.	18.7 wks
"Polish" to $0.1 \lambda$	1.5 wks
"Scratches" ( $\rho \sim 50\%$ )	4.4 wks
Handling	0.8 wks

**TOTAL: 29.6 wks**

**Note:** A three-shift labor force would reduce polishing time by 7 weeks.

Figure 5.3-8. Single-Shift Polishing Schedule  
(crew size = 5 men)

The factor shown called "scratches" is a probabilistic factor based upon specific workshop history and has to do with removing any inadvertent anomalies induced in the mirror during the final polishing stages by pitch lap contaminants or other sources.

Today it costs about \$0.47M to make a 3-m tile to 0.1 wave peak surface quality using automated CCOS techniques, down from over \$1.2M a short time ago. This is based on a 29.6 week schedule (Figure 5.3-8) and a crew size of five people at an average loaded cost of \$80/hr. The geometry used here is the 19 segment "super-lamp" geometry (a central hex, surrounded by two rings of petals, 6 in the first ring and 12 in the second). We have used this geometry because it is one of the viable choices for larger size apertures. However, as the total area of 19 generic 3-m circular tiles is larger than needed for the generic 10-m mirror, we have introduced a 79% fill-factor to account for lowering the size of the aperture, and at the same time fully populating the mirror with contiguous (noncircular) petals. This results in costs for a nineteen 3-m tile geometry of \$7.11M, which are a reasonable approximation to the cost of a 10-m mirror (most likely composed of fewer tiles).

Note that the cost savings achievable due to relaxation of tolerances via phase conjugation are rather modest, a consequence of the overall improvements which have been made in the CCOS process. Tolerances now vary roughly as wavefront quality to the -0.11 power, in contrast to prior CCOS work, in which it varied as wavefront error to the -0.45 power. Thus a 35X relaxation of tolerances today saves only 13% rather than 5X. Similarly, today only small savings are achieved as F# are raised.

Figure 5.3-3 summarizes the results from this section. As indicated in Figure 5.3-4, the substrate represents about 9.5% of the cost of the primary mirror and, because of improvements made in the CCOS process, polishing is now only about 11.1%.

### 5.3.5 Coating and HOE Costs

The present analysis is based on inputs by Battelle, OCLI, and others, along with certain vendor-approved modifications to the input data. The MLD costs are summarized in Figure 5.3-9, and are seen to vary substantially between Battelle and OCLI. Part of the lower cost of Battelle may be due to limited experience with plant production and QA costs, but there are undoubtedly real cost savings associated with Battelle's magnetron assist sputtering process, which should be easier to scale to large sizes than conventional evaporation techniques.

A representative coating will need to be about 99.8% reflective to keep absorption less than 0.1% (assuming half the loss from scatter and half from absorption), and thereby control thermo-optical errors. To scope the coating costs, a generic GBL design was used (a silver base layer overcoated with four sets of alternating layers of magnesium fluoride/zinc sulfide) and the assumption made that coating complexity would not change greatly as the wavelength was shifted up from GBL to SBL (an assumption verified verbally by the vendors).

Since there was, as expected, a fair amount of scatter in the cost data provided to us, and since we had not yet finalized the coating method to be employed, an average cost over both vendors was used in our cost modelling (\$0.34M). At 3 m, Battelle inputs were \$0.16M while OCLI costs were \$0.5M. Costs are for MLDs and include all the experience based factors noted. Metallic coatings are not the current baseline because of their higher absorptions, although their costs are roughly half those for MLDs. In all cases the effects of coating induced wavefront error will require subsequent review to ensure that the coating processes are error budget compatible.

Note that both Battelle and OCLI costs presume facility improvements and upgrades. For example, the largest current unobscured blank which OCLI can coat with an MLD is 2.3 m (2.5 m obscured). Facility modifications are more extensive for Battelle, but they are not inconsequential for OCLI either (i.e., approximately \$15M and 41 months of development and debugging). The Battelle/OCLI "learning curves" vary (Battelle costs started 1.65X OCLIs and wound up 3.24X under OCLIs), but this information

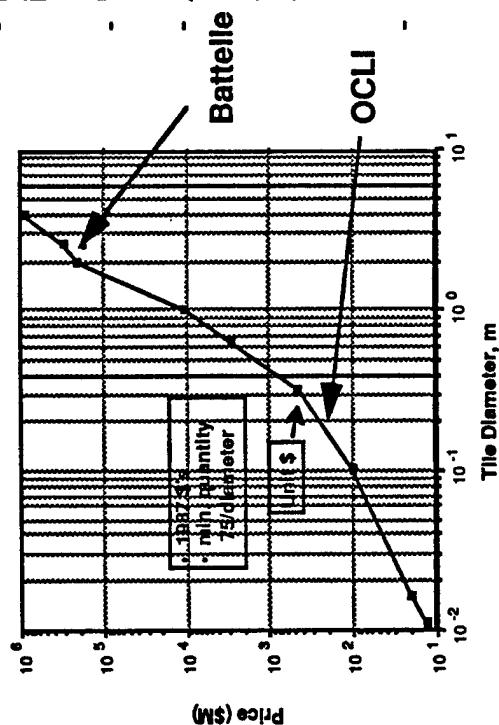
- End-of-life reflectivity should be > 99.8 % to hold absorption to < 0.1 % and thermo-optical error (~50% of loss is scatter rather than absorption, TBR)

- $(Au) \times (MgF_2 ZnS)^4$  - Low/high quarter-wave stack over gold

- Parametric cross-comparison of OCLI & Battelle data (MLD's)

- Battelle costs lower than OCLI

- Battelle magnetron assist process allows easier scale-up in size than standard evaporation techniques
- Battelle not as "tuned in" to production/QA costs
- At 3m: Battelle @ \$0.16M, OCLI @ \$0.50M
  - used average of \$0.34M
  - 19 tiles and 79% fill-factor = \$5.06 M (5% less for testing in APACHE, \$4.8M)
- Battelle has 5.35x "learning curve" (TBR)
  - starts 1.65x over OCLI
  - ends 3.24x under OCLI



- Overcoated metal ~1/2 price (easier runs, monitoring, masking, etc.)
- Includes cleaning, testing, shipping per ALPHA, MIRACL, SKYLIGHT, GBFELTIE, etc.

Figure 5.3-9. Coatings Cost Versus Tile Diameter



is compounded by varying vendor facilities assumptions, and so requires further refinement.

Costs are \$5.06M for SBL and \$4.8M for APACHE, assuming the same generic 10-m mirror/19 tile-79% fill factor assumptions used earlier. These costs allow for cleaning, testing (5% less assumed in APACHE), and shipping, consistent with ALPHA, MIRACL, SKYLIGHT, and GBFELTIE actuals, and presume production runs of tiles with quantities  $> 75/\text{diameter}$  (where diameter is measured in meters). This is 7.9% of the cost of a conventional primary mirror.

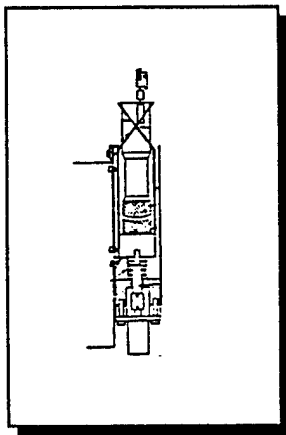
HOEs add another 11.1% to the cost of a conventional AO SBL primary (\$7.07M). For the analysis, we have assumed 10-in aperture gratings etched in Cr subcoatings, one HOE between each actuator, 9 actuators/m<sup>2</sup>, and a Perkin-Elmer based cost of \$10K/HOE. HOEs are not used in the APACHE approach, since an outgoing wavefront sensor is not required for the phase conjugate concept.

#### 5.3.6 Figure and Phase Actuator Costs

Figure 5.3-10 summarizes selected key characteristics of various figure actuators which could be employed in an AO SBL (they are not used in phase conjugate SBLs). The voice coils used in LAMP are heavy, and future generations would be expected to use lower weight voice coils or PMN (Lead Magnesium Niobate) actuators. PZT could also be used, but current versions require higher voltages than PMN, and may possess a more nonlinear response. Assuming an Itek based 14-oz (0.4 kg) actuator at \$2K per, coupled with 707 actuators (9/m<sup>2</sup> over a 10-m aperture), we obtain total costs of \$1.41M and weights of 283 kg (620 lb or 3.6 kg/m<sup>2</sup>). Note that the 14-oz actuators used allow for strokes over 20  $\mu\text{m}$ .

Figure 5.3-11 summarizes similar key characteristics for lead screw, stepper-motor based bi-pod phase actuators. With 3 bi-pods per segment we have 114 individual actuators over 19 tiles. At 0.2 kg/bi-pod and \$4.8K/actuator (Itek's lightweight design data), we computed areal densities of about 0.14 kg/m<sup>2</sup> and costs of \$0.55M. Given the reduced sensitivity to tilt and piston error for phase conjugate systems, realization of further cost and weight reductions would be plausible for

- Required in conventional SBL only



PMN

**LAMP:** first generation voice coil ~4 lb each

future generations have reduced weight  
voice coils or PMN

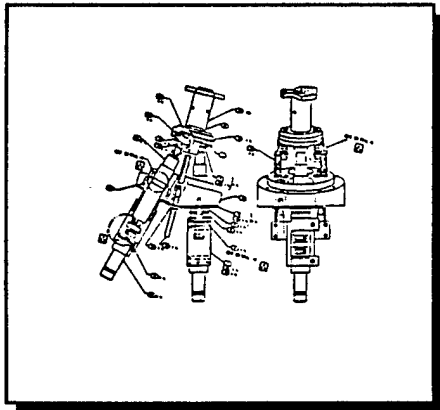
**PMN:** PbMg Niobate ~6 oz. - 14 oz. each, with  
driver/electronics; > 20  $\mu\text{m}$  stroke, 0.02  $\mu\text{m}$   
resolution, > 10 Hz bandwidth

**PZT:** ~7 oz. each  
25  $\mu\text{m}$  stroke, 0.01  $\mu\text{m}$  resolution,  
100 Hz @ 5  $\mu$  bandwidth  
high voltage and linearity concerns

Figure 5.3-10. Figure Actuator Concepts

**Requirements :**  $\leq 35 \mu\text{m}$  stroke,  $0.03 \mu$  resolution, 10 Hz bandwidth

**Solution :** Lead screw/stepper motor (voice coil or PMN are alternates)



- 6 / segment ~114 actuators  
if 19 tiles
- 0.2 Kg / bipod actuator ~  $0.14 \text{ Kg} / \text{m}^2$
- \$4.8 k / actuator ~ **\$0.55 M**
- Lightweight designs for production TBD (ITEK)
- May be able to lock tiles in APACHE  
If so: 20 actuators @  $0.05 \text{ Kg}/\text{m}^2$  and \$0.10 M

Figure 5.3-11. Lamp-Like Segment Phase Actuators

APACHE. For example, if the reduced sensitivity to alignment allows adjacent tiles to be locked together, then it may become possible to lower the number of bi-pod actuators to 20, yielding areal densities as low as  $0.05 \text{ kg/m}^2$  and costs around \$0.10M.

#### 5.3.7 Reaction and Support Structure Costs

Again, five-tier construction is assumed for the present analysis. The fabrication and thermo-optically-induced wavefront errors affect the remaining wavefront error budgets available for slew and random vibration. The residual allowables were computed and used to size the bending stiffnesses needed. These stiffnesses were in-turn used to set the reaction and support structure natural frequencies, depths, and section properties. Weights of the reaction and support structures were then established based upon these conceptual designs. These weights were subsequently related to costs.

A simplified error budget flow-down is shown in Figure 5.3-12. (The complete error budget flow down is presented in Reference 1.) Beam expander residuals set allowable reaction structure bending (tile faceplates are distorted by errors in the reaction structure). They also set allowable support structure bending, because distortion of the support structure results in intersegment piston and tilt errors.

Error sources for a representative bulkhead required to hold a phased array of telescopes in position relative to each other are also shown in the budget. The simplified budget is in turn based upon much more detailed budgets which cover and define each term.

Table 5.3-13 further summarizes how the error budget drives various structural requirements. Segment dynamic wavefront tolerances influence the design of the reaction structure. Likewise, segment-to-segment dynamic misalignment tolerances (piston and tilt) set constraints on the support structure. These allowables depend, in part, on the wavefront correction capability which can be accessed using other parts of the control-loop (i.e., the figure actuators and deformable mirrors). The larger error values, prior to correction via control loops, drives the design of the structure, thereby avoiding over-design of the structure stemming from overly restrictive error tolerances. Reaction structure natural frequency

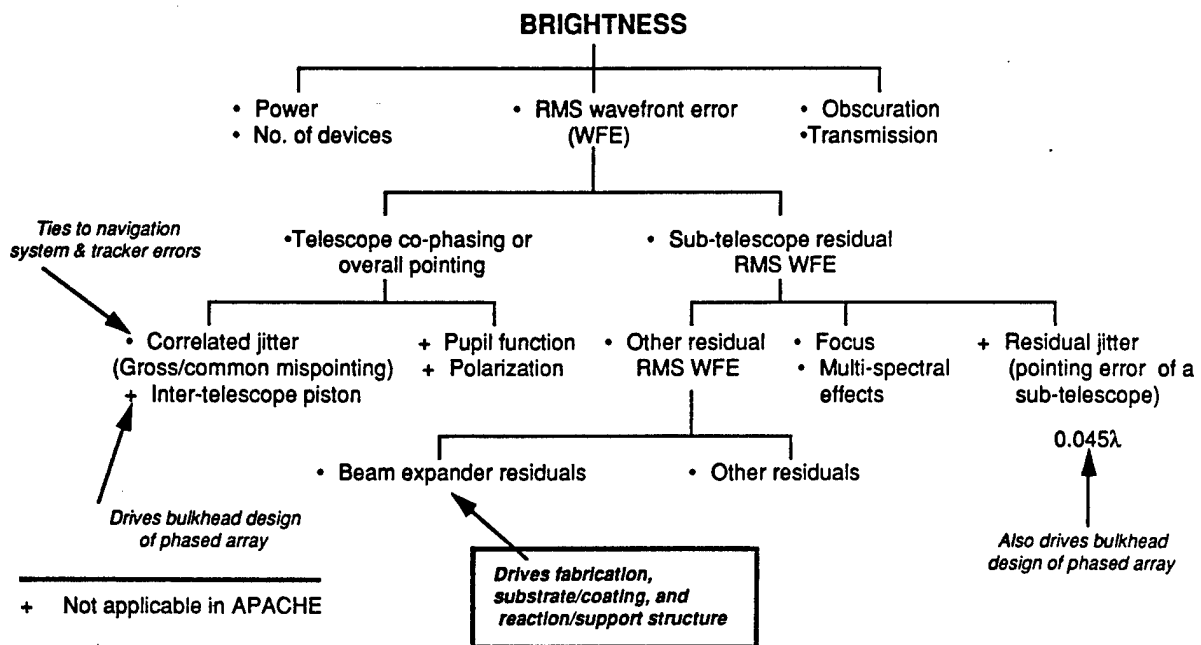


Figure 5.3-12. Flowdown of Error Budgets to Set Requirements for Reaction and Support Structures

<u>PARAMETER</u>	<u>APACHE</u>	<u>SBL</u>	<u>DRIVER</u>
Structure material	Metal matrix composite (or graphite-epoxy)	Metal matrix composite (or graphite-epoxy)	Potential outgassing/ survivability, lower weight but higher cost
Reaction structure natural frequency	25 Hz	40 Hz	Segment dynamic higher order wavefront tolerances set required bending stiffness and depth/weight
Support structure natural frequency	10 Hz	20 Hz	Segment-to-segment dynamic piston and tilt tolerances set required bending stiffness and depth/weight
Structural gauges	0.015"	0.015"	6 tier layup of 2.5 mil Gr/Mg metal matrix material ( ≥ 5 mil open weave in Gr/Ep)

Figure 5.3-13. Reaction and Support Structures for APACHE and A0 SBL

requirements will be seen to vary from 40 Hz (AO SBL) to 25 Hz (APACHE), while support structure requirements will be seen to vary from 20 Hz to 10 Hz, respectively, in order to satisfy the error budget.

Our designs are currently based upon using metal matrix composites (MMC). Our baseline uses 6 tier layups of 2.5 mil Gr/Mg material (a more common MMC). Although MMCs provide improved stiffness-to-weight over Gr/Ep (and less potential outgassing), they are more expensive and less mature than Gr/Ep. The material choice needs further review, including trades with emerging materials like SiC, where costs could decrease as molds are amortized over a larger number of units.

As shown in Table 5.3-14, figure actuators are slow but have fairly large stroke. Conversely, deformable mirrors are fast but have smaller strokes. If the vibration of the reaction structure exceeds either 100 Hz or  $3.3\text{ }\mu\text{m}$ , the errors will be beyond the bandwidth and range of the deformable mirror and must be absorbed in the error budget. For this reason, the budget for allowable reaction structure vibration had been previously set at about  $3.3\text{ }\mu\text{m}$ . Here, we attempt to control high-frequency slew and vibration-induced reaction structure deformations to under  $3\text{ }\mu\text{m}$ , to keep tile wavefront errors (WFEs) within budget with some margin (10%) for safety.

Figure 5.3-15 indicates that support structure deformations of 0.15 to  $0.22\text{ }\mu\text{m}$  are allowed by the error budget without using the control system (the deformable mirror in this case) to ease tolerances. Considering the correction capability of the deformable mirror, it might initially appear that "raw" support structure deformation errors could be allowed to grow to as large as 15.6 to  $22.6\text{ }\mu\text{m}$ . However, errors this large exceed the nominal  $2\text{-}\mu\text{m}$  stroke of the deformable mirrors (DM). We must therefore limit the errors to the range of the deformable mirror(s) plus the error budget allowance (i.e., the  $2\text{-}\mu\text{m}$  DM stroke plus the approximate 0.2 micron error budget allowance). We have used a 10% safety factor similar to the reaction structure in sizing structural components.

To scope the thermo-optical/facesheet portion of the error budget and thereby establish an allowable residual for the support and reaction structure dynamics, we initially assume 0.1% absorption and a 10-mm-thick solid facesheet. Under these conditions, temperature soaks (average

	<u>Unconjugated SBL</u>		<u>APACHE</u>	<u>Comments</u>
Correction Mechanism:	Figure Actuators	Deformable Mirrors	SBS Cell	-----
Bandwidth:	10 Hz	100 Hz	MHz	-----
Deflections allowed by correction mechanism:	20 $\mu\text{m}$	2 $\mu\text{m}$ (to 10 $\mu\text{m}$ ) 3.3 $\mu\text{m}$ used	20 $\mu\text{m}$	SBS Cell limited by beam expander configuration
Deflections by higher order WFE budget:	3.3 $\mu\text{m}$		9.2 $\mu\text{m}$	With correction factor of control loop easing tolerances
Resultant R/S deflection design criteria:	3.0 $\mu\text{m}$		8.2 $\mu\text{m}$	Allows 10% safety

Figure 5.3-14. Deformation of APACHE and AO SBL Reaction Structures



- Note:
- High brightness APACHE S/S is 2.6 times the size of that used in a conventional SBL S/S
  - Unconjugated SBL weight & cost must account for added stiffness need in inter-telescope bulkhead

	<u>Unconjugated SBL</u>	<u>APACHE</u>	<u>Comments</u>
Correction Mechanism:	Deformable Mirror (DM)	SBS Cell	-----
Bandwidth:	100 Hz	MHz	-----
Deflections allowed by correction mechanism:	2 $\mu\text{m}$ (to 10 $\mu\text{m}$ )	20 $\mu\text{m}$	SBS Cell limited by beam expander configuration
Deflections allowed by piston & tilt error budget:	15.6 $\mu\text{m}$ - 22.6 $\mu\text{m}$ 0.15 $\mu\text{m}$ - 0.22 $\mu\text{m}$	5.6 $\mu\text{m}$ - 11.2 $\mu\text{m}$ (8.4 $\mu\text{m}$ , ave) N/A	With correction factor of DM easing tolerances Without DM easing tolerances
Resultant S/S deflection design criteria:	$0.9 \times (2 \mu\text{m} + 0.2 \mu\text{m})$ 2 $\mu\text{m}$	7.6 $\mu\text{m}$ , ave	Allows 10% safety

Figure 5.3-15. Deformation of APACHE and S0 SBL Support Structures

temperature level changes) of  $6.4^{\circ}\text{C}$  and axial temperature gradients of  $0.82^{\circ}\text{C}$  are produced. These loads generally produce low spatial frequency errors in the faceplate, which are both corrected by the actuators and DM, and initially restrained by the reaction structure upon which the faceplate is flexured and mounted. Even global expansion inhomogeneities and variations of expansion with temperature, as well as anomalies in the HEL profile itself (giving rise to lateral variations in the axial gradient, LVAG) turn out to be relatively inconsequential. The only significant term is the local inhomogeneity (in-between actuators) in the axial expansion coefficient. This gives rise to higher spatial frequency wavefront errors of about  $0.116\text{ }\mu\text{m}$  (about 0.02 waves RMS WFE at HF) which are not correctible, and must therefore be absorbed in the error budget (see the middle line of Figure 5.3-16). Likewise, thermo-optical errors in the HOE's also need to be absorbed in the conventional SBL designs, further decreasing SBL allowables over phase-conjugated APACHE structural requirements.

The possibility exists for further improvements in thermal expansion control within the boules. The degree to which this can be achieved is uncertain at present, and would require further experimentation, possibly in conjunction with the normal tuning of the production process. Note that the ability to limit expansion variations improves as the tile size decreases.

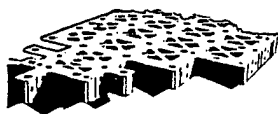
With respect to the reaction and support structure raw materials, metal matrix composites such as Gr/Mg are beginning to come on-line. Tubes and eggcrates have been successfully produced by multiple vendors (see Figure 5.3-17). As noted in the table, mechanical properties are generally better than Gr/Ep (which has its own complexities, such as vapor barriers and humidity control). However, despite its choice as the baseline for the AO SBL, since costs are higher for Gr/Mg (and SiC) than for Gr/Ep, further cost optimization should be possible.

Once the allowable wavefront errors and material properties are known, the bending stiffness of the reaction and support structures can be established. From this, reaction and support structure depths and weights are then computed. Figure 5.3-18 shows both the resultant structural depths and areal densities needed to achieve balanced error budgets as a function of required bending stiffness and web characteristics. Webb

ERROR SOURCE	<u>UNCONJUGATED SBL</u>			<u>APACHE</u>			<u>DRIVES</u>
<u>(Primary Mirror Segment)</u>	<u>Alone</u>	<u>w/ deformable mirror</u>		<u>Unconj.</u>	<u>Conjugated</u>		
		<u><math>\lambda</math>'s</u>	<u><math>\lambda</math>'s</u>		<u><math>\lambda</math>'s</u>	<u><math>\lambda</math>'s</u>	
		<u><math>\mu</math>m</u>	<u>PK surf</u>		<u><math>\mu</math>m</u>	<u>PK surf</u>	
Fabrication tolerance (@ 4 cycles/meter)	0.009	0.009	0.063	0.010	0.1	0.7	Manufacturing
Thermo-optical error	0.02	0.02	0.14	0.014	0.14	0.98	Substrate, coating
<b>Structural-vibration/slew</b>							
Higher order WFE	0.014	0.47	3.3	0.024	1.31	9.2	Reaction structure
Piston	0.032	3.20	22.6	0.013	1.6	11.2	Support structure
Tilt	0.022	2.20	15.6	0.015	0.8	5.6	Support structure
	(0.2 $\mu$ m PK surf)						

Figure 5.3-16. Allowable WFE for APACHE and A0 SBL PM Segments

- Gr/Mg metal matrix material - Composite Specialties Inc., DWA Eng'g, UTRC, Textron
- Zero expansion made in tubes (along tube axis) - DWA Eng'g
- Eggcrates made to match molybdenum expansion - UTRC
- Costs vary as function of construction details, pedigree, (vapor barrier in Gr/Ep), etc.



<u>PARAMETER</u>	<u>Gr/Ep</u>	<u>Gr/Mg</u>
E, Young's Modulus	15 x 10 <sup>6</sup> psi	25 x 10 <sup>6</sup> psi
p, density	0.065 lb/in <sup>3</sup> (1)	0.085 lb/in <sup>3</sup>
v, Poisson's ratio	0.31	0.30
α, thermal expansion	0.06 x 10 <sup>-6</sup> /°F (2)	2.5 x 10 <sup>-6</sup> /°F (3)
Layup state-of-the-art	5 mil open weave	15 mil (4)

(1) Fiber ~ 0.073 lb/in<sup>3</sup>, resin ~ 0.05 lb/in<sup>3</sup>

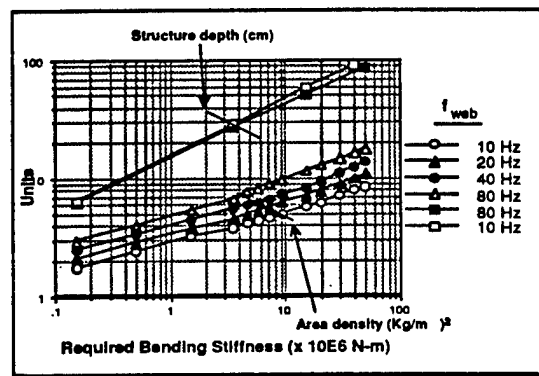
(2) for 60% fiber (typ.)

(3) 13 x 10<sup>-6</sup>/°F perpendicular to plane of sheet stock

(4) 2 1/2 mil stock x 6 sheets (0°, ±60°). 1 1/4 mil stock appears possible but not now in development

Figure 5.3-17. State-of-the-Art Reaction and Support Structure Material Parameters and Costs

- Required bending stiffness (K) established
- Hand calculations of R/S (3m) & S/S (10m) depth  
(15 mil gauges, higher natural frequency,  $F_N$ , of WEBS to decouple)



Parameter	R/S (3m)		S/S (10m)	
	Conventional	APACHE	Conventional	APACHE
$F_N$ , Hz	40	25	20	10
$K$ , $10^6$ N-m	0.39	0.09	16.67	2.39
Depth, cm	29.7	23.2	47.1	34.1
Kg/m <sup>2</sup> (\$5k/lb)	4.52	2.34	11.8	5.17
For now used with 2x safety factor (TBR)				

Figure 5.3-18. Stiffness, Weight, and Cost

natural frequencies are held higher than overall structural natural frequencies to prevent dynamic cross-coupling. Since real structures rarely achieve predicted stiffness due to joint compliance and related factors, we have used a safety factor of 2X on areal density to help ensure design realism at this early stage of conceptualization.

As shown in Figure 5.3-19, we have used a factored, average vendor cost for Gr/Ep of \$2.5K/lb in production (down from today's average \$3.7K/lb). This means we have projected that factory automation will reduce the fabrication/management cost component of the production cost by 50%. Raw material costs were held fixed at current levels. MMC costs were set at approximately \$5K/lb based upon rule-of-thumb scaling (2X) from Gr/Ep.

Costs and areal densities are again summarized in Figure 5.3-3 in spread sheet format: \$7.82M and 9.04 Kg/m<sup>2</sup> for a conventional SBL reaction structure, \$4.05M and 4.68 Kg/m<sup>2</sup> for a phase conjugated reaction structure like APACHE, and \$20.42M, 23.6 Kg/m<sup>2</sup>, \$8.96M, and 10.34 Kg/m<sup>2</sup> for the same parameters, but for the support structure, respectively.

#### 5.3.8 Assembly, Test and Management Costs

The assembly process used in current support structures is fairly complex. An effort needs to be devoted to improved tooling and assembly techniques. For example, the assembly and production process currently involves over 15 steps which are all currently hand work (panel layup, rough cutting diameters, machining in mortise-tenons, closure rings, main rings, ribs and actuator holes, cutting honeycomb assemblies, bonding ribs, machining access panels, mounting rivnuts for panels, assembling and bonding subassemblies and assemblies, mounting actuators, and so forth). Clearly, many opportunities exist to lower production costs through automation.

Figure 5.3-20 extends our preliminary review of structural assembly and test to the other components in the primary mirror. A rough parts count and work crew size is estimated for each component of the primary. Here we assume that some processes will be sufficiently automated (actuator assembly) or different enough in character (construction of the HOEs), that

- Graphite/Epoxy (Gr/Ep) structural cost estimates show wide variability
  - BSTS @ \$1.9 k/lb
  - Boeing @ \$2.0 k/lb
  - LAMP @ \$3.2 k/lb
  - STARLAB @ \$7.5 k/lb
 } Average = \$3.7 k/lb
- Structural cost likely to come down with automation

	<u>1st runs</u>	<u>In production</u>	<u>Comments</u>
Tools	50%	—	—
Material	15%	30%	—
Fabrication	25%	} 70%	Might cut in-half with automation
Management	10%		

- Gr/Ep costs with automation  $\sim 2/3 \times \$3.7 \text{ k/lb} = \$2.5 \text{ k/lb}$

Gr/Mg metal matrix costs approximately twice Gr/Ep (TBR) per "rule-of-thumb"

- Boeing
- TEXTRON
- Composite Optics, Inc.

Figure 5.3-19. Summary of Vendor Survey Used to Establish Cost Base for Lightweight Structures

• **Assembly & Test**

Unconjugated SBL			APACHE		
Item	# components	crew size	# components	crew size	Comments
Segments	19	4	19	4	
Holographic Patches	707	2	---	---	Assume "special" treatment on 10%
Figure Actuators	707	4	---	---	Assume "special" treatment on 10%
Reaction Structure	19	4.5	19	4.5	Crew also works on support structure
Phase Actuators	114	4	<114	4	
Support Structure	1	above	1	above	Crew covered under reaction structure
<hr/>					
	> 295	18.5	153	12.5	"Effective" parts-count total (see above)
<hr/>					
Assembly/Test Cost		\$3.7 M		\$2.5 M	At \$0.2 M/man-yr assuming 1-yr schedule
- Assembly (~4%)		\$2.12 M		\$1.43 M	RCA "Price" model plus rules-of-thumb
- Test (~3%)		\$1.58 M		\$1.07 M	Airborne Optical Adjunct plus rules-of-thumb
<hr/>					
• Management-cost ( ~10%)	\$4.75 M		\$3.57 M		APACHE @ 4.5 players x 4 yrs (Mgr, APM, QA, Admin.); Unconjugated SBL @ 6 players x 4 yrs (additional QA & sub-contracts mgmt.)

Figure 5.3-20. SBL PM Assembly, Test, and Management Costs



we can use only 10% of the parts count to get a measure of system complexity (i.e., an "effective" parts-count). Rough costs are computed from these estimated crew sizes assuming an average cost of \$0.2M/man-year assuming a 1-year schedule. These costs (\$3.7M for a conventional SBL and \$2.5M for APACHE) were subsequently further subdivided into assembly and test costs based on the RCA "Price" Model and rules of thumb generated under the Airborne Optical Adjunct Program. This results in approximately 4% for assembly costs and 3% for test costs (beyond the testing associated with mirror fabrication).

Likewise, the number of persons needed in the program office for both conventional and phase conjugated approaches has been estimated based upon the nature of the work and the number of hardware components. Taken over a 4-year production period, costs are \$4.75M (SBL) and \$3.57M (APACHE), which turn out to be roughly 10% of the total costs anticipated.

#### 5.3.9 Scale-Up Issues

The scale up of a single segmented mirror telescope (SMT) is fairly straightforward and goes roughly as the number of tiles. Scale-ups to high brightness systems, however, are more complex; for phased array systems, for example, a central inter-telescope support structure needs to be scaled. This is currently an area of interest in the astronomical community (e.g., for the so-called "super hubble" telescope), and significant developments in this area are expected to benefit the scale-up analysis for SBL systems.

Various scale-up approaches have been previously proposed, including, for example, the multiple-mirror telescope (MMT, pointing via a common mount), the VLT (or BIG EYES, venetian blind pointing), or the rotating shoe (a "skate board" mirror scans in azimuth while the secondary sweeps the skate board for elevation). However, in-depth cross comparisons have not been carried out, as these systems have generally been pursued to take advantage of some special opportunity or serendipity (e.g., availability of government surplus mirror blanks in the case of the MMT). It remains for future work to systematically address the relative advantages and disadvantages of the various approaches, and to adapt existing cost and weight models to these configurations.

#### 5.4 LASER DEVICE COST AND WEIGHT ESTIMATES

The purpose of this section is to provide weight and cost estimates for the laser device subsystem of the baseline APACHE and phased array point designs, and provide insight into the methodology that was utilized to develop the weight and cost models. Table 5.4-1 summarizes the requirements for output power per module (module size) and number of modules for both the APACHE and phased array design points. These requirements flow down from the system-level performance budget.

The weight and cost models employed in this comparison were developed utilizing a modular approach. The laser device subsystem was divided into assemblies and subassemblies as depicted in Table 5.4-2. The advantage of this "bottom-up" approach is that it allows the weight and cost algorithms to be developed by engineers that are familiar with the specific device area. This leads to a model that is more easily updated as new information becomes available in a particular area. One of the disadvantages of this approach is that it requires coordination on the system level to assure that a consistent set of model development guidelines are being followed.

While the APACHE system and the adaptive optics system are very different, on the device level they are essentially equivalent. In this modeling effort, for the two laser systems, the amplifier modules use the same cost and weight algorithms.

The algorithms utilized to model the laser device weight were originally developed on the ALPHA Program (1986). The gain generator assembly (GGA) and optical resonator assembly (ORA) were modelled in detail on this program to examine the impact of scaling to an ALPHA II device. These algorithms have been recently reexamined under the Space-Based Laser Concept Formulation and Technology Development Program (SBL CF&TDP) and required only minor modifications. The weight model for the reactant storage and supply assembly (RSSA) has been reformulated under SBL CF&TDP to incorporate the most recent data available on long-term cryogenic fluid management in a space environment.

Table 5.4-1. HEL power Requirements Are Derived Directly from System Requirements

	APACHE	Phased Array
Power per Module (x ALPHA)	20.0	23.8
Number of Modules	6	7

Table 5.4-2. Weight and Cost Algorithms Developed for the Laser Device on the ALPHA and SBL CF&TDP Programs

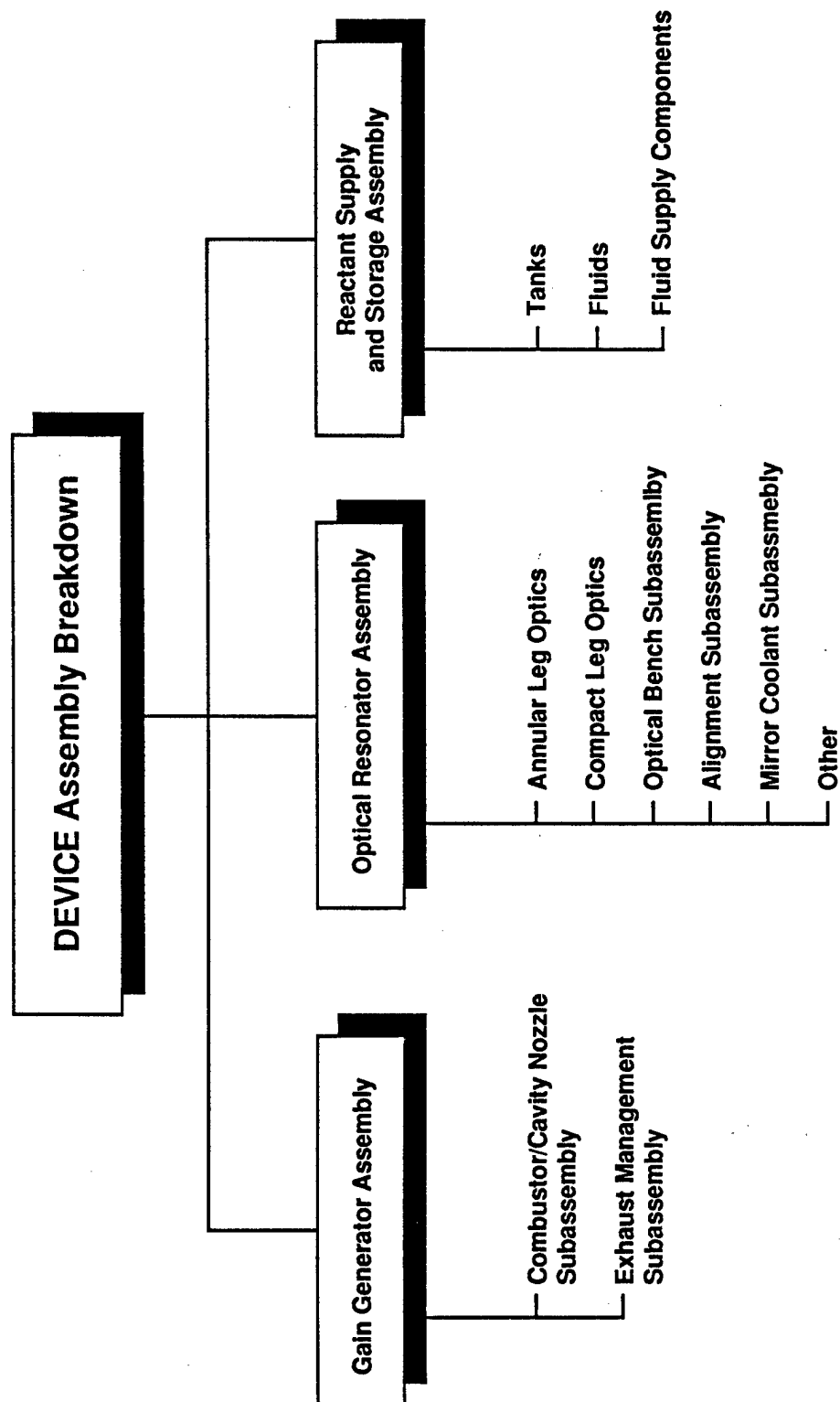


Figure 5.4-1 illustrates that the laser device weight is primarily a function of the required output power and runtime. Figure 5.4-2 depicts the major impact runtime (fluids) has on the overall device weight. Even at half the required runtime, fluids dominate the overall weight of the device.

The cost algorithms used in this model were originally developed for SBL CF&TDP in 1988. As seen in Figure 5.4-3, cost algorithms, like weight algorithms were developed with a bottom-up approach. There are several groundrules or assumptions that affect the cost estimating relationships (CERs) utilized in this comparison. The CERs are for a first production unit recurring cost, there is no "learning factor" applied to these algorithms. The algorithms do not include development costs, design costs, or facility construction costs. The cost basis for the gain generator assembly (GGA), and the optical resonator assembly (ORA) was the ALPHA Program. The ALPHA actual costs were examined to determine the recurring portion of this cost. A complexity factor was then determined to account for the transition from a ground-based demonstration device to an operational space-based laser. The Mirror Coolant System (MCS), which is included in the ORA, and RSSA are substantially different, for an SBL application, than the analogous assemblies on the ALPHA device. Vendor estimates, with applied complexity factors, were used to develop the cost basis for these components. Scaling relations were then developed for each device component. These scaling relations were combined to yield assembly level cost algorithms. The overall device subsystem cost estimating relationship is produced by combining the assembly level cost algorithms and adding in the program level cost on cost.

Figure 5.4-4 illustrates that device cost (for a fixed runtime) is primarily a function of the required output power. Due to its increased power requirement, the adaptive optics amplifier system is always more expensive than an APACHE amplifier. Figure 5.4-5 illustrates how dominant the hardware costs are over the fluid costs. While the runtime dependent (fluid weight) is the major weight contributor, it is only a minor contributor towards cost.

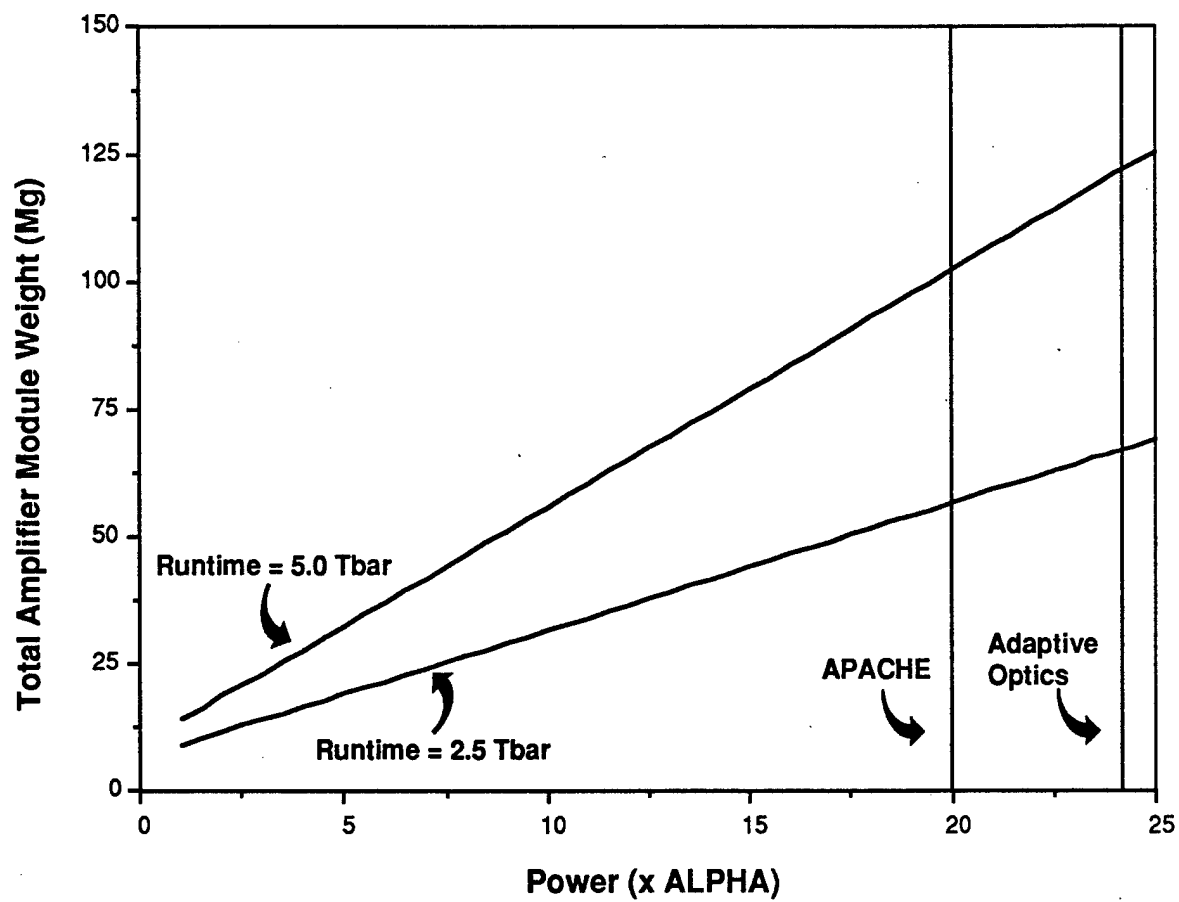


Figure 5.4-1. Weight Is Primarily Dependent Upon Power and Runtime

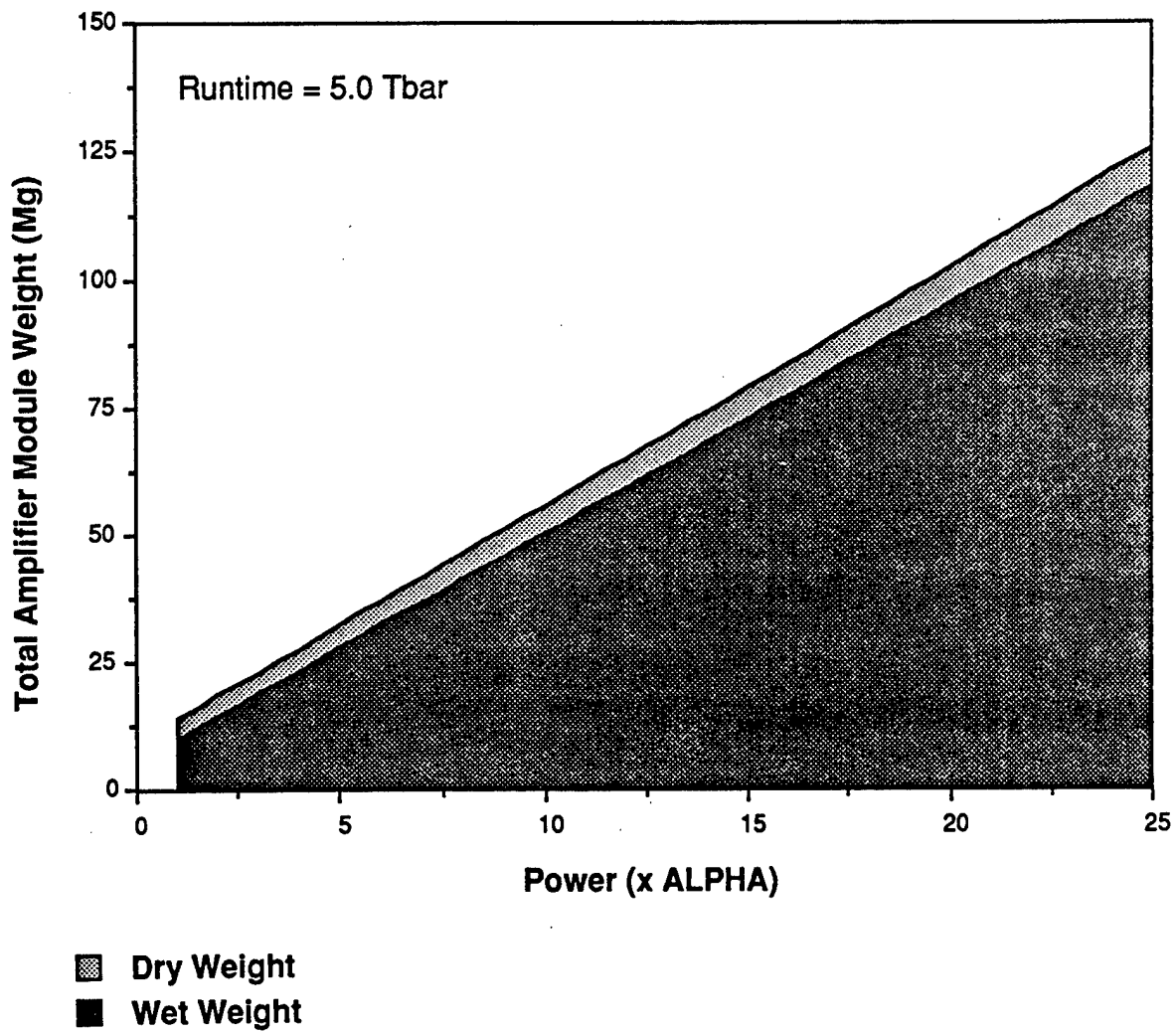


Figure 5.4-2. The Runtime Dependent Components Are the Dominating Weight Drivers

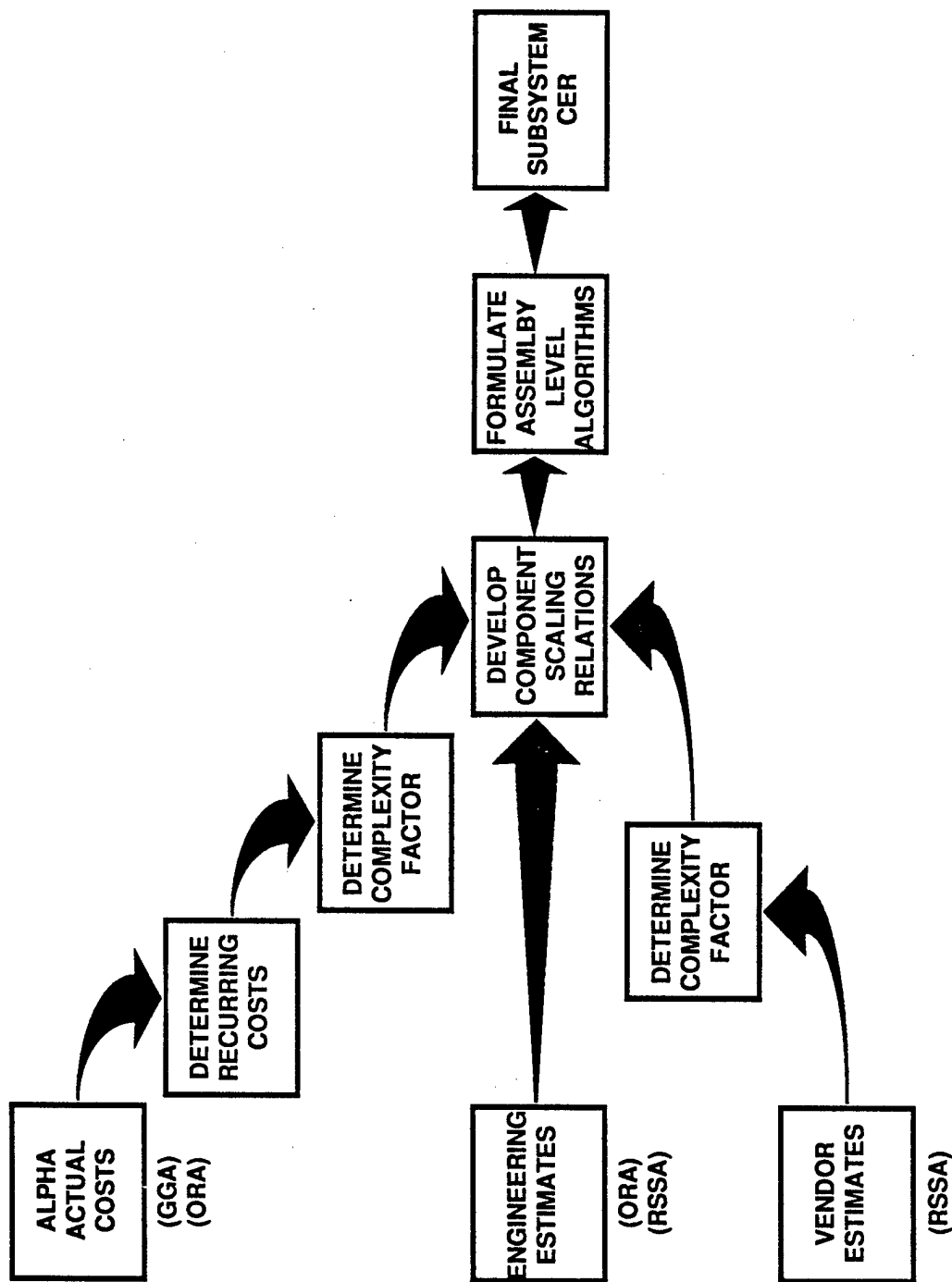


Figure 5.4-3. Cost Estimating Relationship (CER) Development Methodology



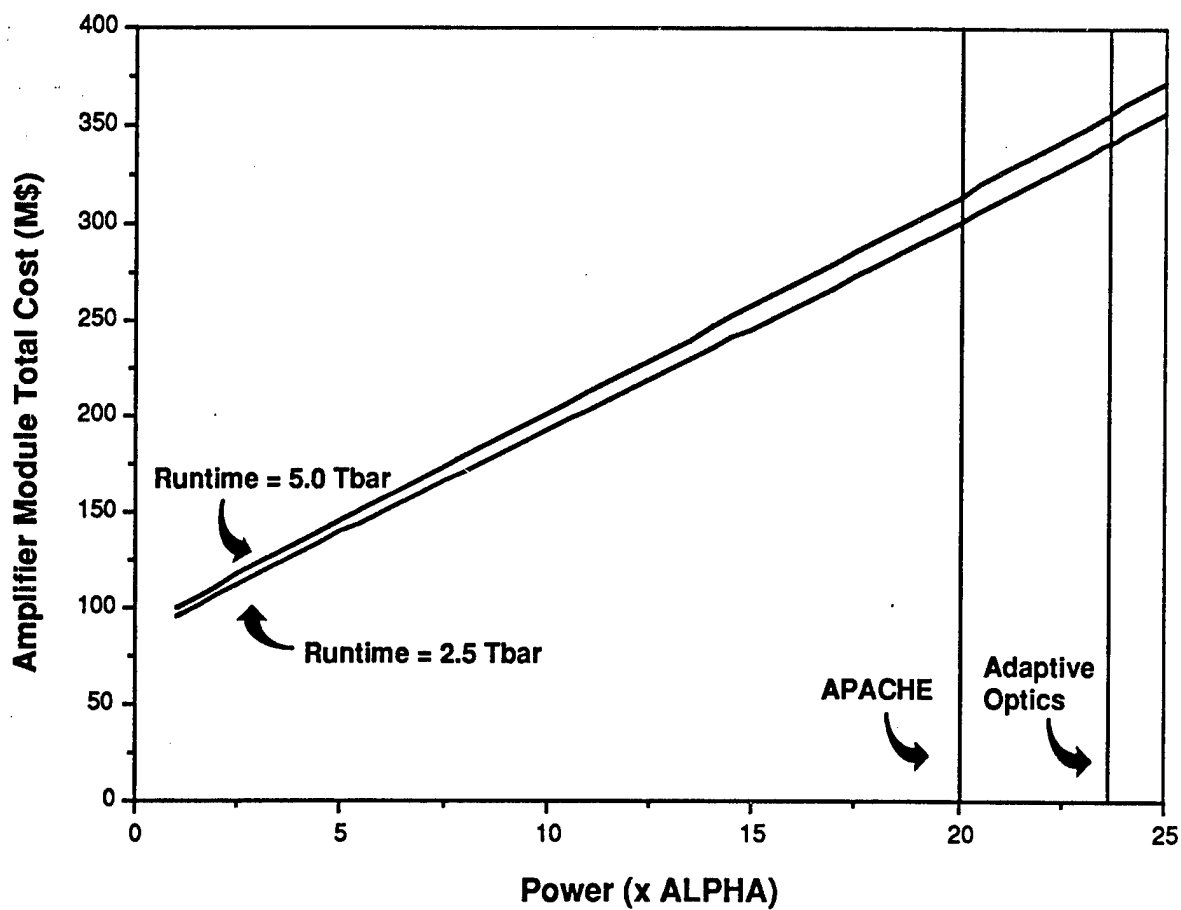


Figure 5.4-4. Cost Is Mainly Driven by Power Requirements

In Table 5.4-3, a summary of the two systems' cost and weight is presented; these costs include the cost for program management. Program management cost is simply a multiplication factor of 1.56 times the hardware cost. As indicated in the cost and weight curves in Figures 5.4-1 and 5.4-4, weight and cost scale linearly with power. The APACHE amplifier module is always less expensive than the adaptive optics amplifier module. This is due to a reduced power per module needed and fewer number of modules required. The cost per pound for an HEL with no reactants and with full runtime reactants are given as well. While the APACHE system has a lower overall device cost and weight, the cost per pound for the two systems is very comparable. This is expected since the cost and weight functions are linear.

Table 5.4-3. Laser and Reactant Cost and Weight Summary

Program Level Cost Included	APACHE SBL	Adaptive Optics SBL
Cost per Module (M\$)	493	561
Number of Modules per SBL	6	7
Total HEL Device Cost (B\$)	3.0	3.9
Total HEL Device Weight (Mg)	612	840
Cost Per Pound (K\$/lb)		
Total HEL Device (without reactants)	33.3	34.1
Total HEL Device (with reactants)	2.2	2.1

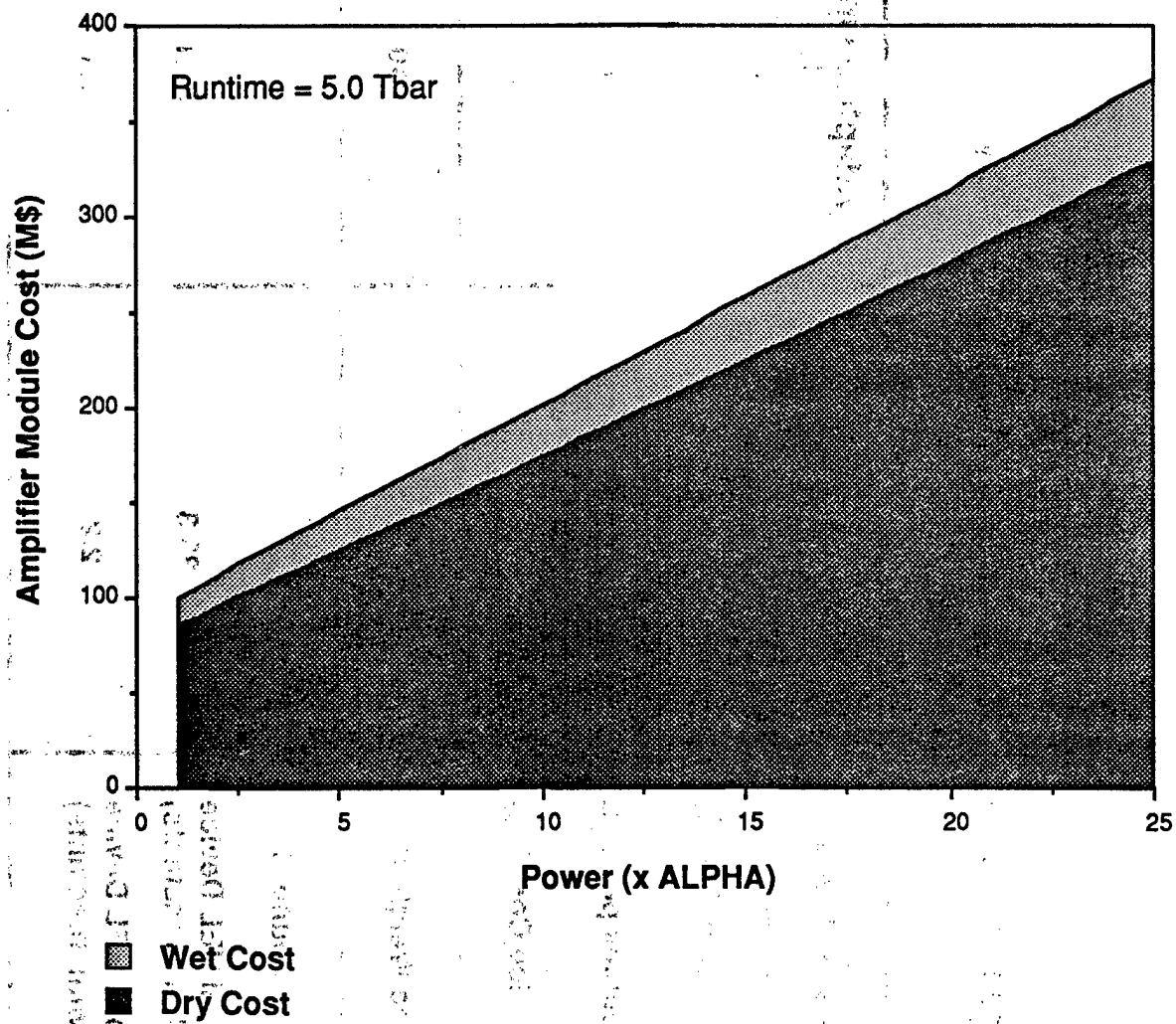


Figure 5.4-5. The Nonruntime Dependent Costs Are Dominating